Investigation of the mechanical performance of natural fibres and their composites

A thesis in fulfilment of the requirements for the degree of

Doctor of Philosophy

By

José Luis Rudeiros Fernández

Department of Mechanical and Aerospace Engineering

University of Strathclyde

Glasgow

Scotland

UK

2016

Declaration of Authenticity and Author's Rights

This thesis is the result of the author's original research. It has been composed by the author and has not been previously submitted for examination which has led to the award of a degree.

Signed:

Date:

Acknowledgements

First and foremost I would like to thank my supervisor, Professor James Thomason, for his continual support, supervision, guidance and advice throughout my PhD. I am truly grateful and indebted to him, for all knowledge he has given me, and most importantly, the scientific thinking and values he has helped me to cultivate. I would also like to express my gratitude to Dr John Liggat as my second supervisor for his support and assistance.

I am thankful for the financial support of SABIC and the EPSRC. I would like to express my special thanks to Dr Maria Soliman and Dr Ajay Taraiya from SABIC, for their continual support and advice. Their expert advice on polymers and composites from an industrial research perspective have been an invaluable input for this project, for which I am sincerely grateful. I also wish to thank the University of Strathclyde, the Department of Mechanical & Aerospace Engineering, and in particular the Advanced Composites Group (ACG) for their continual support during this project. I would like to thank my friends and colleagues with whom I have worked, collaborated and shared many enjoyable moments at the ACG, especially Dr Liu Yang, Dr Chih-Chuan Kao, Dr Fiona Gentles, Susan Roch, Dr Peter Jenkins, Kerrie Downes, Dr Eduardo Sáez Rodriguez, and Dr Ulf Nagel. I would also like to extend my thanks to the Advanced Materials Research Laboratory, and especially to Dr Fiona Sillars and Gerry Johnston for their support and assistance. I also wish to acknowledge the assistance from the Department of Mechanical & Aerospace Engineering Technicians, with special mention to James Kelly, Chris Cameron, James Gillespie, and Jim Doherty.

Last but not least, I would like to show my deepest thanks to my family and girlfriend Lesley, for their unconditional love, support and encouragement throughout this work.

Abstract

During the last decades, natural fibres, considered to be an environmentally sustainable alternative to some human-made fibres and mineral fillers, have been increasingly used as reinforcements in composite materials. Aspects such as governmental environmental regulations, and increasing social awareness of sustainability, have been driving the increasing interest of these "green" materials, and particularly natural fibre reinforced polymer matrix composites. However, despite the potential of this kind of composite, especially with regards to natural fibre reinforced thermoplastics composites (NFTCs), different issues in relation to their performance and technical applicability have to be resolved before their implementation on a larger industrial scale.

This thesis addresses the task of generating a deeper understanding of the processing-structure-performance relationships of natural fibres and NFTCs. The mechanical properties of coir and date palm fibre, along with their thermo-mechanical degradation at thermoplastic processing temperatures have been characterised. Furthermore, the interfacial interaction of coir fibre with polypropylene (PP) and low density polyethylene (LDPE) was investigated. In addition, the mechanical performance of injection moulded coir reinforced PP and LDPE composites was analysed.

The complex stress-strain behaviour of date palm and coir fibre was investigated through single fibre testing and direct observation of the fibres' cross sectional area. Two theoretical models were developed, postulating an apparent elastic modulus dependant on the fibres' cross sectional area, which successfully correlated with experimental observations. The thermal degradation of natural fibres was explored within the range of thermoplastic composite processing temperatures, revealing severe degradation of performance in terms of failure strain and tensile strength.

The interfacial behaviour of coir-thermoplastic systems, and the effect of maleic anhydride grafted polyolefins (MAPOs), was analysed by pull-out testing at room temperature using a tensile testing machine, and at low and elevated temperatures using a dynamic mechanical analyser (DMA). In general terms, it was found that the

addition of MAPOs led to an increase of the apparent interfacial shear strength (IFSS). Furthermore, the analysis based on different theoretical models revealed an apparent dependency of the IFSS on the geometry of the pull-out samples, which was also experimentally observed. In addition, the pull-out study at different temperatures revealed an inverse dependency of the apparent IFSS on the testing temperature.

The mechanical behaviour of injection moulded coir reinforced-thermoplastics was investigated through tensile and impact composite testing, along with the observation of fibre morphology, and SEM observation of composite fracture surfaces. The dependence of composite tensile and impact properties on fibre content and interfacial performance was characterised, revealing that enhancement of the apparent interfacial shear strength does not always translate into improved overall composite properties.

Contents

List of symbols and abbreviations

a	Crack length
A	Estimated fibre cross section area
A_c	Area of an hexagonal cell
A_f	Real fibre cross section area
A_n	Area of the hexagonal n-level
A_n	Area of the outer level in natural fibre models
A_T	Area of the total number of cells
C	Compliance
CLTE	Coefficient of linear thermal expansion
CSA	Cross section area
D_f	Fibre diameter
DMA	Dynamic mechanical analyser
DTG	Derivative of thermogravimetric analysis
E	Young's modulus
E_f	Fibre axial tensile Young's modulus
E_{fr}	Theoretical *real* fibre Young's modulus
E_t	Fibre transverse modulus
EPDM	Ethylene-propylene-diene monomer
F	Force
F_b	Force at fibre break
F_d	Debonding force

F_{max}	Maximum force
FE-SEM	Field emission scanning electron microscope
FTIR	Fourier transform infrared spectroscopy
G	Shear modulus
G_i	Energy release rate
G_{ic}	Interfacial toughness
GF	Glass fibre
HDPE	High-density polyethylene
HMWPE	High molecular weight polyethylene
IFSS	Interfacial shear strength
l	Side length of hexagonal cell
L_0	Initial length
L_e	Embedded length
LDPE	Low density polyethylene
LLDPE	Liner low-density polyethylene
MAH	Maleic anhydride
MAPE	Maleic anhydride modified high density polyethylene
MAPOs	Maleic anhydride grafter polyolefins
MAPP	Maleic anhydride grafted polypropylene
MFA	Cellulose microfibril angle
MFR	Melt flow rate
MS	Mass spectrometer
n	Level in a natural fibre structure

n_{pc}	Number of hexagonal cells at the n-level
n_{tc}	Total number of hexagonal cells in a structure with n-levels
NI	Notched impact strength
NF	Natural fibre
NFCs	Natural fibre composites
NFTCs	Natural fibre reinforced thermoplastics composites
OCT	Optimal cutting temperature
PE	Polyethylene
PP	Polypropylene
P_f	Fibre perimeter
P_n	Perimeter of the n-level
R	External radius of a pull-out specimen
r	Fibre's radius
r_c	Radius of a single elementary fibre.
r_{cc}	Radius of circumscribed circumference to the hexagonal cells
r_{ci}	Radius of inscribed circumference to the hexagonal cells
r_n	External radius of each level in a natural fibre circular model
SEM	Scanning electron microscope
STEX	Steam explosion method
T	Temperature
T_g	Glass transition temperature
T_r	Stress free temperature
TGA	Thermogravimetric analysis

TMA	Thermomechanical analysis
TVA	Thermal volatilisation analysis
u	Displacement
UI	Un-notched impact strength
UHMWPE	Ultrahigh molecular weight polyethylene
V_f	Fibre's volume fraction
V_m	Matrix's volume fraction
VLDPE	Very low-density polyethylene
W_a	Work of adhesion
α	Coefficient of linear thermal expansion
α_f	Fibre axial coefficient of thermal expansion
α_t	Fibre transverse coefficient of thermal expansion
β	Shear-lag parameter
γ	Surface energy
ΔL	Elongation
ΔT	Temperature difference
ε	Strain
ε_f	Fibre strain
η	Efficiency factor of interfacial stress transfer
ρ	Density
σ_{*f}	Fibre tensile strength
σ_f	Stress in the fibre

σ_{rr}	Radial tensile stress
σ_{ult}	Interfacial strength
τ	Shear stress
τ_{app}	Apparent interfacial shear strength
τ_e	Shear stress function
τ_f	Frictional stress in debonded areas
$\tau_{i\,max}$	Maximum shear stress
τ_i	Interfacial shear stress
τ_{therm}	Thermal shear stress
τ_{ult}	Ultimate shear stress
ν	Poisson ratio
ν_f	Fibre axial Poisson's ratio
ν_t	Fibre transverse Poisson's ratio

List of Figures

List of tables

Chapter 1 Introduction

1.1 Background

In principle, a composite can be defined as a material having two or more distinct constituents or phases [1]. In most cases, there is a strong and stiff component, normally referred to as *reinforcement*, embedded in a material, termed the *matrix* [2]. From this perspective, composites are not really new. In fact, in nature, plants and animals are mostly formed by natural composite materials, of which wood and bone are good examples. Wood is formed by longitudinal hollow cells, made up of spirally wound fibrous chains of cellulose, in a matrix of lignin and other constituents. And bones are mainly made up of hard inorganic crystals in a matrix of collagen [2].

Natural materials, such as wood, generally show a clear anisotropy (i.e. significant variation of properties depending on the measured direction), which normally comes from the fact that the harder constituent, usually in the form of fibres, is preferentially oriented in particular directions [2, 3]. Furthermore, one or more of the constituents could also exhibit inherent anisotropy due to their crystal structure [2]. The observed anisotropy is normally associated with the intrinsic function of the material within the natural structure. For instance, in the case of plants, in order to overcome the loads created by gravity and wind, a high strength in the axial direction of the overall structure is required, which is usually created by fibres oriented parallel to the axis of the trunk or branch [2].

Similarly to what occurs in natural materials, in human-made composite materials (or artificial/synthetic composites), two or more different constituents are combined on a macroscopic scale to form a new material, which exhibits, if well designed, the best qualities of its basic constituents, and others, which none of the constituents have [4]. In the case of human-made composites, reinforcements could be normally classified as fibrous or particulate, while their arrangement within the matrix material can be random or with a preferred orientation [1]. Fibrous reinforcements are characterised by having a much greater length in relation to their cross-section.

The individual properties of the constituents, geometry of the reinforcement, transfer load capability between reinforcement and matrix through the *interface* (i.e. common boundary between reinforcement and matrix), and reinforcement orientation, determine the properties of the overall composite material. By varying these parameters, the levels of anisotropy can be controlled, which can then be exploited to generate optimised materials for specific applications [2].

Looking at the development of these materials, during the second half of the 20th century, there has been a rapid expansion on the application of synthetic composites, especially those incorporating fine fibres in different polymers [1, 2]. Nowadays, composite materials are widely used in almost every industrial sector, with a considerable world annual production growth. The major success of fibre polymer composites, largely used as replacement for metals, is mainly related to their relative low density, which leads to higher specific properties, such as Young's modulus, E, against density, ρ (E/ρ). These good mechanical properties are a consequence of using the special characteristics of reinforcement fibres such as carbon, glass or aramid.

In the last decades, increasing social, environmental, and economic awareness, combined with the concepts of sustainability and new governmental environmental regulations have stimulated the development of *greener* materials [3, 5]. Likewise, factors such as issues with waste disposal, regulations towards cleaner and safer environment, high worldwide availability of natural fibres, and abundant agricultural crop residues, are also responsible for an increasing interest in research in natural fibre composites (NFCs).

Regarding the use of NFCs, and although natural materials, such as wood, and natural fibres have been used by different civilisations for thousands of years [1, 6, 7], complex human-made NFCs are relatively recent. For example, looking at aerospace applications, the use of NFCs can be traced back to the 1920s where they were used to make airscrews [8]. Regarding the application of NFCs in the automotive industry, as early as 1942, Henry Ford developed a prototype of a composite car made from hemp fibre reinforced composites [8]. Nowadays, natural fibre composites are extensively used in automotive applications [9–11], with an ever-growing development. As an

example, in 2005, about 30000 tonnes of natural fibre composites were used by the German automotive production [12].

In general terms, natural fibres represent a more environmentally friendly [12], biodegradable, with low carbon footprint and relative low cost, and with much lower associated health hazards in relation to human-made fibres, such as E-glass and carbon fibres. Typical properties of natural and human-made fibres are shown in Table 1.1, and their distinctive morphologies are compared in Figure 1.1.

Fibre	Density ρ [g/cm^3]	Young's modulus E_f [GPa]	Tensile strength σ_{*f} [Mpa]	E_f/ρ [GPa·cm^3/g]	σ_{*f}/ρ [GPa·cm^3/g]
Flax	1.5	27.6	345-1035	18	230-690
Hemp	1.5 [13]	37.5	594	25	401
Jute	1.3	26.5	393-773	20	302-595
Ramie	1.5 [13]	65	950	43	633
Sisal	1.3-1.5	9.4-22	511-635	6-17	341-488
Coir	1.2	4-6	175	3-5	146
E-glass	2.5	70	2000-3500	28	800-1400
Carbon (Standard)	1.4	230-240	4000	164-171	2857

Table 1.1: Fibre properties. Adapted from [7] and [13].

As previously discussed, the strong growth in the applications of composites, especially in the case of mineral/inorganic fibres and fillers reinforced thermoplastic composites, is mainly related to their mass processability and attractive performance-price ratio. In this regard, natural fibre reinforced thermoplastic composites (NFTCs) have attracted increasing interest as a potential alternative to some of these composites in specific applications [7, 9, 13–20].

Notwithstanding the benefits of NFTCs, there are still major technical concerns that must be addressed before envisioning their wide-scale implementation. From the point of view of fibre properties, it is often the case, when considering the potential of natural

fibres in relation to other mineral/inorganic fibres, that their high anisotropy, low transverse properties [21, 22] and variability are often overlooked. Their mechanical properties are determined by their chemical composition, structure, age, and variable circumstances, such as harvest and growth climate conditions, or retting process [3, 5–7, 12]. Furthermore, the hierarchical complexity of natural fibres' structure, creates a very complex fibre stress-strain response, where two or three different stress-strain phases [12], and a dependency of the stiffness on the fibre cross section area (CSA) [23], can often be observed. Moreover, the variable and non-circular CSA of natural fibres represents an additional challenge when characterising their mechanical properties. If all these aspects are considered, it is essential to have a profound understanding of the mechanical behaviour of the fibres used as reinforcement, as they greatly influence the overall performance of the composite.

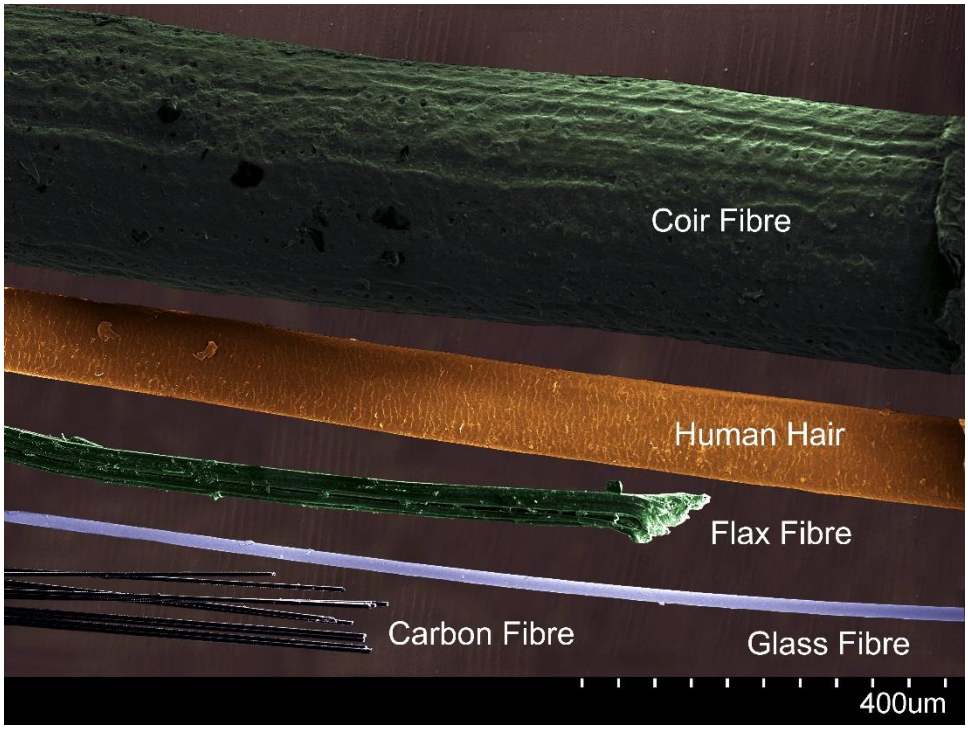

Figure 1.1: Composite image of human made fibres and natural fibres. Created by overlapping colour-enhanced electron micrographs by José Luis Rudeiros-Fernández.

Also in relation to the mechanical properties of natural fibres, one of the critical aspects of their use as reinforcement in thermoplastics, is the risk of fibre degradation at high thermoplastic processing temperatures [7]. In this regard, there is a clear limitation in the number of thermoplastics that can be used for NFTCs. As the above

mentioned thermo-mechanical degradation influences the fibres' properties, it is crucial to understand and characterise their behaviour at composite processing temperature conditions.

Natural fibres are usually polar, having inherently low compatibility with non-polar matrices, such as polypropylene (PP) and polyethylene (PE) [24]. For this reason, in order to fully exploit their potential in NFTCs, it is necessary to enhance the stress transfer capability of the fibre-matrix *interface* [14]. Established treatments, such as maleic anhydride grafted polyolefins or silane modifications, normally applied for human-made mineral/inorganic fibres, have not been as successful in NFTCs [22, 25]. Taking the previously discussed arguments into consideration, a deeper understanding of the fibre-matrix interfacial behaviour, including the dependency of apparent properties on the geometry of the fibre and of the samples, is a fundamental requirement. Moreover, understanding the relationship between fibre, matrix and interfacial properties, and NFTCs performance is vital, as it should provide clear insights into potential routes for improvement. Additionally, concerns in relation to impact resistance of NFTCs are particularly relevant [13, 22].

1.2 Project objectives

The main objective of this research programme is to generate a deeper understanding of natural fibres and NFTCs. In this project, coir and date palm as fibres, and PP and low density polyethylene (LDPE) as matrices, are analysed, considering coir and PP with particular interest. All natural fibres used in the context of this thesis were supplied by SABIC (Saudi Basic Industries Corporation). Coir and date palm fibres are abundant and have minimal impact on the environment during their production.

The first detailed objective is to precisely analyse the mechanical behaviour of coir and date palm fibres. As previously discussed, it is fundamental to understand the complex stress-strain behaviour, and mechanical properties variability, which this research programme further investigates. Furthermore, their non-circular and irregular CSA, might be a source of inaccuracy in the determination of mechanical properties.

In this regard, the impact of considering the real CSA, based on direct observation, on the characterisation of natural fibre properties is examined.

When considering the use of natural fibres as reinforcement in thermoplastics, it is essential to control the degradation of their properties while they are subjected to composite processing temperature conditions. For this reason, the second detailed objective, is to precisely characterise the thermo-mechanical degradation of palm and coir fibres at temperatures equivalent to PP injection moulding processing conditions. Moreover, the differences in the degradation of fibres, in the presence of air or nitrogen atmospheres are also investigated.

The third detailed objective is the analysis of the stress transfer ability of the fibre-matrix *interface,* which is thought to be one of the critical aspects that influence the overall composite behaviour. Considering the low compatibility between the polar natural fibres and the non-polar PP and LDPE, the effect of the addition of maleic anhydride grafted polyolefins to PP (including homopolymer and copolymer) and LDPE on the apparent interfacial shear strength (IFSS) for coir systems, are investigated. On this topic, the influence of the geometry of the fibre and sample on the apparent IFSS are examined through different theoretical models. Moreover, the temperature dependence of apparent IFSS, which has been explored for other systems, such as glass fibre-PP [26], is analysed for coir-PP samples.

Finally, the fourth detailed objective is to investigate the mechanical properties of NFTCs, and the relationship between composite performance and fibre, matrix and interfacial properties, in particular of injection moulded coir reinforced PP and LDPE composites. Tensile and impact properties are examined, for which a better understanding of the fundamental mechanisms relating the mentioned properties and the overall composite behaviour, could eventually provide useful insights for potential routes for improvement.

1.3 Thesis outline

The thesis is divided into seven different chapters. This chapter, *Chapter 1*, provides a general introduction to the subject and background to the research programme, including the main objectives and outline of the thesis. *Chapters 2-6* form the core of

the thesis, with each of them including an introduction and literature review regarding each specific topic.

Chapter 2 presents the research carried out in characterising the mechanical properties of the considered natural fibres, providing a complete description of experimental procedures. This chapter also details the analysis of the data, where two theoretical models are proposed and developed.

Chapter 3 describes the investigation of the thermal degradation of the considered natural fibres, containing a full explanation of the experimental techniques. The range of analysed temperatures coincides with the temperatures used in standard PP injection moulding processing.

Chapter 4 contains the research undertaken in characterising the thermo-mechanical properties of PP and LDPE, and their respective maleic anhydride modifications. The chapter also gives all details concerning the experimental methods.

In *Chapter 5*, the interfacial properties of coir fibre as reinforcement, and PP and LDPE as matrices (along their respective maleic anhydride modifications) are investigated, including a complete description of the techniques used, and developed experimental methods. This chapter also contains an extensive analysis of results based on different theoretical models.

Chapter 6 details the investigation of the mechanical properties of coir reinforced injection moulded PP and LDPE composites, detailing the experimental methods used. Tensile and impact properties are analysed, linking the information gathered in preceding chapters regarding matrix and reinforcement properties, with the observed overall composite behaviour.

Chapter 7 presents a review and summary of key observations and findings gathered throughout the thesis, drawing main conclusions, along with recommendations for future work.

1.4 References

1. Matthews, F.L., Rawlings, R.D.: Composite materials: engineering and science. Woodhead Publishing Limited (1999).

2. Hull, D., Clyne, T.W.: An introduction to composite materials. Cambridge University Press (1996).
3. Stokke, D.D., Wu, Q., Han, G.: Introduction to wood and natural fiber composites. John Wiley & Sons (2014).
4. Jones, R.M.: Mechanics of composite materials. Taylor & Francis Group (1998).
5. Kalia, S., Kaith, B.S., Kaur, I. eds: Cellulose fibers: bio- and nano- polymer composites: green chemistry and technology. Springer (2011).
6. Fuqua, M.A., Huo, S., Ulven, C.A.: Natural Fiber Reinforced Composites. Polym. Rev. 52, 259–320 (2012).
7. Bledzki, A.K., Gassan, J.: Composites reinforced with cellulose based fibres. Prog. Polym. Sci. 24, 221–274 (1999).
8. Hodzic, A., Shanks, R. eds: Natural fibre composites: materials, processes and properties. Woodhead Publishing (2014).
9. Koronis, G., Silva, A., Fontul, M.: Green composites: A review of adequate materials for automotive applications. Compos. Part B Eng. 44, 120–127 (2013).
10. Bledzki, A.K., Faruk, O., Sperber, V.E.: Cars from Bio-Fibres. Macromol. Mater. Eng. 291, 449–457 (2006).
11. Al-Oqla, F.M., Sapuan, S.M.: Natural fiber reinforced polymer composites in industrial applications: Feasibility of date palm fibers for sustainable automotive industry. J. Clean. Prod. 66, 347–354 (2014).
12. Mussig, J. ed: Industrial Applications of Natural Fibres. John Wiley & Sons (2010).
13. Wambua, P., Ivens, J., Verpoest, I.: Natural fibres: can they replace glass in fibre reinforced plastics? Compos. Sci. Technol. 63, 1259–1264 (2003).
14. Eichhorn, S.J., Young, R.J.: Deformation micromechanics of natural cellulose fibre networks and composites. Compos. Sci. Technol. 63, 1225–1230 (2003).
15. Joshi, S.V., Drzal, L.T., Mohanty, A.K., Arora, S.: Are natural fiber composites environmentally superior to glass fiber reinforced composites? Compos. Part A Appl. Sci. Manuf. 35, 371–376 (2004).
16. Nabi Saheb, D., Jog, J.P.: Natural fiber polymer composites: A review. Adv. Polym. Technol. 18, 351–363 (1999).
17. Graupner, N., Herrmann, A.S., Müssig, J.: Natural and man-made cellulose fibre-reinforced poly(lactic acid) (PLA) composites: An overview about mechanical characteristics and application areas. Compos. Part A Appl. Sci. Manuf. 40, 810–821 (2009).
18. Jayavani, S., Deka, H., Varghese, T.O., Nayak, S.K.: Recent Development and Future Trends in Coir Fiber Reinforced Green Polymer Composites: Review and Evaluation. Polym. Compos. (2015).
19. Ku, H., Wang, H., Pattarachaiyakoop, N., Trada, M.: A review on the tensile properties of natural fiber reinforced polymer composites. Compos. Part B Eng.

42, 856–873 (2011).

20. Malkapuram, R., Kumar, V., Negi, Y.S., Yuvraj Singh Negi: Recent Development in Natural Fiber Reinforced Polypropylene Composites. J. Reinf. Plast. Compos. 28, 1169–1189 (2008).
21. Cichocki Jr., F.R., Thomason, J.L.: Thermoelastic anisotropy of a natural fiber. Compos. Sci. Technol. 62, 669–678 (2002).
22. Thomason, J.L.: Dependence of Interfacial Strength on the Anisotropic Fiber Properties of Jute Reinforced Composites. Polym. Compos. (2010).
23. Baley, C.: Analysis of the flax fibres tensile behaviour and analysis of the tensile stiffness increase. Compos. Part A Appl. Sci. Manuf. 33, 939–948 (2002).
24. Xie, Y., Hill, C.A.S., Xiao, Z., Militz, H., Mai, C.: Silane coupling agents used for natural fiber/polymer composites: A review. Compos. Part A Appl. Sci. Manuf. 41, 806–819 (2010).
25. Eichhorn, S.J., Baillie, C.A., Mwaikambo, L.Y., Ansell, M.P., Dufresne, A., Entwistle, K.M., Herrera-Franco, P.J., Escamilla, G.C., Groom, L., Hughes, M., Hill, C., Rials, T.G., Wild, P.M.: Review: Current international research into cellulosic fibers and composites. J. Mater. Sci. 36, 2107–2131 (2001).
26. Thomason, J.L., Yang, L.: Temperature dependence of the interfacial shear strength in glass–fibre polypropylene composites. Compos. Sci. Technol. 71, 1600–1605 (2011).

Chapter 2

Mechanical Characterisation of Natural Fibres

2.1 Introduction / Literature Review

Natural fibres derived from plants are lignocellulosic structures, normally found in nature as elementary fibres (individual plant cells) assembled together into bundles (natural fibre or fibre will denote, in this thesis, an assembly of elementary fibres), which are generally produced in the stem of the plant or as part of the leaves [1, 2]. Natural fibres have been successfully, directly or indirectly, used as reinforcement in composite structures or as textiles, ropes, canvas or paper throughout world history by several civilisations [3, 4]. This section will focus on the review of the literature regarding plant derived natural fibres.

2.1.1 Natural fibre chemistry

The properties of natural fibres are directly related to their chemical composition and internal structure [2, 3, 5]. Natural fibres are formed by cellulose, hemicelluloses and lignin as main components. Other minor components, such as pectin, waxes, protein, tannins, ash and inorganic salts [3] are also present. The proportions of these components vary depending on the type of fibre, the source, growing conditions, extraction processes and plant age.

2.1.1.1 Cellulose

Cellulose is the most important component of all plant derived natural fibres [4]. Cellulose is a linear polymer that consists of two D-anhydroglucose rings joined via a β-1,4-glycosidic bonds [3, 4, 1, 6], Figure 2.1. The molecular structure of cellulose determines many of the fibre's physical and chemical properties. The length of the cellulose polymer chains varies according to the type of natural fibre. Solid cellulose is formed into microcrystalline structures with crystalline (i.e. highly ordered) and amorphous (i.e. low ordered) regions [4]. Cellulose exists in different forms, however as found in nature (cellulose I), it crystallises in monoclinic sphenodic structures, where the molecular chains are orientated along the main fibre axis. Cellulose I may

be transformed into other types of cellulose (e.g. cellulose II) through chemical or thermal treatment [3]. While cellulose II is more thermally stable, cellulose I shows higher mechanical properties.

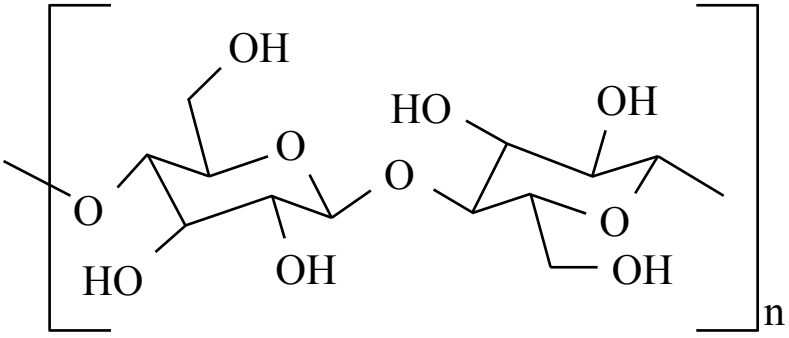

Figure 2.1: The repeat unit of cellulose, based on [6].

2.1.1.2 Hemicellulose

Hemicelluloses are considered the second most abundant carbon compound of the plant cell wall [7]. They designate a group of amorphous polysaccharides (excluding pectin), such as xylose, mannose, glucose, galactose and arabinose [3, 4, 8]. Hemicellulose is a copolymer containing several different sugar units, unlike cellulose, which only contains 1,4-β-D-glucopyranose. As in the case of cellulose, the structure of hemicelluloses varies depending on the type of fibre. Hemicelluloses form what is normally considered as the matrix of the cell walls, where they are associated with pectins, cellulose and aromatic constituents [7, 2]. Hemicellulose is believed to be a compatibiliser between cellulose and lignin [9].

2.1.1.3 Pectin

Pectins designate a group of different substances called heteropolysaccharides, associated in the cell walls and natural fibres [3, 7]. They essentially consist of polygalacturon acid [10]. Similar to hemicellulose, pectins are also called matrix polysaccharides, holding tissues and fibres together [7]. Being pectins, one of the main components that cements cells (i.e. elementary fibres) together, they highly influence the process of retting (i.e. the separation of non-fibrous materials from the fibres).

2.1.1.4 Lignin and aromatic compounds

Lignins are cross-linked polymeric compounds that are extremely diverse and present in many forms in plants [3]. They are made up of three different relatively simple components [11, 3, 7]: p-coumaryl alcohol, coniferyl alcohol and synapyl alcohol, Figure 2.2. There are different kinds of lignins, which vary depending on different factors, such as the type of plant, the cell wall fraction, the type of tissue and the type of plant organ.

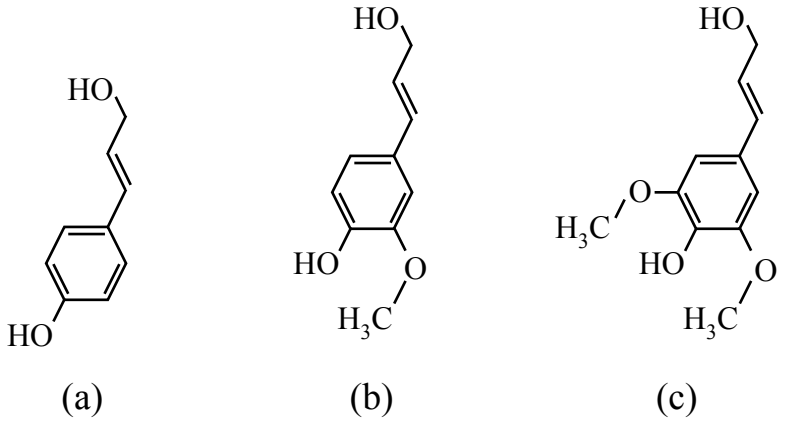

Figure 2.2: Lignin components. (a) p-coumaryl alcohol. (b) coniferyl alcohol. (c) synapyl alcohol, based on [11].

The tensile mechanical properties of lignin are significantly lower than those of cellulose [3, 4]. Lignin is developed during the biosynthesis of plant cell walls between cellulose and hemicellulose, binding them together [3]. The main task of lignin is to provide compressive strength and stiffness to the cell wall [2]. A cell wall without lignin will be able to deal with tensile loads, but it will be extremely weak against compressive forces. In fact, during evolution, it was the addition of lignin to the cell walls which allowed terrestrial plants to increase their height and branch systems that could support large photosynthetic surfaces [2].

Lignin, a hydrophobic compound, also provides waterproofing to the cell walls and protects the cell against microbial pathogens. In this respect, the kind of lignin present in the tissues of the fibre will strongly influence the level of response of chemical treatments, degree of biodegradability, efficiencies of the retting processes or susceptibility to microbial action.

2.1.1.5 Fats, waxes and lipids

These hydrocarbon components have diverse functions within the plants [7]. Lipids are very important on the outside of plants, but especially in fibres. Waxes provide a protective barrier against microbial attack and prevent water loss. Waxes and fatty substances are related to the hydrophobic nature of the surface of natural fibres [12], therefore influencing the fibre-matrix interaction in natural fibre composites (NFCs).

2.1.2 Natural fibres structure

An elementary plant fibre is a single cell typically of a length from 1 to 50 mm and a diameter of around 10 to 50 µm [10]. The plant cell (i.e. elementary fibre) is made up by two major parts, the protoplast and the cell wall [2]. The cell wall provides a rigid frame, limiting the actual size of the protoplast. The cell wall prevents the rupture of the plasma membrane when the protoplast gets bigger due to the uptake of water by the cell. There is a direct relationship between the cell wall function and cell wall structure. It is well known that there is a large variation between plant cell's structural dimensions depending on the function, age, and position of the cell in the plant.

Plant cell walls are formed by stiff cellulose fibrils embedded in matrices of complex macromolecules [3, 7], (e.g. hemicelluloses, pectin and/or lignin) Figure 2.3.

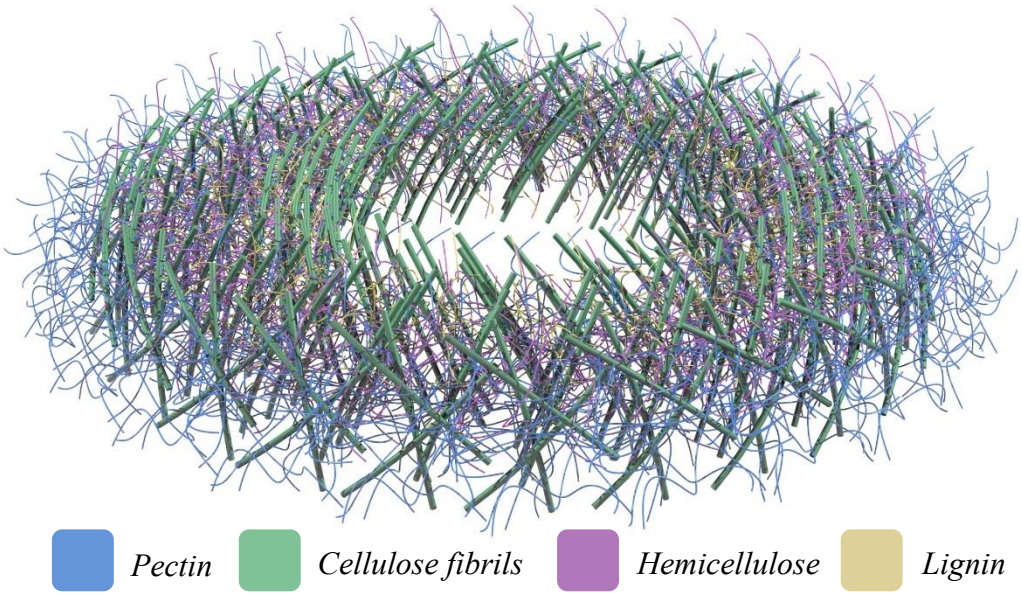

Figure 2.3: Natural fibre's cell wall structure, illustrating main components. Rendering by José Luis Rudeiros-Fernández.

These cellulose fibrils are made up of 30 to 100 cellulose molecules , with a diameter of 10 to 30 nm [3]. Cellulose fibrils define an angle against the longitudinal axis of the cell that normally is called “cellulose microfibril angle” (MFA) [3, 4, 7]. The protoplast of the cell forms each wall from the outside to the inside, so the youngest layer is the innermost, right next to the protoplast. The outer layer of the cell is known as the primary cell wall, and is externally surrounded by a region called the middle lamella, which cements the different cells together. The main component of the middle lamella is normally pectin [2]. However, in general terms, authors established that the middle lamella could be a pectin-rich and/or lignin-rich layer.

Once the cell has reached its final shape and size, in many cases, it starts synthesising the secondary cell wall [3, 4, 7]. In the secondary wall, the cellulose fibrils are wound around the longitudinal axis in different ways depending on the plant [4]. It is often possible to divide the secondary layer into three other layers, normally designated as S1 for the inner, S2 for middle and S3 for the outer layer [10, 3, 4]. The difference between them being the orientation of the cellulose fibrils in each layer (e.g. the structure of flax fibre, Figure 2.4).

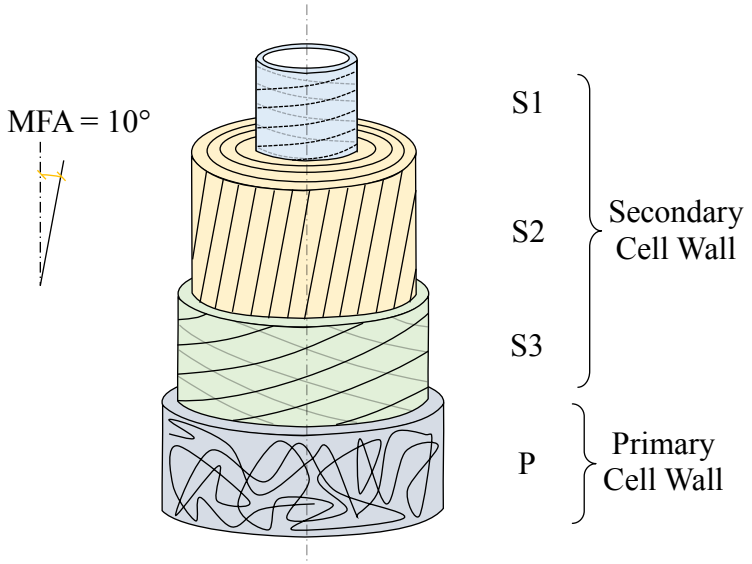

Figure 2.4: Flax fibre structure, based on [13].

The secondary wall is considered to be more rigid than the primary wall due to its higher content of cellulose and lower content of pectins. The matrix of the secondary wall is mainly formed by hemicellulose. Hemicellulose functions to bind cellulose and

lignin together through hydrogen bonding or even covalent bonding to lignin [7]. Ligninification occurs after the cellulose and hemicellulose have been structured in the basic wall assembly. It is also recognised that the fibres can increase the degree of lignification of the cell wall depending on the development stage [7]. In the primary wall glycoproteins and enzymes are abundant but not present in the secondary cell walls.

It is sometimes difficult to appreciate any difference between the middle lamella and the primary wall, especially if the secondary wall is much thicker than the primary wall. In cases like this, the primary wall, middle lamella and in some occasions the first layer of the secondary wall could be called a compound middle lamella.

2.1.3 Fibre extraction, separation and processing

In order to fully utilise the mechanical properties of natural fibres, they must be separated and extracted from the woody tissue of the fibre crop [10]. The process that causes the separation of the technical fibre bundles from the central stem is called retting. Most retting methods rely on biological activity to degrade the pectic polysaccharides from the non-fibre tissue and separate the fibre bundles. Pectilolytic enzymes are essential in the retting process, recent investigations have shown that just a pectinase, either a pectate lyase or an endopolygalacturonase, can satisfactorily separate the fibres [7]. In general, retting methods can be divided into biological, mechanical, chemical and physical fibre separation processes [10].

Rao et al. [14] showed how the method of extracting the fibres affects their final mechanical properties. There are remarkable differences between mechanical and chemical procedures. As an example, the average tensile strength and modulus of bamboo when a chemical method of extraction is applied are 341 MPa and 19 GPa respectively. For the same fibre when a mechanical method is applied the values are 503 MPa and 35 GPa respectively.

Other authors analysed the values of strength and modulus of bamboo (G. angustifolia) for plants of different age and also showed the importance of the correct timing in the fibre extraction method [15]. They also looked at the variation of properties depending on which part of the plant the fibres are extracted from. The

values for fibre strength varied depending on the age and part of the plant the fibres were extracted from. In a later study, [16], based on a new mechanical extraction method, the results showed a positive effect in terms of increasing the mechanical performance of the fibre in comparison with previous studies. For a gauge length of 5 mm, the tested fibres showed a tensile strength of 860 MPa and a Young's modulus of 46 GPa.

In general, fibre extraction has a big influence on the final fibre quality and yield. Homogeneously clean and fine fibres can only be obtained by wet-retting processes (ultrasound, steam explosion, Duralin process, enzyme retting and chemical and surfactant retting). The different retting processes are further analysed in the following sections.

2.1.3.1 Biological retting

Dew or field retting is the most commonly applied retting process [3, 17]. After mowing the crops are left on the field while microorganisms separate the fibres from the cortex and xylem. The crops must be turned over at least once to make sure the retting process is homogenous. This process takes between three and six weeks, overretting leads to the degradation of the cellulose in the bast fibres. The dependence on climatological parameters makes the process difficult to control and with a certain level of unpredictability.

In the stand-retting process, the process is artificially thermally induced. The plant bases are heated up to approximately 100 °C and then dried. The mechanical properties of the fibres are not affected by the heat treatment. This allows a more controlled process.

In cold-water retting, the straw bundles are submerged into water and anaerobic bacteria break down the pectin of the plants [3]. The process produces environmental pollution due to the organic fermentation wastewaters and was abolished in 1918 in Germany [17].

Warm-water retting processes are prohibited in Europe because of the impact on the environment. Plant bundles are submerged in warm water (28 °C to 40 °C) [3, 17]. After the retting process, fibres are extracted from the raw fibres through a mechanical

breaking process. The processed fibres are passed through fluted rolls to break the remaining woody portion. This process can reduce the time of retting to 3 to 5 days.

Enzyme retting uses pectin-degrading enzymes to separate the fibres. Enzyme retting is able to provide undamaged individual fibres with higher fibre strength. The high cost of the process did not allow it to go further than pilot-scale experiments[17].

2.1.3.2 Mechanical or green retting

Mechanical or green retting is a more cost-effective alternative. The raw material for this method is either slightly retted or field dried plant straw. The bast fibres are separated from the woody part by mechanical means. The resulting fibres are much coarser and less fine when they are compared to natural processes [3].

2.1.3.3 Physical

In ultrasound retting, the stems are broken and washed after harvest. Then the slightly broken stems are immersed in a hot water bath, which includes surfactants and alkali. Thereafter, they are exposed to high intensity ultrasound [3, 17], which separates the fibres from the woody components.

In the steam explosion method (STEX), the steam and other additives penetrate the fibre interspaces of the bast fibre bundles (under pressure and increased temperature) [17]. The subsequent sudden relaxation of the steam leads to an effective breaking up of the bast fibre composite into finer fibres.

The Duralin process consist of a steam or water-heating step of the straw at temperatures above 160 °C for thirty minutes in an autoclave [17]. The second step is the heating and drying above 150 °C for two hours. The lignin and hemicellulose are depolymerized into lower molecular weight phenolic and aldehyde functionalities, combined with the curing reaction into a water-resistant resin that cements the cellulose microfibrils together. The final fibres are some kind of fibre bundles.

2.1.3.4 Chemical

In chemical and surfactant retting processes, the pectin component is dissolved by sequentially submerging the fibre crops in heated tanks containing water solution of

sodium or potassium hydroxide, sulphuric acid, chlorinated lime and soda ash [17]. The quality of the fibres is high but the process adds costs to the final product.

2.1.4 Mechanical properties of natural fibres

The mechanical properties of natural fibres are influenced by their chemical composition, structure, age, growth climate conditions, harvest and retting process [11, 10, 3, 4, 7]. Mechanical properties vary greatly depending on the type of natural fibre, as illustrated Table 2.1. Furthermore, mechanical properties also vary within the same type of plant. Some of this variability comes from the adaptational growth of plants, which leads to a scenario where within-plant variation is as large as between-plant variation of fibre properties [7]. Intra-fibre variation may be due to cell wall disparities in terms of size, MFA or chemical compositions. Additionally, structural defects or inherent patterns (e.g. pits, which are interruptions of the primary wall [2] that allow for nutrients and water to flow from one cell to the next one [7]) may also be responsible for intra-fibre variation.

Fibre	Cellulose [wt%]	Hemicelluloses [wt%]	Pectins [wt%]	Lignin [wt%]	MFA [°]	Young's modulus [GPa]	Tensile strength [Mpa]
Flax	71	18.6	2.3	2.2	10-11	27.6	345-1035
Hemp	74.4	17.9	0.9	3.7	6	37.5±3.4	594±106
Jute	61	20.4	0.2	13	7-9	26.5	393-773
Ramie	68.6	68.6	1.9	0.6	8	65	950
Sisal	78	10	-	8	19.7	9.4-22	511-635
Coir	43	4	4	45	45	4-6	175

Table 2.1: Typical values for chemical composition, MFA and mechanical properties of various natural fibres. Adapted from [4] and [7].

In terms of structural parameters, MFA has a high impact in determining fibre mechanical properties. A low MFA (i.e. cellulose fibrils are almost axially oriented) leads to a high axial Young's modulus while high MFA leads to low axial Young's modulus fibres. When the MFA is high, the mechanical behaviour of the fibre is strongly influenced by the interactions between the cellulose fibrils and the components in which they are embedded [18–21]. These interactions lead to a complex fibre stress-strain response, where two or three different phases can be identified [7, 22]. Some authors proposed that just after the yield point, there is a viscous flow of

the matrix components (e.g. hemicelluloses, pectins and/or lignin) and a gliding of the cellulose fibrils along the components that form the matrix [7].

When characterising natural fibre mechanical properties, it is important to take into consideration the non-circular nature of their cross section area (CSA) [23]. Considering a circular CSA and calculating fibre properties based on diameter measurements from transverse observations could lead to significant error. It has also been reported that fibres' diameter has a further indirect effect on the mechanical properties. The Young's modulus dependence on CSA has been described for natural fibres [13, 22, 24–28]. Baley [13] showed how flax Young's modulus decreased for increasing fibre diameter, suggesting that ignoring the lumen when calculating the CSA, non-constant CSA along the fibre length, presence of defects and variability in fibres' composition could cause the observed correlation. Other authors [25–27], attempted to use an empirical expression, based on Griffith model [29], to fit their observations.

2.2 Experimental

2.2.1 Materials

Date palm and coir fibres were both provided by SABIC.

2.2.2 Observation of fibres' internal structure

On a square of paper card, a layer of superglue was distributed uniformly. Thereafter, the individual natural fibres were placed using tweezers in a perpendicular position to the card as is showed in Figure 2.5 (a). Once the superglue reacted, the fibres were placed in a plastic mini-mould that was filled with optimal cutting temperature (OCT) embedding matrix (normally used for embedding tissue samples). The samples were then placed in a freezer where the embedding matrix solidified, Figure 2.5 (b). After the matrix completely solidified, the resulting block was extracted from the mini-mould and attached to a cryotome machine. The block was cut into slices with a thickness of 16 microns, Figure 2.5 (c). The slices were placed on a glass slide for observation under the scanning electron microscope (SEM). Samples were gold coated and attached to the sample holder by a carbon tape, Figure 2.5 (d).

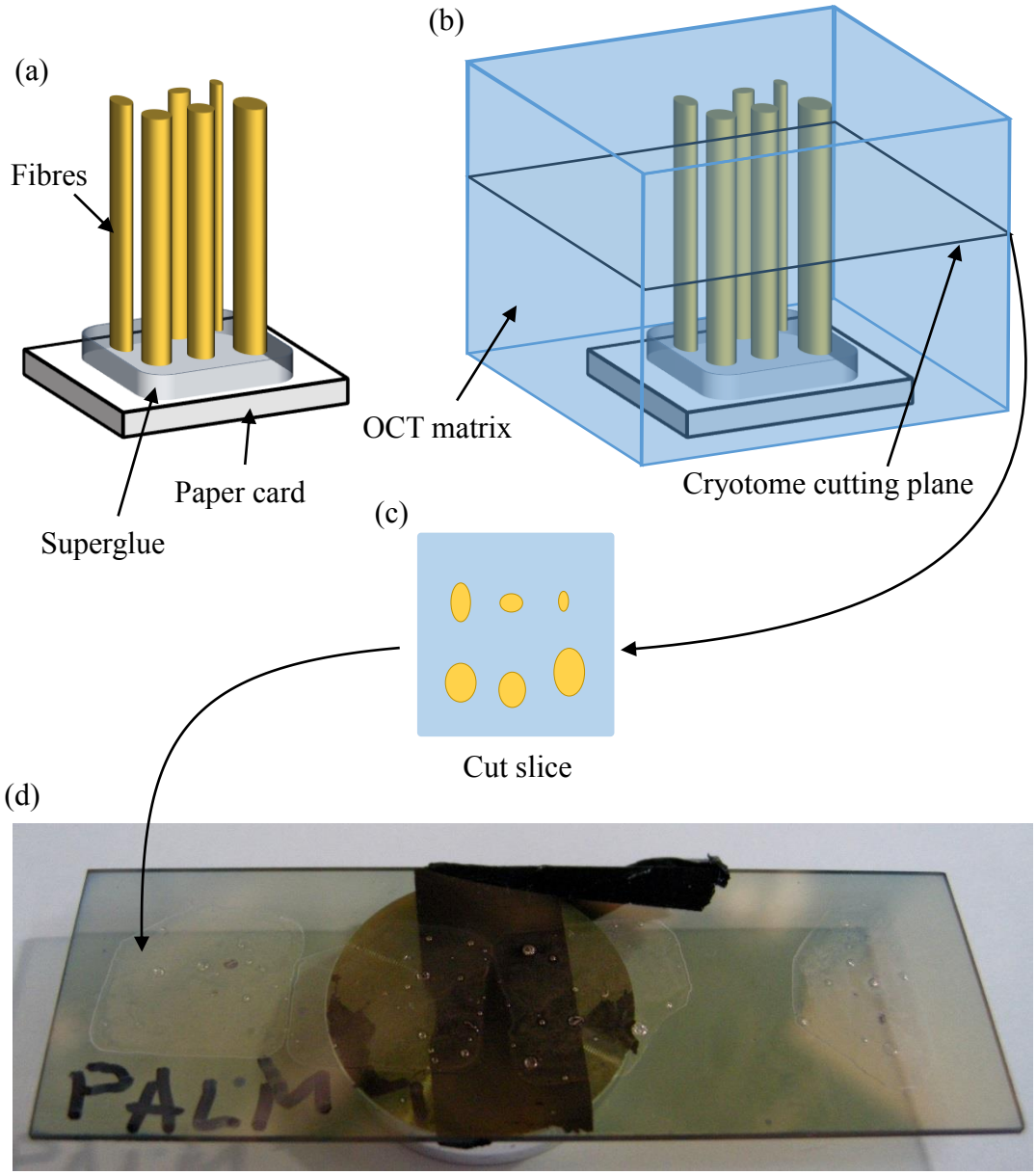

Figure 2.5: Sample preparation for observation of internal structure.

2.2.3 Single fibre tensile testing

Single fibre testing was carried out following the main recommendation on standards [30, 31]. Palm and coir fibres were individually separated until no fraying could be seen with the naked eye. Thereafter, fibres were mounted on paper card frames made from 250 g/m^2 card, where a window with the desired gauge length had been previously cut out. Initially fixed to the card frames by double-sided tape, fibres were

subsequently fixed by LoctiteTM Gel Superglue, Figure 2.6. After the glue had dried, all fibres were photographed at the middle point of the gauge length under transverse observation using a Leica microscope at 10x magnification. Three diameters in each picture were measured using the software ImageJ as is illustrated in Figure 2.7. For this initial stage, fibre diameter (D_f) was estimated as the average of these three measurements. The fibre cross section area (A) was first estimated by assuming a circular cross section.

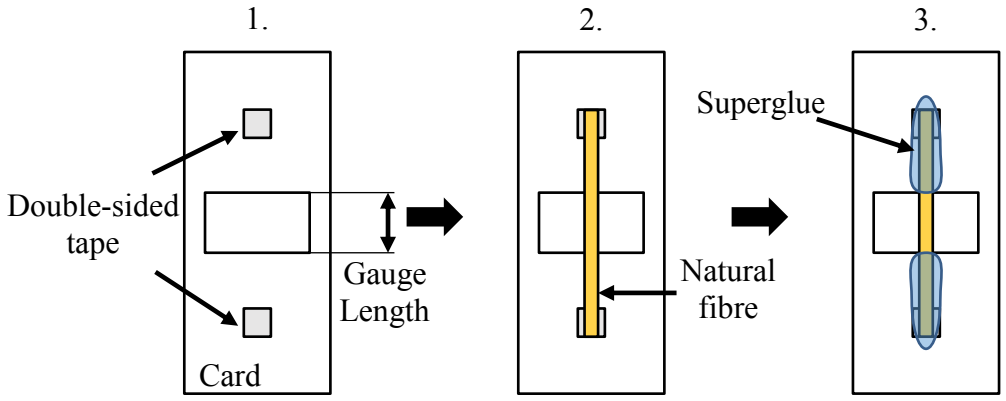

Figure 2.6: Single fibre test sample preparation.

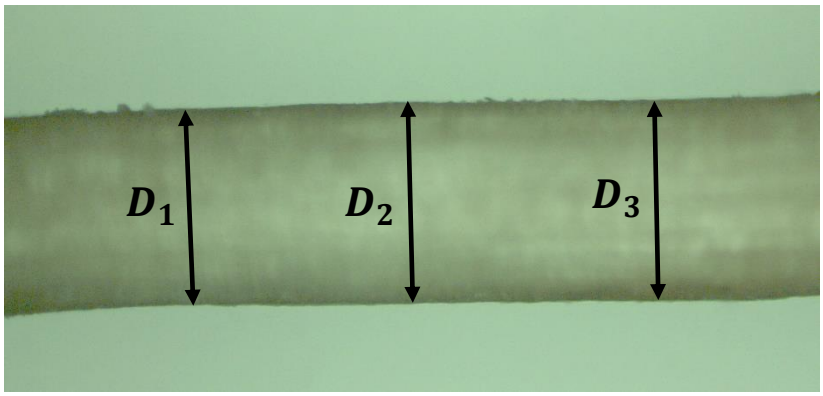

Figure 2.7: Diameter transverse observation.

Fibre strength and Young's modulus was characterised by tensile testing, using an Instron 3342 tensile testing machine with a 100 N load cell. The cross-head displacement rate was set at 5% strain per minute. For the tensile test, card and fibre were clamped up to the gauge length as shown in Figure 2.8, in order to avoid any slippage.

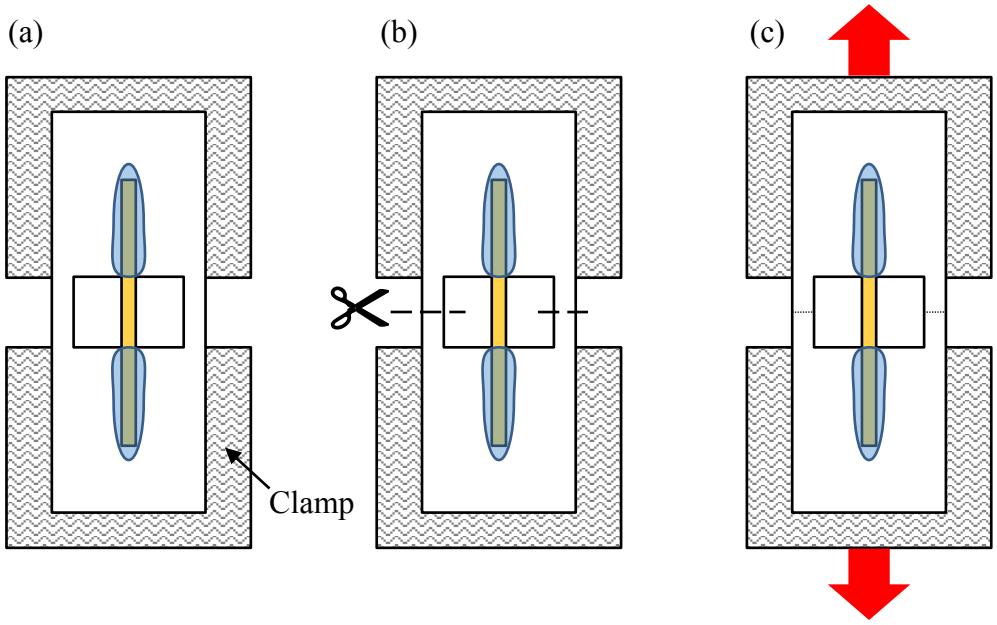

Figure 2.8: Tensile test diagram.

For each fibre, Bluehill® 2 Software (which controls the Instron testing machine) recorded the load as a function of cross-head displacement. Subsequently, it was used to analyse the generated curve, and to calculate the fibre strength and Young's modulus.

$$\sigma_{*f} = \frac{F_b}{A_f} \tag{2.1}$$

Fibre strength is calculated following (2.1), where σ_{*f} is the fibre strength, F_b is the force at fibre break and A_f is the cross sectional area of the fibre (estimated area A is used if A_f is not available).

$$C \cong \frac{\Delta F_f}{\Delta L} \tag{2.2}$$

$$E = \frac{\sigma_f}{\varepsilon} = \frac{\Delta F_f L_0}{A_f \Delta L} \cong \frac{C L_0}{A_f} \tag{2.3}$$

Young's modulus is calculated using the slope, C (2.2), of a straight line fitting the initial linear deformation on the load-extension curve. Young's modulus is then calculated according to (2.3), where F_f is the force exerted on the fibre, σ_f is the stress

in the fibre, ΔL is the increase in length of the fibre due to F_f and L_0 is the initial gauge length.

Three different gauge lengths were used for each fibre in order to correct the fibre Young's modulus (5, 10 and 20 mm) for compliance effects [31]. The total measured elongation ΔL can be divided into the elongation of the fibre ΔL_f and the elongation of the system ΔL_s, (2.4).

$$\Delta L = \Delta L_f + \Delta L_s \tag{2.4}$$

$$\Delta L_s = F_f C_s \tag{2.5}$$

$$\Delta L_f = \frac{F_f L_0}{A_f E_f} \tag{2.6}$$

$$\Delta L = \frac{F_f L_0}{A_f E} \tag{2.7}$$

If we assume that ΔL_s is proportional to the compliance of the system C_s as in (2.5), and substituting (2.5), (2.6) and (2.7) in (2.4), the true fibre modulus E_f can be related to the measured Young's modulus E, (2.8).

$$\frac{1}{E} = \frac{1}{E_f} + C_s \frac{A_f}{L_0} \tag{2.8}$$

Assuming E_f and C_s are constants, equation (2.8) could be interpreted as the generic equation of a straight line, $y = ax + b$. Therefore, E_f could be obtained by fitting a straight line by the least squares method and using the value of b, (2.9).

$$b = \frac{1}{E_f} \tag{2.9}$$

2.2.4 Cross section area and perimeter measurement

The true CSA (A_f) and perimeter (P_f) of natural fibres were characterised in order to improve the estimation of the mechanical properties of natural fibres due to the possible differences between A_f and A (see Figure 2.9). Young's modulus and strength from tensile testing data were initially calculated by using the estimated CSA A

(obtained from the transverse observation of the fibre's "diameter" and assuming a circular CSA).

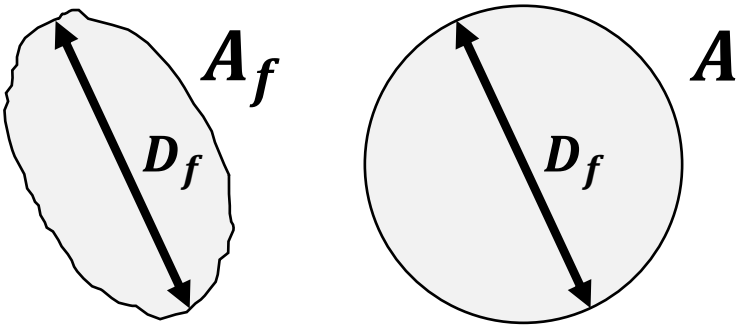

Figure 2.9: Real CSA A_f and estimated A.

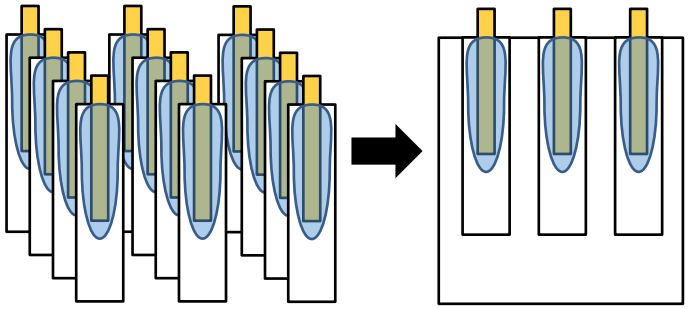

Figure 2.10: Arranging fibres in a paper card.

Once the fibres were tensile tested, the bottom and top ends were cut off from the remaining card. The two parts were then fixed to 250 gr/m2 card in vertical position for later manipulation, Figure 2.10. The cards with the fibres fixed were then inserted into a mould that was subsequently filled with resin, Figure 2.11 (a). Resin blocks were then ground down and polished using progressively finer grinding papers for final CSA analysis, Figure 2.11 (b).

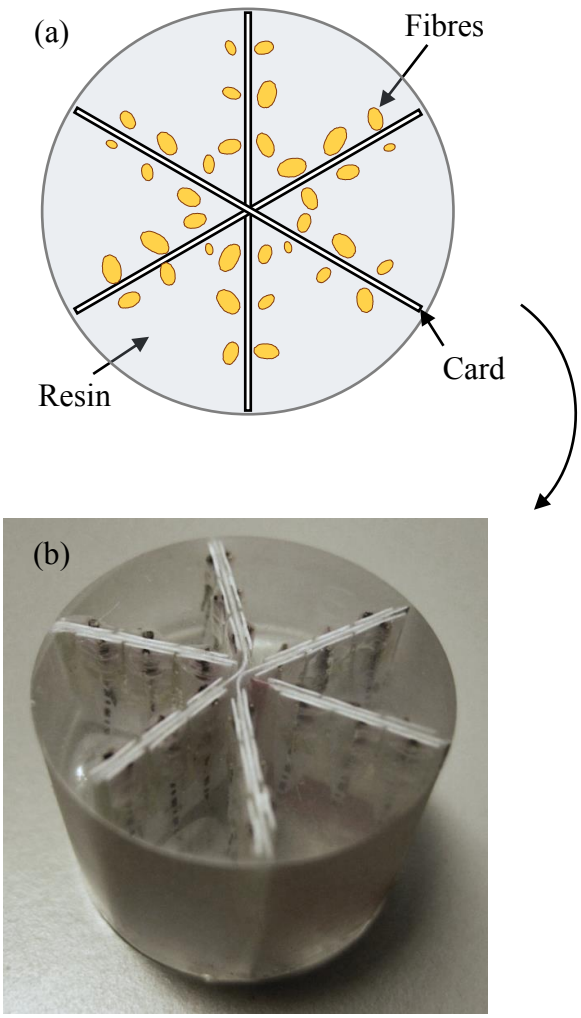

Figure 2.11: Diagram of CSA measurements (a), and resin block (b).

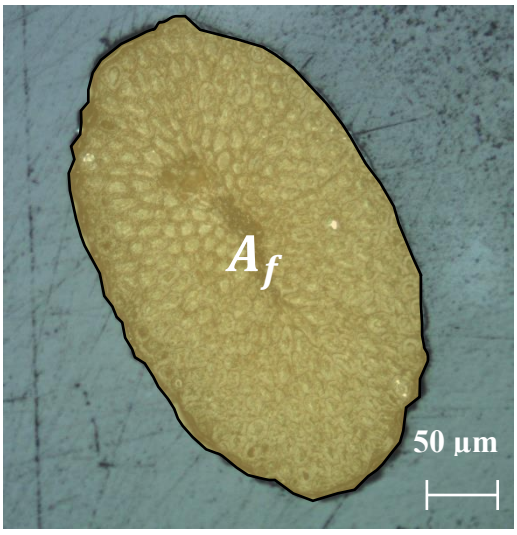

Figure 2.12: Real CSA of fibre.

Fibre cross section was photographed using an Olympus GX51 microscope at different magnifications depending on the size of the fibre. The true cross section area A_f is defined as illustrated in Figure 2.12. For every picture, the cross-section was traced and exported for post-treatment as is illustrated in Figure 2.13.

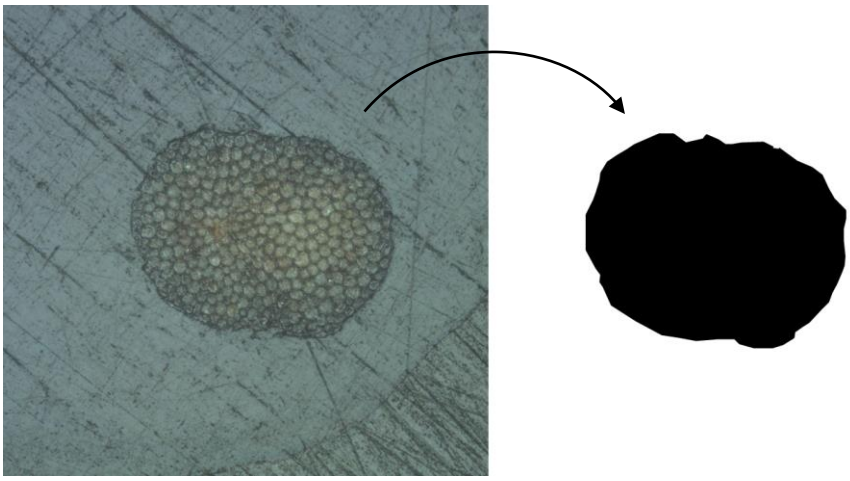

Figure 2.13: CSA determination, initial image and exported image for analysis.

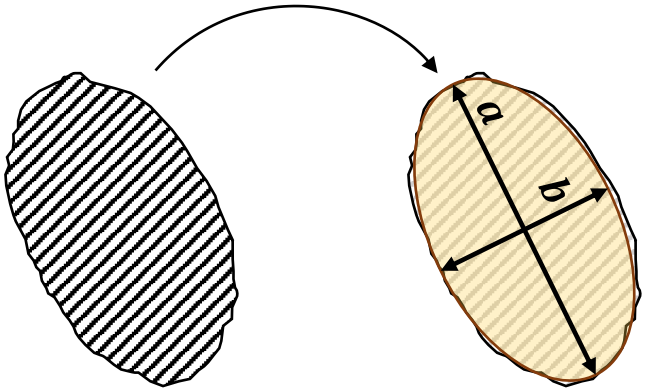

Figure 2.14: Calculation of ellipse major and minor axis. This analysis is complemented with the maximum and minimum Feret's diameters.

The resulting images were analysed by a macro written for ImageJ. The macro-program converted each image file to a binary image and subsequently, after applying the respective scale, measured each area and perimeter by using the "analyse particles" feature of ImageJ. The program also fits an ellipse to the CSA (calculating the major and minor axis) and maximum and minimum Feret's diameters, Figure 2.14. The final CSA was estimated as the average of the two measurements on each fibre. These

measured CSA values were used to correct the fibre Young's modulus and strength data obtained from tensile testing.

The photographs of the CSAs, Figure 2.15, were also used to characterise the internal structure of palm and coir fibres in terms of CSA and aspect ratio of elementary fibres. As in the case of the analysis of the overall CSA, ImageJ was used for the measurements.

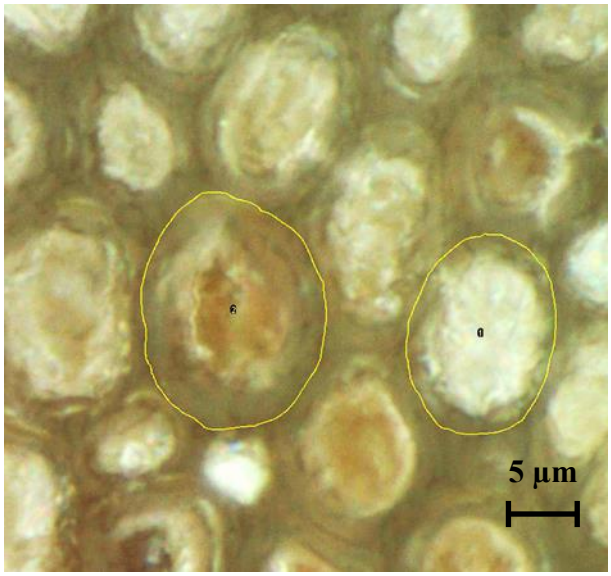

Figure 2.15: Detail of the CSA of palm fibre. Measurement of elementary fibres.

2.3 Results and discussion

2.3.1 Natural fibre internal structure

The complex internal structure of coir and palm fibres was observed using SEM. It could be clearly observed how both fibre types are made up by the addition of many elementary fibres or cells joined together. As discussed in section 2.1, cells are cemented together by the middle lamella, which is generally a pectin-rich and/or lignin-rich layer.

In the case of both fibres, the shape and size of elementary fibres and thickness of the cell's wall varied greatly through the CSA, Figure 2.16 and Figure 2.17. Especially remarkable were the central areas of the CSA, where in most of the cases, voids were observed. The overall CSA (which in most of the cases differed from a circular

estimate of CSA) also varied in shape and size depending on the fibre. These variations can lead to high levels of anisotropy, non-symmetrical stress distributions within the fibre and high variability of fibre properties.

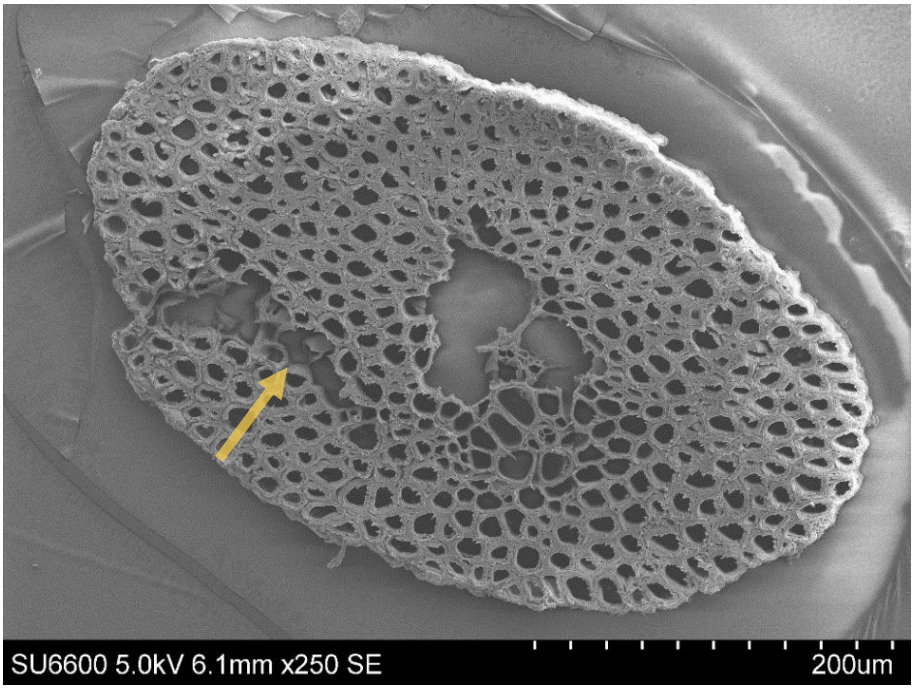

Figure 2.16: Coir fibre. Cryotome cut sample.

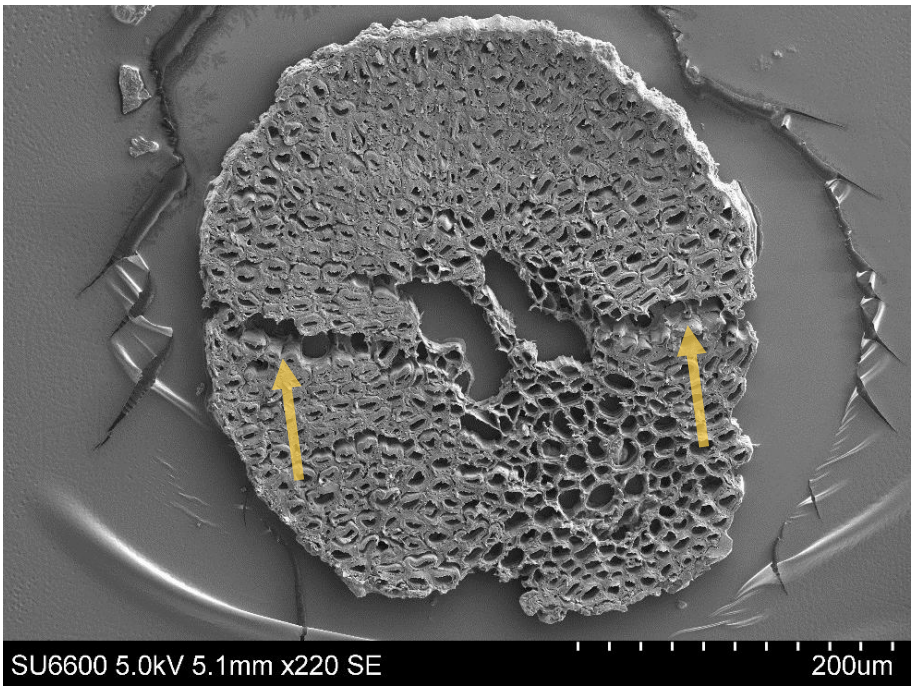

Figure 2.17: Palm fibre. Cryotome cut sample.

Furthermore, internal failure running across the internal *interface* between elementary fibres could often be observed, Figure 2.16 and Figure 2.17. This kind of debonded interface could be due to sample preparation, where fibres undergo shear stresses while being cut in the cryotome. In any case, these internal failures (including debonded intra-fibre interfaces and elementary fibre micro-cracks) could lead to sudden mechanical failure or a decrease of the fibre's mechanical properties, as was discussed for other fibres [32, 33]. Additionally, when these kinds of fibres are embedded into a composite matrix system, internal failures could rapidly propagate from the fibre to the fibre-matrix interface and subsequently to the matrix. If the composite fibre-matrix IFSS is higher than the inter-elementary fibre IFFS, the failure initiation will take place within the fibre [34, 35].

Closer inspection of the elementary fibres (Figure 2.18, Figure 2.19 and Figure 2.20) revealed further non-uniformity of cellular walls. In some cases, considerable separation could be observed between the different parts of the cell wall, giving the appearance that the primary and secondary walls may not be well bonded. As was previously discussed, this could ultimately lead to sudden mechanical failure under load, reduction of fibre properties or non-uniform stress distributions within the fibre.

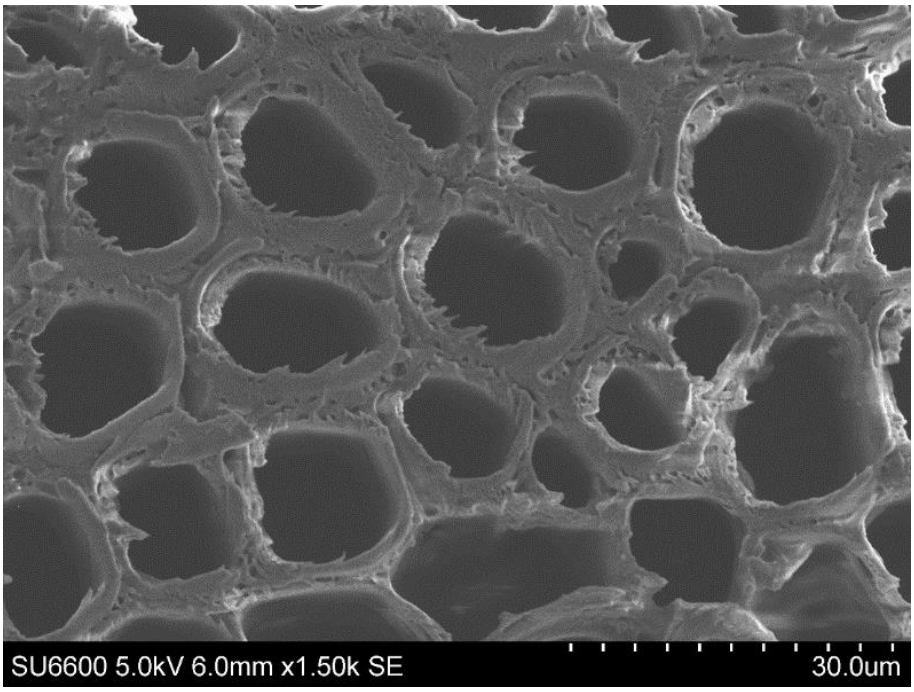

Figure 2.18: Coir fibre. Cryotome cut sample.

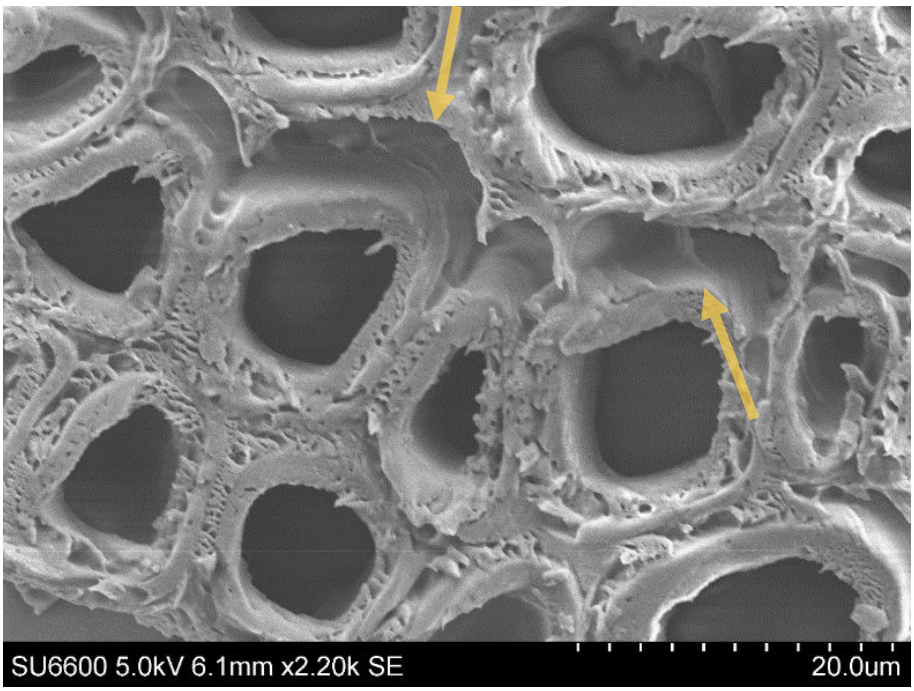

Figure 2.19: Coir fibre. Cryotome cut sample. Considerable separation, and debonded intra-fibre interfaces could be observed.

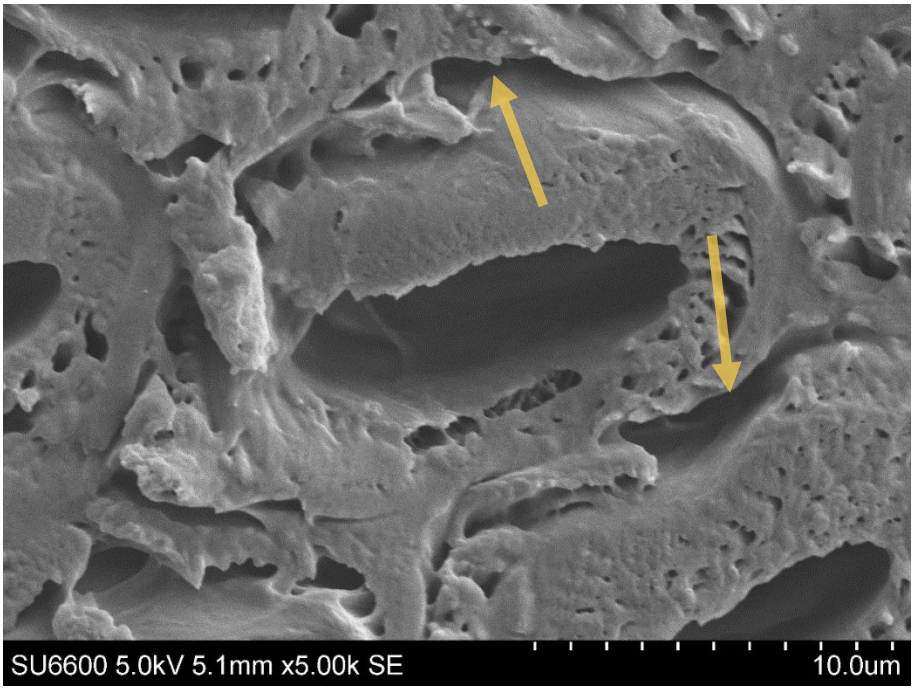

Figure 2.20: Palm elementary fibre detail. Cryotome cut sample. Substantial debonding and separation could be observed between the different parts of the cell wall.

2.3.2 Fibres' tensile and geometrical properties

2.3.2.1 Geometry of fibres

Coir and palm fibre CSA varied greatly as could be observed from fibre transverse and direct observations through optical microscopy. The initial transverse observation, revealed that the range of "diameters" for palm fibres varied from approximately 100 to 1000 μm. In the case of coir fibres, the range was slightly smaller, where fibre diameters varied from approximately 100 to 500 μm.

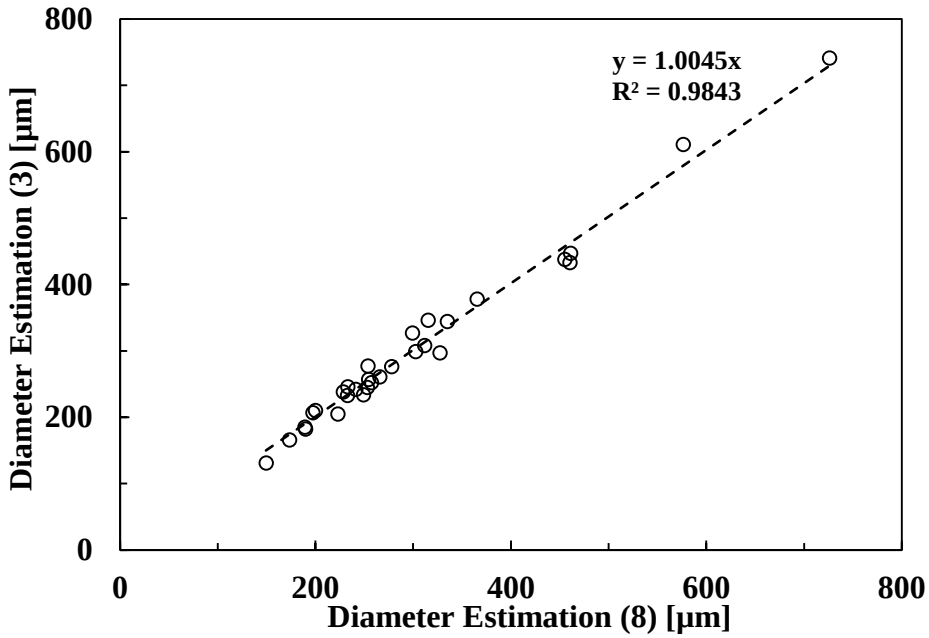

Figure 2.21: Diameter estimation method comparison for palm fibre at 20 mm gauge length.

As described in 2.2.3, the diameter used for the calculation of the estimated fibre CSA was calculated from the average of three measurements from a single photograph, taken at a given point of the fibre's gauge length. In order to further explore how precisely this approach estimated the average diameter of the fibre, for a set of 30 samples of palm fibres and 20 mm gauge length, an evaluation study was carried out. For each fibre, 4 photographs were taken along fibre's gauge length, making 2 diameter measurements for each photograph. In Figure 2.21, diameter estimation (3) corresponds to the use of a single photograph and 3 measurements to generate the average diameter value. Diameter estimation (8) corresponds to the use of 4

photographs with 2 measurements per photograph to generate the average diameter value. When both average diameter measurement methods are compared, Figure 2.21, no significant difference is observed, which indicates a low intra-fibre diameter variation and therefore, the diameter estimation (3) method represents a good "diameter" estimation method.

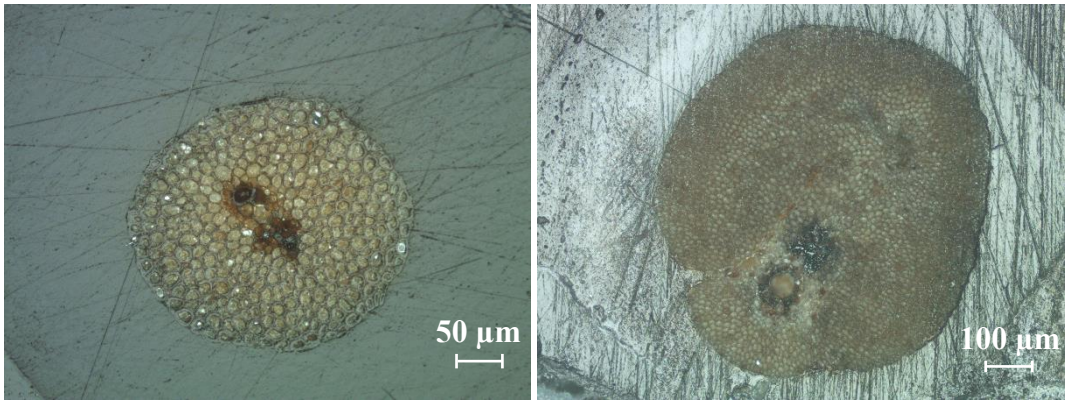

Figure 2.22: Palm fibre comparison.

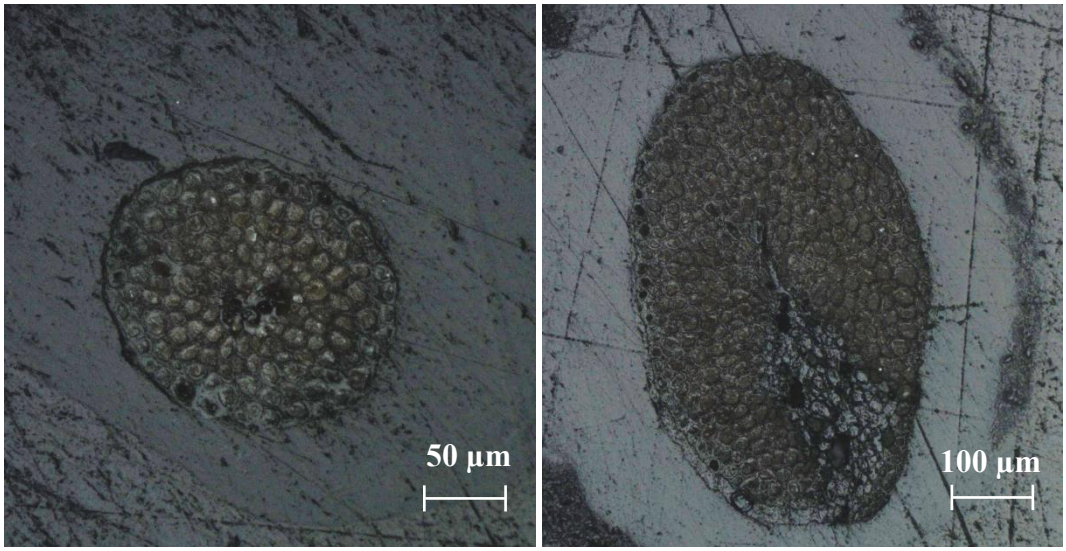

Figure 2.23: Coir fibre CSA comparison.

Direct observation through optical microscopy of post-tested fibres, Figure 2.22 and Figure 2.23, confirmed the large CSA range (especially for palm fibre).

Figure 2.24 and Figure 2.25 compare the CSA based on diameter (i.e. calculated from diameter measured from transverse observation, assuming a circular CSA) and CSA based on direct observation (considered as real CSA). As Thomason et al. [23]

pointed out, the CSA based on diameter method is the most extended procedure and normally leads to underestimation of the true fibre mechanical properties. In this case, from the slope of the least squares fitted straight line, it can be asserted that an overestimation of the CSA could be approximately 20% for palm fibres and 40% for coir fibres. The relative difference between true and estimated CSA is not as high as for other fibres, such as sisal or flax, where overestimations of 100% for sisal and 155% for flax have been documented [23].

The ratio between the major and minor axis of the fitted ellipse, as explained in 2.2.4, and the ratio between the major and minor Feret's diameters were used to analyse the circularity of fibres. Both methods proved to give almost identical results, Figure 2.26. In the case of both fibres, there was no clear dependency of the level of circularity on the initially estimated diameter, Figure 2.27. The average aspect ratio (i.e. a/b) was 1.26 and 1.28 for palm and coir respectively. These results indicate that palm and coir have almost equivalent levels of circularity, a two-sample *t*-test of the average values showed no significant difference at 95% confidence level (*p*-value = 0.64).

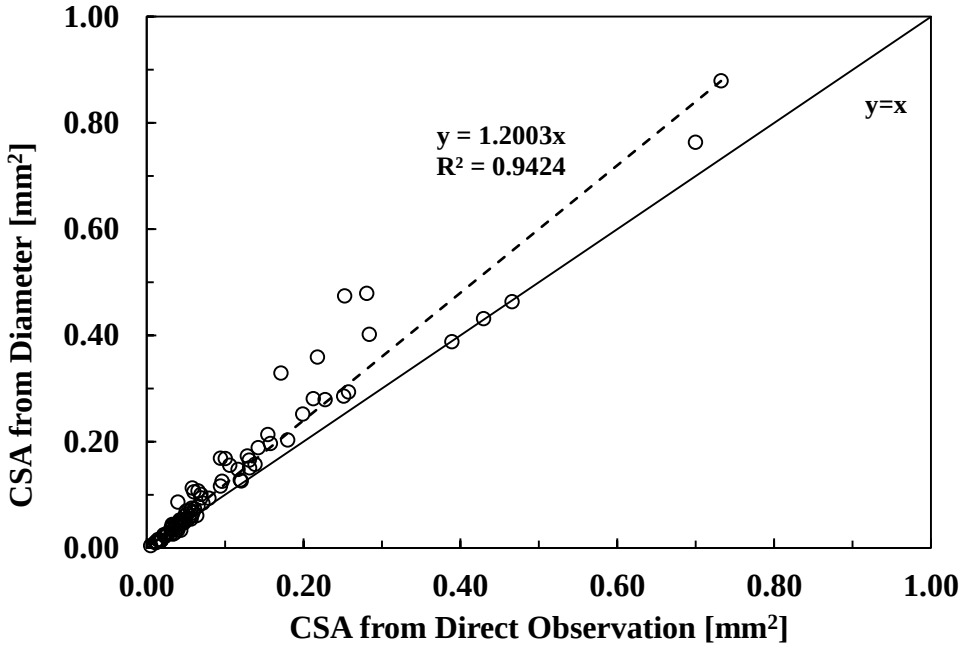

Figure 2.24: Palm's CSA measured through direct observation versus CSA calculated from transverse diameter measurement assuming a circular CSA.

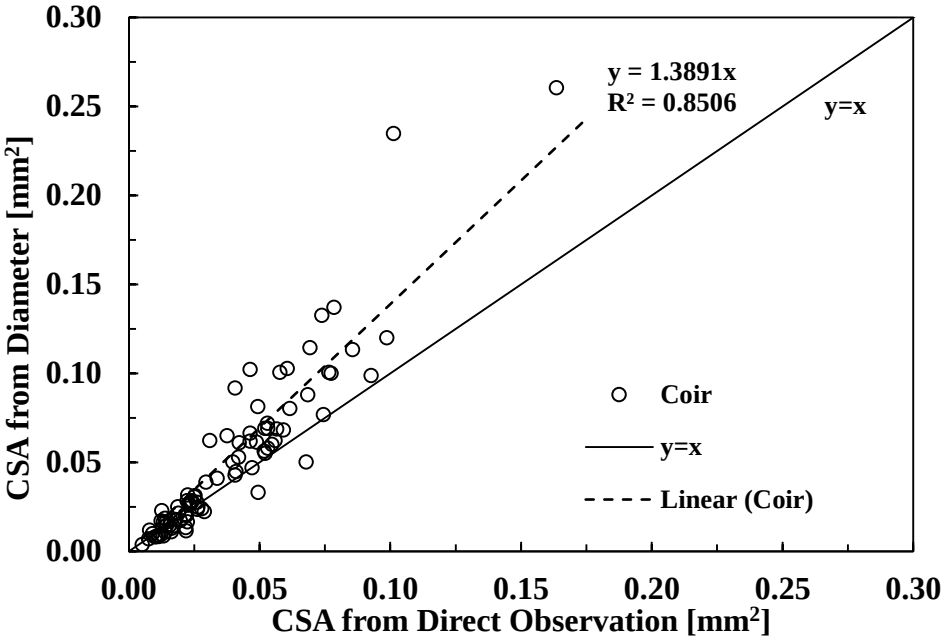

Figure 2.25: Coir's CSA measured through direct observation versus CSA calculated from transverse diameter measurement assuming a circular CSA.

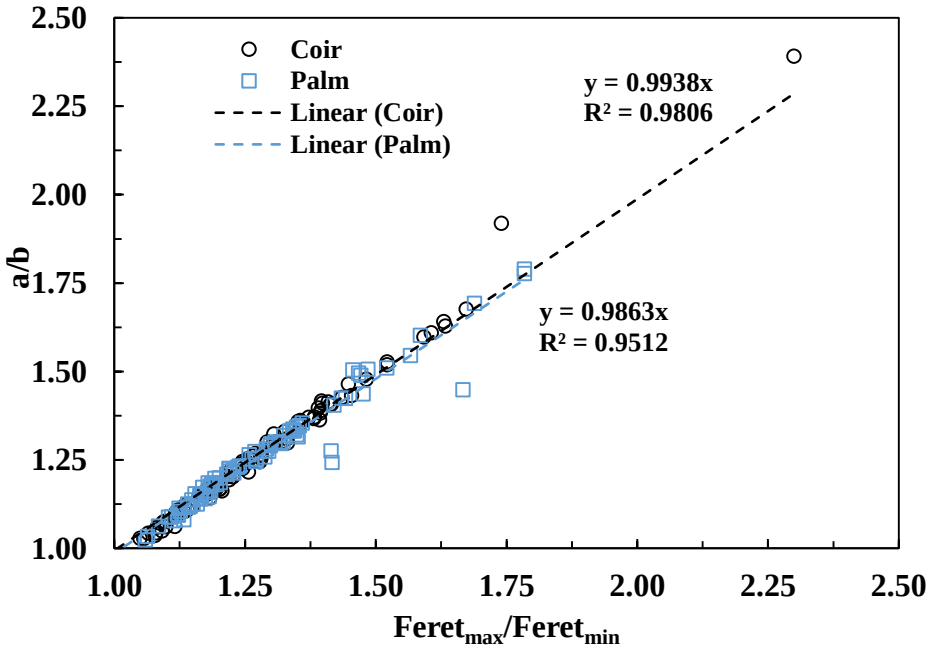

Figure 2.26: Ellipse's axis ratio versus Feret's diameters ratio.

If the ratio between true and estimated CSA is represented against the transverse estimated diameter, Figure 2.28, an apparent correlation can be observed. With the

variation of aspect ratio discarded, Figure 2.26, this could indicate some effect of sample preparation. A similar trend would be observed if the probability of positioning fibres with the major axis (assuming an elliptical CSA) parallel to the plane represented by the card (i.e. paper card where the fibre is placed) would be proportional to the size of the fibre. This could be induced by the manual handling of fibres when sticking them to the card, 2.2.3. For high diameter fibres, Figure 2.29 scenario (a) would be the more likely than (b). As the size of the fibres decreases, the probability of scenarios (a) and (b) tends to equilibrate (the manual handling would not affect as much due to the difference of scale). This artefact could lead to the overestimation or underestimation of the mechanical properties depending on the fibre CSA.

Figure 2.30 and Figure 2.31 compare the fibre perimeter based on diameter (i.e. calculated from diameter measured from transverse observation, assuming a circular CSA) and perimeter based on direct observation (considered as true perimeter). In contrast with the differences in CSA, the perimeter is almost equivalent for both methods.

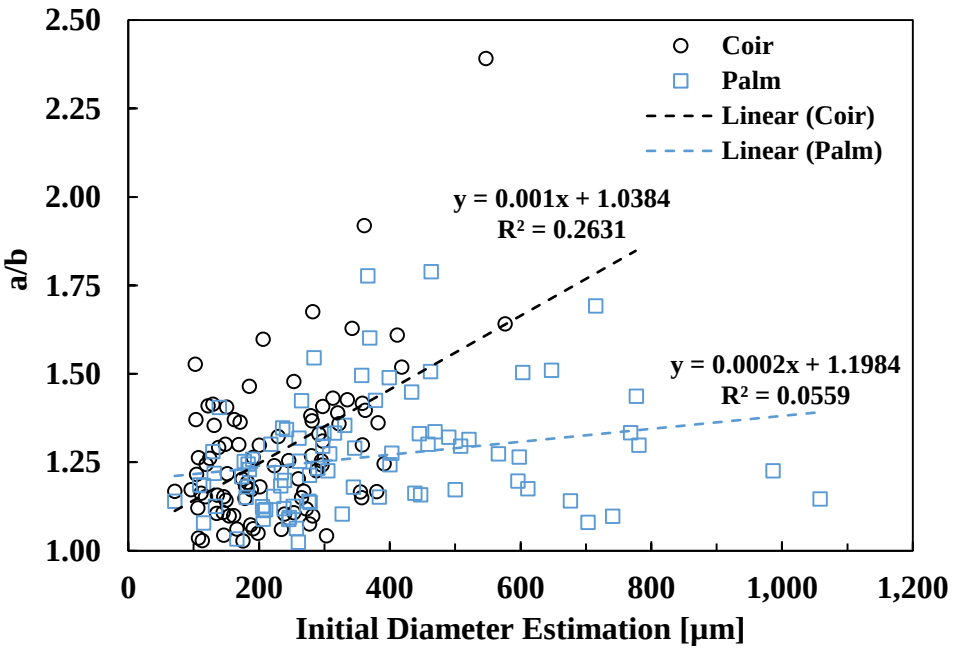

Figure 2.27: a (major axis)/b (minor axis) of the fitted ellipse versus Initial diameter estimation. a/b is here considered as a parameter to analyse the circularity of the fibre (i.e. a/b=1 for a perfectly circular fibre).

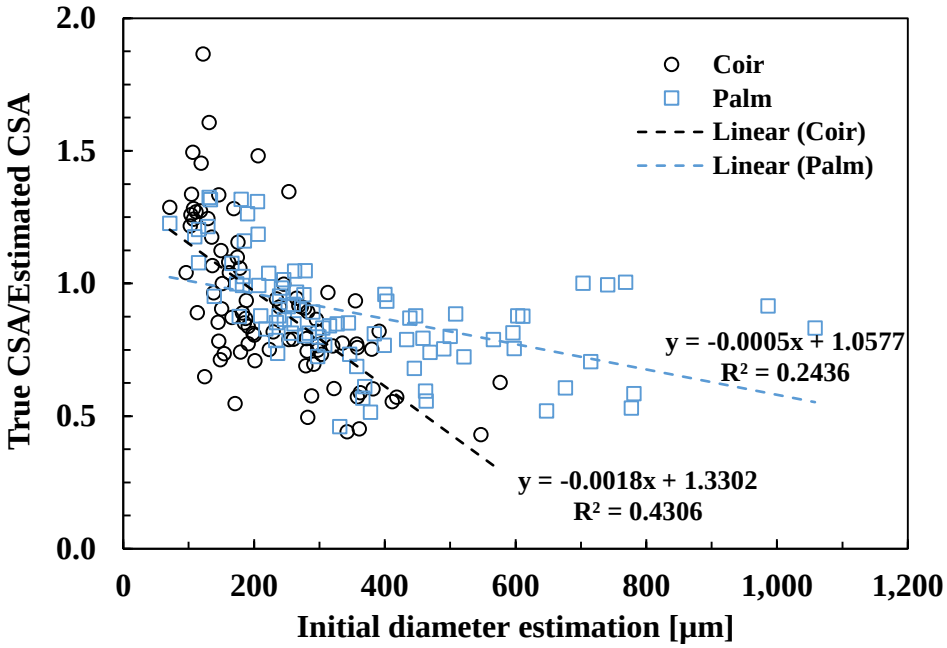

Figure 2.28: Real CSA/Estimated CSA versus Initial diameter estimation. *Initial diameter estimation* is considered as the initial measurement through transverse observation. *Real CSA* is considered as the measurement through direct observation. *Estimated CSA* is considered as the area calculated from initial diameter estimation assuming a circular CSA.

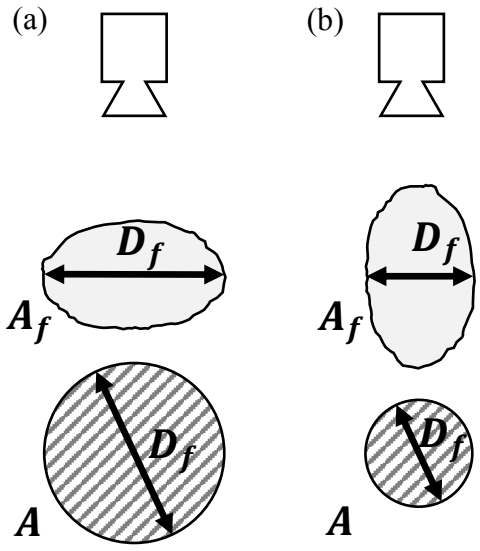

Figure 2.29: Extreme cases in estimating CSA through transverse observation. Translating this effect to mechanical properties: (a) Underestimation. (b) Overestimation.

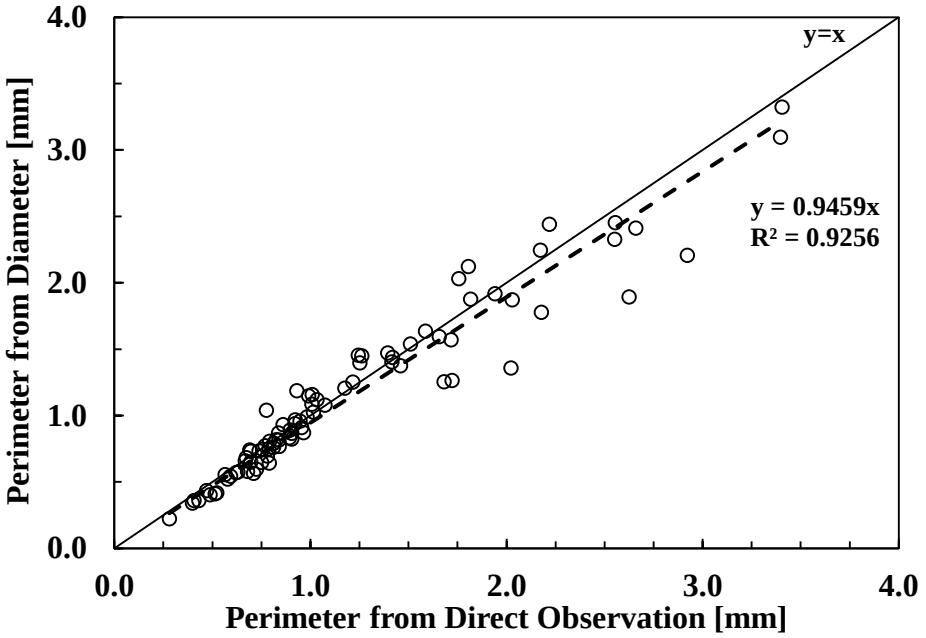

Figure 2.30: Palm fibre perimeter from diameter versus perimeter from direct observation.

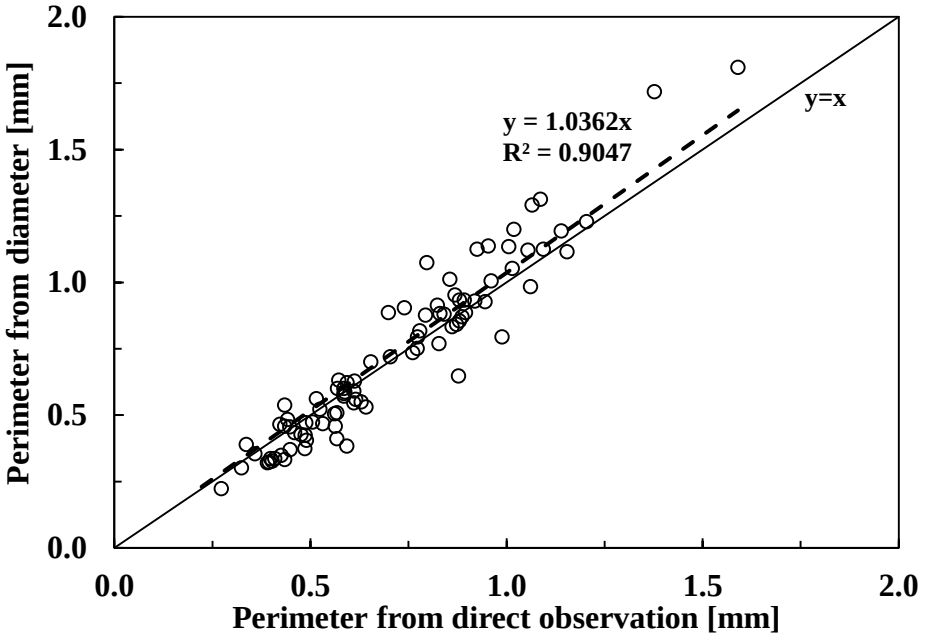

Figure 2.31: Coir fibre perimeter from diameter versus perimeter from direct observation.

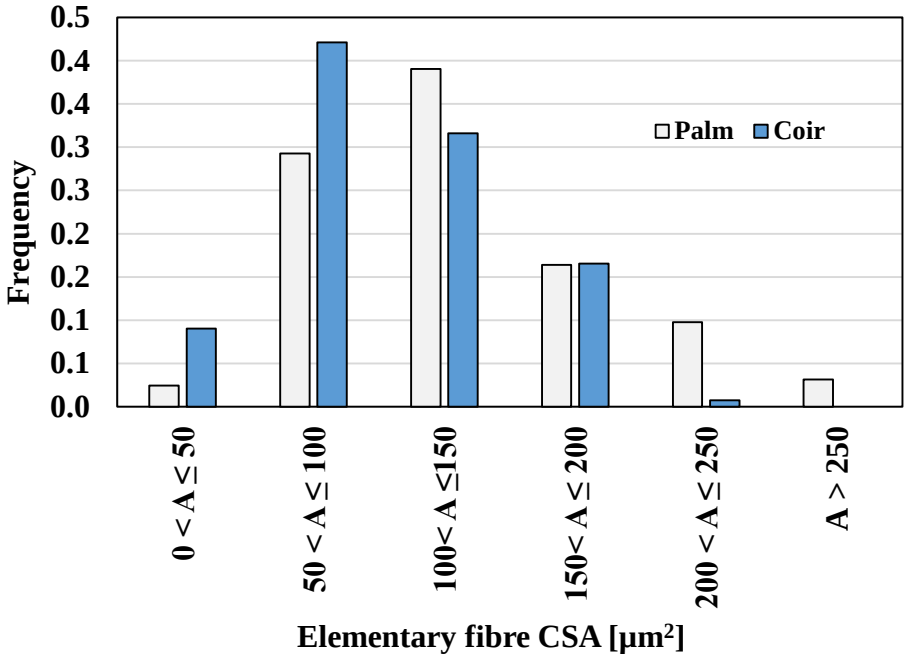

Figure 2.32: Elementary fibre CSA distribution.

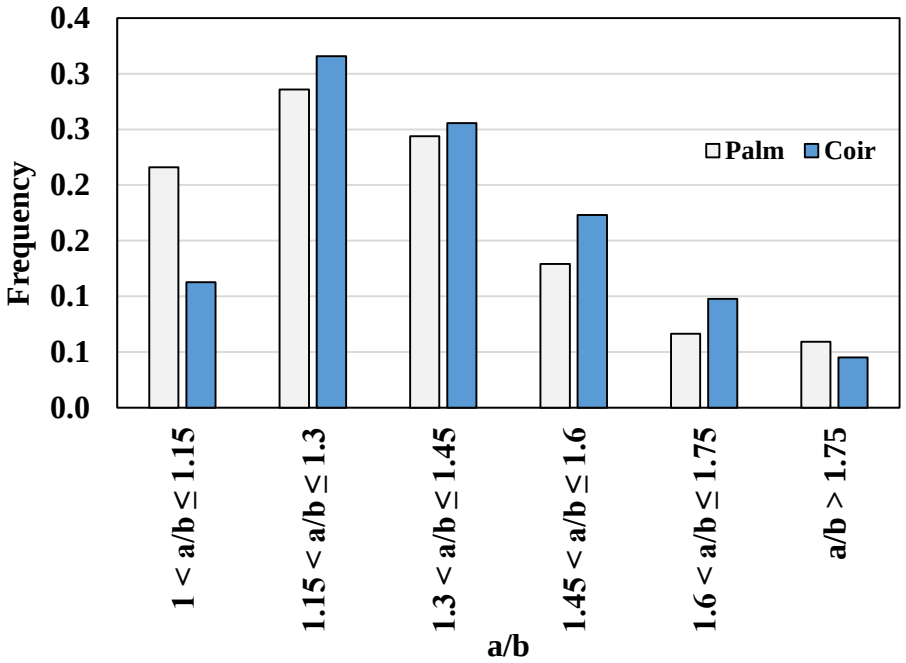

Figure 2.33: Elementary fibre aspect ratio distribution. a (major axis)/b (minor axis) of the fitted ellipse.

Figure 2.32 and Figure 2.33 illustrates the geometrical properties of palm and coir elementary fibres. A total of 420 elementary fibres were measured for this analysis,

see Figure 2.15. The average CSA of elementary fibre was 130 µm^2 for palm and 103 µm^2 for coir. A two-sample *t*-test of the average values showed this to be a significant difference even at 99% confidence level (*p*-value = $1.1 \cdot 10^{-7}$). The average aspect ratio of the elementary fibres was 1.34 for palm and 1.37 for coir. In this case, a two-sample *t*-test of the average values showed no significant difference at 95% confidence level (*p*-value = 0.2).

2.3.2.2 Tensile properties

Typical stress-strain curves for coir and palm fibres are illustrated in Figure 2.34. Distinctive regions could be observed for both fibres. The initial elastic deformation region is followed by a longer plastic deformation region. The elastic behaviour on the stress-strain curve of coir and palm fibres could be observed up to strain values of around 2%. Similar values have been previously identified for coir [36].

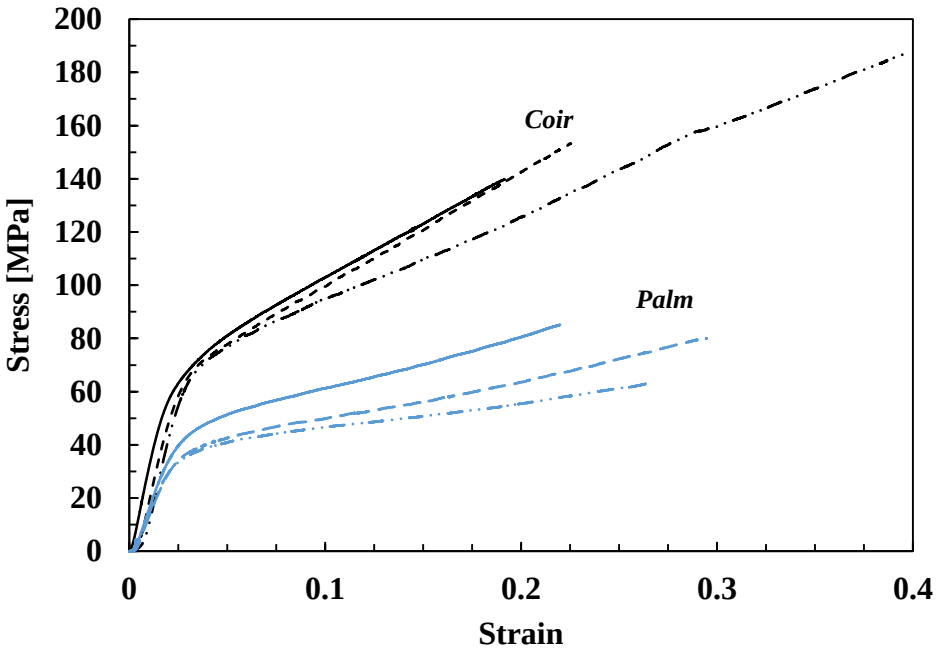

Figure 2.34: Typical coir and palm stress-strain curves at 20 mm gauge length.

Coir and palm are both fibres with high MFA [4, 36–38]. These kind of fibres normally exhibit bi-phasic stress-strain behaviour, which is related to the variation of MFA during deformation [36, 39, 40] and the interaction between cellulose microfibrils and the rest of the cellular wall matrix components (i.e. hemicellulose,

lignin, pectin and other components) [18–21]. At the yield point, the shear stress of the matrix components of the cellular walls is exceeded and cellulose microfibrils start sliding [18]. It has also been reported that coir fibres could partially recover their mechanical properties even after plastic deformation [36].

For each of the three different gauge lengths (i.e. 5, 10 and 20 mm) thirty samples were tested. The real CSA distributions for each different test are illustrated in Figure 2.35 and Figure 2.36. For palm, most of the fibres were within the range between 0.02 and 0.1 mm^2. In the case of coir, the range is significantly smaller, with most of the fibres within the range between 0.01 and 0.03 mm^2.

Non-corrected and CSA corrected values for coir and palm Young's modulus and tensile strength, are illustrated in Figure 2.37, Figure 2.38, Figure 2.39 and Figure 2.40. All results are illustrated with error bars representing 95% confidence limits. CSA corrected values for Young's modulus, tensile strength and failure strain are summarised in Table 2.2.

Sample	Young's modulus [GPa]		Tensile strength [MPa]		Failure strain [%]	
	Mean	95% Confidence limits	Mean	95% Confidence limits	Mean	95% Confidence limits
Palm all	**2.4**	**0.2**	**116**	**10**	**39.1**	**8.9**
Palm 5 mm	1.7	0.3	125	19	65.3	21.0
Palm 10 mm	2.5	0.3	114	17	28.8	8.1
Palm 20 mm	2.8	0.3	109	15	21.5	4.5
Coir all	**2.4**	**0.2**	**149**	**12**	**38.1**	**3.0**
Coir 5 mm	1.9	0.3	169	21	49.9	4.6
Coir 10 mm	2.1	0.2	122	18	39.2	3.7
Coir 20 mm	3.2	0.3	156	22	24.9	2.3

Table 2.2: Palm and coir fibres tensile properties.

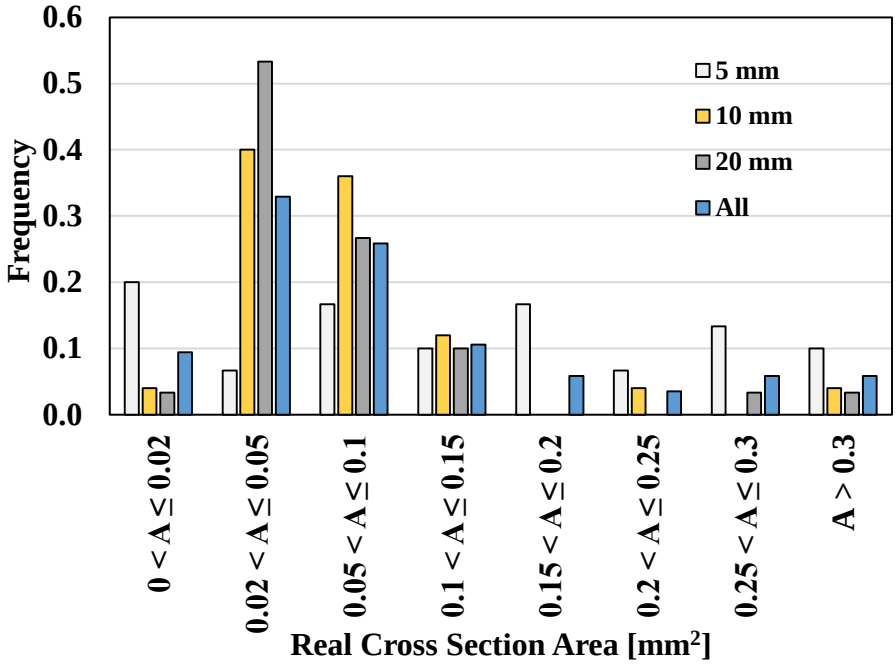

Figure 2.35: Palm real CSA distribution for tested samples, for different gauge lengths.

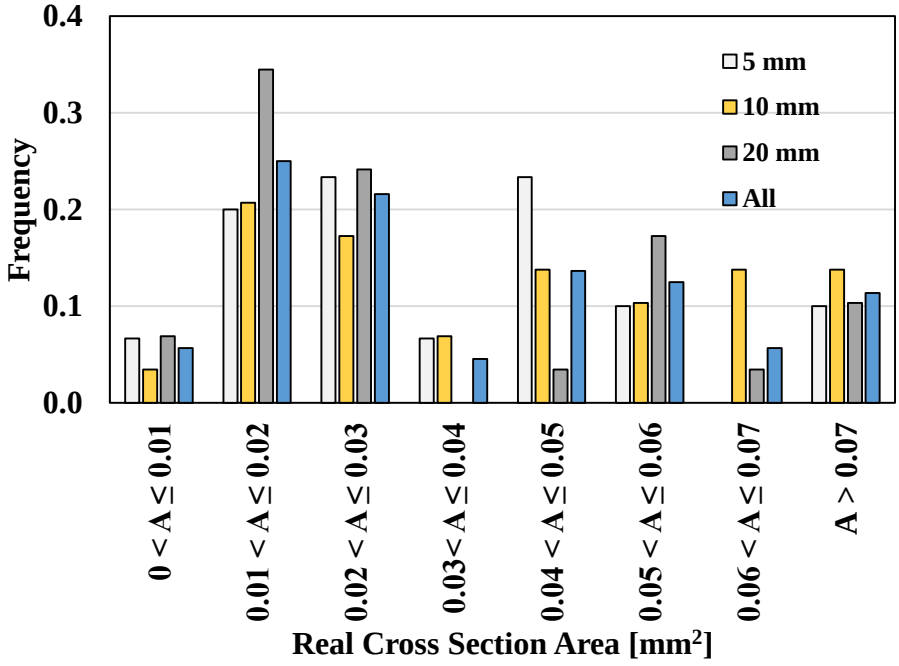

Figure 2.36: Coir real CSA distribution for tested samples, for different gauge lengths.

Figure 2.38 and Figure 2.40 illustrate the average fibre strength of palm and coir against gauge length where error bars represent the 95% confidence limits. When analysing the CSA corrections for palm and coir, *t*-tests of the overall average strength

of non-corrected and CSA corrected showed no significant differences at 95% confidence level (p-values = 0.085 for palm and 0.068 for coir). It should be noticed that although the CSA correction resulted in an increase in the average fibre strength at all gauge lengths, this effect was still "hidden" for statistical analysis in the case of overall average values, due to the large variability in natural fibre strength. However, for coir (where the overestimation of CSA is approximately 40%) the increased fibre strength from CSA correction starts to appear significant even above the variability.

Regarding CSA corrected strength values, for palm fibre, the average decreased for increasing gauge length. However, two-sample t-tests of the average CSA corrected strength at the three different gauge lengths revealed no significant differences at 95% confidence level. In this regard, and considering that there was no significant difference in palm fibre strength, it may be valid to take an overall average value. In the case of coir fibre, two-sample t-tests of the average CSA corrected strength at the three different gauge lengths showed significant differences between 5 - 10 mm and 10 - 20 mm at 95% confidence levels. However, no significant difference was found between 5 and 20 mm. These differences could indicate that the CSA distribution, slightly different for each gauge length, as illustrated in Figure 2.36, along with natural fibre variability, may have had a certain effect on the average tensile strength. A two-sample t-test of the overall CSA corrected average strength of palm (116 MPa) and coir (149 MPa) showed a significant difference in the averages at the 95% confidence level.

Single fibre tensile strength (σ_{*f}) variability is normally analysed using the Weibull distribution which has been extensively applied to data from brittle fibres such as carbon and glass. In the case of natural fibres, the application of Weibull analysis often requires modification of the theory and complicated analysis regimes [23]. The analysis relies on the assumption that the failure of fibres as a function of applied load is controlled by the random distribution defect along the length of the fibres. In the case of natural fibres, the above discussed results indicate the complex challenges of precisely characterising natural fibres, where their inherent variability (i.e. size, composition and structure) directly influences the measured value of fibre mechanical properties. Attending to the discussed variability and the non-significant difference

between sets, it is not meaningful to attempt a Weibull analysis in terms of gauge length trends.

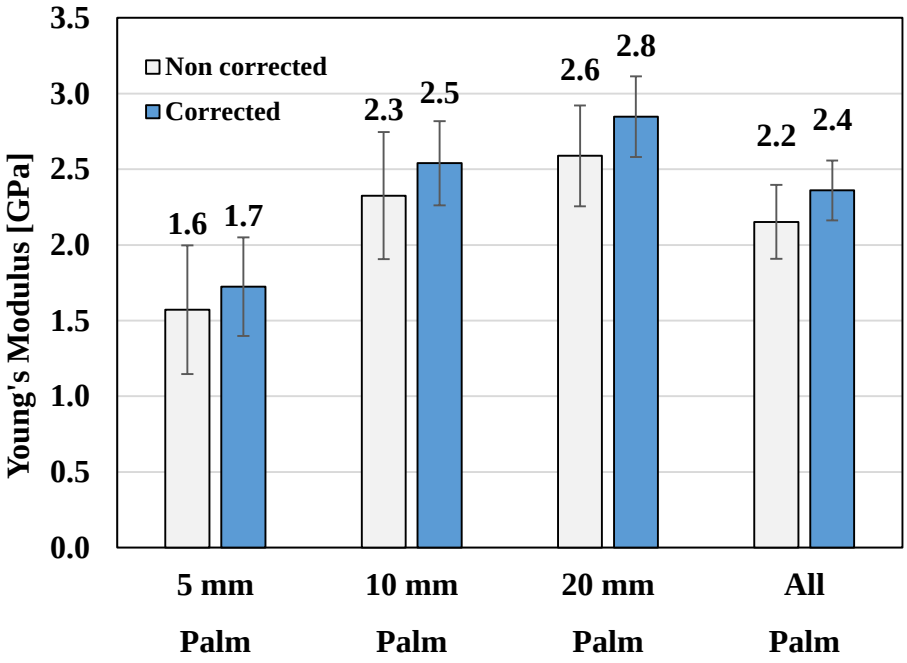

Figure 2.37: Palm fibre average Young's modulus and CSA corrected Young's modulus for three different gauge lengths and overall average.

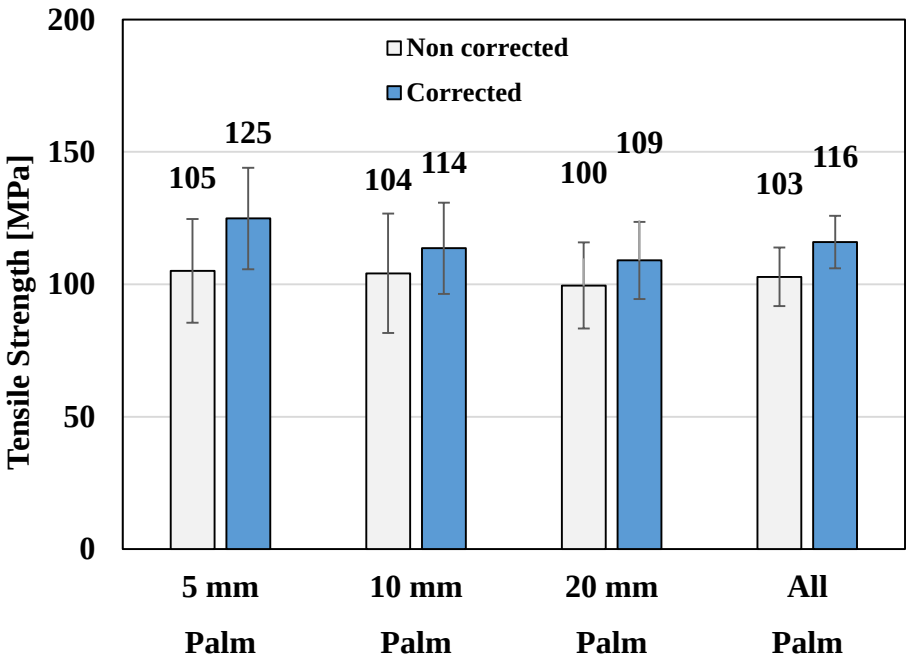

Figure 2.38: Palm fibre average tensile strength and CSA corrected tensile strength for three different gauge lengths and overall average.

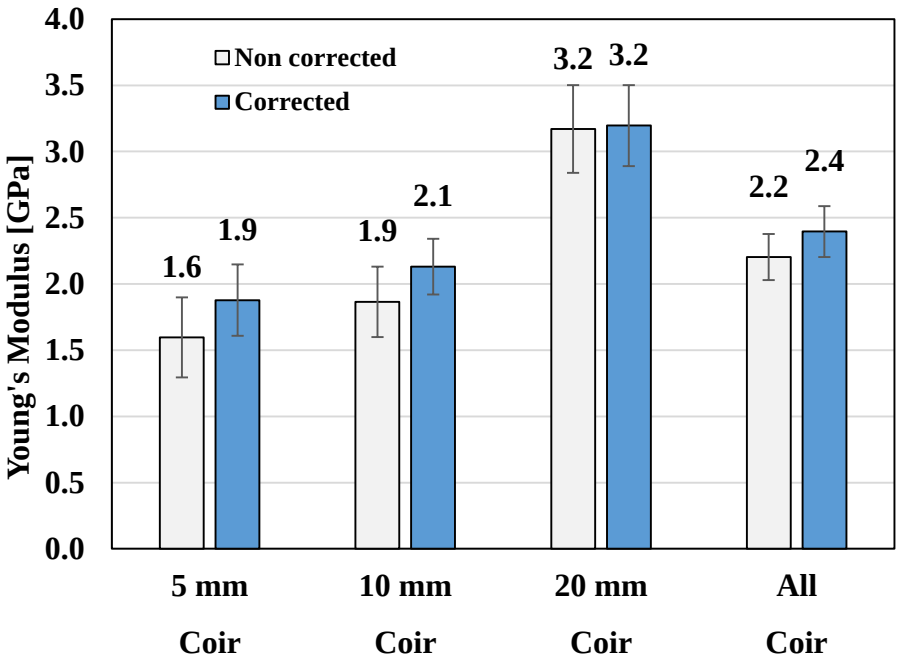

Figure 2.39: Coir fibre average Young's modulus and CSA corrected Young's modulus for three different gauge lengths and overall average.

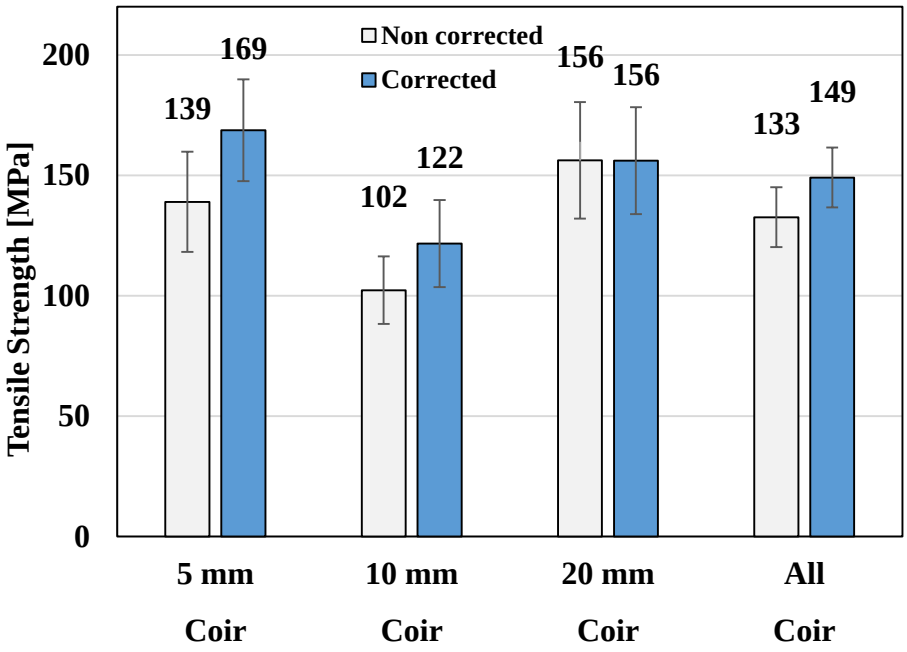

Figure 2.40: Coir fibre average tensile strength and CSA corrected tensile strength for three different gauge lengths and overall average.

From Table 2.2, it can be noticed that failure strain, for both fibres, decreased for increasing gauge length. However, in the case of palm, two-sample *t*-tests of the average failure strain showed no significant differences at 95% confidence level between 10 mm and 20 mm sets (*p*-value = 0.134). Nevertheless, in the case of coir, two-sample *t*-tests of the average failure strain showed significant differences at 95% confidence level between 5, 10 and 20 mm sets. As in the case of fibre strength, natural fibre variability and differences in the diameter distribution of sets may have had a certain influence.

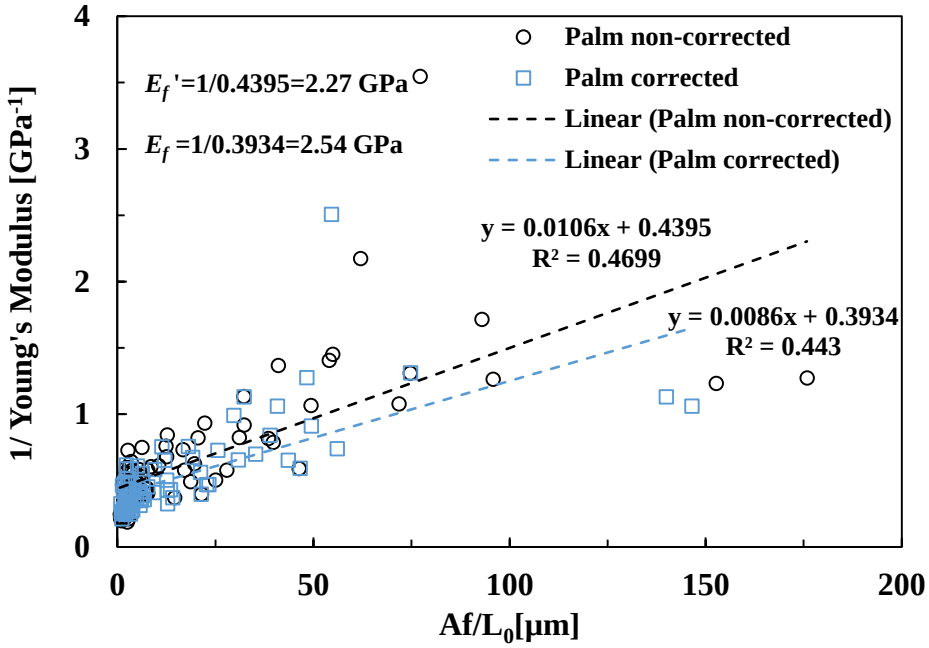

Figure 2.41: Palm's compliance corrections for non-corrected and CSA corrected values.

Regarding the analysis of Young's modulus, in the case of both fibres, there was a clear gauge length effect. It is well recognised that the values obtained during single fibre testing can be affected by the gauge length of the fibre and that these effects must be analysed [23]. Tensile data was plotted as described in (2.8), Figure 2.41 and Figure 2.42. A straight line was fit to the cloud of points by the least squares method. With the value of the intersection between the straight line and the vertical axis, the true modulus E_f was calculated according to (2.9).

For both fibres, the compliance corrected Young's modulus was calculated for non-corrected data ($E_f{}'$) and CSA corrected data (E_f). Final E_f values revealed similar Young's modulus for palm (2.54 GPa) and coir (2.94 GPa). The CSA correction datasets showed an increase of E_f in relation to $E_f{}'$ of approximately 8 and 4% for palm and coir respectively.

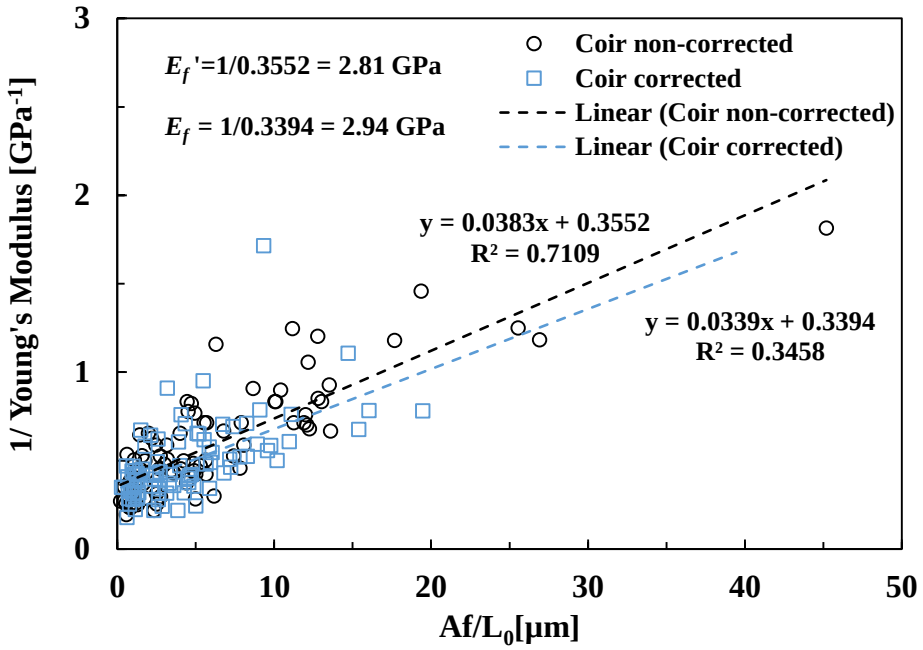

Figure 2.42: Coir's compliance corrections for non-corrected and CSA corrected values.

2.3.3 Young's modulus dependence on cross-section area

When analysing the effect of fibre CSA (A_f) on the Young's modulus, certain patterns started emerging, Figure 2.43 and Figure 2.44. In general terms, average Young's modulus decreased for increasing CSA. As discussed in section 2.1.4, Baley [13] suggested that, non-constant CSA, ignoring the lumen when calculating the CSA, the presence of defects, and variability in the composition of fibres, could cause the observed correlation. However, a fundamental issue was exposed in 2.3.1 that could be responsible for this behaviour. As previously discussed, natural fibres are made up of single elementary fibres or cells, joined together by the middle lamella. The middle lamella is mainly composed by pectin and lignin and its main purpose is to hold

together the collection of cells. While analysing the internal structure of natural fibres, several signs of damaged or weak inter-elementary fibre interface were observed.

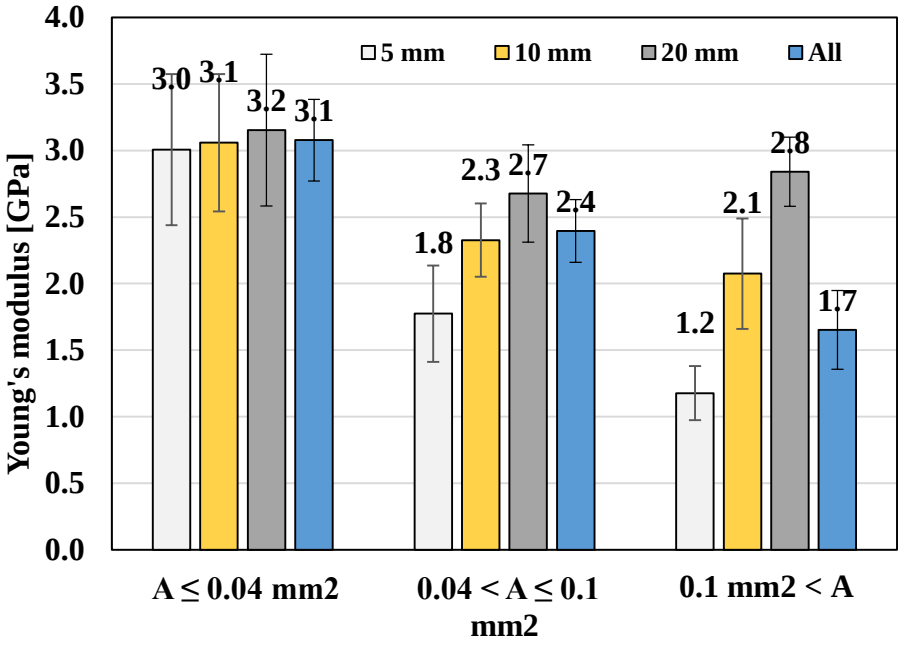

Figure 2.43: Palm Young's modulus for three different CSA (A) ranges, and for different gauge lengths. Three CSA ranges were arbitrarily chosen.

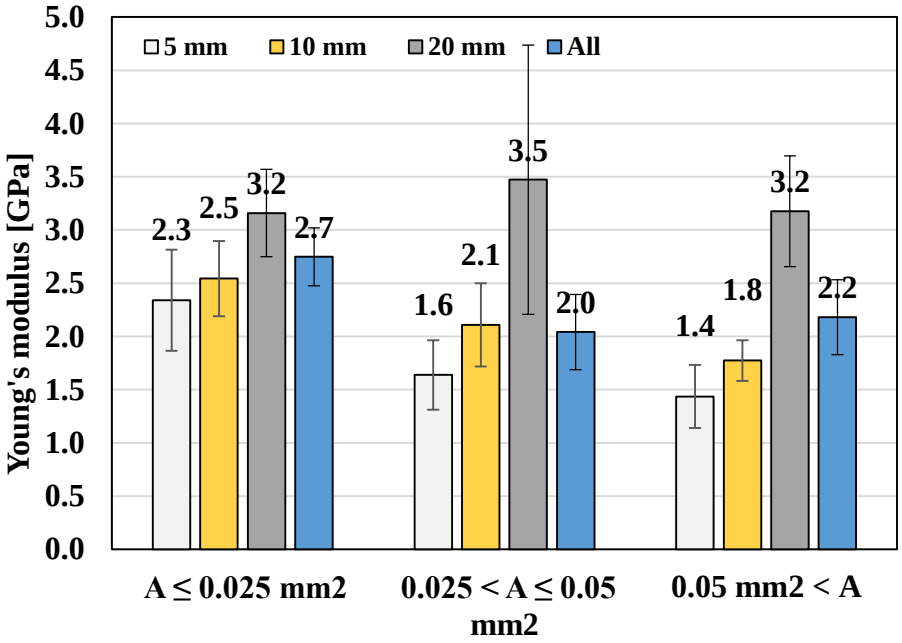

Figure 2.44: Coir Young's modulus for three different CSA (A) ranges, and for different gauge lengths. Three CSA ranges were arbitrarily chosen.

When analysing the micro-mechanical behaviour of fibres, shear-lag theories [41] assume no or little stress transfer through fibres' ends. Consequently, most of the stress (in a tensile test or when embedded in a matrix system) is transferred through fibres' external surface, known as fibre-matrix interface. A lack of efficiency in transferring stress to the individual elementary fibres across the CSA would therefore result in a CSA dependency of the Young's modulus.

If the middle lamella is not able to efficiently transfer stress from outer to inner elementary-fibres, this could ultimately lead to the elementary fibres located in the perimeter of the CSA to support considerably higher levels of stress compared to elementary-fibres in the interior of the fibre. Similar Young's modulus effects due to the lack of stress transfer have been previously observed in multi-walled carbon nanotubes (MWCNT) [42, 43]. The shear-lag nature of the problem also leads to the prediction that this effect would be less evident for higher gauge lengths, as observed in Figure 2.43 and Figure 2.44. For this reason, the treatment of experimental data focused on the Young's modulus of fibres tested at 5 mm gauge length. In the case of palm, the trend appeared to be clearer, perhaps, due to a higher range of CSA included in the study in comparison with coir.

2.3.3.1 Honeycomb and circular models

In this analysis, palm and coir fibres were analysed as cellular solids (i.e. formed by the addition of units or cells, hexagonal prisms in this case). This approach has been previously used to analyse a broad range of natural materials [44–50] such as wood, cork, bone, etc. A mathematical model of the structure of natural fibres was developed in order to analyse the effects of stress transfer on the observable Young's modulus. The fibre was considered to be made up of equally sized, perfectly hexagonal cross section elementary-fibres or cells arranged together to form a honeycomb structure. Every element of the structure is assumed to have the same isotropic mechanical properties. In the honeycomb model, the elements are assumed to be continuous (in the longitudinal direction) and have the same length as the natural fibre structure.

The basic hexagon is defined in Figure 2.45. , where the side length of the hexagon l is related to h as in (2.10). The area of each cell is A_c, as defined in (2.11). The

structure builds up around a central cell, considered as the centre of the fibre as illustrated in Figure 2.46.

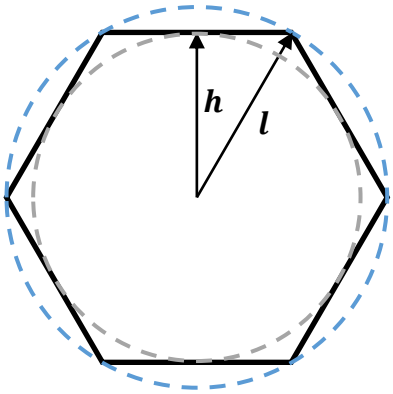

Figure 2.45: Hexagon structure

$$h = \frac{\sqrt{3}}{2} l \tag{2.10}$$

$$A_c = l^2 \frac{3\sqrt{3}}{2} \tag{2.11}$$

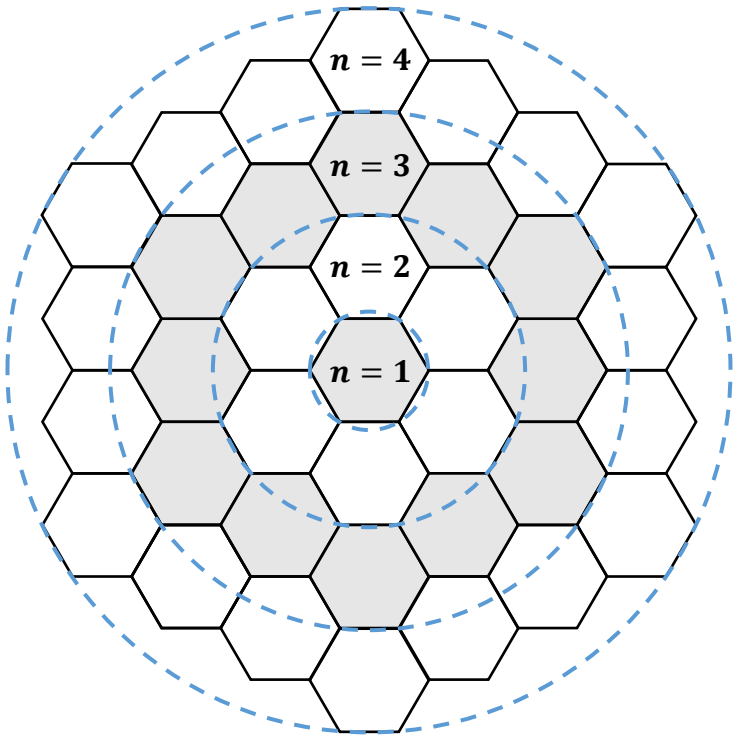

Figure 2.46: Natural fibre model structure.

The variable n is defined as the number of *levels* of the structure, where the central cell is considered as the first level (i.e. $n = 1$). It was assumed that all the elements in the same n-level are under the same homogenous stress. Normal stresses and Poisson's ratio effects were neglected in the model. The number of cells in the n-level, n_{pc} is given by (2.12).

$$n_{pc} = 6(n-1);\ n \in \mathbb{N} \setminus \{1\} \tag{2.12}$$

Consequently, the area of the n-level is defined,

$$A_n = 9\sqrt{3}(n-1)l^2;\ n \in \mathbb{N} \setminus \{1\} \tag{2.13}$$

The external perimeter of the n-level P_n is defined in (2.14).

$$P_n = 6(2n-1)l;\ n \in \mathbb{N} \tag{2.14}$$

At the same time, the total number of cells n_{tc} for a fibre made up by n-levels is given by the expression (2.15). Figure 2.47 illustrates how the total number of cells and number of cells in the perimeter increase for increasing n-levels.

$$n_{tc} = 1 + 6\sum_{i=2}^{n}(i-1)\ ;\ n \in \mathbb{N} \tag{2.15}$$

For each n-level, a circumference can be defined where the cells can be inscribed as it is showed in Figure 2.46. The radius of the circumscribed (r_{cc}) and inscribed (r_{ci}) circumference to the cells is given by (2.16) and (2.17) respectively.

$$r_{cc} = \frac{l}{2}[1 + 3(2n-1)^2]^{\frac{1}{2}};\ n \in \mathbb{N} \tag{2.16}$$

$$r_{ci} = \frac{\sqrt{3}}{2}l(2n-1);\ n \in \mathbb{N} \tag{2.17}$$

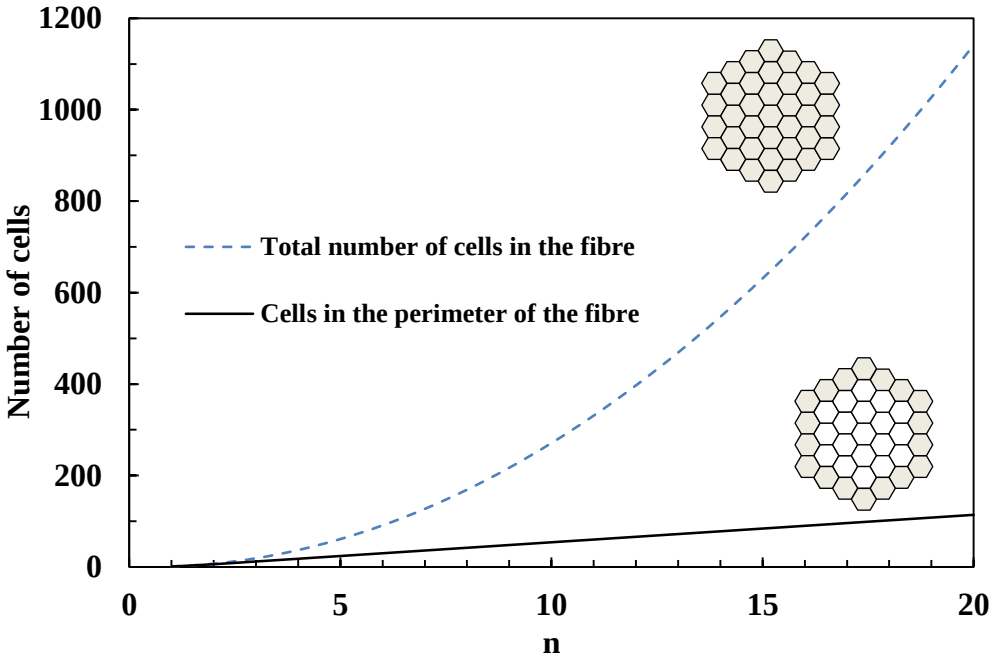

Figure 2.47: Total number of cells and cells in the perimeter comparison versus n.

Therefore, a fibre with a CSA A_f, for a defined l would have an equivalent fibre of n-levels, approximating $A_f \sim \pi {r_{cc}}^2$ (2.18) or $A_f \sim \pi {r_{ci}}^2$ (2.19). For a defined value of l, (2.18) and (2.19) will provide a non-integer n. The value of n would be approximated as the nearest integer to the number provided by (2.18) or (2.19).

$$n = \frac{1}{2}\left(1 + \frac{1}{\sqrt{3}}\sqrt{\left(\frac{4A_f}{\pi l^2} - 1\right)}\right) \tag{2.18}$$

$$n = \frac{1}{2}\left(1 + \frac{2}{l\sqrt{3}}\sqrt{\frac{A_f}{\pi}}\right) \tag{2.19}$$

As the first consideration, if there is no stress transfer between the cells in the perimeter and the internal cells, fibres would be equivalent to hollow fibres, Figure 2.48.

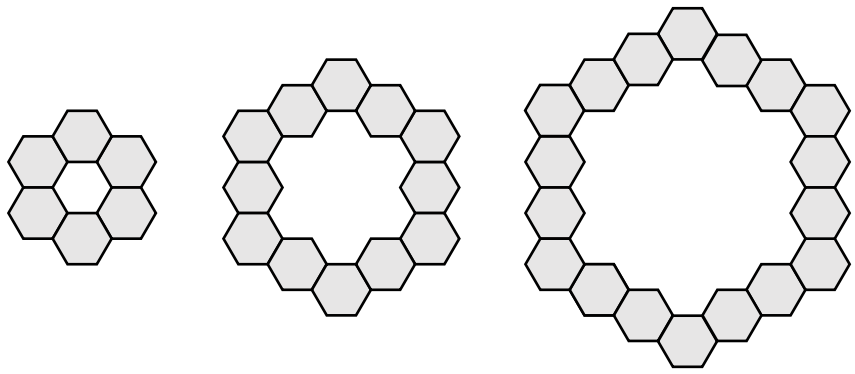

Figure 2.48: Equivalent hollow fibres.

The measured tensile Young's modulus of the fibres E_f is calculated according to (2.20). If it is corrected for the effective CSA (of a hollow fibre in this case, A_n), the true (under no interfacial stress transfer conditions) Young's modulus E_{fr} is calculated according to (2.21). In the case that a void exists in the centre of the fibre and that it could be determined for each fibre, it would be introduced as A_0.

$$E_f = \frac{F}{A_T + A_0}\frac{1}{\varepsilon} \tag{2.20}$$

$$E_{fr} = \frac{F}{A_n}\frac{1}{\varepsilon} \tag{2.21}$$

The relationship between (2.20) and (2.21) is illustrated in (2.22).

$$E_f = \frac{A_n}{A_T + A_0}E_{fr} \tag{2.22}$$

If A_c is the area of a single cell and $A_0 = 0$, according to this model (A_n is the area of the cells in the outer level and A_T is the area of the total number of cells), (2.22) could be re-written as in (2.23), where n is calculated according to (2.18) or (2.19).

$$E_f = \frac{A_n}{A_T}E_{fr} = \frac{n_{pc}A_c}{n_{tc}A_c}E_{fr} = \frac{6(n-1)}{1 + 6\sum_{i=2}^{n}(i-1)}E_{fr}\ ;\ n \in \mathbb{N} \setminus \{1\} \tag{2.23}$$

In (2.23), it was assumed that there is no stress transfer between the different levels. As previously discussed, stress transfer issues between the different graphene layers

are also involved in MWCNT [43]. In a similar manner, the shear stress transfer could be implemented in this honeycomb model.

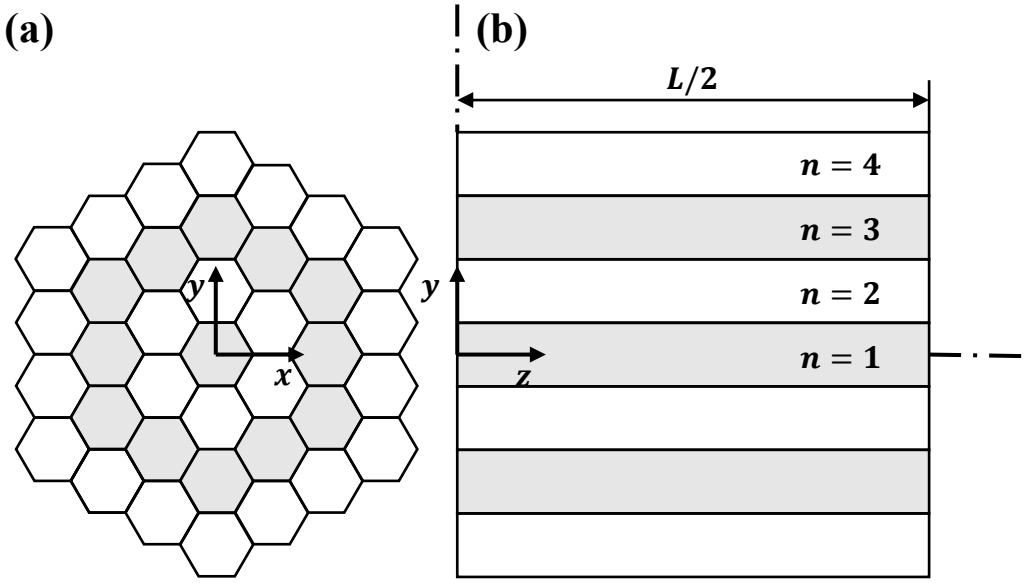

Figure 2.49: Natural fibre honeycomb model. (a) Cross section view of the model, where the origin xy is located in the centre of the central cell (i.e. $n = 1$) and the middle point of the fibre length L. (b) Longitudinal view of the model in the plane yz.

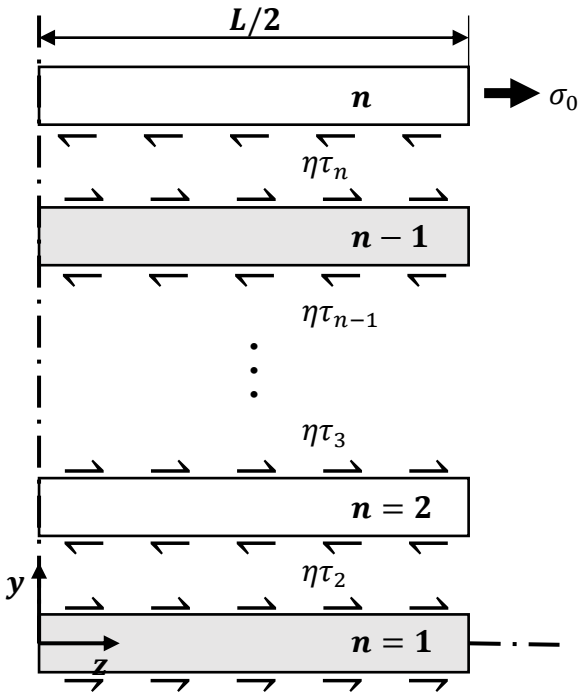

Figure 2.50: Stress transfer between levels. The fibre is made up by the n-levels.

The honeycomb fibre structure, with a cross section illustrated in Figure 2.46 and Figure 2.49 (a), could also be represented by the plane yz perpendicular to x, running along the fibre's longitudinal axis, Figure 2.49 (b).

The interactions between the different levels of a fibre with n-levels are illustrated in Figure 2.50. The shear stress transfer is expressed through a series of τ_i which are defined as apparent interfacial shear stress along the inter-level interfaces. The efficiency of interfacial stress transfer is defined as η, where $0 \leq \eta < 1$ (i.e. $\eta = 0$ represents a situation where no stress is transferred through the interface). The stress applied to the fibre σ_0 is directly transferred to the outer level.

For the case where $\eta = 1$ (i.e. perfect stress transfer), the extension of the outer level (i.e. level n) is illustrated in (2.24). E_{fr}, P_n and A_n have been previously defined.

$$\Delta L_n = \frac{\sigma_0 L}{2E_{fr}} - \frac{P_{n-1}L^2}{4A_n E_{fr}}\tau_n \tag{2.24}$$

The extension of any intermediate level ΔL_i is defined according to interfacial stresses as in (2.25).

$$\Delta L_i = \frac{P_i L^2}{4A_i E_{fr}}\tau_{i+1} - \frac{P_{i-1}L^2}{4A_i E_{fr}}\tau_i \tag{2.25}$$

At the central level (i.e. level 1), the extension is defined as in (2.26).

$$\Delta L_1 = \frac{P_i L^2}{4A_1 E_{fr}}\tau_2 \tag{2.26}$$

For the case here analysed, where $\eta = 1$, it is mandatory that the extension of all levels is identical (2.27).

$$\Delta L_n = \Delta L_i = \Delta L_1 \tag{2.27}$$

Consequently, in order to satisfy (2.27), it is required that the apparent interfacial shear stress τ_i varies according to (2.28).

$$\tau_i = \frac{2\sigma_0 A_n}{P_{i-1} L}\left(1 - \frac{\sum_{j=i}^{n} A_j}{A_T}\right) \tag{2.28}$$

Once the variation of τ_i is obtained, by substituting (2.28) in (2.24) and adding the η parameter, the extension of the external level could be re-written as in (2.29).

$$\Delta L_n = \frac{\sigma_0 L}{2E_{fr}}\left(1 - \eta\left(1 - \frac{A_n}{A_T}\right)\right) \tag{2.29}$$

Substituting (2.29) in (2.30) the measured Young's modulus of the fibres E_f is related to E_{fr} according to (2.31).

$$E_f = \frac{\sigma}{\varepsilon} = \frac{\sigma_0 A_n}{A_T + A_0}\frac{1}{\varepsilon} = \frac{\sigma_0 A_n}{A_T + A_0}\frac{L}{2\Delta L_n} \tag{2.30}$$

$$E_f = \frac{A_n}{A_T + A_0}\left(1 - \eta\left(1 - \frac{A_n}{A_T}\right)\right)^{-1} E_{fr} \tag{2.31}$$

Substituting A_n and A_T and with $A_0 = 0$, the measured Young's modulus of the fibres E_f is defined as in (2.32), for $n \in \mathbb{N} \setminus \{1\}$ (for $n = 1$, $E_f = E_{fr}$)

$$E_f = \frac{6(n-1)}{1 + 6\sum_{i=2}^{n}(i-1)}\left(1 - \eta\left(1 - \frac{6(n-1)}{1 + 6\sum_{i=2}^{n}(i-1)}\right)\right)^{-1} E_{fr} \tag{2.32}$$

For the case where $\eta = 0$, (2.32) is equivalent to (2.23). On the other hand, for a perfect bonding scenario (i.e. $\eta = 1$), $E_f = E_{fr}$ (if $A_0 = 0$). Figure 2.51 illustrates the ratio E_f/E_{fr} according to (2.32).

A circular model could also be compared to the honeycomb model. This model is defined as illustrated in Figure 2.52. In this case, elementary fibres are assumed to join together in a series of homogenous levels. As in the honeycomb model, it was assumed that the stress is uniform within the same n-level. Normal stresses and Poisson's ratio effects were also neglected.

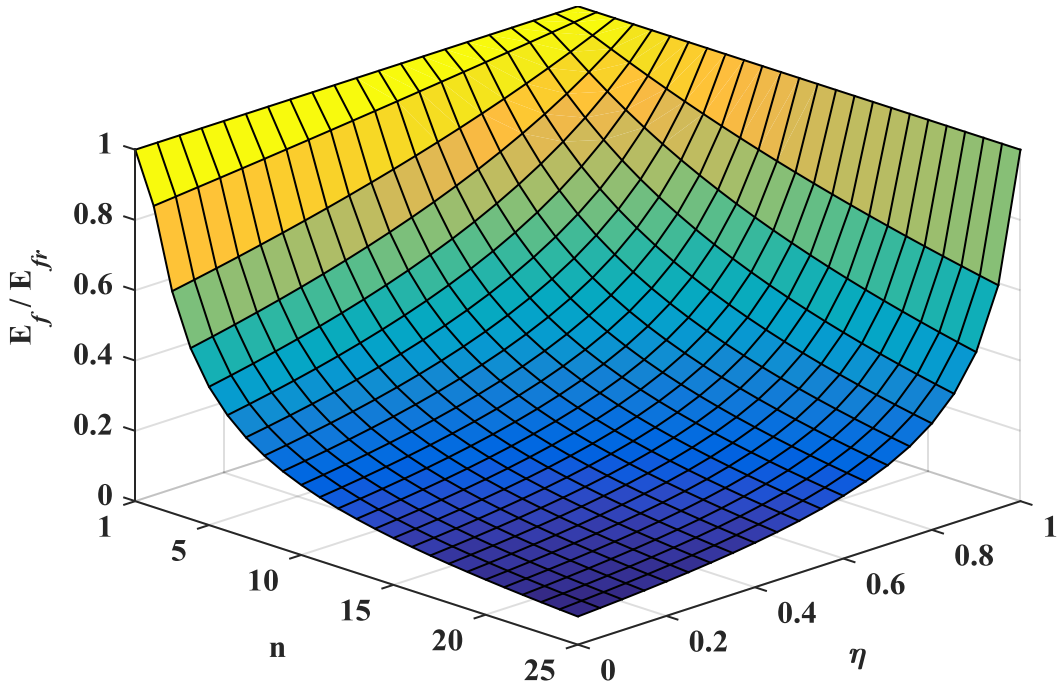

Figure 2.51: E_f/E_{fr} according to (2.32) for variable fibre's number of levels (n) and interfacial stress transfer efficiency (η).

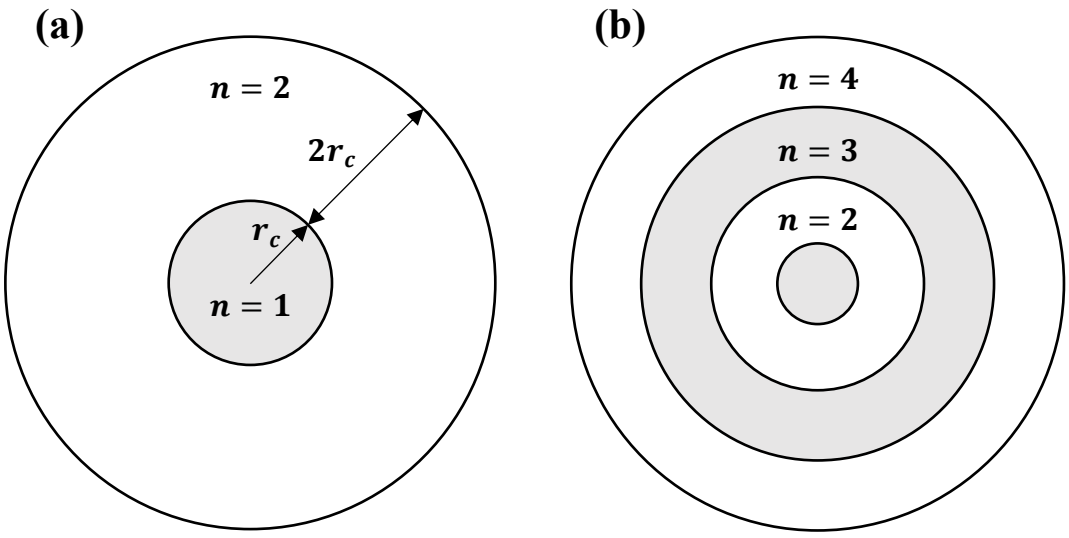

Figure 2.52: Natural fibre circular model.

Based on the definition given in Figure 2.52 (a), the external radius of each level will be determined according to (2.33). The value of $2r_c$ could be understood as the diameter of a single elementary fibre.

$$r_n = r_c(2n-1)\,;n \in \mathbb{N} \tag{2.33}$$

Consequently, the area of each level is given by (2.34).

$$A_n = 8\pi {r_c}^2(n-1)\,;n \in \mathbb{N} \setminus \{1\} \tag{2.34}$$

For a defined value of r_c, the number of levels for a fibre with a CSA equal to A could be calculated according to (2.35). As for the honeycomb model, the value of n would be approximated as the nearest integer to the number provided by (2.35).

$$n = \frac{1}{2}\left(1 + \frac{1}{r_c}\sqrt{\frac{A}{\pi}}\right) \tag{2.35}$$

According to this model, and assuming $A_0 = 0$, (2.32) could be re-written as (2.36).

$$E_f = \frac{8(n-1)}{(2n-1)^2}\left(1 - \eta\left(1 - \frac{8(n-1)}{(2n-1)^2}\right)\right)^{-1} E_{fr} \tag{2.36}$$

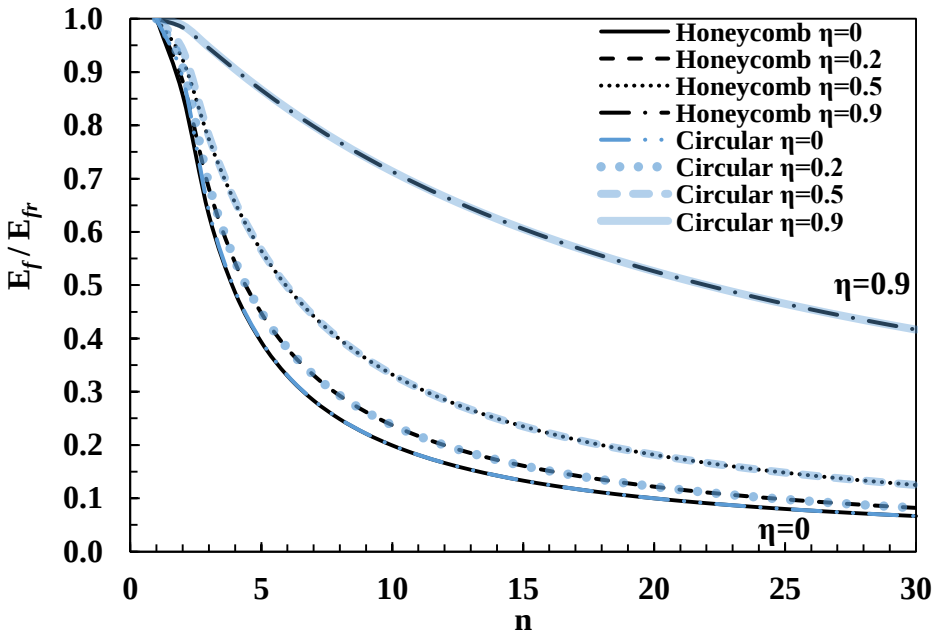

Figure 2.53: Honeycomb and circular model comparison. E_f/E_{fr} according to (2.32) and (2.36) for variable fibre's number of levels (n) and interfacial stress transfer efficiency (η).

Both models, honeycomb and circular models are compared in Figure 2.53, (2.32) and (2.36). It can be clearly appreciated how the two models are approximately equivalent, with overlapping curves for the E_f/E_{fr} ratio versus n. Both models are formulated for n and η, which allow an inclusion of a cell size dependence on CSA (i.e. $n(l, A)$ for (2.18) and (2.19), $n(r_c, A)$ for (2.35)).

2.3.3.2 Experimental data and theoretical predictions

It is necessary to underline that in any attempt to fit these theoretical models to experimental observations it is important to be aware of the limitations of the model if the significant variability of natural fibres' properties is taken into consideration. Moreover, due to the previously discussed effect of fibre length in relation to the shear-lag and compliance effects (that these models do not take into consideration), the theoretically calculated E_{fr} would be restricted to the gauge length of the experimental observations.

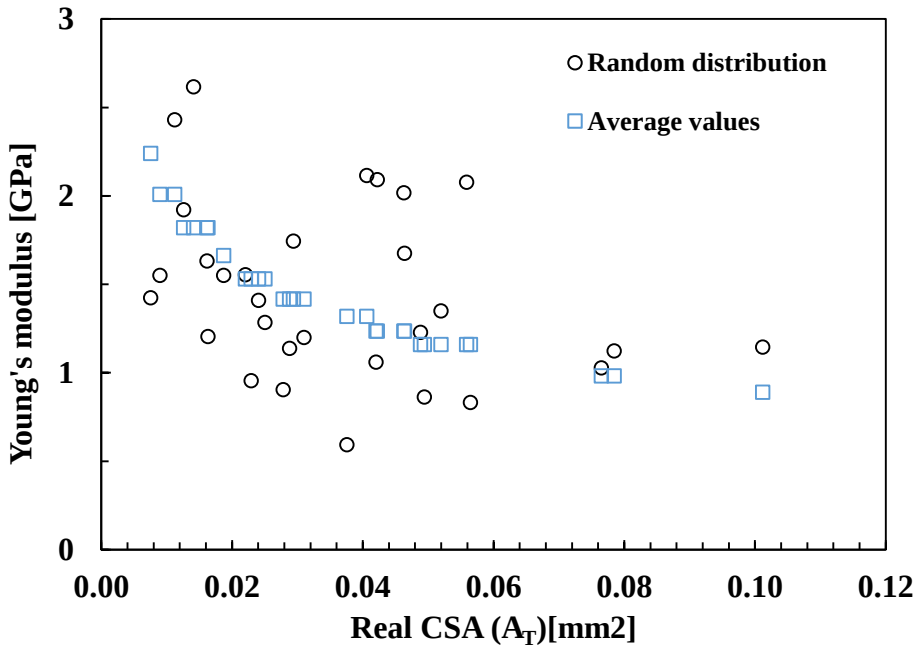

Figure 2.54: Honeycomb model for inter-fibre properties variability.

The main parameters of the honeycomb and circular models are the cell size l ($l \sim r_c$), the Young's modulus of elementary fibres E_{fr} and the interfacial stress transfer efficiency η. In an attempt to probe how the inter-fibre variability of these parameters

affect the predicted value of E_f versus the fibre's CSA (A_T), a random set of parameters was generated. A set of 30 data points $[E_f, A_T]_R$ (i.e. *Random distribution*) were generated based on the CSAs of coir (5 mm gauge length set) and randomly distributed parameters η between 0.5-0.8, l between 5-7 μm and E_{fr} between 2-5 GPa, according to (2.32) and (2.18). Furthermore, another set of 30 data points $[E_f, A_T]_A$ (i.e. *Average values*) were generated based on the same CSAs and the average values $\bar{\eta}$ (0.63), $\bar{l}$ (5.98 μm) and $\overline{E_{fr}}$ (3.51 GPa) of the previous randomly distributed parameters. Results for the prediction of E_f versus CSA are illustrated in Figure 2.54.

It can be clearly seen that a low variability of these three parameters could dramatically affect the distribution of E_f versus A_T. It is clear from these results that, if there is high inter-fibre variability of properties, it becomes a difficult task to estimate for η, l and E_{fr} from experimental observations, especially for a reduced range of CSA.

It should also be noticed that if a Young's modulus dependence on CSA is observed, the validity of the compliance correction is questionable. The correction based on equations (2.8) and (2.9), assumed a value of E_f that is not dependant on CSA. Therefore, individual corrections of Young's modulus were not considered and as an initial approximation, only CSA corrected values were used.

For the treatment of the experimental data, cell size parameters l and r_c, with $l \sim r_c$, were considered constant over the full CSA range. The value of l was calculated as the average of the single l-values generated from each measured CSA of elementary fibre, according to (2.11), see Figure 2.32 and Figure 2.33. The average l was 6.9 μm for palm and 6.2 μm for coir respectively. A two-sample *t*-test of the average values showed a significant difference at 99% confidence level (*p*-value = $2.8 \cdot 10^{-7}$).

The models, based on equations (2.32) and (2.36) which include η and E_{fr} as fitting parameters, give the observable E_f as a function of the fibre's CSA A_T, for certain given cell size l. The models were fitted to the experimental observations $[E_f, A_T]_{exper}$, using the standard least-squares method. A pair of values (η, E_{fr}) were calculated so the total sum squared residuals was minimised (2.37). The total sum of

squares is illustrated in (2.38). The R-squared R^2 value was calculated according to (2.39).

$$SS_{res} = \sum_{i=1} \left[E_{fexper_i} - E_{fmodel_i}(\eta, E_{fr}, \dots) \right]^2 \tag{2.37}$$

$$SS_{total} = \sum_{i=1} \left[E_{fexper_i} - \bar{E}_{fexper} \right]^2 \tag{2.38}$$

$$R^2 = 1 - \frac{SS_{res}}{SS_{total}} \tag{2.39}$$

Palm Young's modulus versus CSA for experimental and fitted models is illustrated in Figure 2.55. As expected from Figure 2.53, both models showed almost equivalent fittings to the experimental data. The calculated values for (η, E_{fr}) based on honeycomb and circular models are summarised in Table 2.3. The R^2 values indicate a good correlation between the models and experimental data.

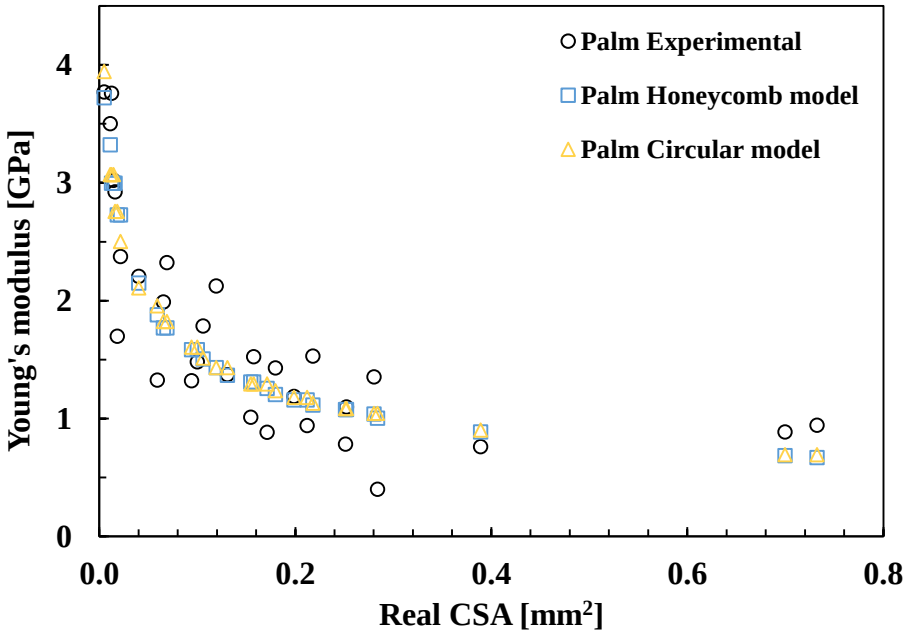

Figure 2.55: Palm Young's modulus versus CSA. Experimental and fitted theoretical models.

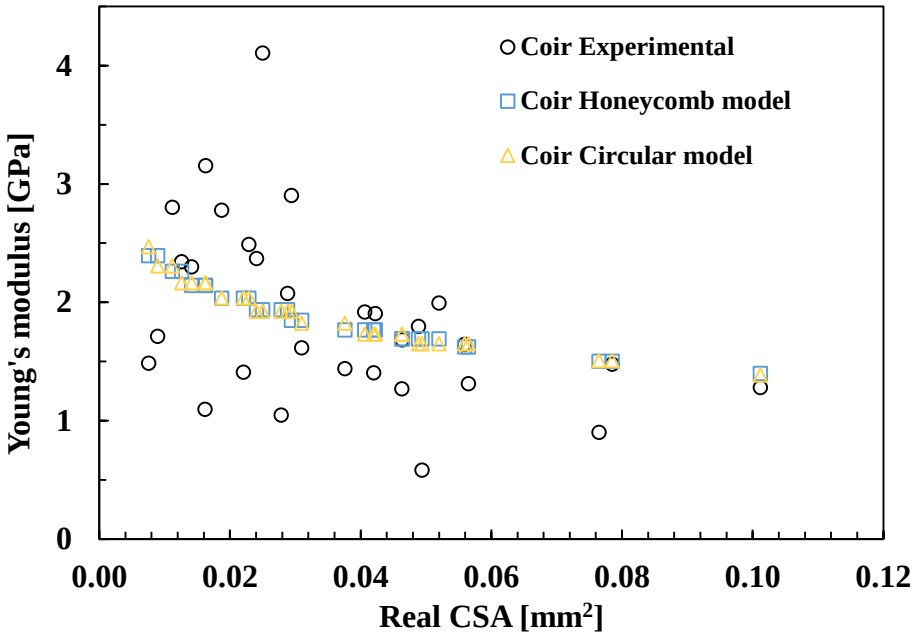

Figure 2.56: Coir Young's modulus versus CSA. Experimental and fitted theoretical models.

In the case of coir fibre, Figure 2.56, a different situation was observed. These results may indicate that a higher inter-fibre variability of properties (as predicted in Figure 2.54) and the lower range of CSA in relation to the variation of Young's modulus could have led to a poorer correlation, as the R^2 values revealed, between predictions and experimental data when compared with the case of palm fibre.

Sample	l [µm]	Honeycomb model			Circular model		
		E_{fr} [GPa]	η	R^2	E_{fr} [GPa]	η	R^2
Palm 5 mm	6.9	5.04	0.67	0.82	4.73	0.65	0.81
Coir 5 mm	6.2	2.93	0.85	0.15	2.90	0.83	0.16

Table 2.3: Theoretical models results.

2.4 Conclusions

The internal structure, cross section area (CSA) and mechanical properties of palm and coir fibres have been investigated. Fibre internal structure was directly observed using cryotome cut samples under the SEM. Young's modulus, tensile strength and failure strain were measured at room temperature, using a tensile testing machine. The

characterisation of the fibres and elementary fibres CSA was carried out on tensile tested samples using an embedding and polishing method.

The complex internal structure of coir and palm fibres revealed high variability in terms of the shape and size of the elementary fibres and their cell wall thickness. These variations along with non-circular and variable overall CSA and internal voids could ultimately lead to high levels of anisotropy, non-symmetrical stress distributions within the fibre and high variability of the fibre properties. Moreover, weak inter-elementary fibre interfaces and non-bonded regions were often observed. This could lead to sudden mechanical failure, reduction of properties, non-uniform stress distributions or reduced ability to transfer stress between consecutive elementary fibres.

By using the circular cross-section assumption, the analysis of the fibre's real CSA showed an overestimation (based on a linear trend-line) of approximately 20 and 40% for palm and coir fibres respectively. The measured average aspect ratio between the major axis and minor axis of the fitted ellipse to the CSA of fibres was 1.26 for palm and 1.28 for coir. In the case of fibre perimeter estimation, lower levels of difference between both methods were detected. The average CSA and aspect ratio of elementary fibres were 130 μm^2 and 1.34 for palm and 103 μm^2 and 1.37 for coir.

The characterisation of the mechanical properties of palm and coir showed lower differences between diameter based and real CSA corrected values than expected from CSA measurements. This lower difference may be caused by the relation between the CSA distribution of tested samples and the variation of diameter based CSA versus real CSA trends according to different CSA ranges. The corrected average strengths of palm and coir were 116 and 149 MPa respectively. While tensile strength showed no gauge length dependence, Young's modulus values were considerably dependent on test gauge length. Compliance corrections revealed similar Young's modulus for palm and coir fibres, 2.5 and 2.9 GPa respectively.

Two theoretical models have been developed to explain the observed Young's modulus dependence on fibre CSA. The models formulated the measureable modulus as a function of fibre's CSA (defined as a multi-level structure) and elementary fibre's size along with the efficiency of the inter-level interface to transfer stress across

consecutive levels. Both models generated almost equivalent predictions. In the case of palm, there was a good correlation between experimental observations and theoretical predictions. On the other hand, in the case of coir, due to higher levels of fibre properties variability and lower CSA range of tested samples, the Young's modulus dependence on CSA was not as defined as for palm, which ultimately led to poorer results in terms of model fitting.

2.5 References

1. Eichhorn, S.J., Baillie, C.A., Mwaikambo, L.Y., Ansell, M.P., Dufresne, A., Entwistle, K.M., Herrera-Franco, P.J., Escamilla, G.C., Groom, L., Hughes, M., Hill, C., Rials, T.G., Wild, P.M.: Review: Current international research into cellulosic fibers and composites. J. Mater. Sci. 36, 2107–2131 (2001).
2. Raven, P.H., Evert, R.F., Eichhorn, S.E., Ray: Biology of plants. W.H. Freeman/Worth Publishers, New York (1999).
3. Fuqua, M.A., Huo, S., Ulven, C.A.: Natural Fiber Reinforced Composites. Polym. Rev. 52, 259–320 (2012).
4. Bledzki, A.K., Gassan, J.: Composites reinforced with cellulose based fibres. Prog. Polym. Sci. 24, 221–274 (1999).
5. Mohanty, A.K., Misra, M., Hinrichsen, G.: Biofibres, biodegradable polymers and biocomposites: An overview, (2000).
6. Eichhorn, S.J., Dufresne, a., Aranguren, M., Marcovich, N.E., Capadona, J.R., Rowan, S.J., Weder, C., Thielemans, W., Roman, M., Renneckar, S., Gindl, W., Veigel, S., Keckes, J., Yano, H., Abe, K., Nogi, M., Nakagaito, a. N., Mangalam, a., Simonsen, J., Benight, a. S., Bismarck, a., Berglund, L. a., Peijs, T.: Review: current international research into cellulose nanofibres and nanocomposites. (2009).
7. Mussig, J. ed: Industrial Applications of Natural Fibres. John Wiley & Sons (2010).
8. Saha, B.C.: Hemicellulose bioconversion. J. Ind. Microbiol. Biotechnol. 30, 279–291 (2003).
9. Kalia, S., Dufresne, A., Cherian, B.M., Kaith, B.S., Avérous, L., Njuguna, J., Nassiopoulos, E.: Cellulose-Based Bio- and Nanocomposites: A Review. Int. J. Polym. Sci. 2011, 1–35 (2011).
10. Kalia, S., Kaith, B.S., Kaur, I. eds: Cellulose fibers: bio- and nano- polymer composites: green chemistry and technology. Springer (2011).
11. Stokke, D.D., Wu, Q., Han, G.: Introduction to wood and natural fiber composites. John Wiley & Sons (2014).
12. Tran, L.Q.N., Fuentes, C.A., Dupont-Gillain, C., Van Vuure, A.W., Verpoest, I.: Understanding the interfacial compatibility and adhesion of natural coir fibre

thermoplastic composites. Compos. Sci. Technol. 80, 23–30 (2013).

13. Baley, C.: Analysis of the flax fibres tensile behaviour and analysis of the tensile stiffness increase. Compos. Part A Appl. Sci. Manuf. 33, 939–948 (2002).
14. Rao, K.M.M., Rao, K.M.: Extraction and tensile properties of natural fibers: Vakka, date and bamboo. Compos. Struct. 77, 288–295 (2007).
15. Moreno Montoya, L.E., Osorio Serna, L.R., Trujillo De los Ríos, E.E.: Estudio de las propiedades mecánicas de haces de fibra de Guadua angustifolia. Ing. Desarro. 20, 125–133 (2006).
16. Osorio, L., Trujillo, E., Van Vuure, a. W., Verpoest, I.: Morphological aspects and mechanical properties of single bamboo fibers and flexural characterization of bamboo/ epoxy composites. J. Reinf. Plast. Compos. 30, 396–408 (2011).
17. Mohanty, A.K., Misra, M., Drzal, L.T.: Natural Fibers, Biopolymers and Biocomposites. Taylor & Francis Group (2005).
18. Spatz, H., Köhler, L., Niklas, K.J.: Mechanical behaviour of plant tissues: composite materials or structures? J. Exp. Biol. 202, 3269–3272 (1999).
19. Köhler, L., Spatz, H.C.: Micromechanics of plant tissues beyond the linear-elastic range. Planta. 215, 33–40 (2002).
20. Bakri, B., Eichhorn, S.J.: Elastic coils: Deformation micromechanics of coir and celery fibres. Cellulose. 17, 1–11 (2010).
21. Altaner, C.M., Jarvis, M.C.: Modelling polymer interactions of the "molecular Velcro" type in wood under mechanical stress. J. Theor. Biol. 253, 434–445 (2008).
22. Tomczak, F., Sydenstricker, T.H.D., Satyanarayana, K.G.: Studies on lignocellulosic fibers of Brazil. Part II: Morphology and properties of Brazilian coconut fibers. Compos. Part A Appl. Sci. Manuf. 38, 1710–1721 (2007).
23. Thomason, J.L., Carruthers, J., Kelly, J., Johnson, G.: Fibre cross-section determination and variability in sisal and flax and its effects on fibre performance characterisation. Compos. Sci. Technol. 71, 1008–1015 (2011).
24. Lamy, B., Baley, C.: Stiffness prediction of flax fibers-epoxy composite materials. J. Mater. Sci. Lett. 19, 979–980 (2000).
25. Biagiotti, J., Fiori, S., Torre, L., López-Manchado, M. a., Kenny, J.M.: Mechanical properties of polypropylene matrix composites reinforced with natural fibers: A statistical approach. Polym. Compos. 25, 26–36 (2004).
26. Peponi, L., Biagiotti, J., Kenny, M., Torre, L., Kenny, M., Kenny, J.M., Mondragon, I.: Statistical Analysis of the Mechanical Properties of Natural Fibers and Their Composite Materials . I . Natural Fibers. Polym. Compos. 1–5 (2008).
27. De Rosa, I.M., Kenny, J.M., Puglia, D., Santulli, C., Sarasini, F.: Morphological, thermal and mechanical characterization of okra (Abelmoschus esculentus) fibres as potential reinforcement in polymer composites. Compos. Sci. Technol. 70, 116–122 (2010).
28. Mukherjee, P.S., Satyanarayana, K.G.: Structure and properties of some

vegetable fibres - Part 2 Pineapple fibre (Anannus Comosus). J. Mater. Sci. 21, 51–56 (1986).

29. Griffith, A.A.: The Phenomena of Rupture and Flow in Solids. Philos. Trans. R. Soc. london. Ser. A, Contain. Pap. a Math. or Phys. character. 221, 163–198 (1921).
30. ASTM: D3822: Standard Test Method for Tensile Properties of Single Textile Fibers. Annu. B. ASTM Stand. 1–10 (2014).
31. ASTM: C1557 : Standard Test Method for Tensile Strength and Young ' s Modulus of Fibers. Annu. B. ASTM Stand. 1–10 (2014).
32. Deshpande, A.P., Bhaskar Rao, M., Lakshmana Rao, C.: Extraction of bamboo fibers and their use as reinforcement in polymeric composites. J. Appl. Polym. Sci. 76, 83–92 (2000).
33. Williams, G.I., Wool, R.P.: Composites from natural fibers and soy oil resins. Appl. Compos. Mater. 7, 421–432 (2000).
34. Juntaro, J., Pommet, M., Kalinka, G., Mantalaris, A., Shaffer, M.S.P., Bismarck, A., Juntaro, B.J., Pommet, M., Kalinka, G., Mantalaris, A., Shaffer, M.S.P., Bismarck, A.: Creating Hierarchical Structures in Renewable Composites by Attaching Bacterial Cellulose onto Sisal Fibers. Adv. Mater. 20, 3122–3126 (2008).
35. Rong, M.Z., Zhang, M.Q., Liu, Y., Yang, G.C., Zeng, H.M.: The effect of fiber treatment on the mechanical properties of unidirectional sisal-reinforced epoxy composites. Compos. Sci. Technol. 61, 1437–1447 (2001).
36. Martinschitz, K.J., Boesecke, P., Garvey, C.J., Gindl, W., Keckes, J.: Changes in microfibril angle in cyclically deformed dry coir fibers studied by in-situ synchrotron X-ray diffraction. J. Mater. Sci. 43, 350–356 (2008).
37. Gassan, J., Chate, A., Bledzki, A.K.: Calculation of elastic properties of natural fibers. J. Mater. Sci. 6, 3715–3720 (2001).
38. Sreekala, M.S., Kumaran, M.. G., Thomas, S.: Oil palm fibers: Morphology, chemical composition, surface modification, and mechanical properties. J. Appl. Polym. Sci. 66, 821–835 (1997).
39. Kulkarni, A.G., Satyanarayana, K.G., Sukumaran, K., Rohatgi, P.K.: Mechanical behaviour of coir fibres under tensile load. J. Mater. Sci. 16, 905–914 (1981).
40. Keckes, J., Burgert, I., Frühmann, K., Müller, M., Kölln, K., Hamilton, M., Burghammer, M., Roth, S. V, Stanzl-Tschegg, S., Fratzl, P.: Cell-wall recovery after irreversible deformation of wood. Nat. Mater. 2, 810–814 (2003).
41. Cox, H.L.: The elasticity and strength of paper and other fibrous materials. Br. J. Appl. Phys. 3, 72–79 (1952).
42. Cui, S., Kinloch, I. a., Young, R.J., Noé, L., Monthioux, M.: The Effect of Stress Transfer Within Double-Walled Carbon Nanotubes Upon Their Ability to Reinforce Composites. Adv. Mater. 21, 3591–3595 (2009).
43. Zalamea, L., Kim, H., Pipes, R.B.: Stress transfer in multi-walled carbon nanotubes. Compos. Sci. Technol. 67, 3425–3433 (2007).

44. Ashby, M.F., Medalist, R.F.M.: The mechanical properties of cellular solids. MTA. 14, 1755–1769 (1983).
45. Gibson, L.J., Ashby, M.F., Schajer, G.S., Robertson, C.I.: The Mechanics of Two-Dimensional Cellular Materials. Proc. R. Soc. A Math. Phys. Eng. Sci. 382, 25–42 (1982).
46. Warren, W.E., Kraynik, a. M.: Foam mechanics: the linear elastic response of two-dimensional spatially periodic cellular materials. Mech. Mater. 6, 27–37 (1987).
47. Warren, W.E., Kraynik, a. M., Stone, C.M.: A constitutive model for two-dimensional nonlinear elastic foams. J. Mech. Phys. Solids. 37, 717–733 (1989).
48. Gibson, L.J.: Biomechanics of cellular solids. J. Biomech. 38, 377–399 (2005).
49. Fratzl, P., Weinkamer, R.: Nature's hierarchical materials. Prog. Mater. Sci. 52, 1263–1334 (2007).
50. Meyers, M.A., Chen, P.-Y., Lin, A.Y.-M., Seki, Y.: Biological materials: Structure and mechanical properties. Prog. Mater. Sci. 53, 1–206 (2008).

Chapter 3

Thermal degradation of natural fibres

3.1 Introduction / Literature Review

This chapter focuses on the characterisation of the mechanical and thermal degradation of date palm and coir fibres as part of the evaluation of their potential for the substitution of high density mineral reinforcements with more "environmentally friendly" lower density natural fibre reinforcements.

In this regard, one of the main issues in the processing of natural fibres is their degradation at high temperatures [1]. High temperatures lead to physical and chemical changes of the complex materials forming natural fibres [2, 3]. When lignocellulosic fibres are heated in the range of 100 to 250 °C, changes in their properties can be explained through physical and chemical variations due to processes such as depolymerisation, oxidation, hydrolysis, dehydration, decarboxylation and recrystallization [4]. The range of temperatures for the thermo-mechanical degradation of the main components of natural fibres has been identified within the range of temperatures used in standard thermoplastic injection moulding processing [5, 6]. This scenario ultimately results in a restriction in the number of thermoplastics that may be considered for natural fibre reinforced thermoplastic composites. The thermal degradation of natural fibres leads to a decrease of their mechanical properties, but also to poor organoleptic properties such as odour and colour [2, 5, 6]. This section will focus on the review of the literature in relation to the thermal degradation of plant derived components, wood and fibres.

3.1.1 Thermal behaviour of natural fibre components

The thermal behaviour of natural fibres could be analysed by the degradation of their individual main components (i.e. cellulose, hemicellulose and lignin). This thermal degradation is different depending on the type of atmosphere (i.e. inert or oxidative atmosphere). Stamm [7] pointed out that the degradation of wood (therefore

its components degradation) is greater in the presence of air than in its absence, because of oxidation by atmospheric oxygen.

Schwenker and Pacsu [8] showed that cellulose decomposes under an inert atmosphere, into a complex mixture of organic acids, aldehydes, ketones, water and levoglucosan. In a later study, Roberts [9] pointed out how the decomposition of hemicellulose mainly takes places between 200 and 260 °C, followed by the cellulose at 240 to 350 °C and lignin at temperatures between 280 to 500 °C. Cellulose, hemicellulose and lignin have quite different reaction kinetics, hemicellulose being the most reactive and lignin the least.

Huanf and Li [10] identified a peak degradation of cellulose under nitrogen between 350 and 400 °C. Dehydration was also observed for temperatures below 100 °C. The peak of the derivative of thermogravimetric analysis (DTG), for cellulose degradation under inert atmosphere, was also showed by Stenseng et al. [11] in the region of 350 °C. Nada and Hassan [12] also studied the thermal behaviour of cellulose under inert atmosphere. The major stages were identified as: initial loss of moisture, initial pyrolysis decomposition of cellulose at 266 °C and major decomposition at 315 °C. They also observed that lignin is more thermally stable and forms more char than cellulose and hemicelluloses. Ward and Braslaw [13] pointed out that lignin may not begin to be pyrolysed at measurable rates until temperatures exceed 280 °C under vacuum conditions.

Yang et al. [14, 15] investigated the pyrolysis of palm oil waste and synthetic biomass formed by the mixing of cellulose, hemicellulose and lignin. The authors stated that the main weight loss of hemicellulose happened at 220-315 °C with a maximum mass loss rate at 268 °C. Cellulose pyrolysis took place at a higher temperature range, 315-400 °C, with a maximum mass loss rate at 355 °C. It appeared that the rich branches of hemicellulose, formed by random and amorphous structures, were very easy to remove from the main stem and to degrade to volatiles that evolved out (e.g. CO, CO_2, and some hydrocarbon) at relatively low temperatures. Cellulose, which consists of a long polymer of glucose without branches, showed a higher thermal stability. Lignin proved to be the most difficult component to decompose. In lignin (containing aromatic rings with various branches), the activity of the chemical

bonds led to a wide degradation temperature range (100-900 °C), but at a very low mass loss rate.

Koufopanos et al. [16] investigated the pyrolysis of plant biomass components. The authors divided the process in three main stages: in the first stage, the pre-pyrolysis phenomena modified the material; in the second process, the main pyrolysis reactions took place, and most of the weight-loss was observed, producing char and other pyrolysis products; the third stage was associated with the continuous devolatilisation of the char through further breakdown of C-C and C-H bonds. The rate of decomposition of lignin appeared to be lower than in the case of cellulose [16].

3.1.2 Thermal behaviour of biomass and natural fibres

Rather than analysing main components, products derived from plants (e.g. natural fibres, wood, biomass) can also be directly analysed. In this case, the superposed degradation of individual components is observed. Thurner and Mann [17] analysed the pyrolysis of wood, detecting, as main degradation products, CO_2, CO, O_2 and C_3+ compounds. Traces of acetylene, ethylene and methane were also detected.

Varma et al. [18] studied the thermal degradation of coir fibres under different conditions. The analysis of the degradation under a nitrogen atmosphere revealed an initial weight loss (40-150 °C) related to the absorbed water. It was followed by a two-step weight loss (289-400 °C), with DTG peaks in the area of 291 and 341 °C. The isothermal degradation of coir fibres in an oven, under an air atmosphere, was also analysed. At 200 and 250 °C, a certain darkening of the colour of fibres was observed. At 250 °C, FTIR studies showed major changes due to oxidation, dehydration and slight depolymerisation of cellulosic components.

Varhegyi et al. [19] analysed the thermal decomposition of cellulose, hemicellulose and sugar cane bagasse. In the degradation of sugar cane bagasse, the authors identified three peaks in the DTG curve between 200 and 400 °C. The first two were identified with hemicelluloses (probably, two different hemicellulose materials were present) and the third peak was attributed to cellulose. In the case of lignin, its slow decomposition did not show a particular peak and only became dominant at high temperatures [19, 20].

Raveendran et al. [21] divided the pyrolysis of biomass into five main areas: zone 1 (< 100 °C) was mainly associated to moisture evolution; zone 2 (100-250 °C) was connected to the start of decomposition of extractives; zone 3 (250-350 °C) was predominantly attributed to hemicellulose decomposition; zone 4 (350-500 °C) was mostly linked to cellulose and lignin decomposition; zone 5 (>500 °C) was attributed to lignin decomposition.

Silva et al. [22] studied the thermal behaviour of coir fibres under air. As in other studies, the initial weight loss was associated with moisture loss. The authors observed a main DTG peak at 334 °C, which had a *shoulder* at lower temperatures. A second major DTG peak was identified after 400 °C. In a later study, Bismarck et al. [23] analysed the thermal behaviour of coir and sisal. They observed a two-step decomposition in an oxygen atmosphere, with onset degradation between 190 and 230 °C.

Nuñez et al. [6] investigated the degradation of treated and untreated wood flour. The first stage of the degradation (200-310 °C) was related to hemicellulose degradation. The second stage (310-400 °C) was attributed to the degradation of cellulose. The second stage was also related to the pyrolytic degradation of lignins, involving fragmentation of interunit linkages (releasing monomeric phenols into the vapour phase), decomposition and condensation of the aromatic rings. The mass loss in nitrogen atmosphere is in all cases lower than the mass loss in an oxidative atmosphere (air).

Müller-Hagedorn et al. [24] analysed the thermal degradation of different wood species. The main degradation peak (in DTG curves) was attributed to cellulose degradation. At lower temperatures, degradation was associated to the decomposition of hemicellulose. A peak due to the degradation of lignin was not observed.

Ouajai and Shanks [25] studied the degradation of hemp under nitrogen and air atmosphere. For the degradation under nitrogen and air, the first decomposition *shoulder* peak at about 250-320 °C, was attributed to thermal depolymerisation of hemicelluloses or pectin (mass loss 10%); the major decomposition peak at about 390-400 °C was attributed to cellulose decomposition (mass loss 55%). Only under air

atmosphere, a major peak was observed at temperatures above 500 °C. Decomposition in air was more complete and proceeded at a lower temperature than in nitrogen.

Tomczak et al. [26] studied the thermal degradation of coir fibres. The initial weight loss, at temperatures below 150 °C was attributed to the presence of absorbed or combined water. The initial degradation of fibre was observed at 200 °C in nitrogen and 197 °C in oxygen atmosphere. Three regions were identified in the degradation process: Initial degradation (200-260 °C) was associated to hemicelluloses degradation; the second stage (240-350 °C) was attributed to the degradation of cellulose; lignin degradation took place in a wider temperature range, between 280 and 500 °C.

Yao et al. [27] investigated the thermal decomposition of natural fibres in an inert atmosphere. All the analysed natural fibres showed a similar thermal decomposition. A main DTG peak was observed for all fibres (which included jute, bamboo, hemp and kenaf), which resulted from the thermal decomposition of cellulose. Furthermore, a "shoulder" (at lower temperatures) in the main peak was related to the thermal decomposition of hemicellulose. "Tails" present in the DTG curves were attributed to the degradation of lignin.

Almeida et al. [28] studied the thermal degradation behaviour of lignocellulose fibres. They pointed out that the mass loss at temperatures below 200 °C are mainly attributed to humidity loss. The authors related the mass loss between 200 °C and peak temperatures, around 400 °C, to the degradation of hemicellulose and cellulose. At high temperatures, it was stated that further decomposition of cellulose oligomers evolved into levoglucosans and low molecular mass volatile compounds, like ketones, aldehydes, furans and pyrans.

Rachini et al. [29] analysed the thermal degradation of hemp fibres under air and inert atmosphere. As observed in other studies, the authors identified an initial moisture loss, between 50 and 150 °C. Among the main chemical components of fibres (i.e. pectin, hemicellulose, cellulose and lignin), pectins exhibited the lowest thermal stability, where maximum decomposition was observed between 200 and 280 °C. Under inert atmosphere, the exothermic peak at 260 °C, identified by differential thermal analysis (DTA), was associated with the simultaneous thermal

depolymerisation of hemicellulose and pectins. Under air, an exothermic peak was also identified at 312 °C, which was related to cellulose decomposition. This peak shifted to 333 °C under inert atmosphere. Hemp fibres exhibited, only under air, a final peak at 427 °C, identified by DTA, which was attributed to the oxidative decomposition of the charred residue.

Tajvidi and Takemura [5] investigated the temperature degradation of rice hulls and wood flour composites. Low temperature decomposition (250-300 °C) was associated, as by other authors, to degradation of hemicelluloses. The second decomposition process (300-400 °C) was associated with cellulose decomposition.

De Rosa et al. [30] analysed the thermal degradation of okra fibres under a nitrogen atmosphere. The initial weight loss was attributed to the vaporisation of water from the fibres, whilst the onset degradation occurred after 220 °C. The degradation was divided in two main stages, where the first stage (220-310 °C) was associated with the thermal depolymerisation of hemicellulose, pectin and the cleavage of glycosidic linkages of cellulose. The authors attributed the second stage (310-390 °C) to the degradation of the α-cellulose present in the fibre. It was stated that the decomposition of lignin, due to its complex structure, occurred slowly over the whole range of temperatures.

El may et al. [31] studied the thermal behaviour of date palm residues under inert and oxidative atmospheres. The authors observed a four stage degradation process of samples under nitrogen atmosphere: moisture loss, hemicellulose decomposition, cellulose decomposition and lignin decomposition. In the case of the degradation under oxidative atmosphere, three stages were differentiated. The first stage (25-125 °C), is associated with the water loss and volatilisation of light molecules. The second stage (141-347 °C) was related to the devolatilisation of the date palm residues. The last stage, at higher temperatures, was related to further oxidation of char. Sait et al. [32] also studied the pyrolysis and combustion of date palm biomass waste. The authors observed a similar onset degradation point for both kinds of degradation (i.e. under nitrogen and air atmospheres).

Dehghani et al. [33] investigated the thermal behaviour of date palm fibre under nitrogen atmosphere. They observed a three stage degradation process. First, the

authors attributed the segment from 40 to 120 °C to moisture evaporation. The second stage was attributed to the degradation of hemicelluloses and cellulose (195-400 °C). The third stage of the decomposition (400-469 °C) was attributed to the degradation of non-cellulosic materials.

3.1.3 Thermal degradation of natural fibres

The degradation of mechanical properties of natural fibres due to heat-treatment has also been observed. Wielage et al. [34] analysed the thermal degradation of flax fibres. The authors observed an increased degradation of the tensile strength owing to higher temperatures and duration of exposure. As previously discussed, it was also pointed out that the endothermic reaction of cellulose takes place by two competing pathways. The first is a depolymerisation process which leads to an intermediate product, levoglucosan, which further decomposes to various volatiles (e.g. aldehydes, ketones, furans, pyrans). The second pathway is a dehydration process which mainly produces char residue, water and carbon oxides.

Van de Velde and Baetens [35] investigated the thermal and mechanical properties of flax fibres. They recognised that natural fibres are subject to degradation under the influence of temperature. Even at relatively low temperatures (120 °C), after two hours, the elongation at break significantly decreased. Exposure to higher temperatures led to faster degradation than for lower temperatures. In the thermo-gravimetric analysis the initial peak was mainly identified with water loss (exposure to 120 °C resulted in the removal of water and degradation of waxes). The second peak (around 330 °C) was related to the degradation of hemicellulose and cellulose, and the third peak, at the highest temperatures (above 450 °C), was associated with other non-cellulosic compounds' degradation. In general terms, the degradation of flax was greater under air than under inert atmosphere. The authors also pointed out that degradation of pectin at 180 °C, which holds the elementary fibres together, has a faster and greater effect on the mechanical properties of the green and under-retted fibres. The heat treatments had a greater effect over the strain properties than on the stress properties.

Gassan and Bledzki [4] analysed the thermal degradation of flax and jute fibres. The authors recognised that mechanisms such as depolymerisation, oxidation,

hydrolysis, dehydration, decarboxylation and recrystallization can change the physical properties of natural fibres. It was also stated that, due to differences in the coefficient of thermal expansion of the main components of fibres (i.e. cellulose, hemicellulose and lignin), the heat-treatment of fibres may cause structural damage affecting their overall mechanical properties. Significant reduction of the tenacity of fibres, which was clearly time dependant, was observed for treatments at 210 °C. On the other hand, treatments at 170 °C did not have an apparent effect on the tenacity of flax or jute. The authors observed a correlation between the degree of polymerisation and a drop in tenacity. A higher temperature or longer time of exposure led to an increase level of depolymerisation (increased number of broken bonds) and to a drop of tenacity. For an exposure of 120 min. at 210 °C, the drop in tenacity was observed to be approximately 70%.

Prasad et al. [36] studied the structure of thermally treated hemp fibres. The weight loss of hemp fibres, under air and inert atmosphere, was comparable below 200 °C. Above 200 °C, weight loss under air was considerably higher than in an inert environment. Furthermore, the authors found that there was a migration of lignin to the surface of the fibres, when they were heated above lignin T_g (around 142 °C). In terms of the organoleptic properties of fibres, authors have observed that fibres turned browner as the temperature increased [36, 37]. Fibres heated under nitrogen were significantly less brown. On the other hand, fibres heated in air atmosphere at 260 °C became very brittle and fragile. The authors stated that fibres would also have undergone dimensional changes. The identified odour of heated fibres was categorised as strong. Moreover, for the same temperature, fibres heated in air had stronger odour than those heated in an inert nitrogen atmosphere.

Gourier et al. [38] investigated the mechanical properties of flax fibres after different thermal cycles. The authors showed that the mechanical properties of fibres were not affected by heat-treatments at 190 °C for 8 min. On the other hand, at 250 °C for 8 min., the authors observed a drop in tensile strength, strain to failure and Young's modulus. It was also stated that the mechanism by which cellular microfibrils slide within the polysaccharide matrix (mainly made by hemicelluloses and pectins) is greatly altered by heat-treatment at 250 °C, ultimately leading to the observed drop in properties.

3.2 Experimental

3.2.1 Materials

Date palm and coir fibres were both provided by SABIC.

3.2.2 Thermogravimetric analysis

A TA instruments Q50 TGA was used to analyse the thermal stability of date palm and coir fibres. Thermogravimetric analysis (TGA) was carried out under nitrogen and air gas flow (60 ml·min^{-1}) in two different configurations. Firstly, a dynamic heating profile was established as a ramp, defined with a heating rate of 10 °C min^{-1}, reaching a maximum temperature at 600 °C. The temperature set up of the second set of experiments, was defined by an initial ramp, followed by an isothermal region. As in the previous configuration, the initial ramp had a heating rate of 10 °C min^{-1}, while the isothermal degradation was established at three different temperatures 180, 200 and 220 °C. In the second configuration, all tests were carried out under air gas flow. Fibres were tested as received.

3.2.3 Thermal Volatilisation Analysis

Chemical analysis of the thermal degradation behaviour of date palm and coir fibres has been characterised using Thermal Volatilisation Analysis (TVA). TVA was carried out in a built in-house TVA line, Figure 3.1, based on the techniques and devices described by McNeill et al. [39]. The system is made up of a sample chamber, connected in series to a primary liquid nitrogen cooled sub-ambient trap and right after a set of four secondary liquid nitrogen cooled cold traps. The entire system is continuously pumped to a vacuum of 10^{-4} Torr by two pumps: a two stage rotary pump and an oil diffusion pumping system. The condensable volatiles could be initially trapped at two points: the cold-ring and the primary sub-ambient trap. The cold-ring is water cooled (at a temperature of approximately 12 °C) and is positioned directly above the heated area of the sample tube.

The primary sub-ambient trap is liquid nitrogen cooled (at a temperature of approximately -196 °C) and is designed to capture all the lower boiling point volatiles. In order to monitor the evolution of condensable and non-condensable volatiles as a

function of pressure versus temperature and time, two linear response Pirani gauges were located at the entrance and exit of the primary sub-ambient trap. The linear response Pirani gauges provide a precise pressure measurement, necessary for the pressure peak integration; where the different areas of the curve are associated with the quantity of evolved volatiles.

The low boiling species that were trapped in the primary sub-ambient trap could be distilled into separate secondary cold traps by slowly heating the primary sub-ambient trap to ambient temperature. The separated fractions could be subsequently removed into gas-phase cells for Fourier transform infrared spectroscopy (FTIR) analysis.

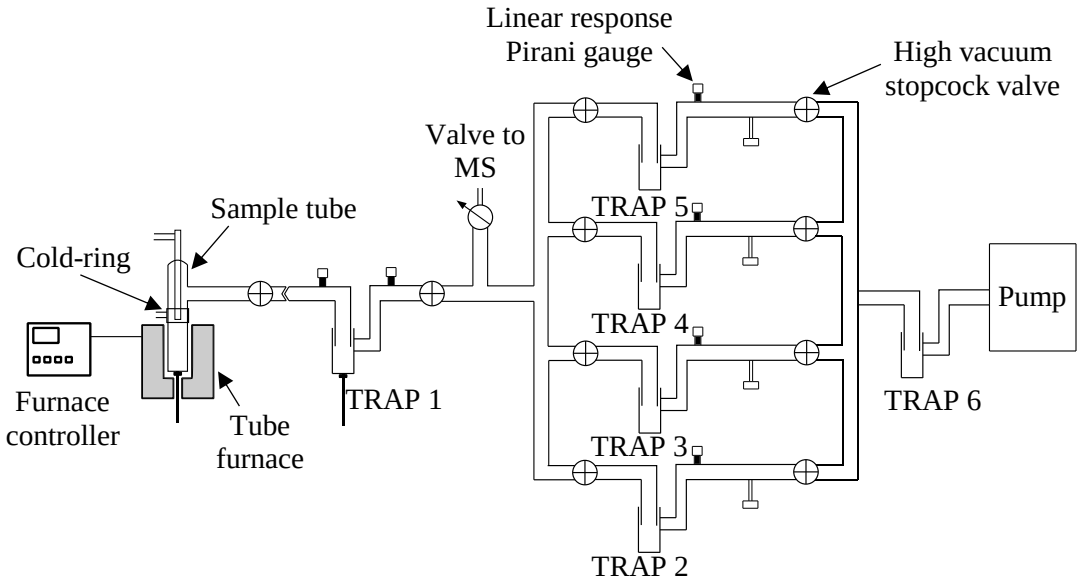

Figure 3.1: TVA line diagram.

The TVA runs were carried out under vacuum, with a heating rate of 10 °C min^{-1} to a maximum temperature of 550 °C. A Hiden HPR-20 QIC mass spectrometer (MS) sampled a continuous product stream during the degradation (1-100 amu) and differential distillation (1-250 amu) runs. The sub-ambient differential distillation of collected volatiles was carried out by heating the primary sub-ambient trap from -196 °C to room temperature. First, coir fibre volatiles were separated into four major fractions, while palm fibre volatiles were separated into three (from coir's run, it was seen that it was sufficient). All the volatiles were then analysed using FTIR. All

FTIR analysis of the collected TVA products was carried out using a PerkinElmer Spectrum 100 in transmission mode.

Fibres were placed within the system (in the sample tube), under vacuum, at least 12 hours before the test started, which allowed the system to extract a significant part of the stored moisture within the fibres.

3.2.4 Heat treatment of fibres and observation

The heat treatment of fibres was carried out in order to accomplish two main goals. The first and most important was to provide heat (or thermally) conditioned fibres for tensile testing. The second aim was to analyse the diameter and surface of the fibres before and after the heat treatment. The parameters of the heat treatment of fibres addressed for tensile testing were established around the normal temperatures for processing reinforced polypropylene, which coincide with the temperatures where the initial degradation is observed. The treatments were defined as the combination of three different temperatures (180, 200 and 220 °C) and two different treatment times (10 and 30 minutes).

All the fibres were individually separated until no fraying could be seen with the naked eye. Subsequently, they were placed in an aluminium tray for the heat treatment. The heat treatments under air were carried out in an oven Nabertherm P-330. The samples were introduced in the oven and then heated up to the temperature of the treatment in a period of 20 minutes. The temperature was then kept constant for the length of the treatment. Afterwards, the samples were taken out of the oven and cooled down at room temperature. The same procedure was followed to treat coir fibres in a specifically dedicated oven, under nitrogen at 220 °C for 30 min.

Fibres addressed to diameter and surface observation, were also individually separated until no fraying could be seen with the naked eye. They were then positioned on a glass slide, as illustrated in Figure 3.2, fixing them to the glass with the help of double-sided tape and bulldog clips. Before the heat treatment, a picture was taken of the middle point of the gauge length, under transverse observation, using a Leica microscope at 10x magnification. Afterwards, the assembly of the fibres mounted on to the glass slide was heat treated in the oven following the same heating process as

the 220 °C and 30 min. profile given for fibres addressed to tensile testing. Subsequently, fibres were again photographed at approximately the same point as before. Finally, in each picture, the diameter was measured at three different points along the fibre length. The final value for the diameter was taken as the average of these three measurements. After the diameter measurements, the surface of fibres was observed, after gold coating, using a Field Emission Scanning Electron Microscope (FE-SEM) HITACHI SU-6600.

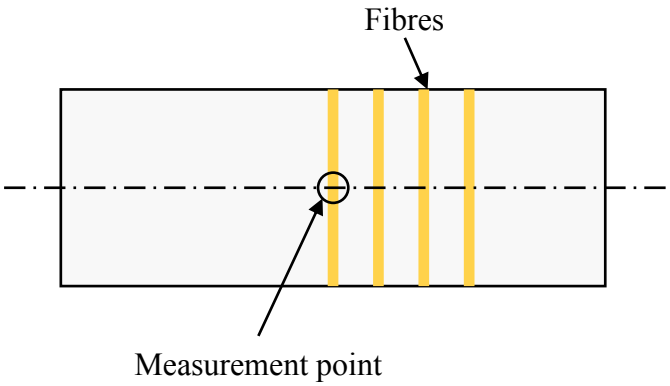

Figure 3.2: Fibres located on a glass slide for diameter observation before and after heat treatment.

3.2.5 Single fibre tensile test

The tensile testing was designed as a set of experiments that analysed the mechanical properties of date palm and coir fibres before and after certain heat-treatments. For each different condition, 30 fibres were tested. A gauge length of 20 mm was used for testing non-treated and treated fibres. In the case of non-treated fibres, they were tested as received (no pre-conditioning or treatment). Tensile testing was carried out according to the experimental methodology explained in Chapter 2.

3.3 Results and discussion

3.3.1 TGA of natural fibres

TGA was used to investigate the thermal stability and degradation of date palm and coir fibres. The mass losses of both fibres, under nitrogen and air atmospheres, are illustrated in Figure 3.3 and Figure 3.4. Degradation curves show that both fibres have

a similar thermal weight loss behaviour. As expected, the degradation under an oxidative atmosphere (i.e. air) led to a higher mass loss at high temperatures.

TGA along with its DTG, revealed a characteristic degradation under nitrogen, where four main regions could be identified. The degradation in the first region (*1* in Figure 3.3 and Figure 3.4), for temperatures lower than 150 °C, was mainly attributed to the loss of moisture in the fibres [5, 23, 29]. The second region, between 150 and 300 °C (characterised by a DTG peak, *2'* in Figure 3.3 and Figure 3.4), is associated with the degradation of hemicelluloses and pectins [5, 18, 21, 29]. The third region, between 300 and 400 °C (characterised by a DTG peak, *3'* in Figure 3.3 and Figure 3.4), was related to the degradation of cellulose. For higher temperatures, lignin degradation is expected to take place. However, due to the nature of lignin, it is expected that, according to some authors [14], its degradation could take place over a wide temperature range.

In the case of the degradation under air, it was observed that the main degradation DTG peak (*3* in Figure 3.3 and Figure 3.4) was shifted to a lower temperature. In this case, it can also be noticed how peaks related to hemicellulose and cellulose are less defined. Furthermore, a DTG peak appeared (*4* in Figure 3.3 and Figure 3.4) at temperatures above 400 °C, which was attributed to the oxidative decomposition of the charred residue [29]. DTG peak temperatures are detailed in Table 3.1. It should be noticed that DTG peaks are taken from single measurements. Therefore, it is not possible to analyse the statistical significance of the difference between various points.

Point	DTG Peak temperature [°C]	
	Palm	Coir
2	297	-
2'	286	291
3	324	324
3'	341	346
4	446	451

Table 3.1: Palm and coir DTG peaks.

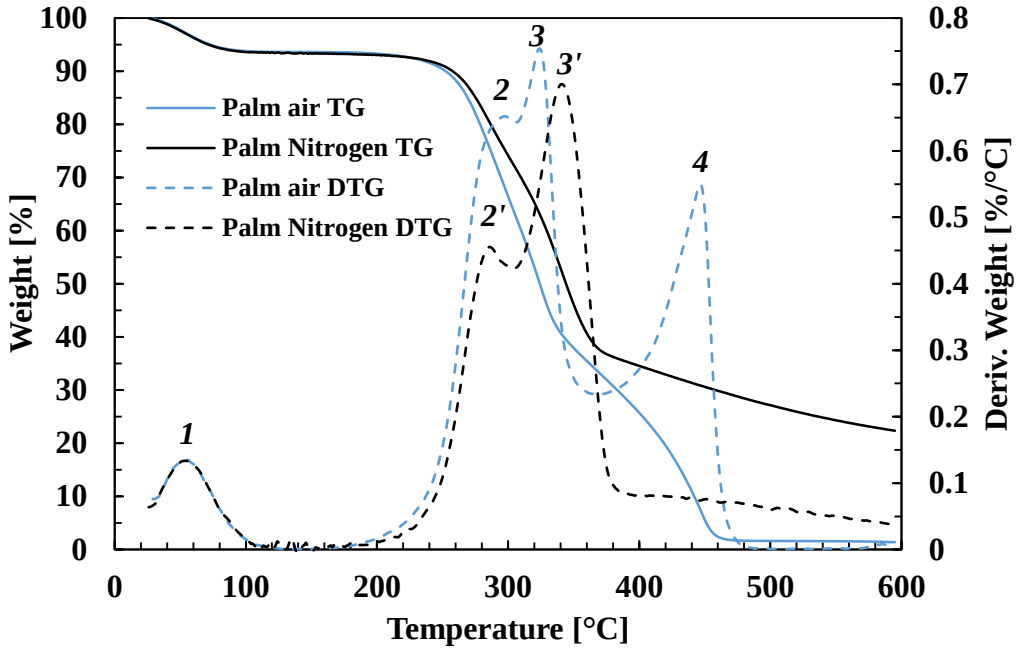

Figure 3.3: Thermo-gravimetric degradation of palm, under nitrogen and air atmospheres, at the heating rate of 10 °C ·min^{-1}.

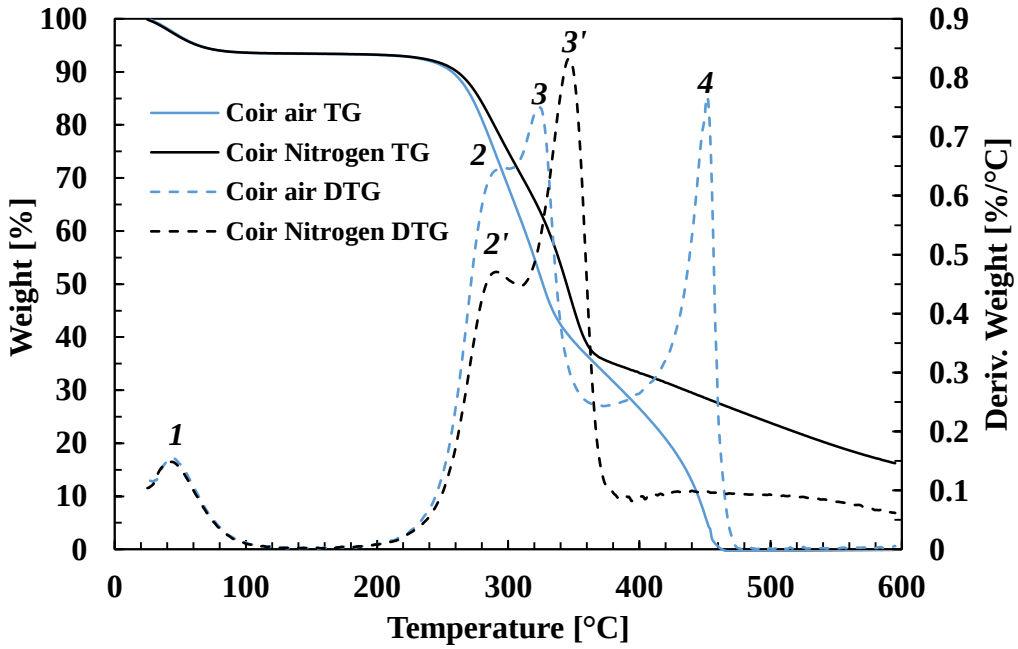

Figure 3.4: Thermo-gravimetric degradation of coir, under nitrogen and air atmospheres, at the heating rate of 10 °C ·min^{-1}.

Above 150 °C, the majority of the moisture that was present in the fibres is supposed to be eliminated, and the mass loss is directly related to the degradation of fibre components. The behaviour is very similar for both fibres. Moreover, at temperatures under 220 °C, the thermal degradation under air and nitrogen is comparable, as seen in Table 3.2. In general terms, dynamic degradation results agree with similar studies on coir fibre [18, 22, 26], and further underline the similarities between date palm and coir fibres' thermal behaviour.

Temperature [°C]	Δ Weight [%]			
	Palm		Coir	
	Nitrogen	Air	Nitrogen	Air
150-180	0.12	0.09	0.09	0.09
150-200	0.29	0.3	0.21	0.2
150-220	0.61	0.83	0.46	0.48

Table 3.2: Mass loss in the dynamic degradation studies.

In the second set of experiments, the decomposition behaviour of palm and coir fibres in air was analysed under isothermal degradation conditions. An initial temperature ramp (10 °C $\cdot min^{-1}$), was followed by an isothermal region at 180, 200 or 220 °C, Figure 3.5 and Figure 3.6.

Natural fibres could quickly absorb moisture from the atmosphere, which could affect TGA measurements. For this reason, in order to compare the different experiments, the weight loss percentage differences between 15 (i.e. after moisture loss) and 45 minutes were analysed. Results are summarised in Table 3.3. The weight loss is similar for both fibres and increased for increasing temperature. It should be noticed that the weight loss is approximately linearly dependent on time, within the isothermal regions.

Isothermal [°C]	Δ Weight 15-45 min [%]	
	Palm	Coir
180	0.55	0.56
200	1.36	1.11
220	4.27	4.65

Table 3.3: Weight loss in isothermal degradation studies.

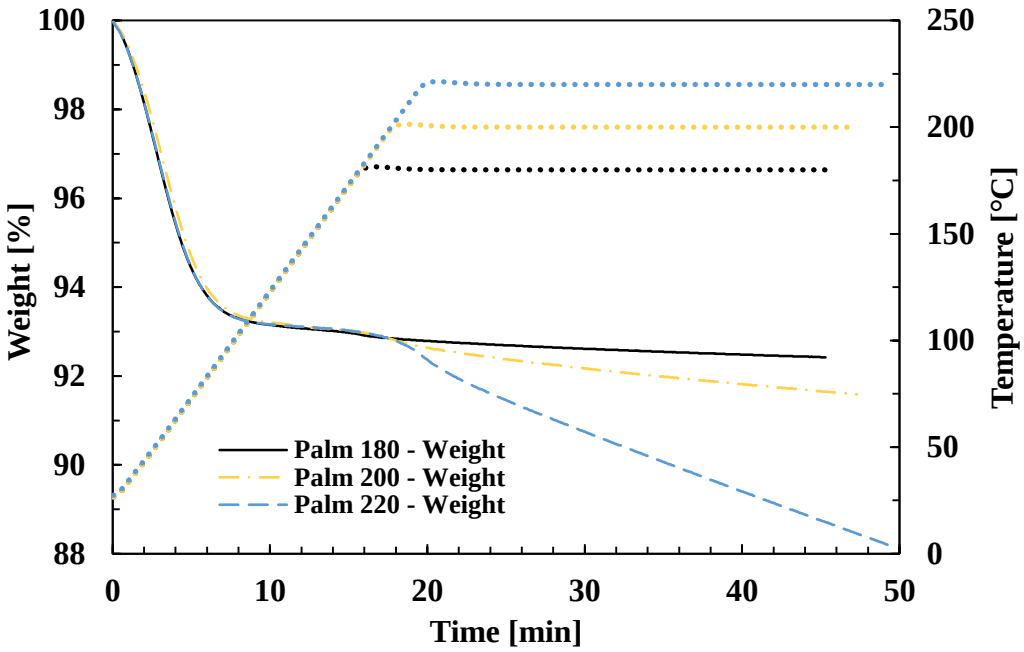

Figure 3.5: Isothermal degradation of palm, under air atmosphere, at 180, 200 and 220 °C.

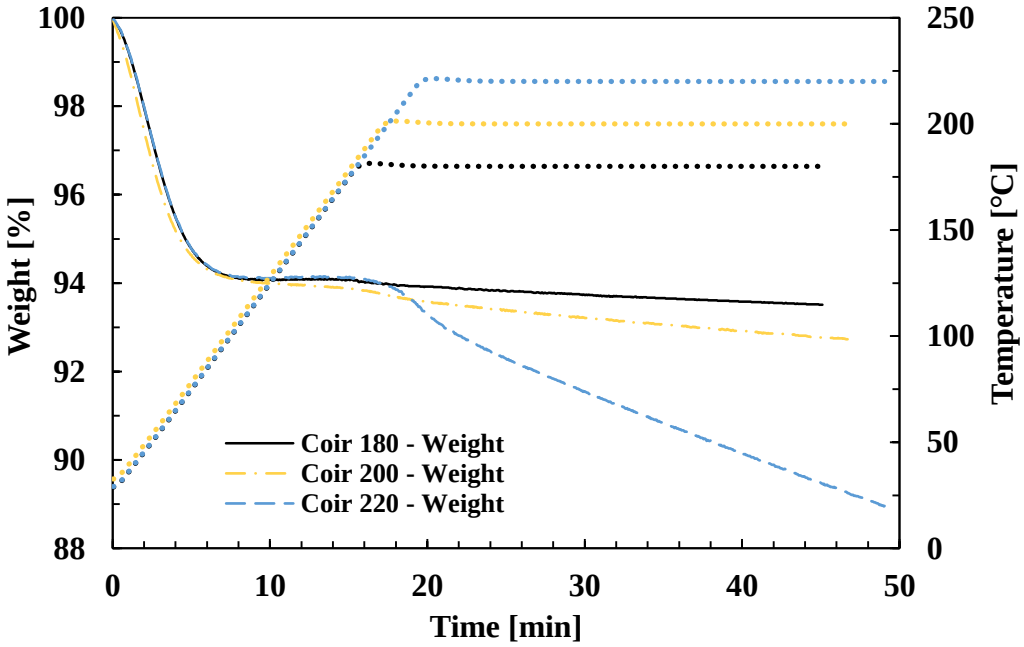

Figure 3.6: Isothermal degradation of coir, under air atmosphere, at 180, 200 and 220 °C.

3.3.2 TVA analysis of natural fibres

The thermal degradation of date palm and coir fibres under vacuum produced, in both cases, a significantly higher amount of condensable volatiles compared with the produced non-condensable. The TVA plots, showing the evolution of the volatiles versus temperature and time for each fibre, are illustrated in Figure 3.7. The onset degradation temperatures, the evolution rate peak maxima and the relative amount of condensable and non-condensable volatiles are summarised in Table 3.4. The relative amounts of volatiles have been calculated through the integration of the pressure versus time curves. The onset degradation temperature was defined as the point at which the system's pressure exceeded $7 \cdot 10^{-5}$ Torr.

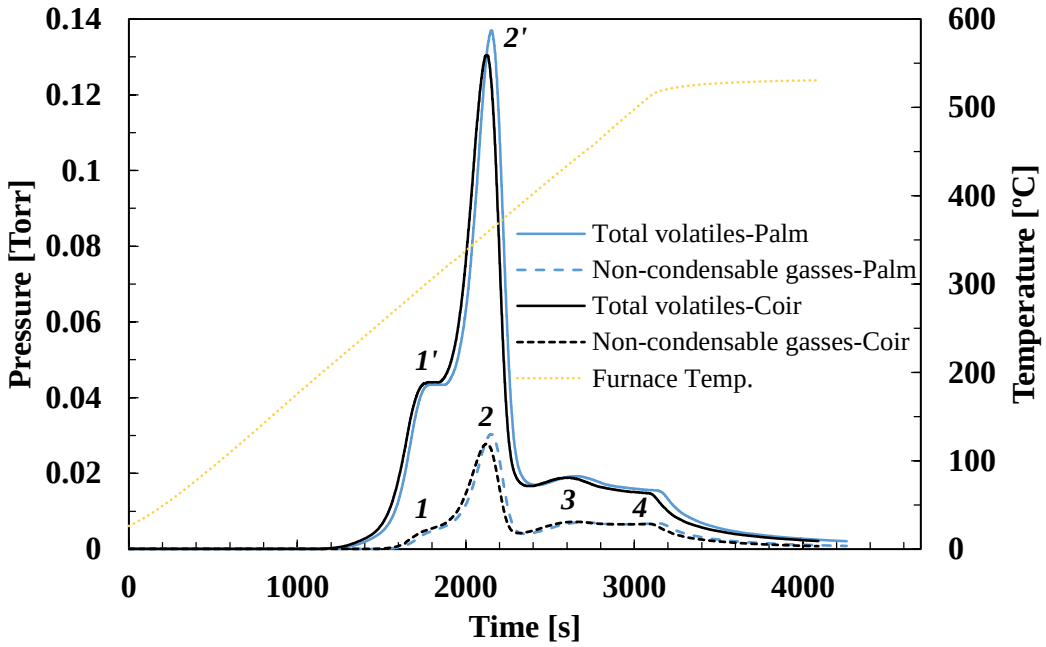

Figure 3.7: TVA degradation profiles of coir and palm fibres.

From Figure 3.7 and Table 3.4, it could be observed that both fibres have a similar degradation profile, with a main degradation peak at a temperature of approximately 357 °C. The shape of the degradation profile is defined by a main peak (*2'* in Figure 3.7), preceded by a big shoulder (at a temperature of approximately 300 °C, *1'* in Figure 3.7) and followed by a smaller broad shoulder. Furthermore, onset degradation temperatures were almost identical for both fibres, being 196 °C for date palm and 200 °C for coir, which indicated similar thermal stability of both fibres.

Fibre	Onset degradation temperature [^{0}C]	Max. evolution rate: Peak temperature [^{0}C]	$\int P_{condensable}(T)$ [Torr s]	$\int P_{non\text{-}condensable}(T)$ [Torr s]
Coir	200	358	64	16
Date palm	197	357	65	15

Table 3.4: Onset degradation temperatures, maximum volatile evolution rate peak temperatures, overall level of evolved volatiles and overall level of non-condensable volatiles.

Total-volatiles pressure profiles showed good correlation with the DTG curves from the TGA dynamic studies under nitrogen atmosphere, Figure 3.3 and Figure 3.4. It should be noticed that the initial moisture loss in the TGA curves was not observed due to the fact that fibres were located in the sample tube under vacuum for 12 hours prior to the heating experiment. This pre-conditioning at extremely low pressure, allowed the fibres to release all their moisture, even at room temperature.

A significant amount of non-condensable volatiles evolved from both fibres, as illustrated in Figure 3.7 and Table 3.4, representing 23 and 25% of the total of volatiles, for date palm and coir respectively. The pressure profile of non-condensable volatiles was divided in 4 regions, as illustrated in Figure 3.7 (i.e. *1*, *2*, *3* and *4*). These regions were analysed by online MS, which indicated that peaks *1* and *2*, in the case of both fibres, mainly consisted of carbon monoxide. In regions *3* and *4*, with similar results for both fibres, the MS revealed a mixture of carbon monoxide, methane and hydrogen.

The collected condensable volatiles from both fibres in the first stage of the analysis were separated into different fractions by sub-ambient differential distillation, and characterised by online MS and gas-phase FTIR analysis. The differential distillation pressure profiles and distillation fractions (i.e. coir C-F_i and date palm P-F_i) for each fibre are represented in Figure 3.8. The individual peaks (numbered from *1* to *4*) represent discrete components of the total volume of collected volatiles. It can be noticed that the pressure profile during differential distillation was almost identical for the two different fibres, and therefore, degradation products were expected to be extremely similar.

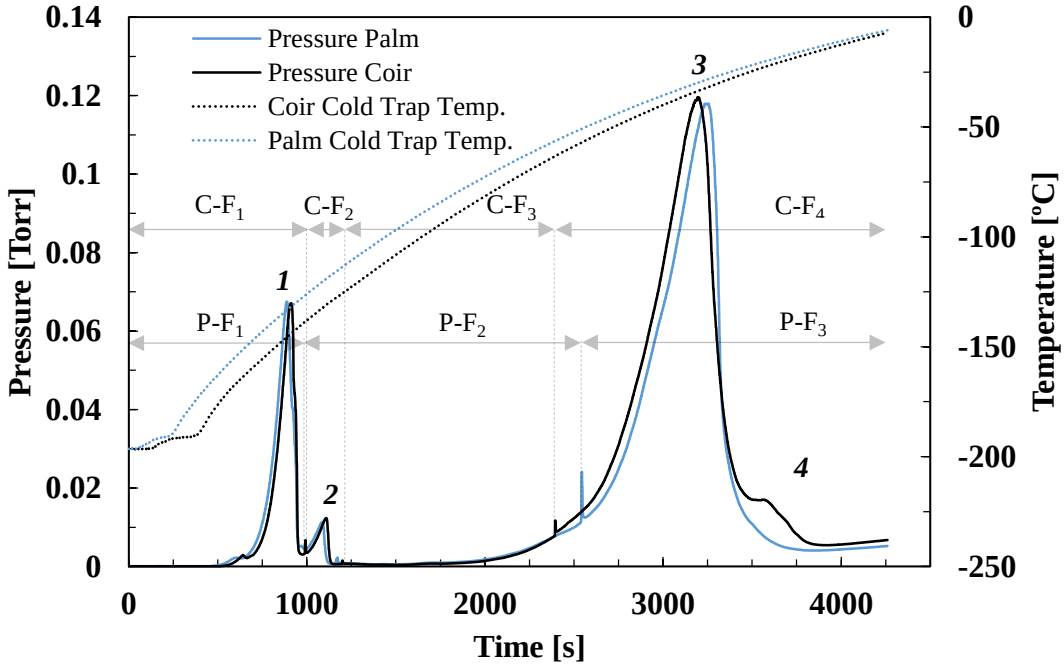

Figure 3.8: Sub-ambient differential distillation traces for condensable fractions collected from palm and coir.

It should be pointed out that, due to the TVA line configuration, within the sub-ambient differential distillation process, minor inter-experiment differences may arise due to differences in room temperature and manual handling of liquid nitrogen. Differences between both fibres in region *4* Figure 3.8, for which the main component was water, could have been caused by the previously mentioned variability.

The main component of each peak was identified by online mass spectrometry and FTIR analysis, Figure 3.9 and Figure 3.10, as: 1- CO_2, 2-Formaldehyde and 3-water. Traces of other volatiles were also identified: methanol, ketenes, acetic acid and long aliphatic fragments from unknown long hydrocarbon molecules. These results agree with the studies on pyrolytic degradation of biomass' main components (i.e. cellulose, hemicellulose and lignin) [8, 14, 40] and wood species [24].

This thermal degradation analysis represents a general study of the degradation process of palm and coir fibres. Due to the high temperatures achieved during the analysis, a high degradation of the fibres was expected. Therefore, the amount of fragments (especially long aliphatic compounds) from low temperature degradation products is high, making it difficult to trace back the initial degradation products.

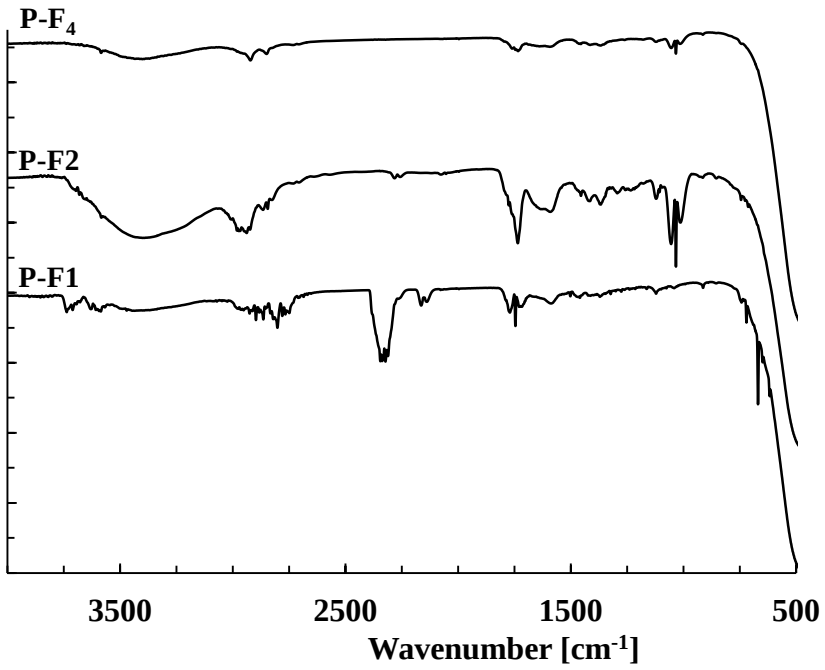

Figure 3.9: Palm's Transmittance FTIR spectrum of the recovered condensable fractions separated by sub-ambient differential distillation.

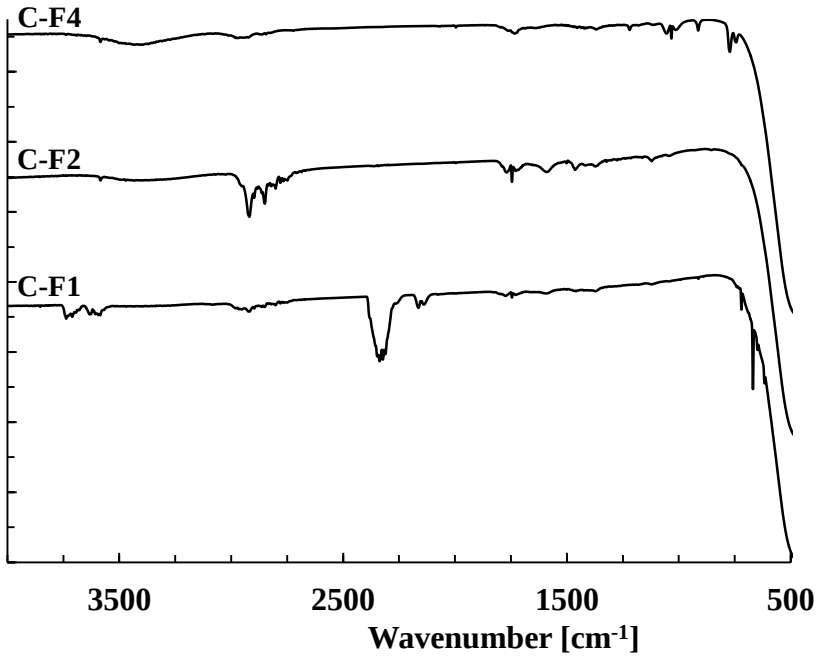

Figure 3.10: Coir's Transmittance FTIR spectrum of the recovered condensable fractions separated by sub-ambient differential distillation.

Palm and coir fibres were very brittle after TVA analysis. Figure 3.11 shows a SEM micrograph of a date palm fibre after TVA analysis, where it can be seen how the cells' external walls have collapsed, and how a major part of the cells' internal wall seems to have been degraded. The structural degradation pattern was in good agreement with the degradation of the three main components of natural fibres: cellulose, hemicellulose and lignin.

As described in Chapter 2, each individual cell is formed by a series of layers. The internal layers are the ones that provide rigidity to the cell and are mainly made up by cellulose and hemicellulose and other organic components [41]. In the external layers the abundance of lignin is much higher than in the internal layers. According to different studies, lignin is the most thermally resistant of the main three components [5, 42], with a wide degradation temperature range [14]. As expected after high thermal degradation, the remaining structure of the fibre was made up by the cells' external walls, as observed in Figure 3.11.

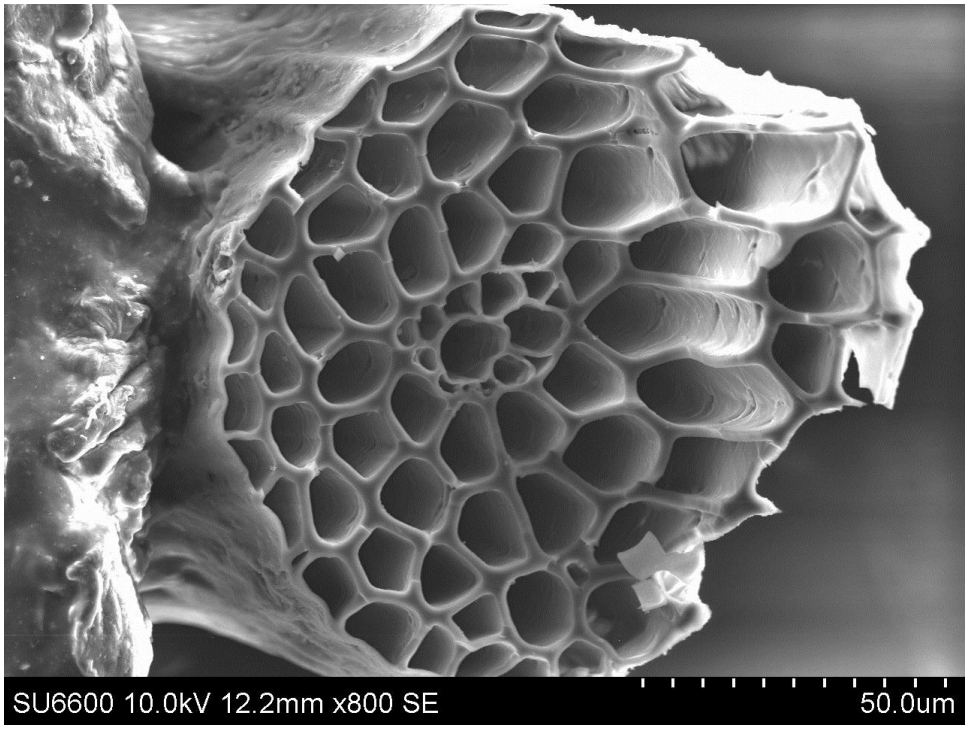

Figure 3.11: Palm fibre after TVA analysis.

3.3.3 Fibre observation

As discussed in the previous chapter, it is well known that the accurate measurement of the cross section area is essential to precisely characterise the mechanical properties of natural fibres [43], however, due to the comparative nature of the study, transverse observation was chosen for practical reasons. The comparison of the diameter measurements of both fibres, before and after the heat treatment, is illustrated in Figure 3.12. From the equations of the least squares fitted straight lines, it was observed how the diameter (based on transverse observation) slightly decreased. The slope of the lines revealed a decrease of approximately 3%. Certain scattering in the data may have emerged from the intra-fibre diameter variability and the fact that pictures could not have been taken at the exact same point.

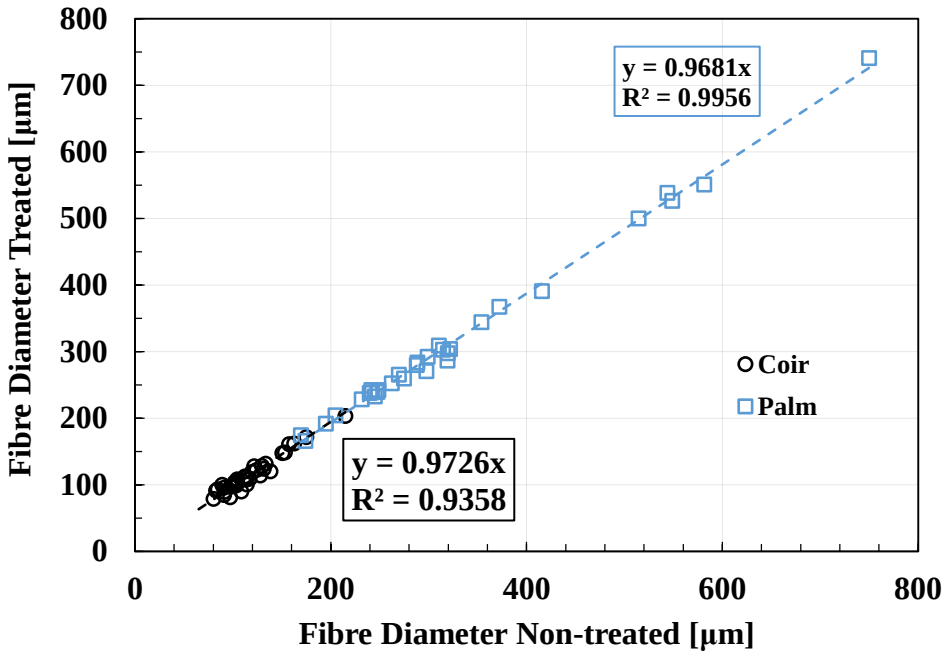

Figure 3.12: Non-treated fibre diameter versus Treated fibre diameter.

The slight reduction of the cross section area provided evidence of structural degradation, which was also observed, to a greater extent, after high temperature non-oxidative thermal degradation in the TVA, Figure 3.11. However, in the case of heat treated fibres at 220 °C, the approximately 3% reduction in fibre diameter, which is equivalent to 6% reduction of the cross section area, may be related to the initial loss of water content (i.e. approximately 6%). Regarding, the analysis of the SEM images

from pre and post-heated fibres (at 220 °C for 30 minutes), no significant differences were observed, Figure 3.13.

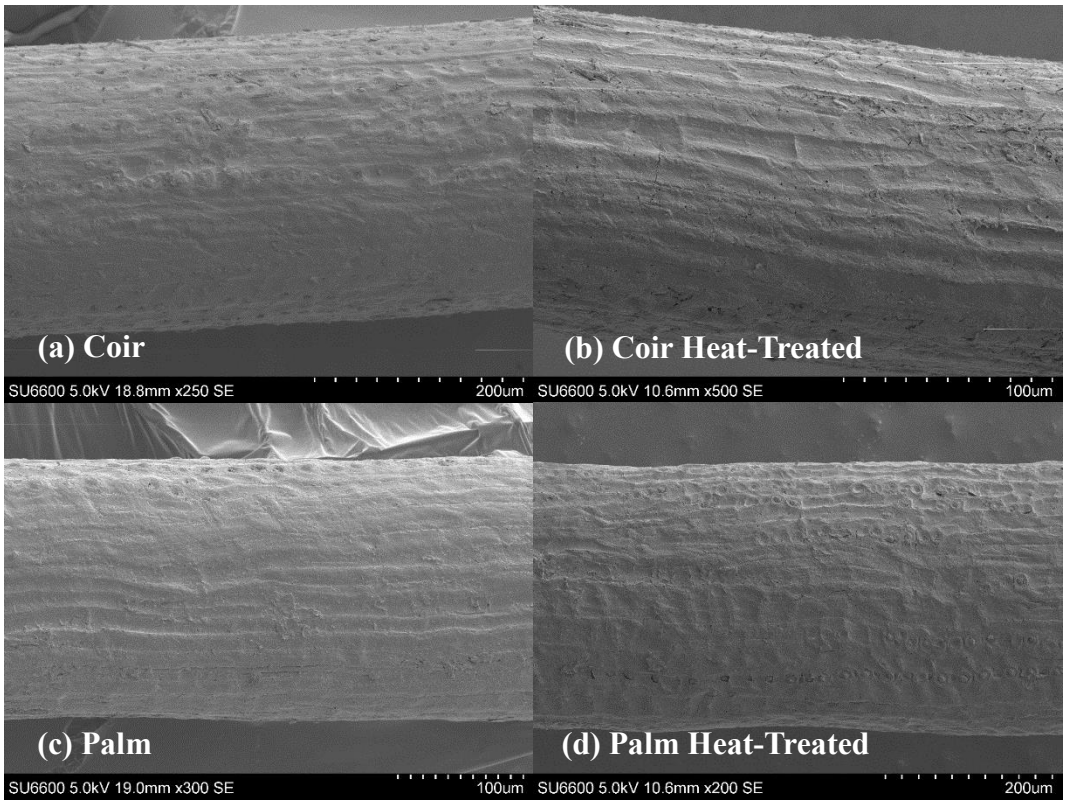

Figure 3.13: SEM surface observation of treated and non-treated fibres.

3.3.4 Degradation of mechanical properties

Single fibre tensile testing of non-treated and heat-treated palm and coir fibres revealed fundamental changes in their mechanical properties. The fibres' tensile strength, strain to failure and Young's modulus are illustrated in Figure 3.14 to Figure 3.19, where error bars represent 95% confidence limits. All results are summarised in Table 3.5. For both fibres, there was a drop of the tensile strength after heat treatment. The duration of the treatment also had a clear influence. The 10 min. heat treatments reduced the average tensile strength less than the respective 30 min. treatments. For palm fibre, Figure 3.14, it was observed how, for the case of 10 min. treatments, the tensile strength of date palm is approximately constant for 180 and 200 °C. A two-sample *t*-test of the average values of non-treated palm in comparison with the 10 min. treatments 180, 200 and 220 °C, only revealed a significant difference at 95% confidence level for the 220 °C treatment (*p*-value = 0.002). Furthermore, a two-

sample *t*-test of the average values showed no significant difference at 95% confidence level, between the tensile strength of non-treated palm and 30 min. treated palm at 180 °C (*p*-value = 0.102).

Sample	Young's modulus [GPa]		Tensile strength [MPa]		Failure strain [%]	
	Mean	95% Confidence limits	Mean	95% Confidence limits	Mean	95% Confidence limits
Coir Untreated	**3.1**	**0.3**	**154.5**	**23.7**	**23.3**	**3**
Coir 180 °C, 10 min	2.9	0.3	121.1	19	18	2.9
Coir 200 °C, 10 min	3.6	0.5	113.4	14	14.7	2.5
Coir 220 °C, 10 min	4.1	0.5	101.5	15.9	6.9	1.7
Coir 180 °C, 30 min	3.2	0.5	111.4	16.9	17.7	2.4
Coir 200 °C, 30 min	3.4	0.4	89.7	11.8	8.4	1.4
Coir 220 °C, 30 min	3.3	0.5	66.8	11.9	2.7	0.4
Coir 220 °C, 30 min, N_2	3.8	0.5	90.0	14.4	4.6	0.6
Date palm Untreated	**3**	**0.4**	**122.9**	**19.6**	**23.9**	**3.9**
Date palm 180 °C, 10 min	3.5	0.5	121	17.4	16.5	3.3
Date palm 200 °C, 10 min	3.9	0.4	118	14.7	11.3	2.1
Date palm 220 °C, 10 min	3.3	0.3	84.6	9.2	5.3	0.6
Date palm 180 °C, 30 min	3	0.4	101.2	16.4	12.9	2.1
Date palm 200 °C, 30 min	3.5	0.4	88.6	14.3	5.7	1
Date palm 220 °C, 30 min	3.1	0.3	62.7	9.3	2.9	0.6

Table 3.5: Tensile properties of single natural fibres.

A different scenario was observed for coir fibre, Figure 3.15, where the degradation of tensile strength was observed in all treatments. A two-sample *t*-test of the average values showed no significant difference at 95% confidence level, between the tensile strength of coir at 180 °C for 10 and 30 min. (*p*-value = 0.459). Moreover, as expected from the TGA isothermal studies under air and nitrogen, the heat treated coir fibres at 220 °C for 30 min. under nitrogen, showed a lower drop of the tensile strength in comparison with the equivalent samples treated on air. In this regard, a two-sample *t*-test of the average values showed a significant difference at 95% confidence level (*p*-value = 0.018). However, when comparing 220 °C 30 min. nitrogen and 220 °C 10 min. air, no significant difference was observed at 95% confidence level (*p*-value = 0.298). It should also be noticed that the values of tensile strength of both fibres, after the 30 min. heat-treatments, are very similar.

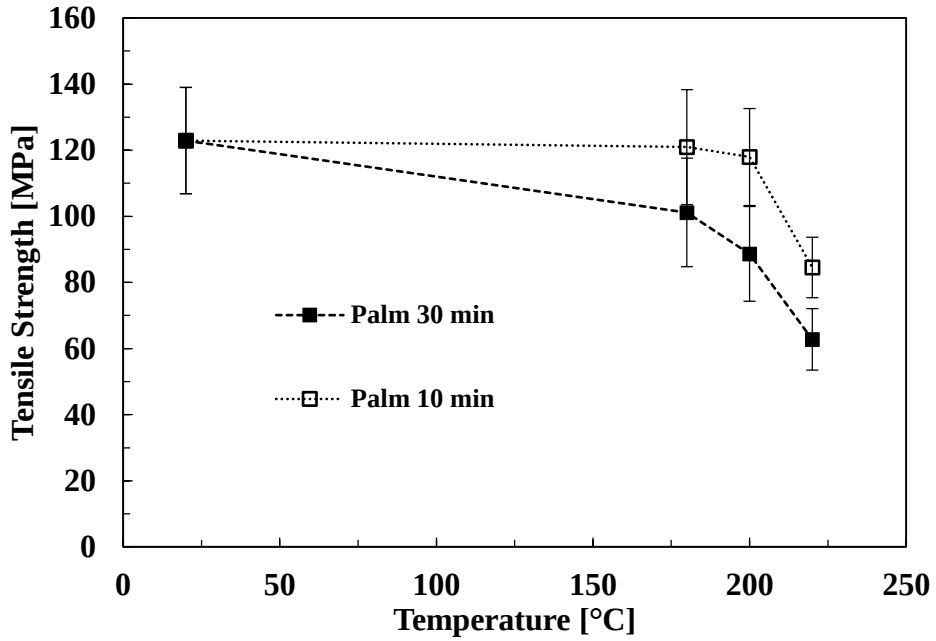

Figure 3.14: Palm's tensile strength versus heat-treatment temperature. 30 and 10 min. heat-treatments.

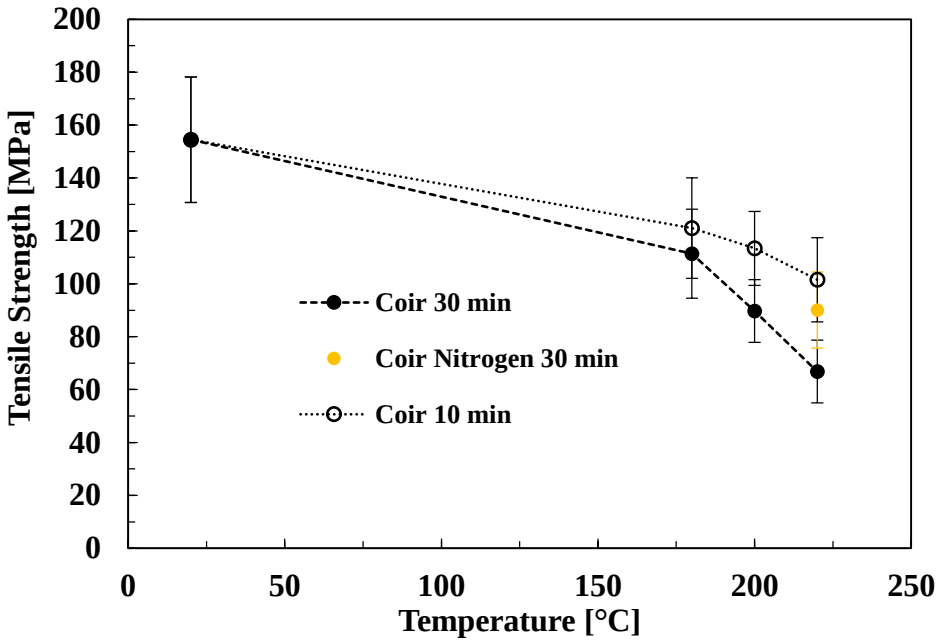

Figure 3.15: Coir's tensile strength versus heat-treatment temperature. 30 and 10 min. heat-treatments.

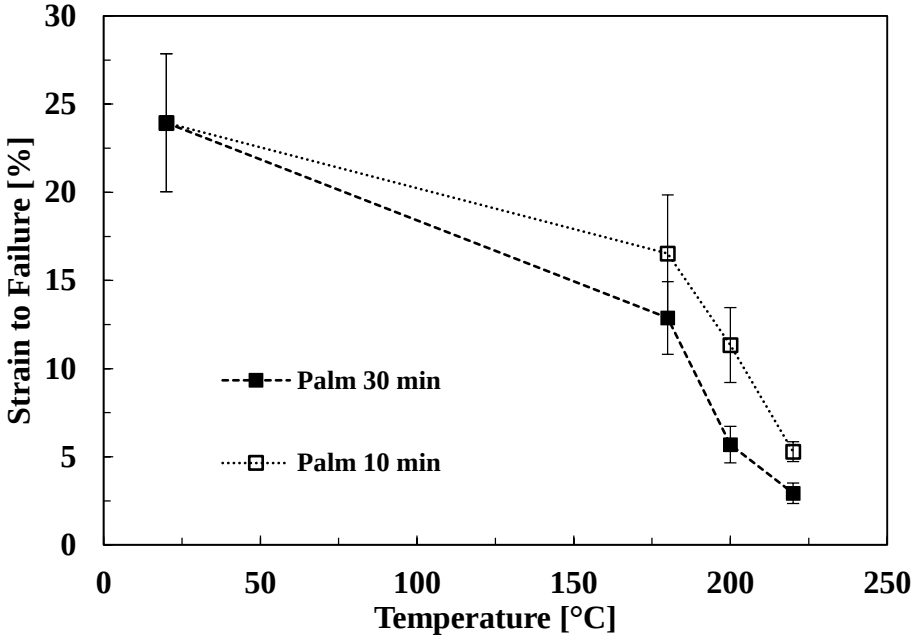

Figure 3.16: Palm's strain to failure versus heat-treatment temperature. 30 and 10 min. heat-treatments.

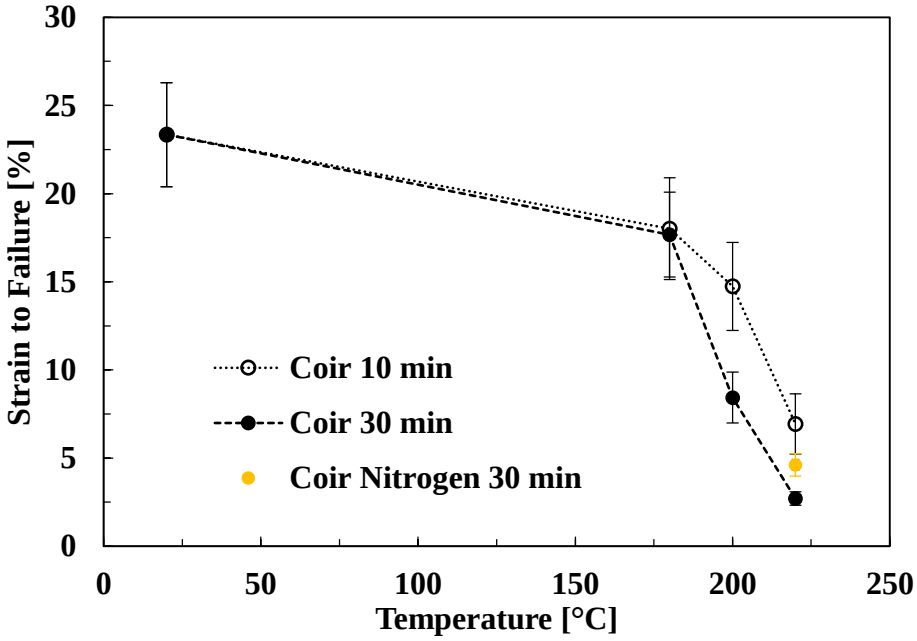

Figure 3.17: Coir's strain to failure versus heat-treatment temperature. 30 and 10 min. heat-treatments.

In the analysis of the strain at failure of heat treated fibres, for palm and coir fibres, a dramatic drop was observed, which was more severe than the decrease of tensile strength. As for tensile strength, the decrease of the strain to failure increased for increasing treatment's time and temperature. In the case of treatments at 180 °C, average values were equivalent for 10 and 30 min. For palm, a two-sample *t*-test of the average values showed no significant difference at 95% confidence level (*p*-value = 0.074). In the case of coir, values were even more similar, where a two-sample *t*-test of the average values showed no significant difference at 95% confidence level (*p*-value = 0.861). As in the analysis of tensile strength, coir fibres heat-treated under nitrogen showed a lower drop of the strain to failure.

In terms of the Young's modulus of heat-treated fibres, no consistent evidence of degradation were observed. In fact, for some of the heat-treatments, an apparent increase of the average values of Young's modulus was observed. For palm fibres, two-sample *t*-tests of the average values revealed no significant difference at 95% confidence level between non-treated and heat-treated samples, with the exception of heat-treated fibres at 200 °C for 10 min. (*p*-value = 0.007). With regard to coir fibres, two-sample *t*-tests of the average values revealed no significant difference at 95% confidence level between non-treated and heat-treated samples, with the exception of heat-treated fibres at 220 °C for 10 min. and 220 °C for 30 min. under nitrogen atmosphere (*p*-values equal to 0.002 and 0.035, respectively).

However, in the case of both fibres, as discussed in Chapter 2, the apparent increase of Young's modulus may have been caused by different diameter distributions of the tested sets. The diameter distribution for each set of experiments is illustrated in Figure 3.18 and Figure 3.19. For palm, it can be noticed that for the only set with significant Young's modulus increase (i.e. heat-treated at 200 °C for 10 min.) the frequency of fibres with a diameter higher than 350 µm, is considerably lower than its 180 and 220 °C equivalent. Regarding coir sets with significant average increase (i.e. heat-treated fibres at 220 °C for 10 min. and 220 °C for 30 min. under nitrogen), it can be seen how the frequency of fibres within the low diameter range, diameter from 100 to 150 µm, is significantly higher than other sets, which could have ultimately led to an apparent increase of the average Young's modulus.

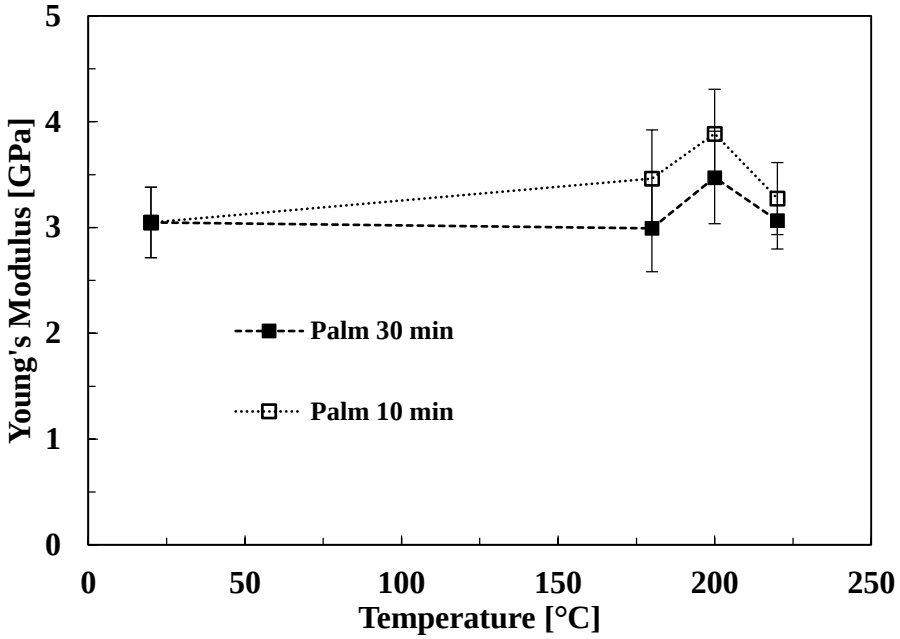

Figure 3.18: Palm's Young's modulus versus heat-treatment temperature. 30 and 10 min. heat-treatments.

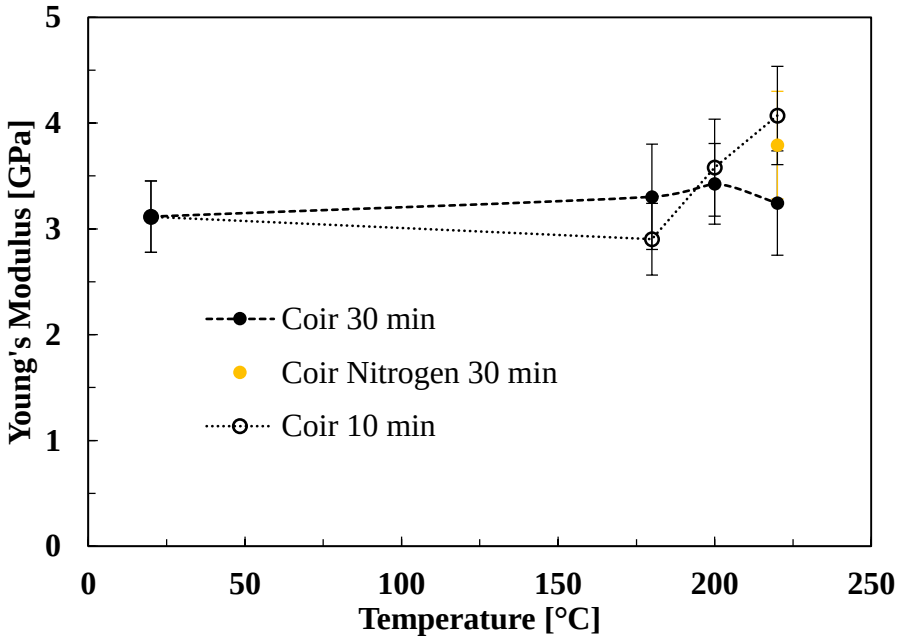

Figure 3.19: Coir's Young's modulus versus heat-treatment temperature. 30 and 10 min. heat-treatments.

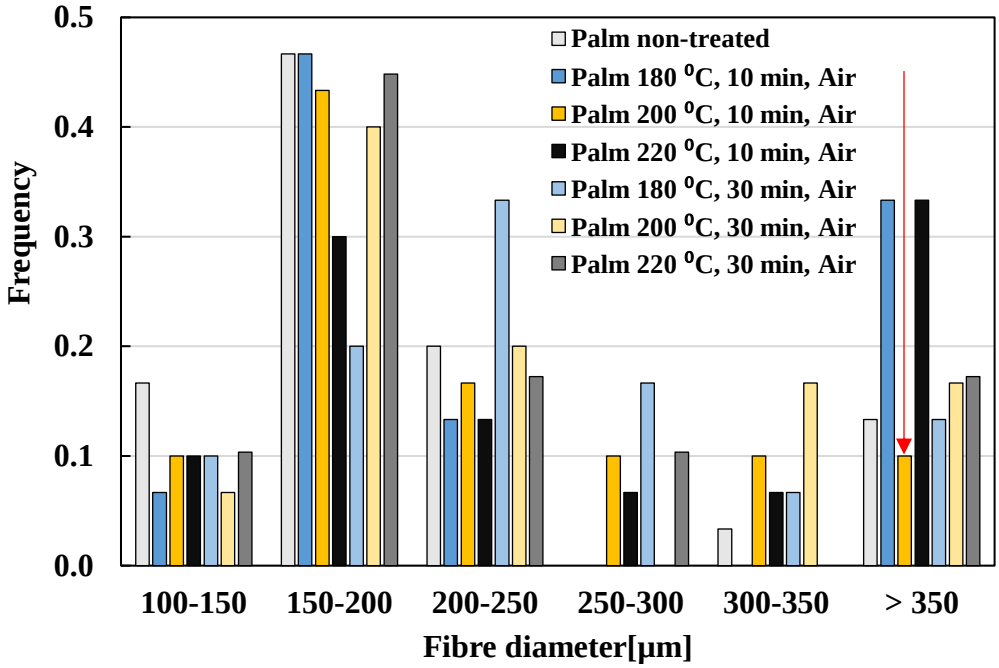

Figure 3.20: Palm fibre diameter distribution for tested samples.

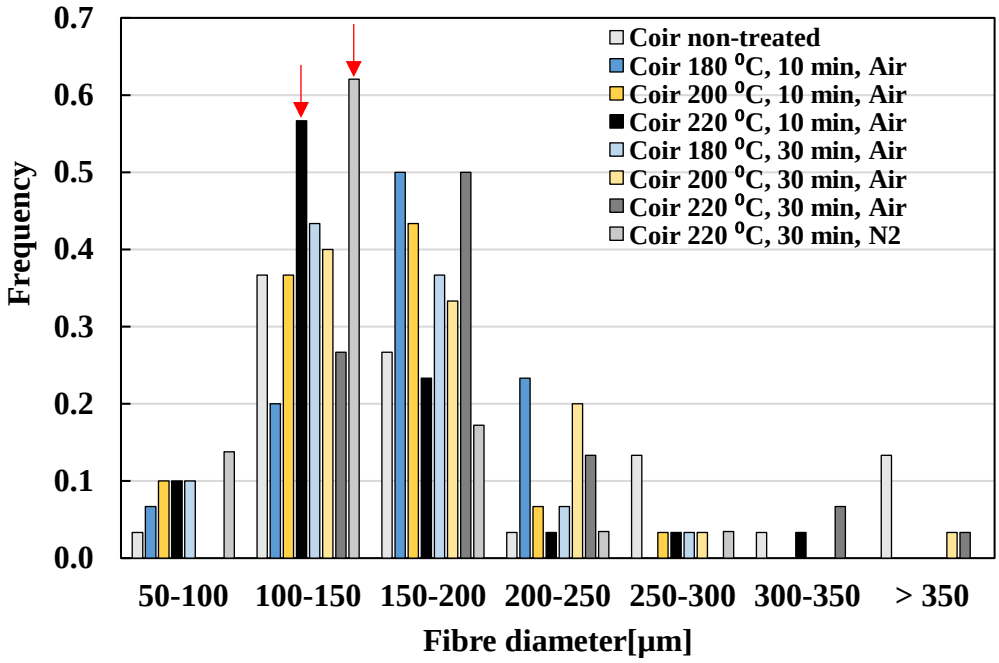

Figure 3.21: Coir fibre diameter distribution for tested samples.

As discussed in Chapter 2, date palm and coir are natural fibres with high MFA, which normally leads to two differentiated regions in their tensile stress-strain behaviour [1, 41, 44, 45]. The initial part of the curve, in which Young's modulus was measured, is almost a linear elastic stress-strain curve. On the other hand, the second region, which in non-treated fibres represents the major region in terms of strain, is considered to be a non-elastic region. It has been pointed out that after the yielding point, the matrix materials of the cellular walls (i.e. mainly hemicellulose, lignin, pectin) undergo plastic deformation while cellulose microfibrils slide with respect to each other [46].

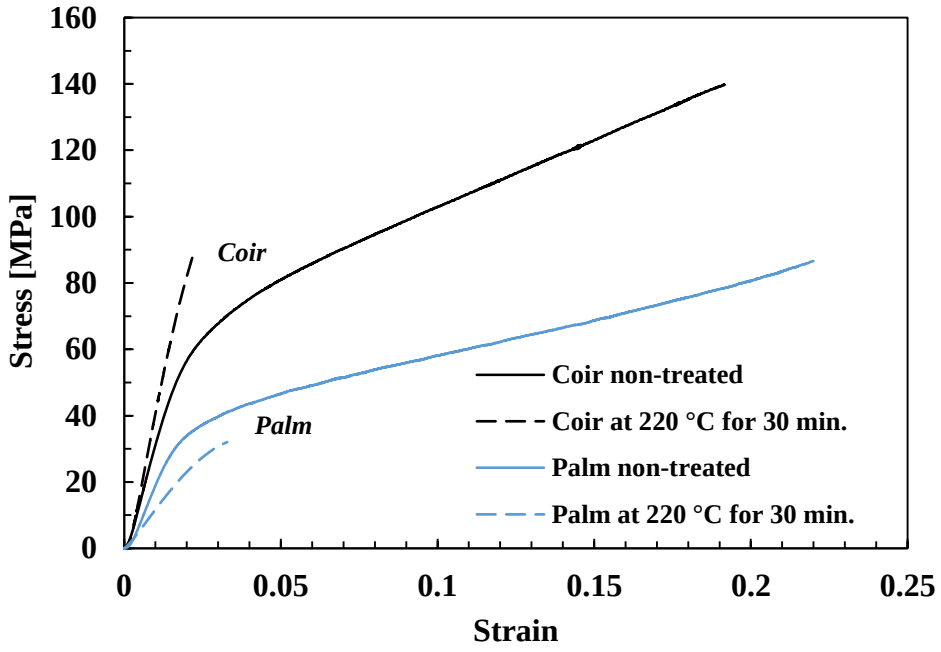

Figure 3.22: Typical coir and palm stress-strain curves for non-treated and heat-treated fibres under air at 220 °C for 30min. It should be noticed that the apparent variation of elastic modulus of the examples choosen for this figure, is due to the inherent variability of properties between fibres, and not related to the thermal treatment effect.

In the case of heat-treated fibres, especially after heat-treatments at 220 °C for 30 min., major changes within the second region of the stress-strain curves were observed. This second region was entirely supressed in most of the cases after 30 min. at 220 °C, as illustrated in Figure 3.22. Heat-treatment temperatures (i.e. 180, 200 or 220 °C) were expected to mainly degrade pectins and hemicelluloses [29, 42], as these components were associated with the initial degradation processes identified by

dynamic TGA and TVA experiments. As discussed in Chapter 2, pectins are one of the main components that cements elementary fibres together. Hemicelluloses are the main component of the secondary wall matrix material, where cellulose microfibrils are embedded, and are meant to bind cellulose and lignin [41]. The degradation of these two components may limit their plastic deformation (i.e. second region of the fibre's stress-strain curve), ultimately leading to sudden failure of the natural fibre. Therefore, degradation of pectins and hemicelluloses would be directly related to the strain to failure and consequently with the tensile strength.

On the other hand, as observed in the dynamic TGA and TVA experiments, at the temperatures of the heat treatments, cellulose microfibrils, which are the main contributor to fibre's rigidity, are not expected to degrade. Cellulose degradation was associated with the second DTG degradation peaks, identified at 324 °C for palm and coir fibres, far above heat-treatment's temperatures. This may explain, as observed in Figure 3.18 and Figure 3.19, why average values of Young's modulus remained almost constant (or slightly increased due to modulus dependence on diameter).

3.4 Conclusions

This work has shown how important it is to control the composite processing conditions of coir and date palm due to the observed thermal degradation. The thermal behaviour of palm and coir fibres, under air and nitrogen atmospheres, was investigated by thermogravimetric analysis (TGA). Dynamic thermal analysis of both fibres revealed, under nitrogen, two characteristic peaks from the derivative of thermogravimetric analysis (DTG), that were associated with pectin-hemicellulose and cellulose degradation. Lignin degradation peaks were not clearly observed. Under air atmosphere, DTG peaks were slightly shifted to lower temperatures. At the same time, an additional peak was detected at high temperatures, which was attributed to the oxidative decomposition of charred residue. Isothermal studies showed higher weight loss for higher temperatures and time of exposure. Furthermore, equivalent experiments under nitrogen, showed lower weight loss in comparison with experiments under air.

The thermal behaviour of palm and coir was also explored using the TVA technique, under vacuum. Long exposure (12 hours) to vacuum at room temperature proved to be effective to remove the moisture absorbed by the fibres. Similar degradation patterns, in comparison with TGA under nitrogen, were observed in the TVA pressure profile. MS and FTIR were used to investigate the considerable amount of volatiles from the degradation processes. The main components identified were carbon monoxide, methane, hydrogen, carbon dioxide, formaldehyde and water. Traces of other volatiles were also identified: methanol, ketenes, acetic acid and long aliphatic fragments from unknown long hydrocarbon molecules. Further investigation of the fibres analysed in the TVA, under the SEM, revealed high structural degradation of the external cells and the secondary layer of internal cells.

The analysis of palm and coir fibres, before and after heat-treatment (at 220 °C for 30 min.), revealed a decrease of their diameter of approximately 3%. At the same time, no significant morphology changes on fibres' surface could be appreciated using SEM. Single fibre testing of palm and coir fibres heat-treated, at 180, 200 and 220 °C for 10 or 30 min. under air atmosphere, showed a significant drop in the failure strain and tensile strength, especially at processing temperatures above 200 °C. Furthermore, above 200 °C, a clear time dependence of the degradation was also observed. However, the fibre Young's modulus remained almost constant, with comparable average values. Coir fibres heat-treated at 220 °C for 30 min. under nitrogen atmosphere showed a lower drop in tensile strength and failure strain than the equivalent air treatment. In the case of both fibres, these heat treatments at 180-220 °C were mainly associated to the degradation of pectins and hemicelluloses, which only affected the high strain region (non-elastic) of the stress-strains curves. Consequently, this led to a significant drop of the natural fibre tensile strength and failure strain, especially after high temperatures and long exposures. The initial low strain elastic region, where the Young's modulus is measured, remained unaffected. The direct observation of fibres and the analysis of the tensile data showed how the thermal degradation affects the structural integrity and mechanical properties of the fibres.

3.5 References

1. Bledzki, A.K., Gassan, J.: Composites reinforced with cellulose based fibres. Prog. Polym. Sci. 24, 221–274 (1999).
2. Nabi Saheb, D., Jog, J.P.: Natural fiber polymer composites: A review. Adv. Polym. Technol. 18, 351–363 (1999).
3. Stokke, D.D., Wu, Q., Han, G.: Introduction to wood and natural fiber composites. John Wiley & Sons (2014).
4. Gassan, J., Bledzki, A.K.: Thermal Degradation of Flax and Jute Fibers. J. Appl. Polym. Sci. 82, 1417–1422 (2001).
5. Tajvidi, M., Takemura, A.: Thermal Degradation of Natural Fiber-reinforced Polypropylene Composites. J. Thermoplast. Compos. Mater. 23, 281–298 (2009).
6. Nuñez, A.J., Kenny, J.M., Reboredo, M.M., Aranguren, M.I., Marcovich, N.E.: Thermal and Dynamic Mechanical Characterization of Polypropylene-Woodflour Composites. Polym. Eng. Sci. 42, 733–742 (2002).
7. Stamm, A.J.: Thermal degradation of wood and cellulose. Ind. Eng. Chem. (1956).
8. Schwenker, J.. R.F., Pacsu, E.: Pyrolytic Degradation Products of Cellulose. Ind. Eng. Chem. Chem. Eng. Data Ser. 2, 83–88 (1957).
9. Roberts, A.F.: A review of kinetics data for the pyrolysis of wood and related substances. Combust. Flame. 14, 261–272 (1970).
10. Huang, M.-R., Li, X.-G.: Thermal degradation of cellulose and cellulose esters. J. Appl. Polym. Sci. 68, 293–304 (1998).
11. Stenseng, M., Jensen, A., Dam-Johansen, K.: Investigation of biomass pyrolysis by thermogravimetric analysis and differential scanning calorimetry. J. Anal. Appl. Pyrolysis. 58-59, 765–780 (2001).
12. Nada, A.M.A., Hassan, M.L.: Thermal behavior of cellulose and some cellulose derivatives. 67, 0–4 (2000).
13. Ward, S.M., Braslaw, J.: Experimental weight loss kinetics of wood pyrolysis under vacuum. Combust. Flame. 61, 261–269 (1985).
14. Yang, H., Yan, R., Chen, H., Lee, D.H., Zheng, C.: Characteristics of hemicellulose, cellulose and lignin pyrolysis. Fuel. 86, 1781–1788 (2007).
15. Yang, H., Yan, R., Chen, H., Zheng, C., Lee, D.H., Liang, D.T.: Influence of mineral matter on pyrolysis of palm oil wastes. Combust. Flame. 146, 605–611 (2006).
16. Koufopanos, C.A., Lucchesi, A., Maschio, G.: Kinetic modelling of the pyrolysis of biomass and biomass components. Can. J. Chem. Eng. 67, 75–84 (1989).
17. Thurner, F., Mann: Kinetic investigation of wood pyrolysis. Ind. Eng. Chem. Process Des. Dev. 20, 482–488 (1981).

18. Varma, D.S., Varma, M., Varma, I.K.: Thermal behaviour of coir fibres. Thermochim. Acta. 108, 199–210 (1986).

19. Varhegyi, G., Antal, J.M.J., Szekely, T., Szabo, P.: Kinetics of the thermal decomposition of cellulose, hemicellulose, and sugarcane bagasse. Energy & Fuels. 3, 329–335 (1989).

20. Várhegyi, G., Antal, M.J., Jakab, E., Szabó, P.: Kinetic modeling of biomass pyrolysis. J. Anal. Appl. Pyrolysis. 42, 73–87 (1997).

21. Raveendran, K., Ganesh, A., Khilar, K.C.: Pyrolysis characteristics of biomass and biomass components. Fuel. 75, 987–998 (1996).

22. Silva, G.G., Souza, D.A.D.E., Machado, J.C., Hourston, D.J.: Mechanical and Thermal Characterization of Native Brazilian Coir Fiber. J. Appl. Polym. Sci. 76, 1197–1206 (2000).

23. Bismarck, A., Aranberri-Askargorta, I., Springer, J., Mohanty, A.K., Misra, M., Hinrichsen, G., Czapla, S.: Surface characterization of natural fibers; surface properties and the water up-take behavior of modified sisal and coir fibers. Green Chem. 3, 100–107 (2001).

24. Müller-Hagedorn, M., Bockhorn, H., Krebs, L., Müller, U.: A comparative kinetic study on the pyrolysis of three different wood species. J. Anal. Appl. Pyrolysis. 68-69, 231–249 (2003).

25. Ouajai, S., Shanks, R.A.: Composition, structure and thermal degradation of hemp cellulose after chemical treatments. Polym. Degrad. Stab. 89, 327–335 (2005).

26. Tomczak, F., Sydenstricker, T.H.D., Satyanarayana, K.G.: Studies on lignocellulosic fibers of Brazil. Part II: Morphology and properties of Brazilian coconut fibers. Compos. Part A Appl. Sci. Manuf. 38, 1710–1721 (2007).

27. Yao, F., Wu, Q., Lei, Y., Guo, W., Xu, Y.: Thermal decomposition kinetics of natural fibers: Activation energy with dynamic thermogravimetric analysis. Polym. Degrad. Stab. 93, 90–98 (2008).

28. Almeida, A.L.F.S., Barreto, D.W., Calado, V., Almeida, J.R.M.: Thermal analysis of less common lignocellulose fibers. J. Therm. Anal. Calorim. 91, 405–408 (2008).

29. Rachini, A., Le Troedec, M., Peyratout, C., Smith, A.: Comparison of the Thermal Degradation of Natural, Alkali-TReated and Silane-TReated Hemp Fibers Under Air and Inert Atmosphere. J. Appl. Polym. Sci. 112, 226–234 (2009).

30. De Rosa, I.M., Kenny, J.M., Puglia, D., Santulli, C., Sarasini, F.: Morphological, thermal and mechanical characterization of okra (Abelmoschus esculentus) fibres as potential reinforcement in polymer composites. Compos. Sci. Technol. 70, 116–122 (2010).

31. El may, Y., Jeguirim, M., Dorge, S., Trouvé, G., Said, R.: Study on the thermal behavior of different date palm residues: Characterization and devolatilization kinetics under inert and oxidative atmospheres. Energy. 44, 702–709 (2012).

32. Sait, H.H., Hussain, A., Salema, A.A., Ani, F.N.: Pyrolysis and combustion

kinetics of date palm biomass using thermogravimetric analysis. Bioresour. Technol. 118, 382–389 (2012).

33. Dehghani, A., Madadi Ardekani, S., Al-Maadeed, M. a., Hassan, A., Wahit, M.U.: Mechanical and thermal properties of date palm leaf fiber reinforced recycled poly (ethylene terephthalate) composites. Mater. Des. 52, 841–848 (2013).

34. Wielage, B., Lampke, T., Marx, G., Nestler, K., Starke, D.: Thermogravimetric and differential scanning calorimetric analysis of natural fibres and polypropylene. Thermochim. Acta. 337, 169–177 (1999).

35. Van de Velde, K., Baetens, E.: Thermal and Mechanical Properties of Flax Fibres as Potential Composite Reinforcement. Macromol. Mater. Eng. 286, 342–349 (2001).

36. Prasad, B.M., Sain, M.M., Roy, D.N.: Structure property correlation of thermally treated hemp fiber. Macromol. Mater. Eng. 289, 581–592 (2004).

37. Prasad, B.M., Sain, M.M.: Mechanical properties of thermally trated hemp fibers in inert atmosphere for potential composite reinforcement. Mater. Res. Innov. 7, 231–238 (2003).

38. Gourier, C., Le Duigou, A., Bourmaud, A., Baley, C.: Mechanical analysis of elementary flax fibre tensile properties after different thermal cycles. Compos. Part A Appl. Sci. Manuf. 64, 159–166 (2014).

39. McNeill, I.C., Ackerman, L., Gupta, S.N., Zulfiqar, M., Zulfiqar, S.: Analysis of degradation products by thermal volatilization analysis at subambient temperatures. J. Polym. Sci. Polym. Chem. Ed. 15, 2381–2392 (1977).

40. Lipska, A.E., Wodley, F.A.: Isothermal Pyrolysis of Cellulose : Kinetics and Gas Chromatographic Mass Spectrometric Analysis of the Degradation Products. 13, (1969).

41. Mussig, J. ed: Industrial Applications of Natural Fibres. John Wiley & Sons (2010).

42. Herrera, A., Soria, S., Araya, C.P.: A kinetic study on the thermal decomposition of six hardwood species. Holz als Roh- und Werkst. 44, 357–360 (1986).

43. Thomason, J.L., Carruthers, J., Kelly, J., Johnson, G.: Fibre cross-section determination and variability in sisal and flax and its effects on fibre performance characterisation. Compos. Sci. Technol. 71, 1008–1015 (2011).

44. Martinschitz, K.J., Boesecke, P., Garvey, C.J., Gindl, W., Keckes, J.: Changes in microfibril angle in cyclically deformed dry coir fibers studied by in-situ synchrotron X-ray diffraction. J. Mater. Sci. 43, 350–356 (2008).

45. Kulkarni, A.G., Satyanarayana, K.G., Sukumaran, K., Rohatgi, P.K.: Mechanical behaviour of coir fibres under tensile load. J. Mater. Sci. 16, 905–914 (1981).

46. Spatz, H., Köhler, L., Niklas, K.J.: Mechanical behaviour of plant tissues: composite materials or structures? J. Exp. Biol. 202, 3269–3272 (1999).

Chapter 4

Thermo-mechanical characterisation of PP and LDPE, and maleic anhydride modifications

4.1 Introduction / Literature review

Polyethylene (PE) and Polypropylene (PP) are today, the most widely used thermoplastic polymers, Figure 4.1. Comparing the average annual growth rate of plastic with other materials, over the past 25 years from 1985 to 2010, the growth rate of plastic was higher than steel and aluminium. Furthermore, on the subject of composite materials, the progression of polymer composites exceeds those of metals [1]. In this regard, thermoplastic composites offer many advantages over thermoset composites [1–4], such as low processing cost, design flexibility and ease of moulding complex parts, compounds are clean and recyclable, and can be welded. Regarding composites based on natural fibres, thermoplastics currently dominate as matrix materials [5].

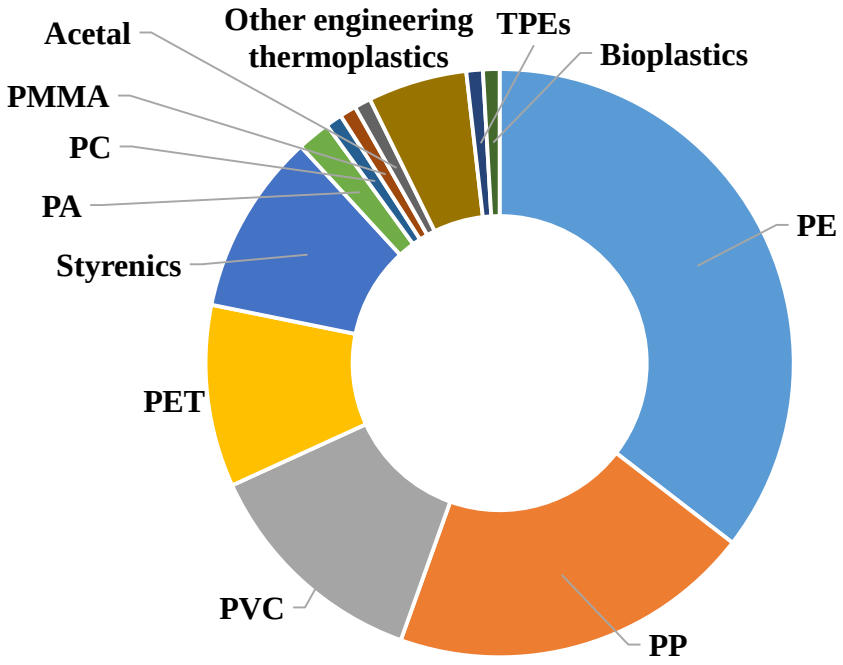

Figure 4.1: Market shares by weight for the main thermoplastics. Based on [1].

This chapter focuses on the characterisation of the mechanical properties and thermal degradation of PP and LDPE, along with their respective modifications with maleic anhydride used in this research.

4.1.1 Polypropylene

4.1.1.1 Chemistry of polypropylene

PP is a linear hydrocarbon polymer containing little or no unsaturation (i.e. carbon-carbon double or triple bonds) [6]. PP is prepared by the polymerising propylene, Figure 4.2., normally obtained as a by-product of petroleum refining, in the presence of a catalyst under carefully controlled heat and pressure [7, 8]. In the polymerisation reaction, propylene monomers are added sequentially to the growing polymer chain, to form a long linear polymer chain composed of thousands of propylene monomers [7]. The degree of polymerisation (n) is defined as the number of repeated units in a PP chain.

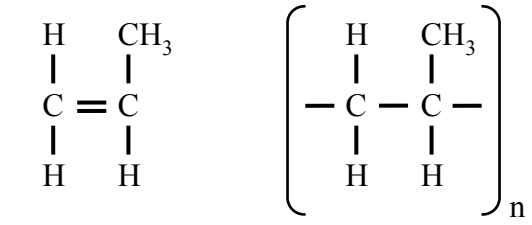

(a) Propylene (b) Polypropylene

Figure 4.2: Chemical structure of propylene and polypropylene. The index (n) denotes the repetition of the monomer according to the degree of polymerisation [7, 9].

4.1.1.2 Structure and morphology

Depending on the orientation of the pendant methyl groups attached to alternate carbon atoms, PP can be isotactic, syndiotactic or atactic, Figure 4.3. In isotactic PP (the most common commercial form), (a) Figure 4.3, pendant methyl groups (attached to alternate carbon atoms) are all in the same configuration and on the same side of the polymer chain [7, 8]. Due to this regular arrangement, isotactic PP has a high degree of crystallinity. In syndiotactic PP, (b) Figure 4.3, alternate pendant methyl groups are on opposite sides of the polymer backbone, with opposite configurations relative to the polymer chain. In atactic PP, (c) Figure 4.3, pendant methyl groups have a random

orientation with respect to the polymer backbone [7, 8]. Amounts of isotactic, atactic and syndiotactic segments in a formulation are determined by the catalyst used and polymerisation conditions. Most of polypropylenes are predominantly isotactic, with small amounts of atactic polymer [7].

PP is a semi-crystalline polymer, where degrees of crystallinity and different crystal structures depend on the stereochemical structure, processing or crystallisation conditions and the presence of additives [6–8, 10]. In polymers, the unit cell (formed by the atomic arrangement) is repeated millions of times, forming the crystalline structure in three dimensional space.

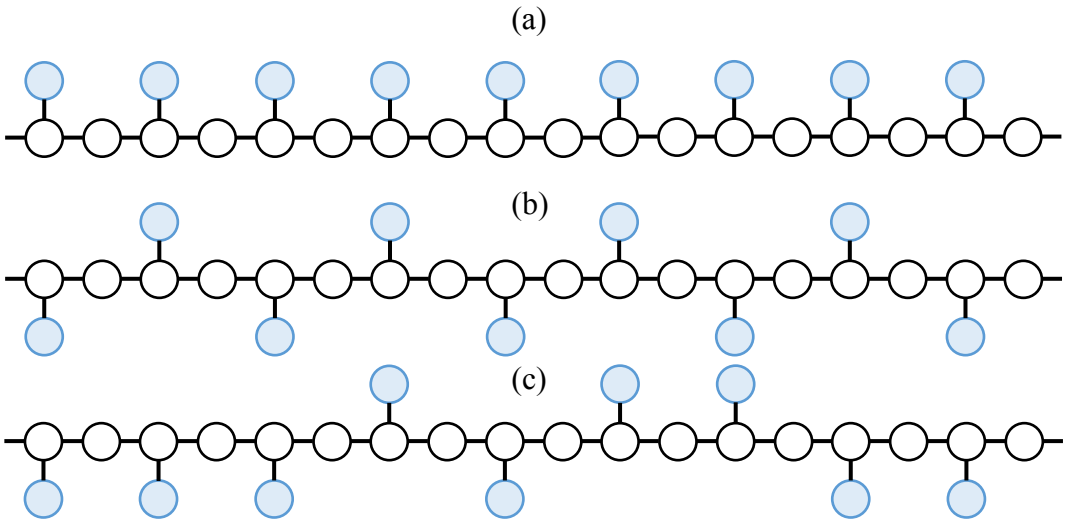

Figure 4.3: Stereochemical configurations of polypropylene, based on [7]. (a) Isotactic, (b) Syndiotactic, (c) Atactic. Polymer backbone are represented in white ○, while pendant methyl groups are represented in blue ○.

PP molecules associate to form supramolecular structures. Depending on the crystallisation conditions (such as cooling rate, temperature and pressure) and tacticity of the polymer, PP can exist in different morphological forms [7]. Regarding isotactic PP, three different configurations are possible: α-form, β-form and γ-form. The most common form in isotactic PP is α-form, in which polymer chains form a helical structure in a monoclinic unit cell. The helical chains fold back and forth to form thin, ordered, plate-like or ribbon-like structures called lamellae. Lamellae that grow in a radial direction form spherulites (i.e. spherical structures that radiate outward from a central nucleus) [7]. Lamellae are connected by amorphous regions, which result from

irregularities in the polymer chain, called tie points. These points provide flexibility and impact resistance to the overall polymer. As discussed, crystallinity and crystal microstructures have a great influence on PP mechanical properties.

Due to its structure, isotactic PP has the highest crystallinity compared to the other stereochemical configurations, which leads to high stiffness and tensile strength [7, 11]. On the other hand, if in a predominantly isotactic PP, the amount of atactic PP (amorphous material) is increased, due to its irregular structure, the room temperature impact resistance increases but the stiffness decreases [6, 7]. PP generally has higher tensile, flexural and compressive strength and higher modulus than PE due to the steric interaction of the pendant methyl groups, which leads to a more rigid and stiff polymer chain in comparison to the PE chain.

The influence of molecular weight is often opposite to that showed by most other polymers [6]. Although an increase in molecular weight results in an increase in melt viscosity and impact strength, as is the case for most polymers, it also leads to lower yield strength and stiffness [6, 7]. This effect may be caused by the fact that high molecular weight polymer does not crystallise as easily as lower molecular weight polymer, ultimately leading to the observed decrease in strength and stiffness.

Apart from the PP solely formed by the polymerisation of propylene (homopolymer), other PP can be formed by the blending and addition of other polymers [1, 6, 7, 12]. Impact copolymers are formed by the addition of ethylene-propylene rubber (EPR), ethylene-propylene-diene monomer (EPDM), PE, or plastomers to PP homopolymers or random copolymers. Impact copolymers are used when increased impact resistance is required. The overall impact properties are determined by the kind, morphology and quantity of the elastomeric phase, while stiffness is dependent on the PP matrix. However, the higher impact strength, caused by the addition of extra components, also leads to a decrease in stiffness of the overall polymer.

4.1.2 Low density polyethylene

4.1.2.1 Chemistry of polyethylene

PE is a long chain aliphatic hydrocarbon [6], formed by the polymerisation of ethylene, Figure 4.4. Unlike conventional organic materials, PE does not consist of identical molecules. PE resins comprise chains with a range of backbone lengths [1, 13]. PE is therefore considered a broad family with versatile properties that depend on which of the three main polymerisation processes is used [1]. PE molecules can be branched to various degrees and contain small amounts of unsaturation.

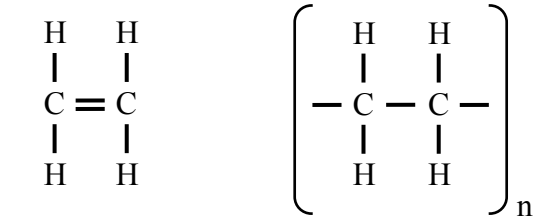

(a) Ethylene (b) Polyethylene

Figure 4.4: Chemical structure of ethylene and polyethylene. The index (n) denotes the repeat of the monomer according to the degree of polymerisation [7, 9].

4.1.2.2 Structure and morphology

PE is a semi-crystalline polymer, it contains crystalline and non-crystalline regions [13]. In the solid state, branches and other defects in the regular PE chain structure limit the crystallinity level. Therefore, chains that have fewer defects have a higher level of crystallinity [13]. As the packing of crystalline regions is higher than non-crystalline regions, the overall density of a PE increases as the degree of crystallinity increases. PEs can be classified versus density and molecular weight [1] as: ultralow-density PE and very low-density PE (VLDPE); low-density PE (LDPE) and liner low-density PE (LLDPE); medium-density PE (MDPE); high-density PE (HDPE); high molecular weight PE (HMWPE); ultrahigh molecular weight PE (UHMWPE).

LDPE contains substantial concentrations of branches that hinder the crystallisation process, which leads to relatively low densities in comparison with HDPE [13]. These branches primarily consist of ethyl and butyl groups together with some long-chain branches. When PE is cooled from melt, certain portions of it crystallise. These

crystallised regions are surrounded by disordered polymer chains. PE tends to crystallise in lamellae, which has two dimensions much greater than the third (in a three dimensional space). The most common large-scale structure composed of crystalline and non-crystalline regions are named spherulites. Spherulites consist of lamellae growing outward radially from nucleation sites, in an approximately spherical configuration [13]. This spherulites can vary in size depending on the number or nucleation points. The size and perfection of these spherulites affect the mechanical properties of the overall polymer.

4.1.3 Maleic anhydride polymer modifications (PP and LDPE)

PP and PE are very versatile polyolefins, however, their lack of reactivity and polarity leads to low compatibility with other materials (e.g. glass and natural fibres) [14, 15]. In polyolefin based composite materials, maleic anhydride (MAH), illustrated in Figure 4.5, grafted polyolefins (MAPOs) have been widely used to improve the compatibility between the polyolefin matrix and polar materials, such as polyamides, glass, metals and natural materials [15–17]. The mechanisms and methods of grafting MAH onto polyolefins have been extensively studied [14, 16, 18–25]. The process can take place while the polyolefin is in molten state, in an extruder or batch mixer, in a solution and in solid state [18]. The ability of MAPOs of bridging polar and non-polar materials, along with their economical production, have made them successful polymer coupling agents [15].

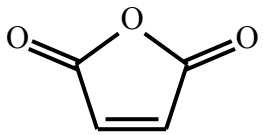

Figure 4.5: Maleic anhydride structure. Based on [18].

4.1.4 Injection moulding of polypropylene and polyethylene

PP and PE can be shaped into different products by multiple fabrication processes [7, 13]. Most of these processes, such as extrusion, injection moulding and blow moulding, include the phases of melting, homogenising, shaping, and cooling to room

temperature. The process of extrusion of PP and PE into pellets is a preliminary step in blow moulding and injection moulding.

The injection moulding of PP and PE consist of a sequence of simple steps [7]. The typical injection moulded machine is illustrated in Figure 4.6. The polymer is fed into the machine through the feed hopper. In the extrusion screw, the polymer resin is melted and homogenised. Thereafter, it is injected into a closed cold mould or die, which defines the final shape of the produced part. After the material is cooled to a solid state, the mould is opened and the part is extracted.

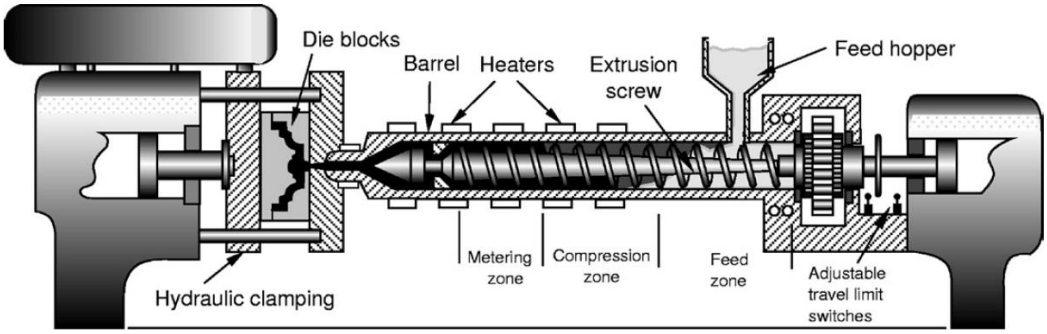

Figure 4.6: Typical injection moulding machine, [26].

4.2 Experimental

4.2.1 Materials

All polymers were supplied by SABIC. In terms of PPs, homopolymer SABIC® PP 579S and copolymer SABIC® PP 513MNK10 with a melt flow rate (MFR) (230 °C and 2.16 Kg) of 47 and 70 g/10 min respectively, were analysed. Maleic anhydride grafted polypropylene (MAPP) Exxelor^{TM} PO 1020 (maleic anhydride content is typically in the range of 0.5 to 1 wt%), with a MFR (230 °C and 2.16 Kg) of 430 g/10 min, was used as modifier/coupling agent.

In the case of LDPE, SABIC® LDPE 1922SF with a MFR (190 °C and 2.16 Kg) of 22 g/10 min. Maleic anhydride modified high density polyethylene (MAPE) POLYBOND® 3029 by ADDIVANT (maleic anhydride content is typically in the range of 1.5 to 1.7%), with a MFR (190 °C and 2.16 Kg) of 4 g/10 min, was used as a modifier/coupling agent.

4.2.2 Injection moulded bars for thermomechanical analysis, tensile and impact testing

Formulations of both PPs (homopolymer and copolymer) with their respective 5 wt% MAPP modifications were made by SABIC. These formulations were then melt mixed between 180-200 °C using an intermeshing, twin screw extruder of Coperion make (Model ZSK-25). A 25 mm screw diameter was used for compounding and screw rotation was maintained at 300 revolutions per minute (RPM) during the melt mixing. All the formulations were extruded into strands, which subsequently were cut into cylindrical shaped pellets using an inline strand cutter. Compounded pellets were dried at 80°C for a minimum of 4 hours in a hot air circulated oven. Subsequently, pellets were injection moulded into standard test (ISO 527-2/1A/1 [27] and ISO 179-1:2010 [28]) specimens using LT Demag 100 ton injection moulding machine of L&T Make. Barrel zones were electrically heated and were maintained between 180-200 °C and the screw speed was 80 RPM. The mould was maintained at ambient temperature.

In the case of LDPE and MAPE modification, the formulation was melt mixed at a lower temperature (maximum temperature of 180 °C). Regarding the injection moulding of pellets, the maximum temperature in the barrel zone was also significantly lower (170 °C) in comparison with PP.

4.2.3 Thermogravimetric analysis

A *TA instruments* Q50 TGA was used to analyse the thermal stability of PP 579S, PP 513MNK10 and LDPE 1922SF along with their respective MAPP and MAPE modifications. The thermogravimetric analysis (TGA) were carried out under nitrogen gas flow (60 $ml \cdot min^{-1}$) in two different configurations. Firstly, a dynamic heating profile was established as a ramp, defined with a heating rate of 10 $°C \cdot min^{-1}$, reaching a maximum temperature at 600 °C. The temperature set up of the second set of experiments, was defined by an initial ramp, followed by an isothermal region and a secondary ramp. As in the previous configuration, both ramps had a heating rate of 10 $°C \cdot min^{-1}$, while the isothermal degradation was established at 200 °C.

4.2.4 Thermomechanical analysis

A *TA instruments* TMA Q400 was used to analyse the thermal expansion of PP 579S, PP 513MNK10 and LDPE 1922SF along with their respective MAPP and MAPE modifications. The thermomechanical analysis (TMA) were carried out under nitrogen gas flow (50 ml·min^{-1}). The coefficient of linear thermal expansion (CLTE) of PP579S, PP513MNK10 and LDPE 1922SF with their respective 5 wt% maleic anhydride modified polymer were measured according to ISO 11359-1,2 [29, 30]. Three specimens of each sample were prepared from injection moulded impact bars. The specimens were rectangular with approximate dimensions of 10 x 5 mm and a thickness of approximately 4 mm. A constant force of 0.1 N was applied during the experiment. The temperature variation was established as the sequence illustrated in Table 4.1, where the preconditioning of each specimen is included in the experiment. The thermal expansion measurements were taken in the last heating cycle (i.e. number 6 in Table 4.1).

Number	TMA Sequence
1	Isothermal for 10 min.
2	Ramp at 5 °C·min.$^{-1}$ to -60 °C
3	Ramp at 5 °C·min.$^{-1}$ to 100 °C
4	Isothermal for 5 min
5	Ramp at 5 °C·min.$^{-1}$ to -60 °C
6	Ramp at 5 °C·min.$^{-1}$ to 100 °C

Table 4.1: TMA sequence for thermal expansion measurements.

The CLTE (α) is defined in (4.1), where L is the length of the sample, T is the temperature, and L_0 is the initial length of the specimen at room temperature.

$$\alpha = \frac{dL}{dT}\frac{1}{L_0} \tag{4.1}$$

4.2.5 Tensile testing

Tensile testing of injection moulded bars was carried out according to ISO 527-2/1A/1 [27], using an Instron 5969 with a 50 KN load cell. Five samples were

characterised for each set. All results are illustrated with error bars representing 95% confidence limits.

4.2.6 Impact testing

Notched and un-notched charpy impact strength were measured at room temperature according to ISO 179-2 [31] with edgewise impact using a Tinius Olsen Model Impact 503. Notched samples were manufactured based on ISO 179-1/1eA [28]. Ten samples were characterised for each set. All results are illustrated with error bars representing 95% confidence limits.

4.3 Results and discussion

4.3.1 TGA of PP, LDPE and maleic anhydride modifications

The thermal stability of PP and PE based polymers was investigated through TGA studies. The mass losses of PP based polymers, under nitrogen atmosphere, are illustrated in Figure 4.7. The mass losses of PE based polymers are represented in Figure 4.8. The peaks of the derivative of thermogravimetric analysis (DTG) for all the degradation studies are illustrated in Table 4.2. Degradation curves showed that PP 579S (homopolymer) and PP 513MNK10 (copolymer) have very similar thermal behaviour. DTG peaks are equivalent for all PP based components. However, in the case of Exxelor PO 1020, as observed in the TG curve, the degradation was higher, with significant degradation at relatively low temperatures.

Polymer	DTG Peak temperature [°C]
PP 579S	458
PP 513MNK10	458
Exxelor^{TM} PO 1020	458
LDPE 1922SF	476
LDPE 1922SF + 5% MAPE	473

Table 4.2: Polymers DTG peaks.

Polymer	Δ Weight 0-40 min [%]
PP 579S	0.26
PP 579S + 5% MAPP	0.27
PP 579S + 10% MAPP	0.29
PP 513MNK10	0.19
PP 513MNK10 + 5% MAPP	0.26
PP 513MNK10 + 10% MAPP	0.32
MAPP (Exxelor™ PO 1020)	1.6

Table 4.3: Weight loss in isothermal degradation studies at 200 °C.

In the case of PE based polymers, the evaluation of LDPE 1922SF and MAPE modified version showed the higher stability of these polymers in comparison with the evaluated PP based polymers. The MAPE modified LDPE showed a clear "shoulder" in the DTG peak which may indicate that the degradation of POLYBOND® 3029 takes place at slightly lower temperatures. This effect is also observed in the slight shift of the DTG peak to a lower temperature.

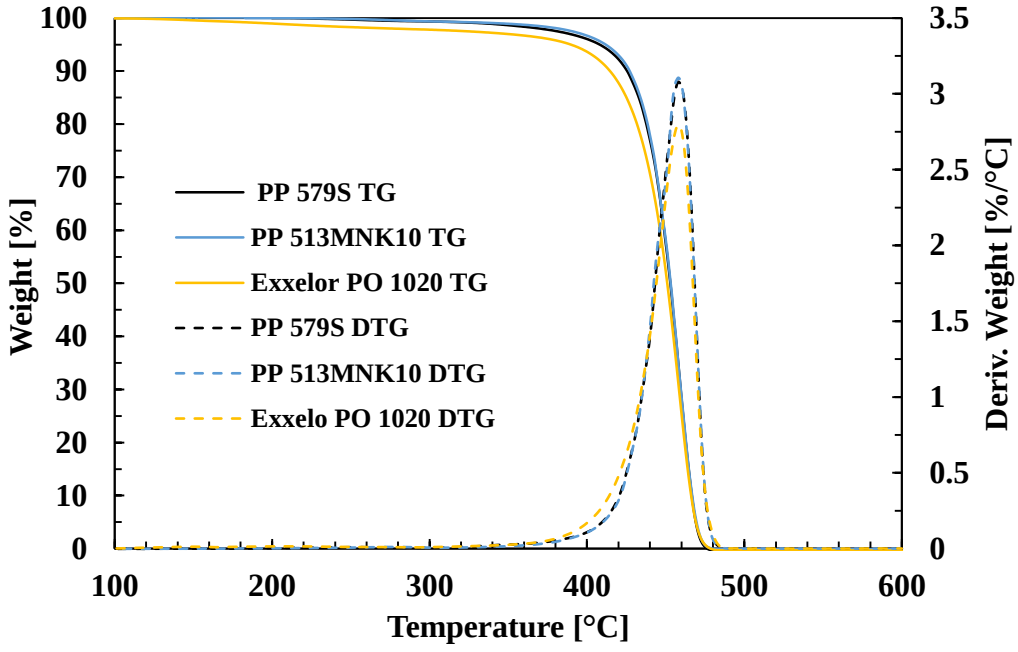

Figure 4.7: Thermo-gravimetric degradation of PP579S, PP513MNK10 and Exxelor™ PO 1020, under nitrogen atmosphere, at the heating rate of 10 °C·min^{-1}.

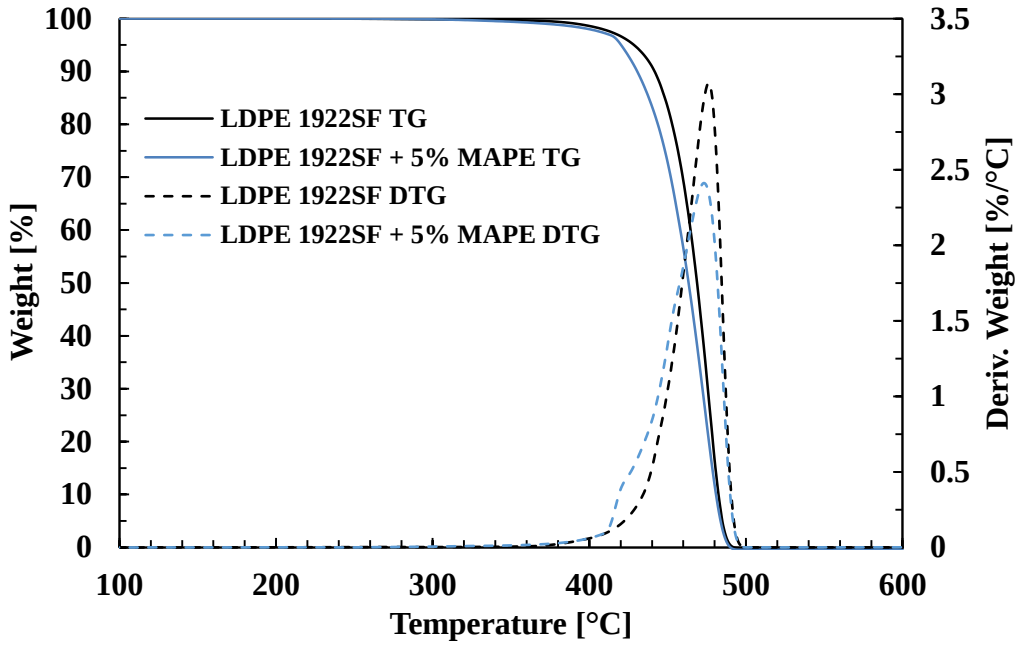

Figure 4.8: Thermo-gravimetric degradation of LDPE 1922SF and LDPE 1922SF+5% POLYBOND® 3029, under nitrogen atmosphere, at the heating rate of 10 °C·min^{-1}.

4.3.2 TMA of PP, LDPE and maleic anhydride modifications

The thermal expansion of injection moulded PP and PE based polymers was investigated through TMA studies. The TMA results for CLTE (α) of all the polymers along with the maleic anhydride modifications, for the range -50 to 90 °C, are illustrated in Figure 4.9 and Figure 4.10. The results are in agreement with CLTE values found in literature for PP and LDPE [1, 7, 8, 13, 32].

From Figure 4.9 and Figure 4.10, it can be seen that the addition of maleic anhydride does not significantly affect the average value of α. Therefore, in terms of CLTE, non-modified and modified polymers can be considered as equivalent. In the case of PP based polymers, the impact copolymer (PP 513MNK10) showed a slightly higher CLTE due to the presence of inclusions such as EPR, which contribute to the overall increase of the CLTE. It can also be seen from Figure 4.10 that the glass transition temperature (T_g) of PP is in the region of -10 °C.

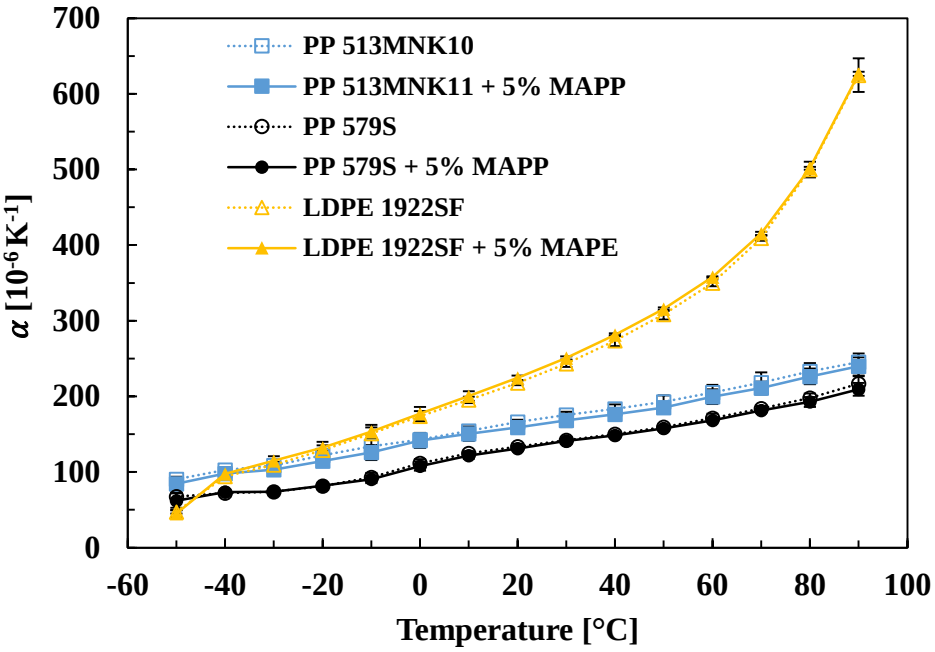

Figure 4.9: α versus temperature for PP and LDPE polymers.

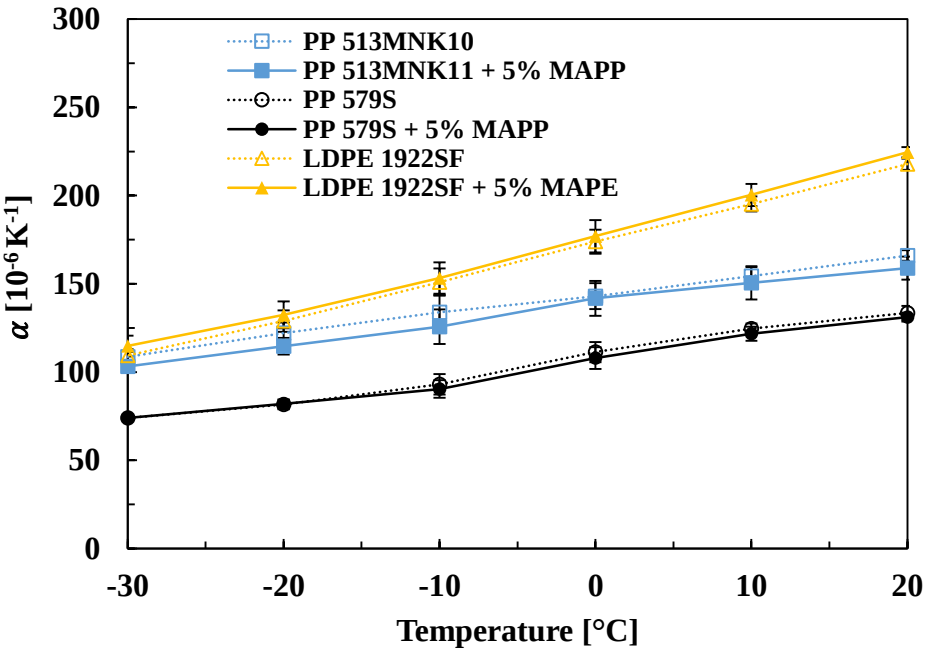

Figure 4.10: Detailed α versus temperature for PP and LDPE polymers.

4.3.3 Mechanical characterisation of injection moulded polymers

4.3.3.1 Tensile properties

The tensile properties of injection moulded polymers are illustrated in Figure 4.11, Figure 4.12 and Table 4.4. The Young's modulus of the PP homopolymer (i.e. PP579S) is slightly higher than the PP copolymer (i.e. PP513MNK10) and significantly higher than the LDPE, as illustrated in Figure 4.11. The addition of maleic anhydride grafted polymer (MAPP and MAPE) led, in the case of the three polymers, to a slight increase of the average Young's modulus. However, two-sample *t*-tests of average Young's modulus values of the polymer and its respective maleic anhydride modified version showed no significant difference at 95% confidence limits for any of the analysed polymers.

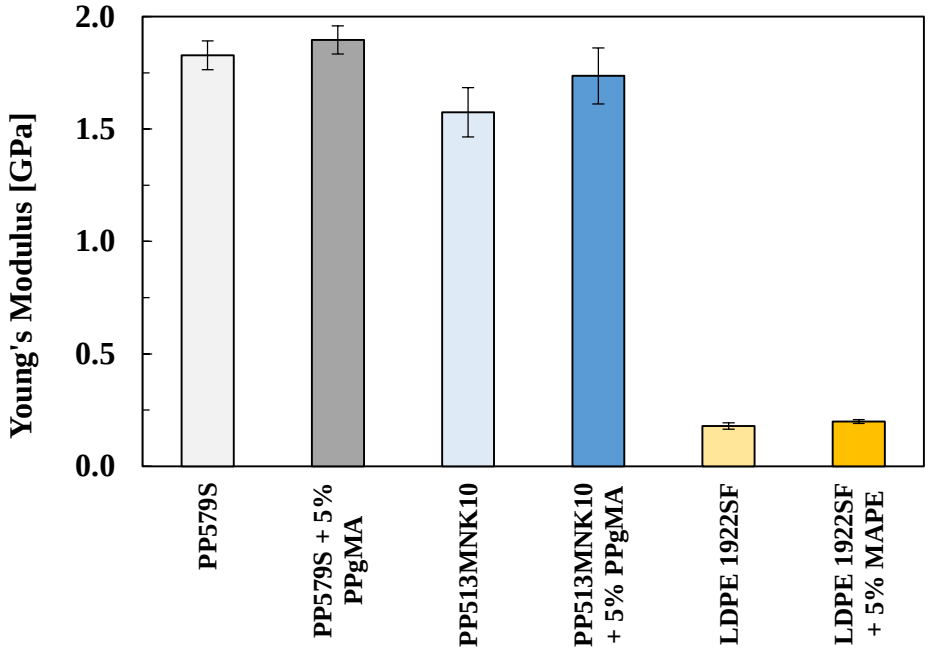

Figure 4.11: Young's modulus of injection moulded polymers.

In the case of the stress at maximum load, the effect of adding maleic anhydride grafted polymer is not consistent for all the polymers. The average tensile stress increased in the case of PP homopolymer and LDPE, and decreased in the case of copolymer. Two-sample *t*-tests of the average values indicated that there is a significant difference in the case of the PP homopolymer and PP copolymer at 95%

confidence limits (*p*-values = 0.010 for PP homopolymer and 0.044 for PP copolymer). On the other hand, the difference was not significant in the case of LDPE.

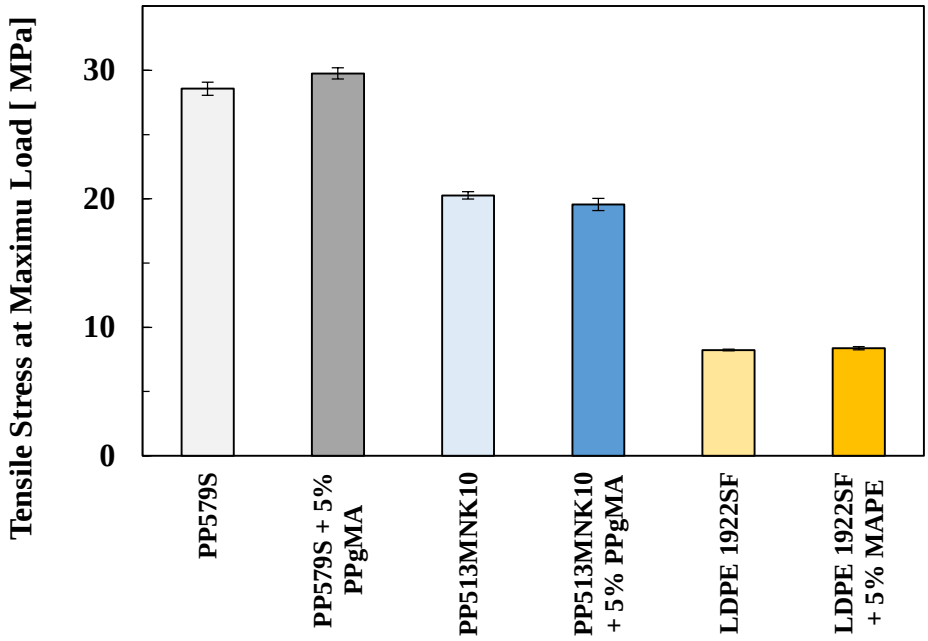

Figure 4.12: Tensile strength of injection moulded polymers.

Regarding the strain at maximum load, the addition of maleic anhydride grafted polymer led to a decrease of the average values in the case of the PP copolymer and LDPE. This decrease was significant at 95% confidence limits (*p*-values = 0.012 for PP copolymer and 0.043 for LDPE). In the case of PP homopolymer, no significant difference was observed.

In the case of the PP homopolymer and LDPE, the effects on the mechanical properties, indicate that MAPOs may act as nucleating agents, which could explain the slight increase in the average Young's modulus and tensile strength. However, the increase of average values was not significant in terms of Young's modulus due to the reduced number of specimens analysed (only 5 specimens are required by ISO 527-2/1A/1). For PP copolymer, an increase of the Young's modulus is observed but, at the same time, the tensile strength decreased. The addition of MAPP may have led to a different interaction between PP and other blended components, such as EPR and PE-inclusions, which ultimately translated into a slight reduction of the average tensile strength.

Sample	Young's Modulus [GPa]		Tensile Stress at Maximum Load [MPa]		Tensile Strain at Maximum Load [%]	
	Mean	95% Confidence limits	Mean	95% Confidence limits	Mean	95% Confidence limits
PP579S	1.827	0.064	28.6	0.5	8.0	0.9
PP579S + 5% MAPP	1.896	0.063	29.8	0.4	8.0	0.3
PP513MNK10	1.574	0.110	20.3	0.3	4.2	0.1
PP513MNK10 + 5% MAPP	1.736	0.125	19.6	0.5	2.4	0.1
LDPE 1922SF	0.179	0.015	8.2	0.1	136.4	20.9
LDPE 1922SF + 5% MAPE	0.199	0.008	8.4	0.1	106.0	7.3

Table 4.4: Tensile properties of injection moulded polymers.

4.3.3.2 Impact properties

The notched and un-notched charpy impact strength of injection moulded PP and PE based polymers was investigated at room temperature. In the case of PE based polymers, it was not possible to measure any impact strength due to the issue illustrated in Figure 4.13. The relatively low stiffness of the LDPE specimen allow the specimens to bend and go through the gauge length between the specimen's supports when hit by the striker.

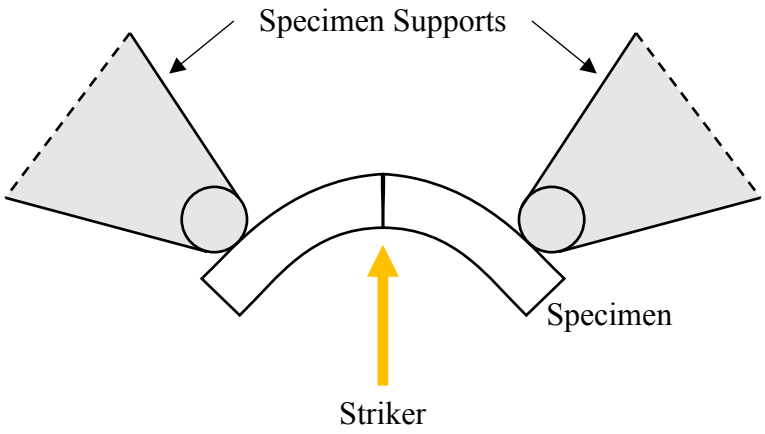

Figure 4.13: Charpy impact test diagram.

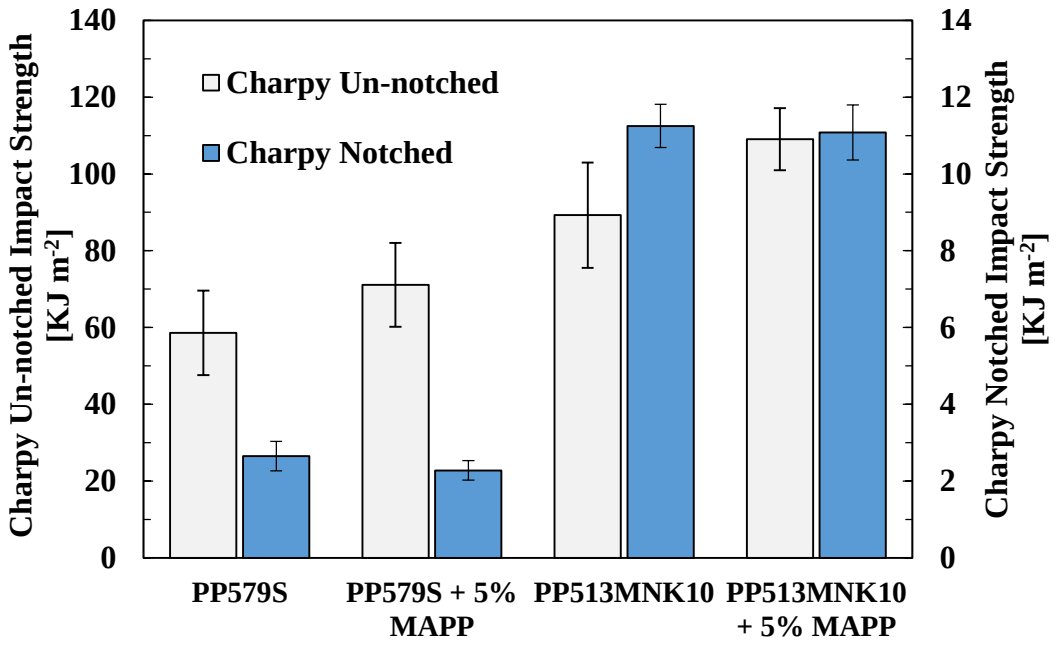

Figure 4.14: Charpy un-notched and notched impact strength of pure PP polymers.

Un-notched and notched charpy impact strength results of injection moulded PP are illustrated in Figure 4.14 and Table 4.5. As it was expected, the PP copolymer (PP 513MNK10) showed higher un-notched and notched impact strength in comparison with PP homopolymer. In relation to PP homopolymer, a 52% increase for un-notched and 315% increase for notched, was observed for PP copolymer.

The addition of 5 wt% MAPP, in the case of both homopolymer and copolymer, led to an increase of the average un-notched impact strength (21% increase for hopolymer and 22% for PP copolymer) and a decrease of the notched impact strength (14% decrease for PP homopolymer and 0.8% decrease for PP copolymer). A two-sample *t*-test of the average un-notched impact strength values of PP copolymer and respective MAPP modified version, showed a significant difference at 95% confidence level (*p*-value = 0.028). On the other hand, two-sample *t*-test of average notched impact strength values showed no significant difference at 95% confidence level (*p*-value = 0.028). In the case of PP 579S, t-tests revealed no significant difference at 95% confidence level between non-modified and modified polymer in terms of un-notched and notched impact strength (*p*-values = 0.131 for un-notched and 0.132 for notched impact strength). These results indicate that the addition of MAPP, in the case of PP

copolymer (no significant increase in the case of PP homopolymer), increased the energy required to initiate a crack.

Sample	Charpy Un-Notched [KJ m^{-2}]		Charpy Notched [KJ m^{-2}]	
	Mean	95% Confidence limits	Mean	95% Confidence limits
PP579S	58.6	11.0	2.7	0.4
PP579S + 5% MAPP	71.1	10.9	2.3	0.3
PP513MNK10	89.3	13.7	11.2	0.6
PP513MNK10 + 5% MAPP	109.0	8.1	11.1	0.7

Table 4.5: Charpy un-notched and notched impact strength.

4.4 Conclusions

The series of thermal analysis showed that the thermal stability of maleic anhydride grafted polyolefins (MAPOs) is relatively lower than the non-modified polyolefins. In the case of polypropylene (PP) based polymers, the homopolymer and copolymer showed similar thermal behaviour. The thermal expansion of PP homopolymer and copolymer, and LDPE was analysed along with the respective 5 wt% MAPO (i.e. MAPP or MAPE) modifications. The addition of MAPP and MAPE did not show any significant difference over the non-modified polymer. Above 0 °C, the coefficient of linear thermal expansion (CLTE) was in the case LDPE, consistently the highest, while for PP homopolymer was the lowest.

In terms of tensile properties, the Young's modulus of PP homopolymer was the highest and LDPE the lowest. The addition of 5 wt% MAPOs led to a (non-significant) slight increase of the average values. In the case of the tensile stress at maximum load, PP homopolymer showed the highest average value, while LDPE the lowest. In this case, the effects of MAPOs were not consistent, increasing the average values of PP homopolymer and LDPE, and decreasing the average value of PP copolymer (the variation for PP homopolymer and copolymer was significant). The LDPE strain at maximum load was the highest, PP copolymer being the lowest. The addition of MAPOs led to a significant decrease of PP copolymer and LDPE average values, while no change was observed in the case of PP homopolymer.

Regarding the impact properties, as expected, the PP copolymer showed a higher notched and un-notched impact strength when compared with PP homopolymer. The addition of 5 wt% MAPP led to an increase of un-notched impact strength of approximately 20% in the case of both PPs. However, this increase was only significant in the case of PP copolymer. The increase of the average values indicate that the MAPP increased the energy required to initiate a crack.

4.5 References

1. Biron, M.: Thermoplastics and thermoplastic composites. William Andrew (2012).
2. Nabi Saheb, D., Jog, J.P.: Natural fiber polymer composites: A review. Adv. Polym. Technol. 18, 351–363 (1999).
3. Thomason, J.L.: The influence of fibre length and concentration on the properties of glass fibre reinforced polypropylene: 6. The properties of injection moulded long fibre PP at high fibre content. Compos. Part A Appl. Sci. Manuf. 36, 995–1003 (2005).
4. Shubhra, Q.T., Alam, A.K.M.M., Quaiyyum, M.A.: Mechanical properties of polypropylene composites: A review. J. Thermoplast. Compos. Mater. 26, 362–391 (2011).
5. Ku, H., Wang, H., Pattarachaiyakoop, N., Trada, M.: A review on the tensile properties of natural fiber reinforced polymer composites. Compos. Part B Eng. 42, 856–873 (2011).
6. Brydson, J.A.: Plastics materials. Butterworth-Heinemann (1999).
7. Maier, C., Calafut, T.: Polypropylene: The Definitive User's Guide and Databook. William Andrew (1998).
8. Karger-Kocsis, J.: Polypropylene structure, blends and composites. Volume 1 Structure and Morphology. Chapman & Hall (1995).
9. Rösler, J., Harders, H., Bäker, M.: Mechanical behaviour of engineering materials: metals, ceramics, polymers, and composites. Springer Science & Business Media (2007).
10. Gahleitner, M., Grein, C., Kheirandish, S., Wolfschwenger, J.: Nucleation of polypropylene homo- and copolymers. Int. Polym. Process. 26, 2–20 (2011).
11. Halpin, J.C., Kardos, J.L.: Moduli of crystalline polymers employing composite theory. J. Appl. Phys. 43, 2235–2241 (1972).
12. Karger-Kocsis, J.: Polypropylene structure, blends and composites. Volume 2 Copolymers and Blends. Chapman & Hall (1995).
13. Peacock, A.: Handbook of polyethylene: structures: properties, and applications. CRC Press (2000).
14. Henry, G.R.P., Drooghaag, X., Rousseaux, D.D.J., Sclavons, M., Devaux, J.,

Marchand-Brynaert, J., Carlier, V.: A Practical Way of Grafting Maleic Anhydride onto Polypropylene Providing High Anhydride Contents Without Sacrificing Excessive Molar Mass. J. Polym. Sci. Part A Polym. Chem. 46, 2936–2947 (2008).

15. Keener, T.J., Stuart, R.K., Brown, T.K.: Maleated coupling agents for natural fibre composites. Compos. Part A Appl. Sci. Manuf. 35, 357–362 (2004).
16. Heinen, W., Rosenmöller, C.H., Wenzel, C.B., de Groot, H.J.M., Lugtenburg, J.: 13 C NMR Study of the Grafting of Maleic Anhydride onto Polyethene , Polypropene , and Ethene-Propene Copolymers. Macromolecules. 29, 1151–1157 (1996).
17. Wambua, P., Ivens, J., Verpoest, I.: Natural fibres: Can they replace glass in fibre reinforced plastics? Compos. Sci. Technol. 63, 1259–1264 (2003).
18. Moad, G.: Synthesis of polyolefin graft copolymers by reactive extrusion. Prog. Polym. Sci. 24, 81–142 (1999).
19. Li, C., Zhang, Y., Zhang, Y.: Melt grafting of maleic anhydride onto low-density polyethylene/polypropylene blends. Polym. Test. 22, 191–195 (2003).
20. Lu, B., Chung, T.C.: Synthesis of maleic anhydride grafted polyethylene and polypropylene, with controlled molecular structures. J. Polym. Sci. Part A Polym. Chem. 38, 1337–1343 (2000).
21. Machado, A. V., Covas, J.A., Van Duin, M.: Effect of polyolefin structure on maleic anhydride grafting. Polymer (Guildf). 42, 3649–3655 (2001).
22. Qiu, W., Endo, T., Hirotsu, T.: A novel technique for preparing of maleic anhydride grafted polyolefins. Eur. Polym. J. 41, 1979–1984 (2005).
23. Gaylord, N.G., Mehta, R., Mohan, D.R., Kumar, V.: Maleation of linear low-density polyethylene by reactive processing. J. Appl. Polym. Sci. 44, 1941–1949 (1992).
24. Yang, L., Zhang, F., Endo, T., Hirotsu, T.: Microstructure of maleic anhydride grafted polyethylene by high-resolution solution-state NMR and FTIR spectroscopy. Macromolecules. 36, 4709–4718 (2003).
25. Bettini, S.H.P., Agnelli, J.A.M.: Grafting of maleic anhydride onto polypropylene by reactive processing. I. Effect of maleic anhydride and peroxide concentrations on the reaction. J. Appl. Polym. Sci. 74, 247–255 (1999).
26. Swift, K.G., Booker, J.D.: Manufacturing Process Selection Handbook: From Design to Manufacture. Butterworth-Heinemann (2013).
27. ISO 527-2, Plastics — Determination of tensile properties — Part 2 : Test conditions for moulding and extrusion plastics. (2012).
28. ISO 179-1, Plastics — Determination of Charpy impact properties — Part 1 : Non-instrumented impact test. (2010).
29. ISO 11359-1, Plastics — Thermomechanical analysis (TMA) — Part 1 : General principles. (2014).
30. ISO 11359-2, Plastics — Thermomechanical analysis (TMA) — Part 2 :

Determination of coefficient of linear thermal expansion and glass transition temperature. (1999).

31. ISO 179-2, Plastics — Determination of Charpy impact properties — Part 2 : Instrumented impact test. (1999).

32. Thomason, J.L., Groenewoud, W.M.: The influence of fibre length and concentration on the properties of glass fibre reinforced polypropylene: 2. Thermal properties. Compos. Part A Appl. Sci. Manuf. 27, 555–565 (1996).

Chapter 5 Mechanical characterisation of the coir-thermoplastic interface

5.1 Introduction / Literature review

Composite materials are formed by the combination of two or more different constituents, which allows to take advantage of the different properties of matrix and reinforcement materials. In this process, an interface between reinforcement and matrix is created. The analysis and understanding of the interfacial region is key to the successful development of composite materials [1–4]. In this regard, the *interface* can be defined as the surface formed by the common boundary between the reinforcement and the matrix [2], which both bonds the constituents and transfers load between them. In addition to this definition, the *interphase* is defined as the finite volume, including the previously defined *interface* region, in which the properties vary between those of the reinforcement and matrix material.

5.1.1 Bonding mechanisms

5.1.1.1 Adsorption and wetting

Wetting takes place when two bodies come into contact at an atomic scale, by bringing them close to each other (generally one of the bodies is in liquid state) [1]. In this case, adhesion is mainly caused by van der Waals forces, although other types of bonding may be present. In the case of a solid – solid interaction, illustrated in Figure 5.1 (a), the contact area is limited to the regions where the asperities touch, generally leading to very low levels of bond strength. On the other hand, in the liquid – solid scenario, illustrated in Figure 5.1 (b), close contact can be established. The Dupré equation, illustrated in (2.36), defines the work of adhesion, W_a, in terms of surface energies, γ (S, L and V refers to solid, liquid and vapour, respectively) [1, 2].

$$W_a = \gamma_{SV} + \gamma_{LV} + \gamma_{SL} \tag{5.1}$$

The contact angle θ or equilibrium wetting is obtained by the balance of horizontal forces, illustrated in Figure 5.1 (b), through the Young equation, (5.2).

$$\gamma_{SV} = \gamma_{SL} + \gamma_{LV} \cos\theta \tag{5.2}$$

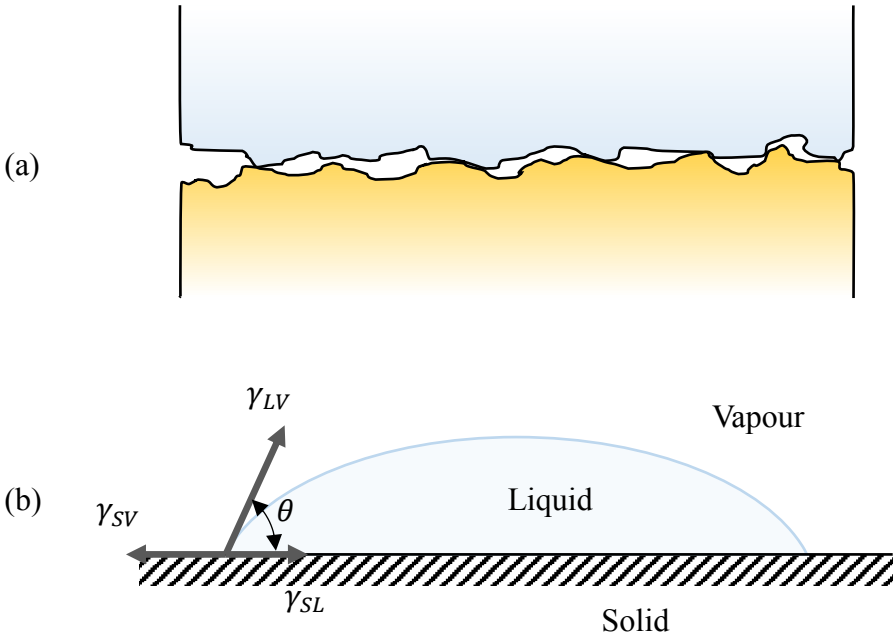

Figure 5.1: (a) Weak adhesion between two rigid rough surfaces due to isolated contact points. (b) Contact angle θ and surface energies γ for a liquid drop on a solid surface. Based on [1].

5.1.1.2 Interdiffusion and chemical reaction

The bond between two surfaces may be created by the interdiffusion of atoms or molecules across the interface [2]. Different types of diffusional phenomena, which increase adhesion, may take place at the interface, such as diffusion of free polymer chain ends, ultimately leading to chain entanglement [1, 2], illustrated in Figure 5.2 (a). On the other hand, chemical reactions may occur at the interface, promoting the adhesive strength, Figure 5.2 (b).

5.1.1.3 Electrostatic attraction

If the surfaces carry net electrical charges of opposite sign, as illustrated in Figure 5.2 (c), then an adhesive force may be created [1, 2], which will depend on the density of the charge. However, these forces are unlikely to be a major contributor to the total strength of the interface.

5.1.1.4 Mechanical keying / interlocking

Considering that good wetting has occurred, the surface roughness may be a contributor to the strength of the interface [1, 2], as illustrated in Figure 5.2 (d). Due to the geometrical configuration, this effect is expected to be more significant under shear loading.

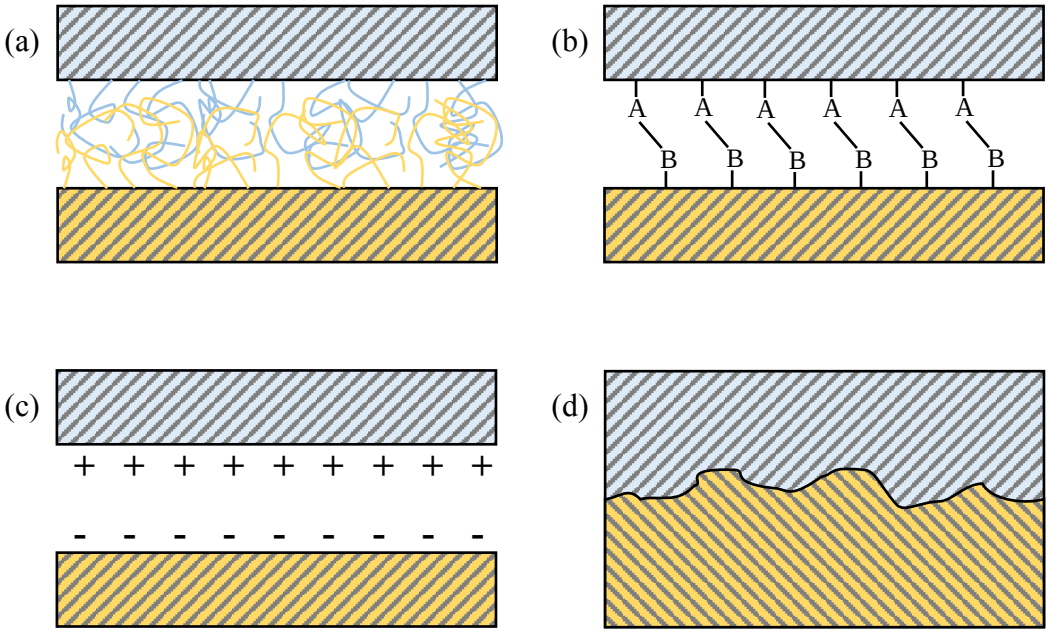

Figure 5.2: Interface bonds formed by (a) molecular entanglement following interdiffusion, (b) chemical reaction, (c) electrostatic attraction, and (d) mechanical keying / interlocking. Based on [1].

5.1.1.5 Residual stresses

The nature of the interfacial interactions is highly influenced by the existence of residual stresses [1, 2, 4]. These stresses may arise from different sources, but mainly from thermal contraction, due to the difference in the thermal expansion coefficients of the matrix and reinforcement materials. The normal stresses across the interface are compressive in nature when, as in most cases, the fibre has a lower coefficient of thermal expansion than the matrix. Several authors have commented on the importance of residual stresses on fibre reinforced polymer systems [5–13]. The radial stresses, σ_r, for an isotropic fibre and matrix, due to the thermal shrinkage can be calculated according to (5.3), as used by Thomason et al. [11, 13], based on the work by Raghava [14], where α is the thermal expansion coefficient, ΔT is the difference between the

stress free temperature and testing temperature, E is the Young's modulus, ν is the Poisson ratio, V_f is the fibre's volume fraction, while the m subscript stands for matrix and f for fibre.

$$\sigma_r = \frac{(\alpha_m - \alpha_f)\Delta T E_f E_m}{(1 + \nu_f + V_f)E_f + (1 + \nu_m)E_m} \tag{5.3}$$

5.1.2 Experimental characterisation of the interfacial region

As previously mentioned, the nature of the interfacial bonding influences the elastic and fracture properties of the composite in different ways [1]. When analysing fibre reinforced composites, single-fibre experiments are normally used to investigate the interfacial bond strength. These micromechanical tests include four main categories: pull-out, microbond, fragmentation, and microindentation, as illustrated in Figure 5.3.

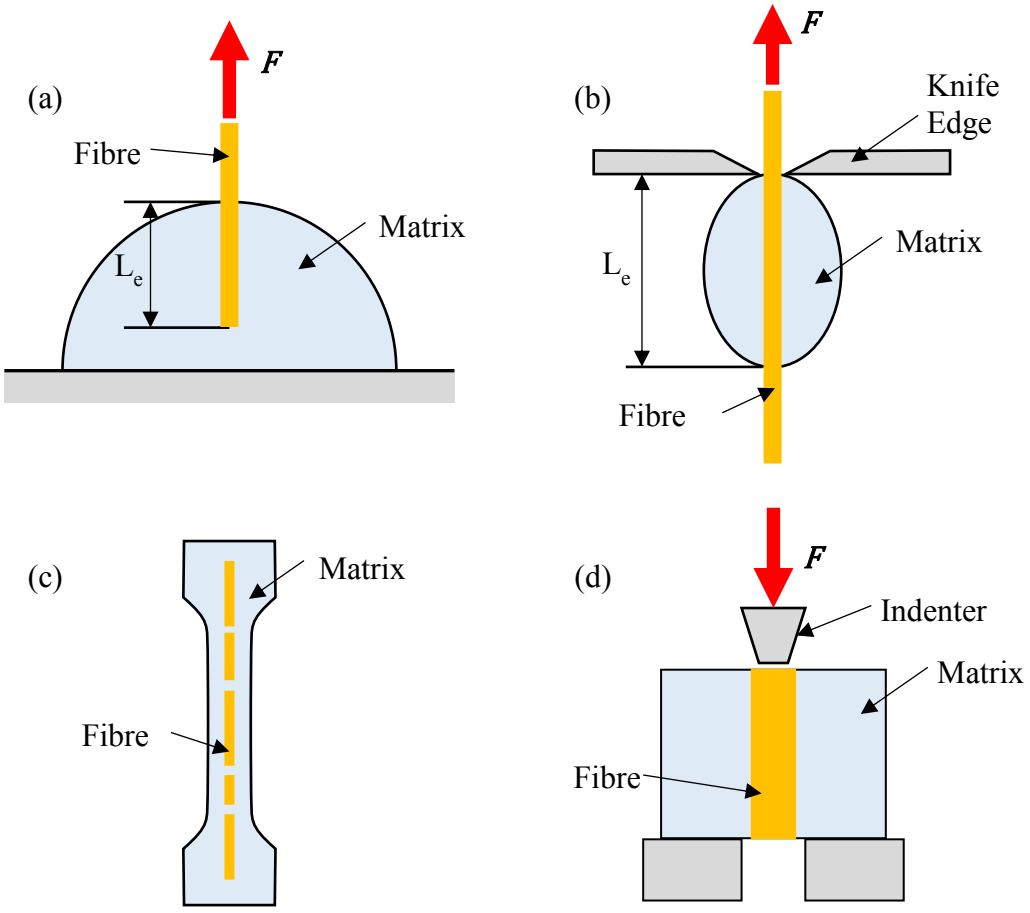

Figure 5.3: Micromechanical tests: (a) pull-out, (b) microbond, (c) fragmentation, and push-out.

The direct measurement of interfacial properties often rely on uncertain assumptions which could potentially lead to serious inaccuracies. The parameters that can affect the interfacial measurements have been long discussed in the literature [15–25], such as fibre diameter, embedded length, geometrical loading configuration or symmetry of the specimen. Moreover, most of these types of measurements involve shear debonding and consequent sliding. However, an interface exhibiting high shear debonding stress may not necessarily exhibit strong normal debonding stress. Therefore, it is necessary to take into consideration this factor when relating interfacial data to macroscopic composite behaviour. Furthermore, the fact that these tests are carried out in *artificial* single-fibre composites, which do not include neighbour fibres, may also lead to different results.

5.1.3 Theoretical models of interfacial failure in micromechanical tests

In the previously described experimental methods, the interface is characterised at the micro level [26], and is described in a variety of failure models that are later discussed. In the analysis of standard pull-out and microbond tests, the load applied to the fibre, force F, is recorded as a function of the extension of the fibre (or displacement of the end of the fibre) in relation to the restricted area of the specimen. The force-displacement curves of these two tests are very similar, due to the fact that the differences in the boundary conditions can often be neglected [26].

Two different force-displacement scenarios are schematically represented in Figure 5.4. Most of pull-out fibre-matrix systems behave in a similar manner to either curve A or B in terms of the debonding process. In the case of curve A, the fibre, which is assumed in this example to have a liner-elastic behaviour, is extended, while the fibre-matrix interface remains intact until the force reaches a maximum at F_{max} (i.e. $0 < F < F_{max}$). In this case, the debonding force, $F_{d,A}$, is equal to the maximum force. At this point, the fibre starts debonding, the crack propagates through the entire interface, and the force drops from F_{max} to F_b. From this moment, the remaining force is due to the frictional force between the fibre and matrix. Consequently, the force will drop to zero in a pull-out sample due to the reduction of the force as the fibre is pulled-

out from the matrix, and will remain constant in a microbond sample, where the total embedded length does not change.

In curve B, the initial region, as in the case of A, consists of a linear extension of the fibre, while the fibre-matrix remains intact. When the force reaches a critical debonding value, $F_{d,B}$, the fibre starts debonding, and there is a stable interfacial crack propagation for $F_{d,B} < F < F_{max}$. After the force reaches a maximum at F_{max}, as in the case of curve A, the crack propagation becomes unstable and propagates through the entire interface, which leads to the force dropping from F_{max} to F_b. If the test frame is stiff and the free fibre length is short, the system will tend to debond in a similar manner to curve B, where F_d can be easily discernible before the force reaches a maximum at F_{max} [27, 28].

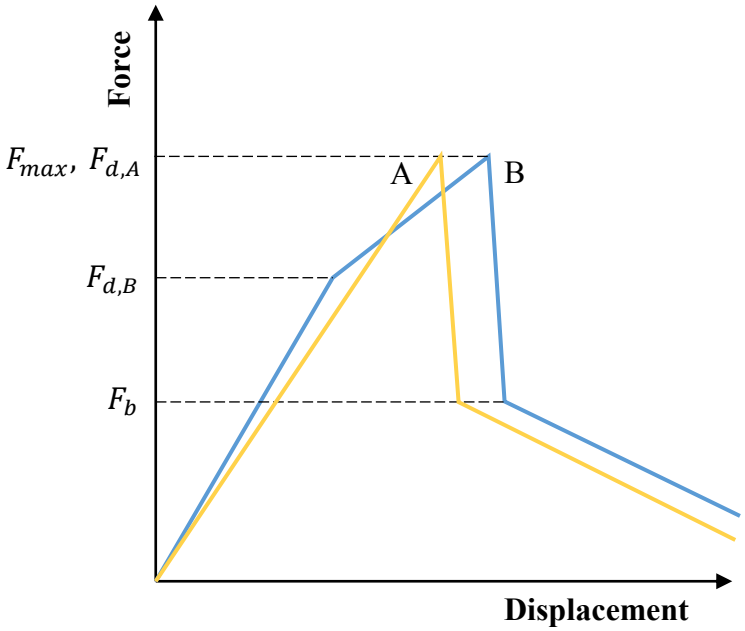

Figure 5.4: Schematic illustration of two different cases of a pull-out test.

In general terms, the interpretation and analysis of the pull-out test can be based on theoretical models that are normally categorised into three main groups: the shear stress controlled debonding, energy controlled debonding and adhesional pressure or normal stress debonding. In this regard, the most extended method to characterise the quality of the interfacial bonding/interaction is the apparent interfacial shear strength (apparent IFSS, τ_{app}), which is a shear stress controlled debonding. The concept of

IFSS is based on the ultimate shear stress (τ_{ult}), which establishes that the fibre debonds from the matrix at the point when the shear stress on the interface reaches the IFSS value. The definition of τ_{app}, as used by Kelly and Tyson [29, 30], is given by (5.4), where r is the fibre's radius and L_e is the embedded length. From the definition of the model, it can be seen how the τ_{app} model assumes a uniform distribution of interfacial shear stress at the debonding event.

$$\tau_{app} = \frac{F_d}{2\pi r L_e} \tag{5.4}$$

Although τ_{app} is a good approximation for some fibre-matrix systems, and represents a good indication to differentiate between "good" and "poor" adhesion or bond strength [26], it does rely on the assumption of uniform stress distribution along the interface. This assumption has been long discussed in literature, and several studies have shown how the stress distribution is not uniform at the interface, which leads to a dependency of the τ_{app} on different parameters, such as embedded length or fibre diameter [1, 3, 27, 31–33]. Attending to different authors, the debonding event takes place when the stress level at any local point of the interface reaches the τ_{ult} value. In this regard, the apparent and ultimate shear strength can be related in a general expression described in (5.5), [34, 35], where A is the embedded area.

$$\tau_{ult} = \lim_{A \to 0} \tau_{app} = \lim_{A \to 0} \frac{F_d}{2\pi r L_e} = \lim_{A \to 0} \frac{F_d}{A} \tag{5.5}$$

According to this expression, a precise characterisation of the fibre-matrix interface through micromechanical testing requires an approach which takes into consideration the local interfacial parameters.

5.1.3.1 Shear stress controlled debonding

As previously described, the distribution of stress in the interface is considered by many authors as not uniform. Originally formulated by Cox [36] and later developed by numerous authors, the shear lag model attempts to describe how the stress is transferred from the matrix to the fibre through interfacial shear stress, in an aligned

short fibre composite, Figure 5.5 and Figure 5.6. This idea was later used to analyse the pull-out test [3, 31, 37–40].

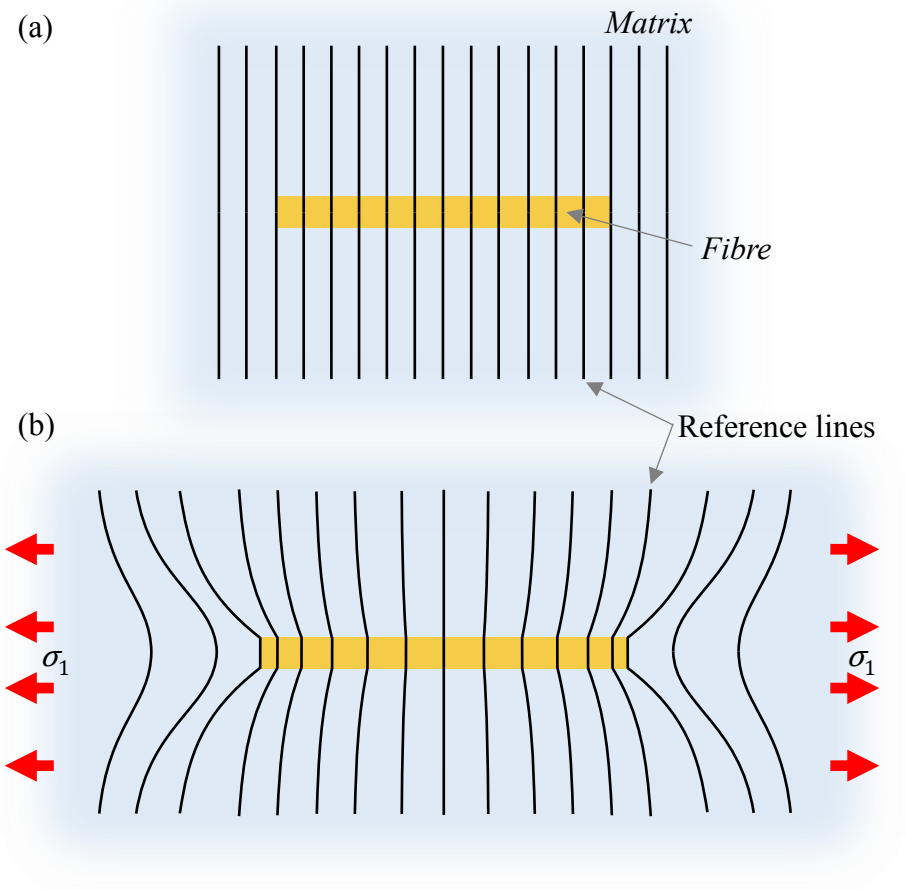

Figure 5.5: Schematic illustration of the shear lag model: (a) unstressed system, and (b) stressed system by applying tension parallel to the fibre. Based on [1].

The development analysed here are those by Greszczuk [3] and the equivalent showed by Hull and Clyne [1]. From the shear lag model, the radial variation of the shear stress (τ) within the matrix, is deduced by equating the shear forces on neighbouring annuli (with radius r_1 and r_2, and a length of dx) as illustrated in (5.6).

$$2\pi r_1 \tau_1 dx = 2\pi r_2 \tau_2 dx \rightarrow \frac{\tau_1}{\tau_2} = \frac{r_2}{r_1} \tag{5.6}$$

Therefore, the shear stress in the matrix (τ) at any radius (ρ), as illustrated in Figure 5.6, is related to the shear stress at the interface (τ_i) by (5.7).

$$\tau = \tau_i \left(\frac{r}{\rho}\right) \tag{5.7}$$

The increment of the displacement, du, when moving away from the fibre axis by $d\rho$, as illustrated in Figure 5.6, is dependent on the shear strain and therefore the shear modulus of the matrix, G_m, as showed in (5.8).

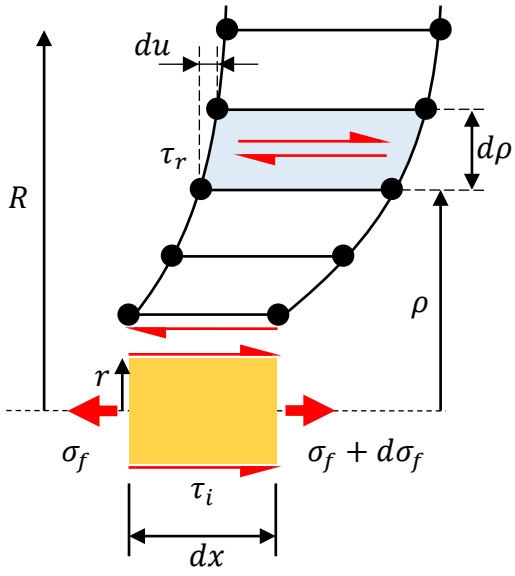

Figure 5.6: Schematic illustration of the shear lag model regarding the radial variation of the shear stress and strain in the matrix. Based on [1].

$$\begin{cases} \tau = \tau_i \left(\dfrac{r}{\rho}\right) \\ \dfrac{du}{d\rho} = \gamma = \dfrac{\tau}{G_m} \end{cases} \rightarrow \frac{du}{d\rho} = \frac{\tau_i}{G_m}\left(\frac{r}{\rho}\right) \tag{5.8}$$

The difference between the displacement of the matrix at a radius R, u_R, and that of the interface, u_r, at any given value of x, is given by the integration of (5.8), as illustrated in (5.9).

$$\int_{u_r}^{u_R} du = \frac{\tau_i r}{G_m}\int_r^R \frac{1}{\rho} d\rho \rightarrow (u_R - u_r) = \frac{\tau_i r}{G_m}\ln\left(\frac{R}{r}\right) \tag{5.9}$$

The equilibrium of forces acting on a cylindrical fibre element of length dx, is shown in (5.10) as in [1], or equivalent (5.11). F is defined as the force on the fibre at any point x, r is the radius of the fibre and τ_i is the interface shear stress.

$$2\pi r\tau_i dx = -\pi r^2 d\sigma_f \rightarrow \frac{d\sigma_f}{dx} = -\frac{2\tau_i}{r} \tag{5.10}$$

$$\frac{dF}{dx} = -2\pi r\tau_i \tag{5.11}$$

If it is assumed that there is no shear strain in the fibre and the interfacial adhesion between fibre and matrix is perfect (i.e. $u_f = u_r$, where u_f is the displacement of the fibre surface), then by substituting (5.9) into (5.11), (5.12) is obtained.

$$\frac{dF}{dx} = -\frac{2\pi G_m}{\ln\left(\frac{R}{r}\right)}(u_R - u_r) \tag{5.12}$$

The displacement conditions for the pull-out system are illustrated in (5.13) and (5.14). In (5.13), a perfectly bonded interface is established, while in (5.14) it is indicated that the matrix remains unstrained in the remote area from the interface (i.e. at a radius R).

$$\frac{du_r}{dx} = \varepsilon_f = \frac{F}{\pi r^2 E_f} \tag{5.13}$$

$$\frac{du_R}{dx} = 0 \tag{5.14}$$

The differentiation of (5.12) with respect to x, taking into consideration (5.13) and (5.14), is illustrated in (5.15).

$$\frac{d^2F}{dx^2} = \frac{2G_m}{r^2 E_f \ln\left(\frac{R}{r}\right)}F \tag{5.15}$$

By considering a parameter β as illustrated in (5.16), (5.15) can be solved as a differential equation showed in (5.17). The parameter β is a shear lag parameter defined as in [36].

$$\beta = \left(\frac{2G_m}{r^2 E_f \ln\left(\frac{R}{r}\right)}\right)^{\frac{1}{2}} \tag{5.16}$$

$$\frac{d^2F}{dx^2} - \beta^2 F = 0 \tag{5.17}$$

The general solution for (5.17) is illustrated in (5.18), where C_i are the constants of integration that can be obtained from the boundary conditions illustrated in (5.19). L_e is defined as the embedded length and F_d is the pull-out force exerted in the fibre outside the embedded area.

$$F = C_1 \sinh(\beta x) + C_2 \cosh(\beta x) \tag{5.18}$$

$$\begin{cases} x = 0, F = F_d \\ x = L_e, F = 0 \end{cases} \tag{5.19}$$

With these boundary conditions, the force at any point x, $F(x)$, is defined in (5.20). Therefore, the maximum force, which is obtained at the point $x = 0$, is F_d.

$$F(x) = F_d[\cosh(\beta x) - \coth(\beta L_e) \sinh(\beta x)] \tag{5.20}$$

The shear stress at any point x, $\tau_e(x)$, can be obtained by introducing (5.20) into (5.11), which results in (5.21). The shear stress is maximum at $x = 0$ (i.e. the point where the fibre enters the matrix), illustrated in (5.22).

$$\tau_e(x) = \frac{F_d \beta}{2\pi r}[\coth(\beta L_e) \cosh(\beta x) - \sinh(\beta x)] \tag{5.21}$$

$$\tau_{i\,max} = \frac{F_d \beta}{2\pi r} \coth(\beta L_e) \tag{5.22}$$

In addition to the shear stresses created by the action of pulling-out the fibre from the matrix, the analysis by Gorbatkina [34] considers the residual thermal stresses created by the difference of the coefficients of thermal expansion of matrix and fibre. These stresses are created by the contraction of the polymer parallel to the longitudinal axis of the fibre, as illustrated in Figure 5.7, and should not be mistaken with the residual stresses in the normal direction to the fibre across the interface (i.e. transversal direction), which are compressive in nature. The distribution of thermal stresses [21, 34] is given by (5.23), where α_m and α_f are the coefficients of thermal expansion of

the matrix and fibre respectively; and $\Delta T = T_r - T$, where T is the test temperature and T_r is the stress free temperature.

$$\tau_T(x) = \tau_{therm} \frac{\sinh\left[\beta\left(\frac{L_e}{2} - x\right)\right]}{\cosh\left(\beta\frac{L_e}{2}\right)} \tag{5.23}$$

$$\tau_{therm} = \frac{E_f}{2}\beta r(\alpha_m - \alpha_f)\Delta T \tag{5.24}$$

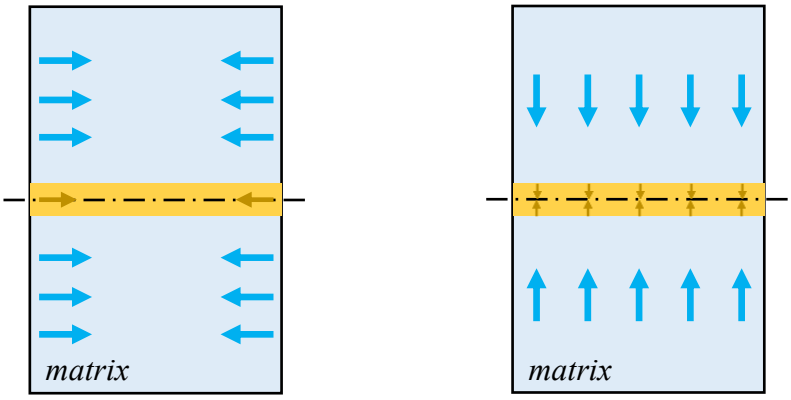

Figure 5.7: Main directions of thermal contraction.

The superposition of (5.21) and (5.23) leads to the equation (5.25), proposed by Zhandarov and Pisanova [21]. This approach has been extensively used to characterise fibre-matrix interfacial properties [26, 27, 33, 41–43].

$$\begin{aligned}\tau(x) = \cosh(\beta x)\left[\frac{F_d\beta}{2\pi r}\coth(\beta L_e) + \tau_{therm}\tanh\left(\beta\frac{L_e}{2}\right)\right] \\ - \sinh(\beta x)\left[\frac{F_d\beta}{2\pi r} + \tau_{therm}\right]\end{aligned} \tag{5.25}$$

This superposition function $\tau(x)$, reaches its maximum at $x = 0$, where $\tau(0) = \tau_{ult}$, illustrated in (5.26), [21].

$$\tau_{ult} = \frac{F_d\beta}{2\pi r}\coth(\beta L_e) + \tau_{therm}\tanh\left(\beta\frac{L_e}{2}\right) \tag{5.26}$$

By substituting (5.26) into the equation of the apparent IFFS (5.4), the relation between τ_{app} and the other parameters is obtained [35], (5.27).

$$\tau_{app} = \frac{\tanh(\beta L_e)}{\beta L_e}\left[\tau_{ult} - \tau_{therm}\tanh\left(\beta\frac{L_e}{2}\right)\right] \tag{5.27}$$

The superposition model illustrated in (5.25), can be adapted to show the force evolution, taking into consideration the crack length (a) and frictional stress in debonded areas (τ_f) [26, 28, 42], as illustrated in (5.28). The parameter τ_f is assumed to be independent of L_e and a.

$$\begin{aligned} F = f_s = \frac{2\pi r}{\beta}\Big\{&\tau_d\tanh[\beta(L_e - a)] \\ &- \tau_{therm}\tanh[\beta(L_e - a)]\tanh\left[\beta\frac{(L_e - a)}{2}\right] \\ &+ \beta a\tau_f\Big\} \end{aligned} \tag{5.28}$$

Regarding the shear lag parameter, β (5.16), used in the original approach by Cox [36], it has been shown that it does not give a valid calculation of stress transfer in concentric cylinder model calculations. The shear lag parameter originally derived by Nayfeh [44], and later by Nairn [45], illustrated in (5.29) is recommended [33, 42] for the analysis of pull-out data based on the previously described models, where G_f is the axial shear modulus of the fibre, and V_f and V_m are the volume fractions of the fibre and matrix, respectively. The expression of the V_f of a pull-out sample that is approximated by cylindrical fibre embedded in a cylindrical matrix as illustrated in Figure 5.8, is showed in (5.30), and $V_m = 1 - V_f$.

$$\beta = \left\{\frac{2}{r^2 E_f E_m}\left[\frac{E_f V_f + E_m V_m}{\frac{V_m}{4G_f} + \frac{1}{2G_m}\left(\frac{1}{V_m}\ln\frac{1}{V_f} - 1 - \frac{V_f}{2}\right)}\right]\right\}^{\frac{1}{2}} \tag{5.29}$$

$$V_f = \left(\frac{r}{R}\right)^2 \tag{5.30}$$

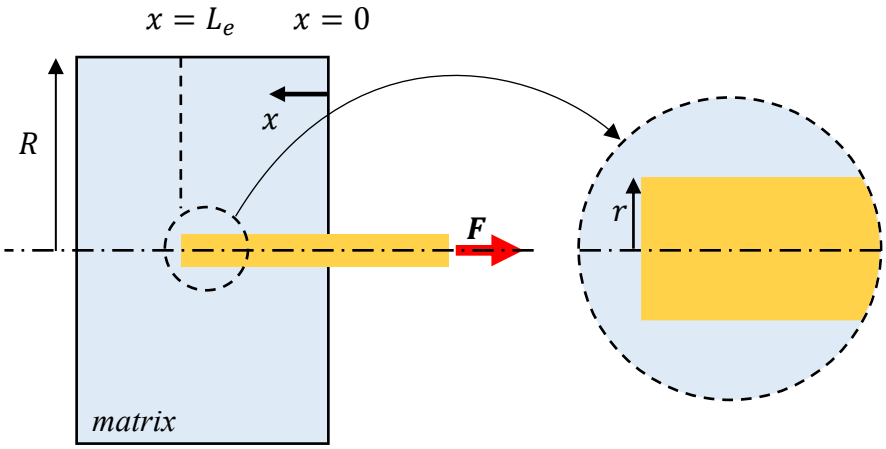

Figure 5.8: Cylindrical pull-out sample.

5.1.3.2 Energy controlled debonding

The debonding event can also be considered from the energy based perspective [26–28, 35]. In this case, the debonding process is considered to be due to the crack propagation. The failure criteria is the energy release rate (G_i), defined as the mechanical energy released by the system on increasing the crack area by the unit area. The crack is assumed to grow when, under increasing external load applied to the free fibre end, the G_i value becomes equal to the critical energy release rate, or interfacial toughness, G_{ic}, which depends on the fibre and matrix properties, and geometry of the system. The value of G_{ic} can be calculated according to (5.31), based on the work by Scheer and Nairn [24], where C_{33s} is defined in (5.32), α_f is the axial coefficient of thermal expansion of the fibre, α_m is the coefficient of thermal expansion of the matrix, and ΔT is the difference between the test temperature and the stress-free temperature.

$$G_{ic} = \frac{rC_{33s}}{2}\left[\frac{F_d}{\pi r^2} + \frac{(\alpha_f - \alpha_m)\Delta T}{2C_{33s}}\right]^2 \tag{5.31}$$

$$C_{33s} = \frac{1}{2}\left(\frac{1}{E_f} + \frac{V_f}{V_m E_m}\right) \tag{5.32}$$

5.1.3.3 Adhesional pressure

It has been suggested by a number of authors that the debonding process in pull-out tests occurs in normal tension on the interface (Mode I) [46–48]. The variational mechanics theoretical analysis by Scheer and Nairn [24, 49, 50] showed that the shear stress is zero at the point where the fibre enters the matrix (i.e. $x = 0$ as in (b) Figure 5.9), while the tensile radial stress is maximum at this point. The adhesional pressure, or critical interfacial normal stress could be defined then as a stress based failure criterion [28, 48]. If two surfaces are considered to be kept together by molecular forces (as in (a) 1 Figure 5.9), the integral of these forces represents the total force of surface interaction between the bodies. The specific value of this force per unit of interfacial area (stress) is defined as the adhesional pressure. Therefore, the interfacial strength, σ_{ult}, is defined as the stress numerically equal to the adhesional pressure, but opposite in direction, necessary to break this adhesional contact, as illustrated in (a) 2 Figure 5.9. The theoretical description of the method used to calculate σ_{ult} is given in Appendix A.

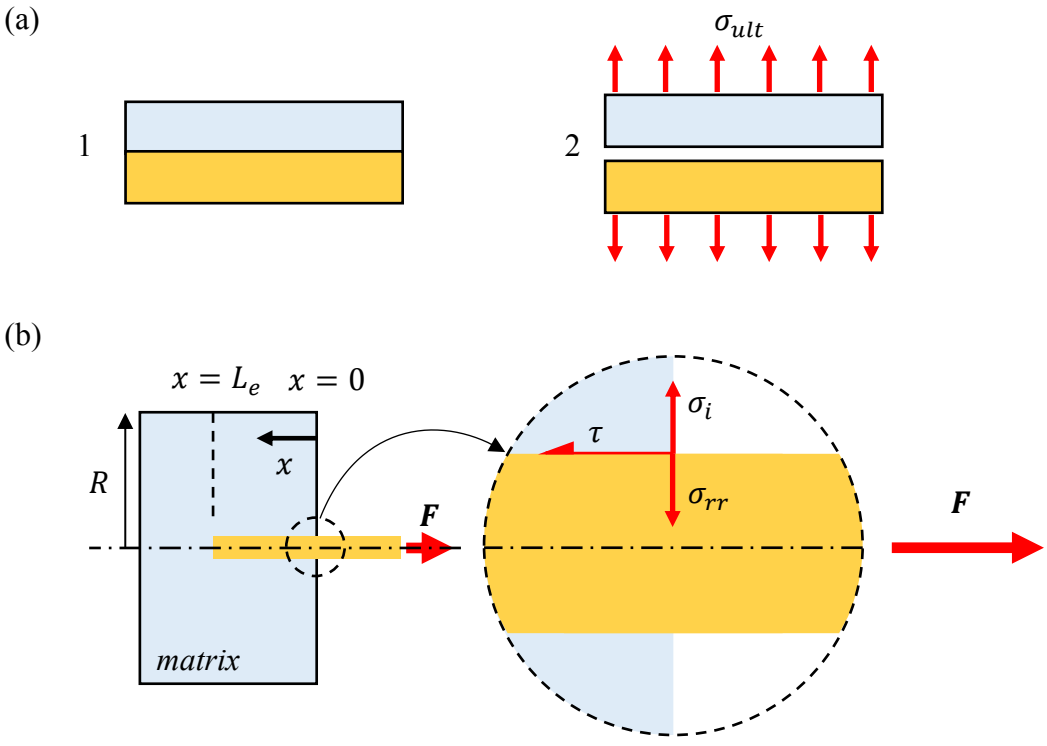

Figure 5.9: Adhesional pressure concept in: (a) Two flat surfaces and (b) cylindrical pull-out sample.

The analysis by Scheer and Nairn [24] predicts that the radial tensile stress, σ_{rr}, increases for increasing force, F, (i.e. pulling-out force). Based on the adhesional pressure failure criterion, the debonding process starts when σ_{rr} reaches the value of σ_{ult}. The value of σ_{rr} depends on the geometry of the specimen, fibre and matrix properties, residual thermal stresses, and the value of F. Furthermore, some authors have also investigated the relationship between the "fundamental" adhesion (considered as the work of adhesion, W_a) and the "practical" adhesion (considered as the adhesional pressure, or interfacial strength σ_{ult}) [26, 28, 48, 51]. In this regard, Pisanova et al. [48], who considered adhesional pressure to be caused by molecular forces acting across the interface, found a linear relationship between the work of adhesion and adhesional pressure. The algorithm, and equations from Scheer and Nairn variational mechanics, used for the determination σ_{ult} are discussed in Appendix A. As it will be later discussed, the model was fitted to the experimental observations, using the standard least-squares method.

5.1.4 The effect of maleic anhydride polymer modifications

The use of maleic anhydride grafted polyolefins (MAPOs) to improve the compatibility between the polyolefin matrix and polar natural fibres have been widely investigated [52–63]. According to some authors [56], the addition of maleated coupling agents, such as maleic anhydride grafted polypropylene (MAPP), could lead to the creation of covalent bonds between the cellulosic fibre and the PP chain, as illustrated in Figure 5.10. This results in improved interfacial fibre-matrix bonding. As a consequence, the addition of MAPOs to the polymer blend, leads to an increase of the apparent IFSS [54, 63].

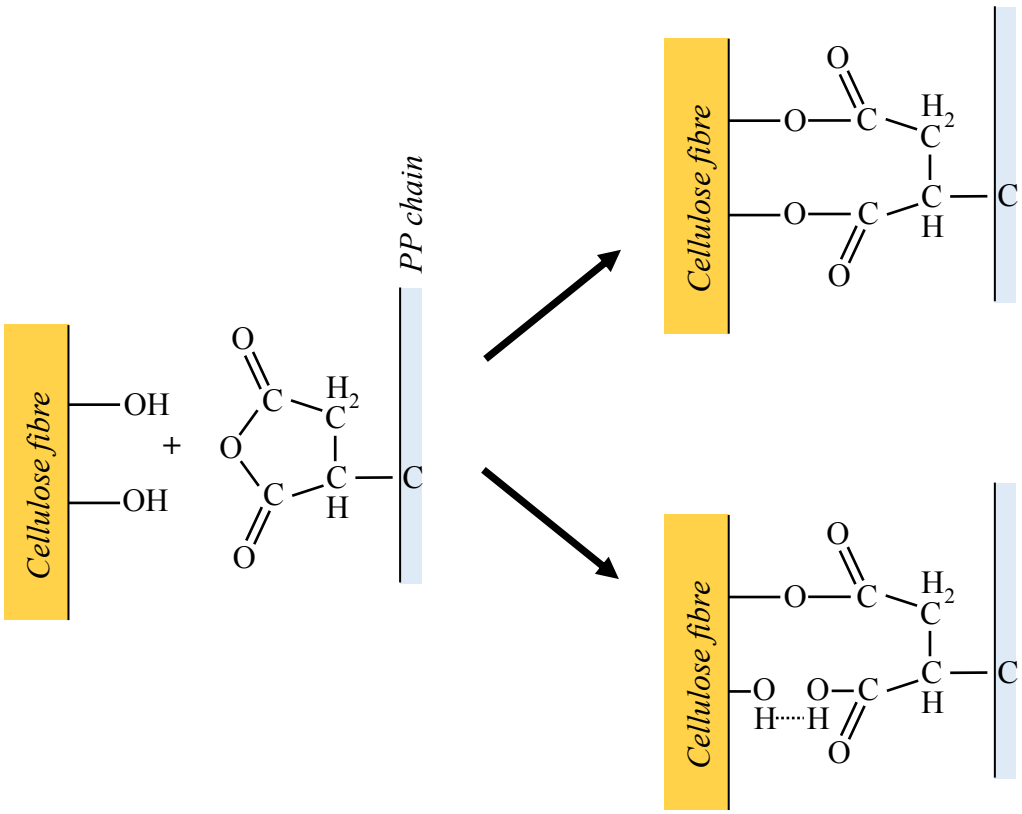

Figure 5.10: Reaction of cellulosic fibre with MAPP copolymer. Based on [56, 59].

5.2 Experimental

5.2.1 Materials

As in the case of previous chapters, coir fibres, and all polymers were supplied by SABIC. In terms of PPs, homopolymer SABIC® PP 579S and copolymer SABIC® PP 513MNK10 with a melt flow rate (230 °C and 2.16Kg) of 47 and 70 g/10 min respectively, were used in the studies. For commercial reasons, the composition of the copolymer is not disclosed. Maleic anhydride grafted polypropylene (MAPP) Exxelor™ PO 1020 (maleic anhydride content is typically in the range of 0.5 to 1 wt%) was used as modifier/coupling agent. The effect of MAPP on the interfacial properties of coir-PP samples was investigated for 0, 3, 5, 10, and 100 wt% MAPP content.

In the case of LDPE, SABIC® LDPE 1922SF, with a melt flow rate (190 °C and 2.16Kg) of 22 g/10 min, was used. Maleic anhydride modified high density polyethylene (MAPE) POLYBOND® 3029 by ADDIVANT (maleic anhydride content is typically in the range of 1.5 to 1.7%) was used as a modifier/coupling agent. The

effect of MAPE on the interfacial properties of coir-LDPE samples was initially investigated for 0, and 5 wt% MAPE content.

5.2.2 Sample preparation

Two different sample preparation methods were developed. In both cases, a single fibre was embedded in a polymer block for later testing. The development of these techniques had to take into consideration the high curvature and diameter variability of coir fibres, which is illustrated in Figure 5.11. Furthermore, coir fibres are subject to degradation within the range of temperatures necessary to form samples, as discussed in Chapter 3. Within the technique development process, it was also evident that the polymer was subjected to degradation, as was also pointed out by Yang et al. [12]. In this regard, Yang et al. recommended forming samples under an inert atmosphere, such as nitrogen, in order to avoid the thermo-oxidative degradation of the polymer.

Figure 5.11: Coir fibres as received.

In the case of both sample preparation methods, the aim was to create a pull-out sample with similar geometrical configuration to the idealised sample proposed by Scheer and Nairn [24], illustrated in Figure 5.12. In this pull-out configuration, a cylindrical sample, in which a fibre is embedded within the central axis of the cylinder, is restrained on the top surface of the cylinder as can be seen in Figure 5.12.

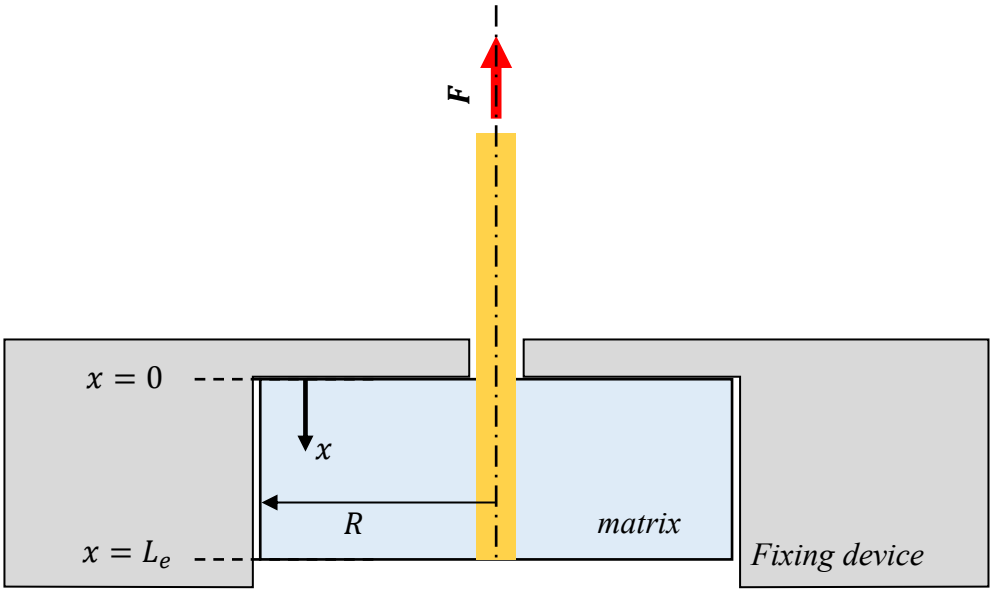

Figure 5.12: Cylindrical pull-out sample in the pull-out configuration.

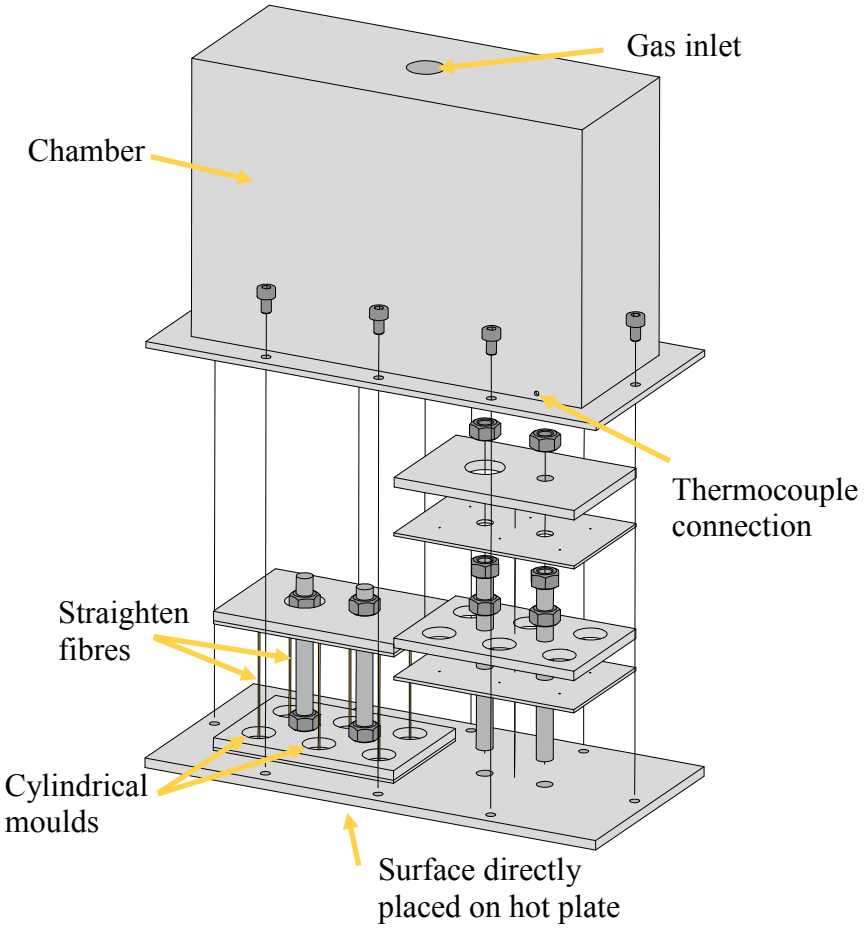

Figure 5.13: General diagram of the sample preparation frame.

Due to the degradation of coir fibres at high temperatures, the sample preparation methodology had to minimise the exposure of the fibres to high temperatures, while maintaining the process in an inert atmosphere. In the developed sample preparation methods, the fibres are straightened with the help of a metal frame, which has a series of cylindrical moulds for transforming the polymer pellets into cylindrical blocks in which the fibres are embedded, Figure 5.13 and Figure 5.14. The moulds have a diameter of 10 mm.

Figure 5.14: Metal frame and chamber with the gas connection.

5.2.2.1 Method 1

The steps necessary for the first sample preparation method (M1) are illustrated in Figure 5.15. First, the fibres are put through holes on plate 1, and thereafter fixed on one side of the plate with double sided tape, as showed in Figure 5.15 (a). Once all the fibres are put through the respective holes in the plate, it is then placed on the base plate, which will provide additional gripping of the fibres, Figure 5.15 (b). These actions are repeated for the other plate 1. Thereafter, the two plates with the cylindrical moulds are then put through the fibres and located on top of plates 1. Mould plates are compressed against the base plate with the help of two nuts mounted on perpendicular threaded bars, which are directly screwed in the base plate.

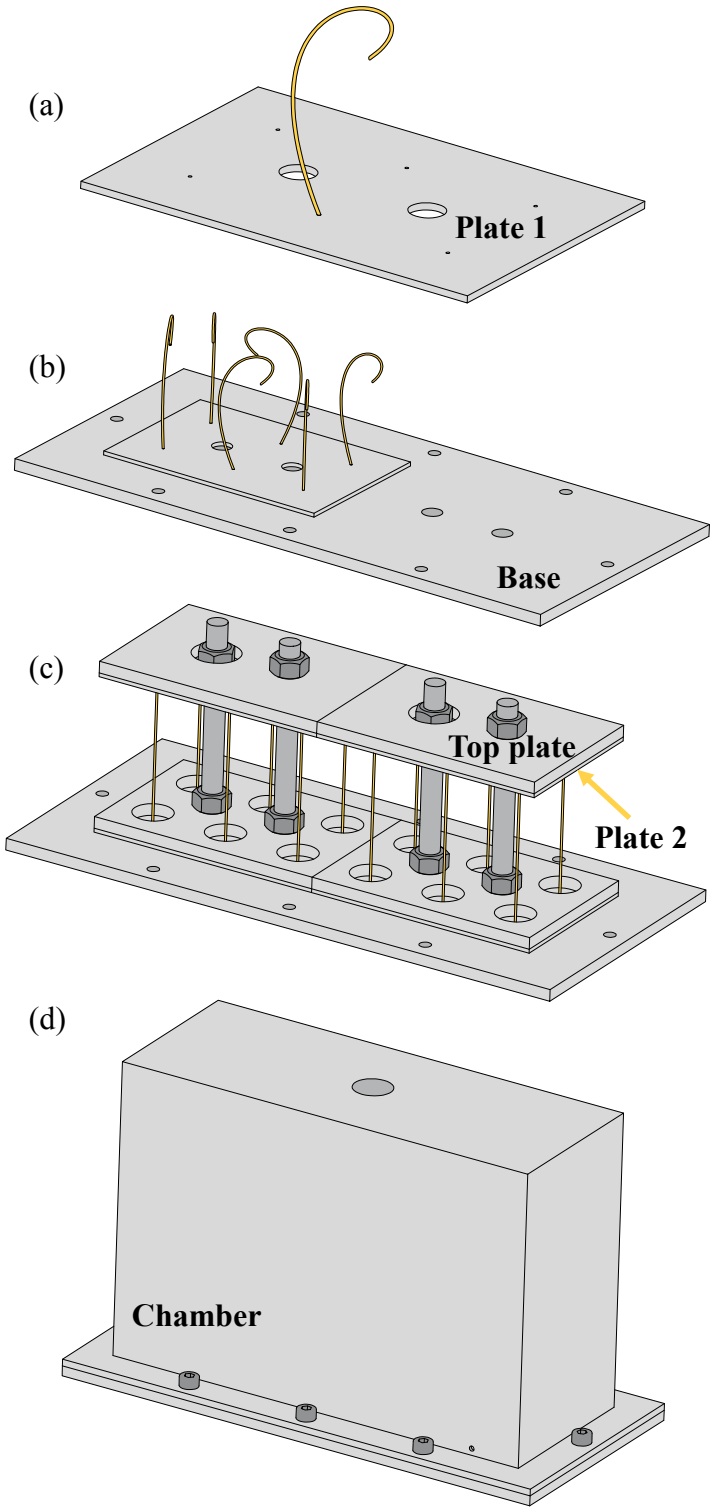

Figure 5.15: Pull out sample preparation schematic sequence.

Once this operation is completed, the fibres are put through the holes of the second plate (i.e. plate 2), and once they are perfectly straight between both plates (i.e. the

fibres are perpendicular to the planes represented by plate 1 and plate 2), they are fixed to them with double sided tape. Both plates 2 are supported and fixed by nuts on the threaded bars. Thereafter, two additional plates are compressed against plates 2 for additional gripping of the fibres, as it can be seen in Figure 5.15 (c).

At this point, the holes are filled with polymer pellets. After this operation is completed, the assembly is enclosed with the chamber, which is fixed directly to the base, as shown in Figure 5.15 (d). A thermocouple wire and the gas inlet are then connected to the chamber. In order to melt the pellets into the cylindrical shape, the base of the assembly (i.e. base plate) is directly placed on the surface of a pre-heated hot plate. The hot plate is pre-heated in all cases at 230 °C, which proved to be enough to melt the analysed polymers.

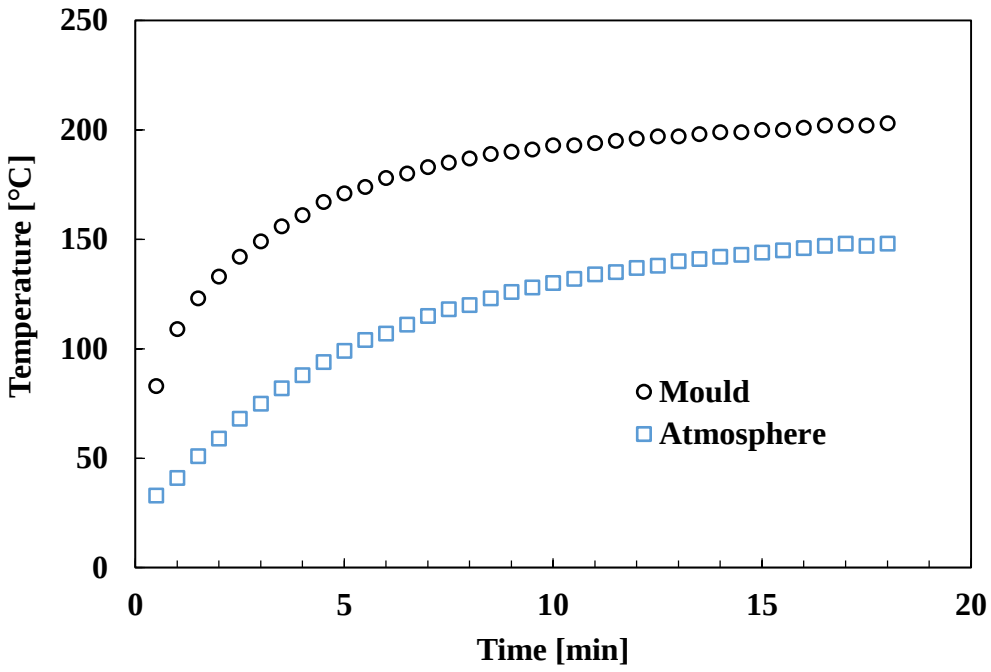

Figure 5.16: Evolution of temperature of the mould and atmosphere versus time for the hot plate at 230 °C with a N_2 flow of 200 ml/min.

The total time that the assembly was placed on the hot plate was fixed at 18 minutes for PP and PE samples, which was found to be enough to completely melt the polymers. The temperature in the base plate, which is in direct contact with the polymer pellets reach a maximum temperature of approximately 200 °C, after 18 minutes on the hot plate, as illustrated in Figure 5.16. It can also be noticed that the

monitored temperature of the atmosphere between the base and the top plate did not reach 150 °C after the 18 minutes, which according to Chapter 3 should reduce the likelihood of degradation of the free fibre.

Figure 5.17: PP579S cylindrical pull-out samples.

After the 18 minutes, the assembly is taken off the hot plate, the chamber is removed, and the rest of the assembly is left to cool down at room temperature. Once the assembly reaches room temperature, the parts are disassembled. Fibres are cut next to the points where they were fixed by the double sided tape. This allows for easy demoulding of the cylindrically shaped polymer samples. Thereafter, the remaining part of the fibre below the polymer block is cut with a scalpel. Additionally, any sharp edges in the outer cylinder face were also removed with a scalpel. An example of the samples produced is shown in Figure 5.17.

5.2.2.2 Method 2

The second sample preparation method (M2) is a variation of method 1, which was developed in order to overcome some difficulties in demoulding MAPE modified LDPE blocks from the metal moulds. Additionally, this sample preparation method provides the opportunity to form samples with much lower embedded lengths in relation to method 1.

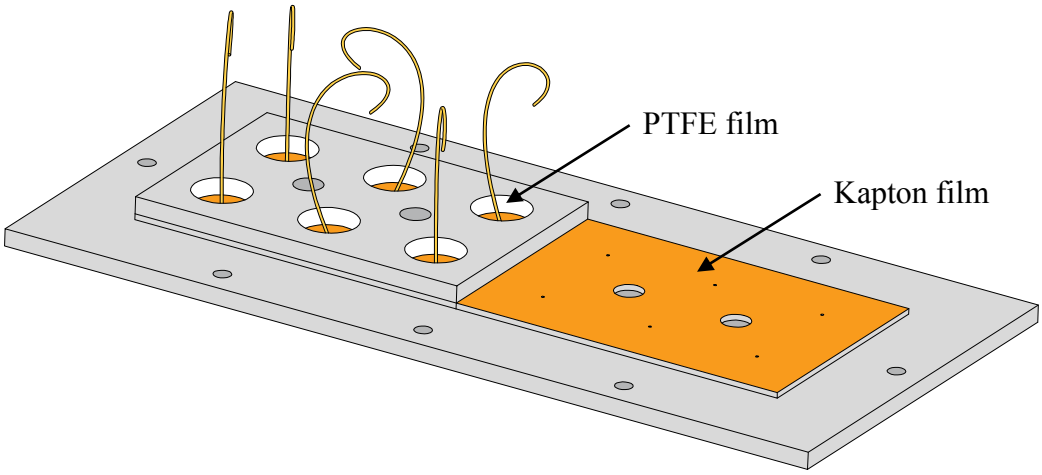

Figure 5.18: Additional components in sample preparation method 2.

The main difference, in relation to method 1, is that in this case the matrix is in the form of a film instead of pellets, when the matrix material is placed on the metallic mould for melting. The polymer films are pre-formed by placing polymer pellets on a glass slide, which is, at the same time, placed on a hot plate. When the polymer pellets begin to melt, they are compressed with the help of a second glass slide until a film of approximately 1 mm is formed. The temperatures used to form the films are 220 °C for PP and 180 °C for LDPE. The polymer films are then trimmed to form circular shapes with an approximate diameter of 8 mm, and punched in the centre to allow fibres to go through. The aim of creating films with a lower diameter than the nominal diameter of the moulds was aimed to avoid direct contact of the polymer with the mould walls during sample preparation. Additionally, in order to prevent any contact between the metallic parts and the polymer, a Kapton film was placed on top of plate 1, and the walls of the moulds were covered with PTFE tape, as illustrated in Figure 5.18.

The circular films with the punch in the centre were passed through the fibres at the point where the mould plates were in place. One or two films were put through a single fibre in order to create pull-out samples with a greater range of embedded lengths. From this point, the same steps and conditions as in method 1 were followed. An example of the formed pull-out sample is illustrated in Figure 5.19.

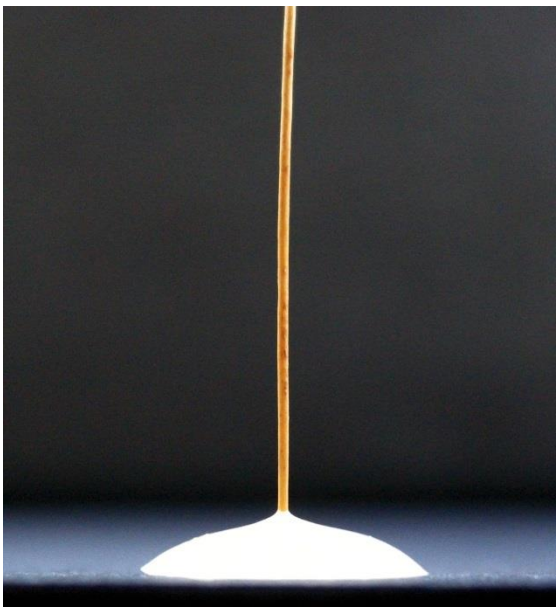

Figure 5.19: PP 579S pull-out sample.

5.2.3 Room temperature pull-out test

A cylindrical fixing device was manufactured, illustrated in Figure 5.20, to be fitted to the main frame of an Instron 3342 tensile testing machine, which was used for the pull-out testing. A 100 N load cell was used for the measurements. After positioning the pull-out samples in the frame as showed in Figure 5.12, fibres were clamped at approximately 5 mm above the top surface of the pull-out frame, which resulted on a total free length of approximately 7 mm. Samples were tested at room temperature with a crosshead extension of 0.5 mm/min.

As showed in Chapter 2, coir's cross-section area (CSA) is non-circular. Moreover, natural fibres' CSA varies along fibres' longitudinal direction [64]. In this study, as an approximation, coir fibres were assumed to have a circular CSA. In this regard, as showed in Chapter 2, the perimeter based on transverse diameter measurements, assuming circular CSA, is a good approximation of the real perimeter from direct observation, with a difference of approximately 3% based on the least-squared fitted straight line.

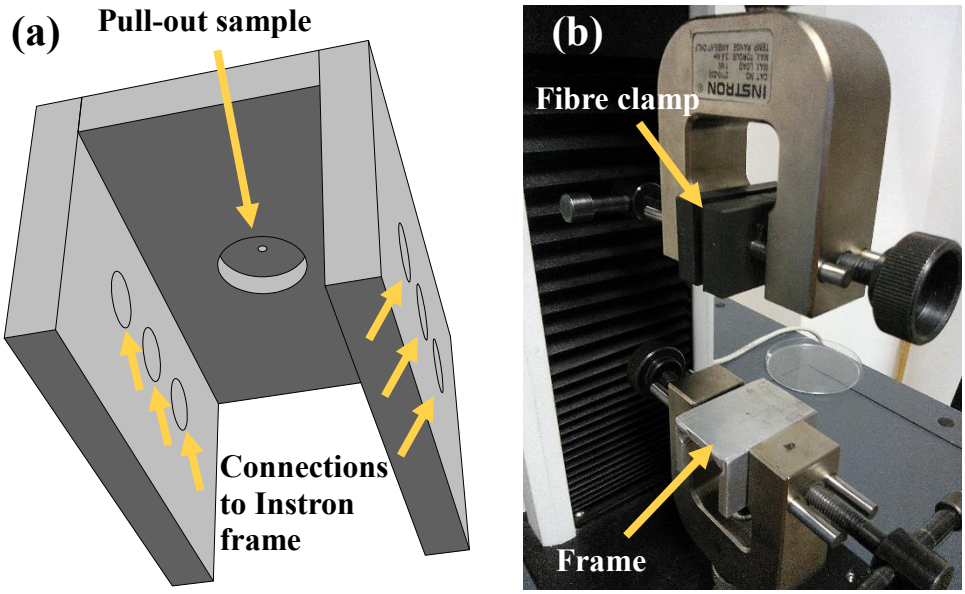

Figure 5.20: Instron's pull-out frame. (a) Schematic drawing of the frame. (b) Instron set-up.

After testing, each sample was characterised in terms of embedded length and diameter. The embedded length was measured directly on the polymer cylinder using a calliper. The pulled-out region of the fibres was transversally photographed using an Olympus GX51 microscope. In the case of each fibre, and as in Chapter 2, the diameter was measured at three different points using the software ImageJ. The diameter of each fibre was estimated as the average of these three measurements.

The load as a function of cross-head displacement was recorded for each test using Bluehill® 2 Software (which controls the Instron testing machine) and post-processed to find the peak load. Subsequently, the peak load, fibre diameter and embedded length were used to calculate the apparent IFSS according to (5.4). Other theoretical models, presented in Section 5.1.3, which were also used to further analyse pull-out data, will be extensively discussed in Section 5.3 (i.e. Results and discussion).

5.2.4 Controlled environment DMA pull-out testing

The temperature dependence of coir-polypropylene IFSS was investigated by developing a frame that could fit into a dynamic mechanical analyser (DMA), in which temperature can be precisely controlled. A DMA Q800 from TA instruments was used in tension mode, to adapt the pull-out configuration that was previously illustrated in

Figure 5.12, and which was used in the tests carried out at room temperature in the Instron tensile testing machine. The schematic diagram of the metallic frame that was developed to perform pull-out testing within the DMA, and test set-up are shown in Figure 5.21 (a) and (b).

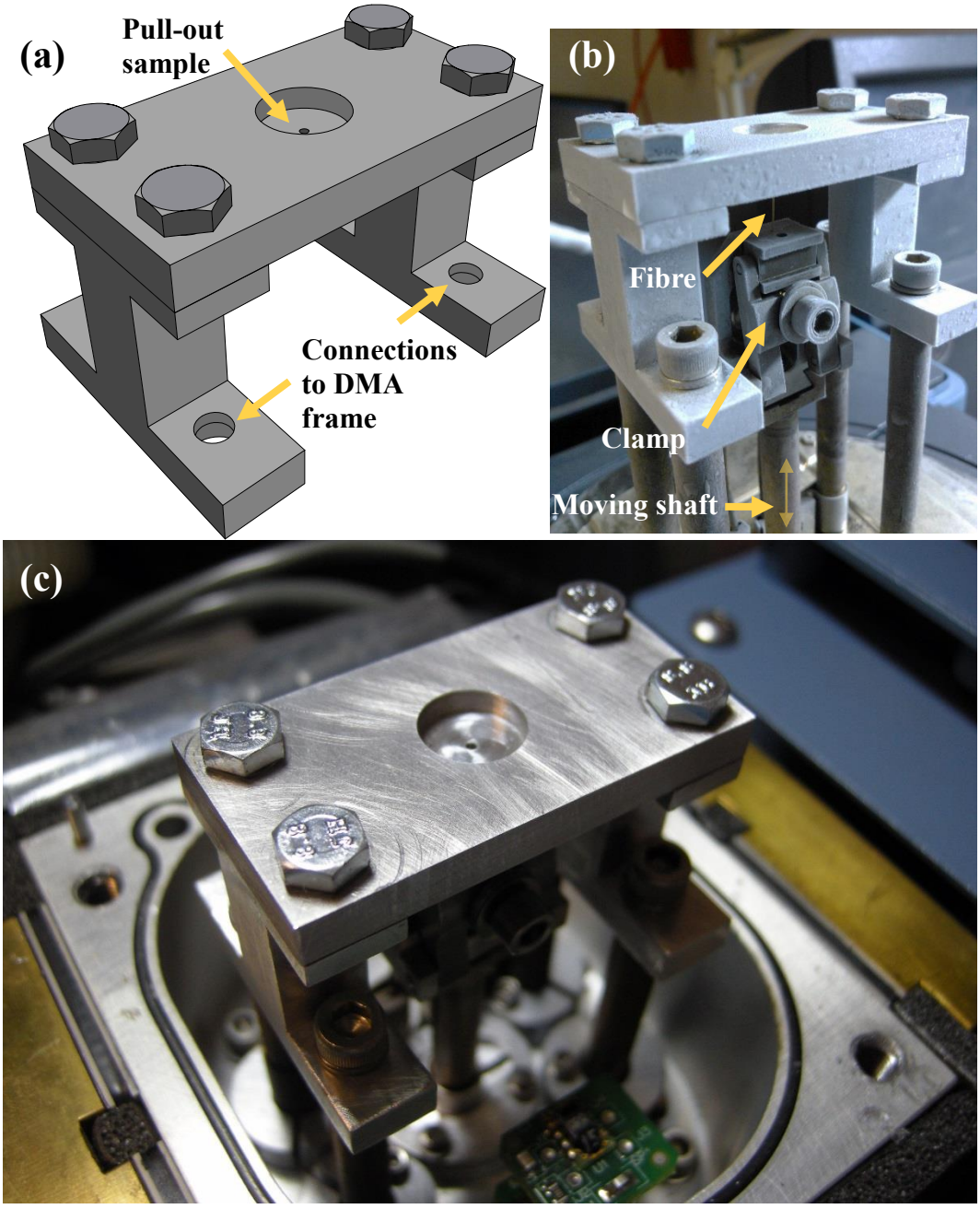

Figure 5.21: DMA's pull-out frame. (a) Schematic drawing of the frame. (b) DMA set-up (picture taken after a test at – 40 °C). (c) DMA pull-out frame fitted inside the DMA's humidity chamber.

In the case of the DMA test, the position of the pull-out sample was opposite to the one used in the Instron test. The sample was placed in position, putting the fibre through the hole on the frame, and clamping the fibre at approximately 5 mm below the bottom surface of the plate in which the sample is positioned. Although not used in this study, the developed frame is also able to fit within the DMA humidity chamber, as illustrated in Figure 5.21 (c), which potentially enables investigating the effects of humidity on interfacial properties.

The testing protocol that was developed, aimed to replicate the test on the Instron tensile testing machine. After the samples were in position and ready for testing, the DMA furnace was closed, and thereafter, equilibrated at the test temperature. This was followed by a 5 minutes isothermal segment, in order to ensure a constant equilibrium temperature in the sample. Immediately after, a strain ramp, which was equivalent to a displacement ramp of 0.5 mm/min, was applied to the fibre. The force-displacement curve was recorded by the TA software, and post-processed to find the peak load. The same process as in the Instron pull-out method was followed after this point, in which the fibre diameter and embedded length are characterised, and used to calculate the apparent IFSS.

The homopolymer PP 579S was used as the matrix for this study. In order to analyse the comparability between the pull-out results from the Instron tensile testing machine and from the DMA, two sets of pull-out samples based on M2 were compared. Three different temperatures were investigated by the DMA pull-out set-up, -40, 20 (which was also used for the comparison with Instron results) and 100 °C. In the case of the runs carried out at -40 °C, a gas cooling accessory (GCA) connected to the DMA furnace was used.

5.2.5 Analysis of pull-out curves

As discussed in Section 5.1.3, and more specifically around Figure 5.4, during the pull-out test, the crack in the interface may start without initiating a subsequent, almost instantaneous, crack propagation along the entire interface. In this case, as previously discussed, the debonding force, F_d, and maximum force, F_{max}, are different, and can be used to calculate the frictional stress in debonded areas, τ_f, by taking into

consideration the force exerted on the fibre and the crack length [26, 28, 42]. In these cases, F_d is detected in a slight change of the slope of the force-extension pull-out curve in the region $0 \leq F < F_{max}$.

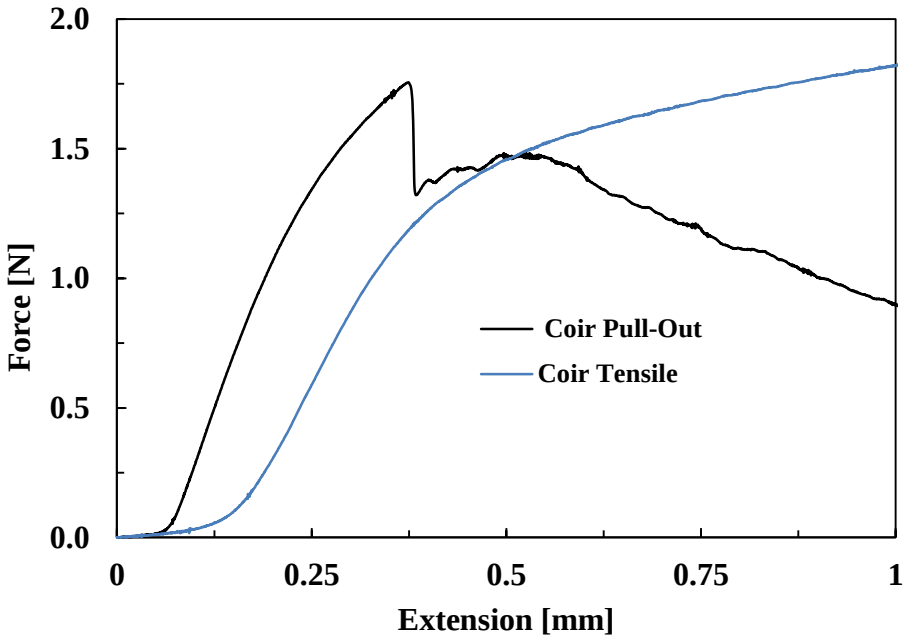

Figure 5.22: Typical coir pull-out and tensile curves. It should be noticed that the difference of the elastic modulus between the two examples choosen for this figure, is due to the inherent variability of properties between fibres, and not related to the testing set-up.

However, in the case of coir fibre, the change of slope in the force-extension pull-out curve within the region $0 \leq F < F_{max}$, in relation to crack initiation (if it actually occurs in this system) might be impossible to detect due to the non-elastic behaviour of the fibre. This is illustrated in Figure 5.22, where two typical coir pull-out and tensile curves are shown, the change of slope in the pull-out curve could potentially be driven by the bi-phasic stress-strain behaviour of coir, as discussed in Chapter 2. In this regard, and for this study, all pull-out curves were assumed to be of type A, as defined in Section 5.1.3 and Figure 5.4, where the debonding force, F_d, is equal to the maximum force, F_{max}, in the pull-out curve.

5.2.6 Analysis of pull-out data through theoretical models

As discussed in Section 5.1.3, the dependency of the τ_{app} on the samples' geometrical parameters has long been debated in literature. However, in order to properly analyse pull-out data, an almost complete characterisation of the fibre's elastic constants is necessary. As can be seen from the equations involved in most of shear stress controlled models, and with the variational mechanics approach by Scheer and Nairn [24, 49, 50] considering adhesional pressure as debonding criteria, an extensive range of fibre and matrix parameters is required.

It is necessary to mention that some of the elastic constants needed for these models (e.g. fibres' transverse modulus, axial shear modulus or Poisson ratio) are difficult to measure and not often found in literature. In this regard, in most of the cases, when these models are applied to natural fibres, it is not clear how these the parameters are measured, they are poorly referenced or simply not mentioned. Furthermore, as it was shown in Chapter 2, the observed variability of fibres' Young's modulus is a reason to think that the other elastic constants of these fibres will most probably have a similar variability. This variability of the elastic properties only adds further complexity to the analysis of pull-out data based on these models.

Before the assumptions made for the parameters required by the models are discussed further, and attending to the above discussed arguments, it should be clearly stated that the theoretical analysis, was only intended to investigate and comprehend the consequences of the variation of different parameters, such as fibre radius or embedded length, on the apparent IFSS. In this regard, the main objective was to investigate if the models could explain the experimentally observed trends in the pull-out data, and therefore, was not envisioned to precisely characterise any interfacial parameter.

Typical values of elastic constants for different natural fibres are listed in Table 5.1, where E_f is the axial tensile modulus, E_t is the transverse modulus, G_f is the axial shear modulus, v_f is the axial Poisson's ratio, v_t is the transverse Poisson's ratio, α_f is the axial coefficient of thermal expansion, and α_t is the transverse coefficient of thermal expansion.

For the analysis of the experimental pull-out data, a Young's modulus of 2.94 GPa was assumed (based on the data from Chapter 2). Coir's transverse and shear modulus were assumed to be proportional to the axial Young's modulus, with coefficients of proportionality based on jute data (i.e. $E_{t,jute} = k_t E_{f,jute}$ and $G_{f,jute} = k_g E_{f,jute}$), measured by Cichocki and Thomason [65]. Therefore, transverse modulus was taken as 0.41 GPa, and shear modulus as 0.26 GPa. The high anisotropy observed by Cichocki and Thomason [65], has also been shown by Gentles [66]. The axial coefficient of thermal expansion was taken as -0.6 μm/m °C, measured for jute by Cichocki and Thomason [65], and also taken by Tran et al. [43] for the analysis of coir. In the transverse direction, the same reference was used [65], and was taken as 77.2 μm/m °C. The axial Poisson's ratio was taken as 0.11, while it was taken as 0.01 in the transverse direction. Regarding matrix properties, polypropylene's stress free temperature was taken as 120 °C, as suggested by Thomason and Yang [11]. The measured Poisson's ratio was 0.42 for PP 579S.

	Jute [65]	Sisal [66]	Flax [66]
E_f [GPa]	39.4	15.5	57
E_t [GPa]	5.5	1.3	1.3
G_f [GPa]	3.5	1.1	-
ν_f	0.11	-	-
ν_t	0.01	-	-
α_f[μm/m °C]	-0.6	-45.3	-1.6
α_t[μm/m °C]	77.2	76.3	72.5

Table 5.1: Typical values for anisotropic properties of natural fibres. Adapted from [65, 66].

5.3 Results and discussion

5.3.1 Room temperature coir-polypropylene study

Results of the pull-out test of coir-PP 579S system and its respective variations in terms of MAPP content, carried out on the Instron machine at room temperature and based on samples from method 1 (M1), are illustrated in Figure 5.23. The value of the apparent IFSS for each system, is represented in the figure as the slope of the least-squares fitted straight line forced through the origin. From the R-squared values

showed in the figure, and the individual data points, it can be seen that there is a clear scattering of the data. This relative scattering is observed to different extents through all the studied systems. The average apparent IFSS values will be further discussed in this section.

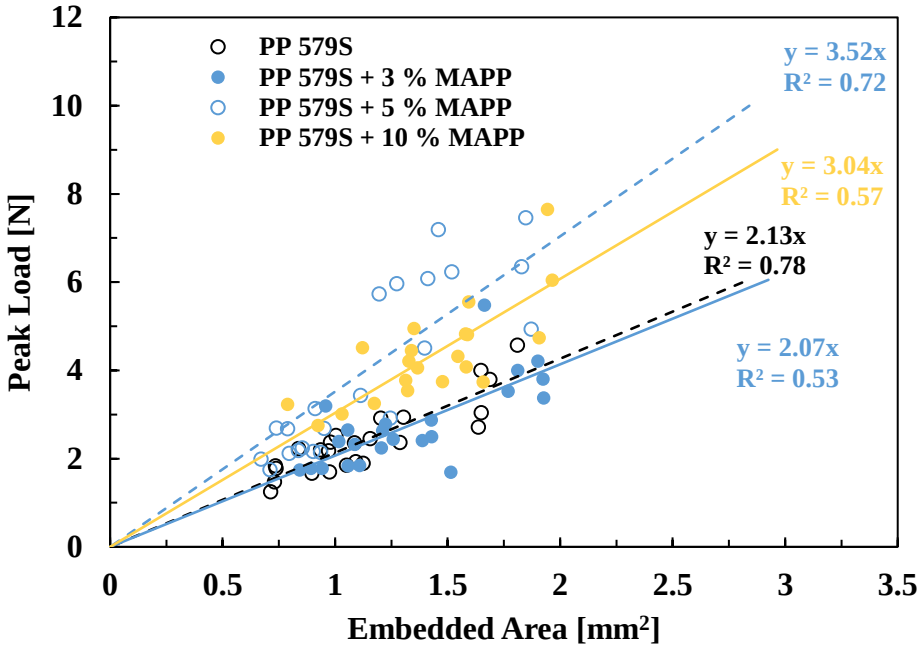

Figure 5.23: Peak load versus coir's embedded area. Results for coir-PP 579S with different MAPP contents.

Examples of the examination under the SEM of PP 579S based pull-out samples, are illustrated in Figure 5.24. In the case of the PP 579S and MAPP modified systems, no clear evidence of residual polymer on fibres' surfaces was observed. Fibres' embedded length appear clean and only in exceptional cases, a small residual meniscus was detected.

Results of the pull-out test of the coir-PP 513MNK10 system and its respective variations in terms of MAPP content, carried on the Instron machine at room temperature (M1) are illustrated in Figure 5.25. As in the previous analysis, the value of the apparent IFSS for each system, is represented in the figure as the slope of the least-squares fitted straight line forced through the origin. A similar scattering of the data was observed in the case of PP 513MNK10 based samples.

Examples of the examination under the SEM of PP 513MNK10 based pull-out samples, are illustrated in Figure 5.26. In this case, in contrast to what was observed in PP 579S samples, the investigation of the embedded area of debonded fibres revealed residual polymer and the existence of a polymer meniscus, which was especially evident at higher concentrations of MAPP (i.e. 5 and 10 wt%). In Figure 5.26 (b), it can be seen that remains of polymer stayed adhered to the fibre's surface after debonding. Detailed examination of this kind of fibre surfaces revealed that the remaining polymer was sheared in the direction of the pull-out force. Figure 5.26 (c) and (d) clearly illustrates, in a sample that failed while the fibre was being pulled-out, how the polymer meniscus remained adhered to the fibre, while residual polymer could also be seen on the pulled-out fibre surface.

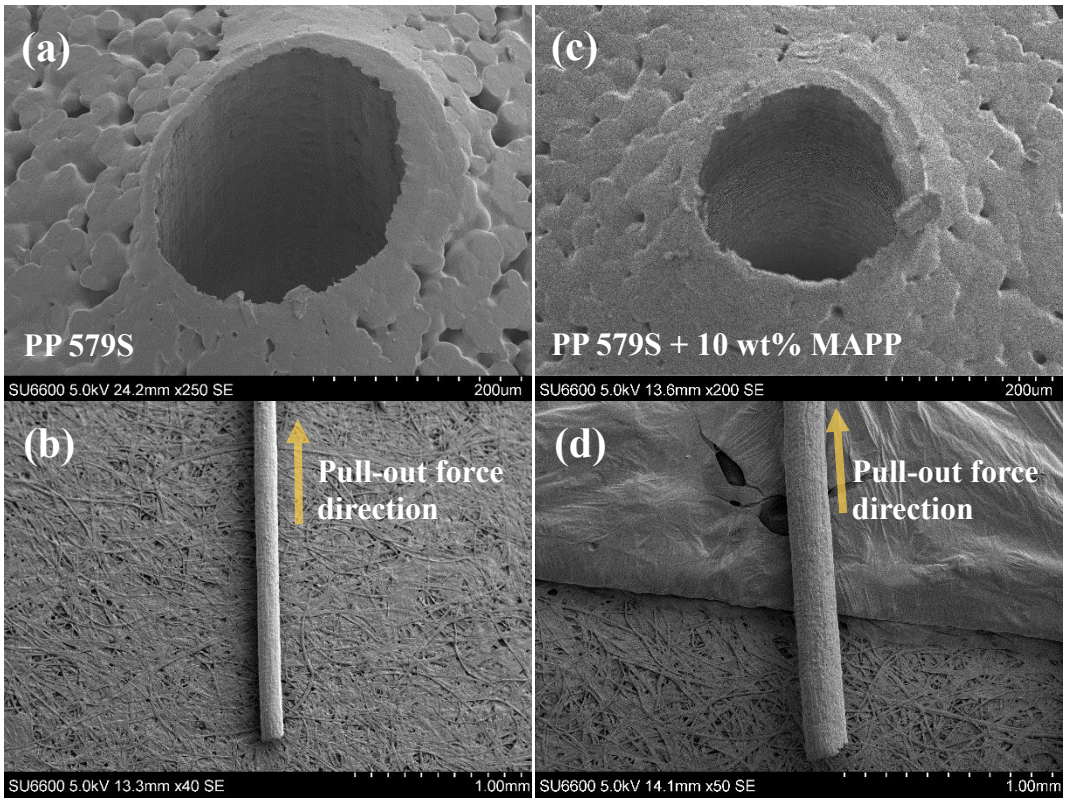

Figure 5.24: SEM examination of debonded PP579S based pull-out samples (M1). (a) (c) Typical observation of the hole of respectively PP 579S and PP 579S + 10 wt% MAPP cylinders, after the fibre had been pulled-out. (b) (d) Coir fibres after being debonded from respectively PP 579S and PP 579S + 10 wt% MAPP samples.

The average values of the apparent IFSS are illustrated in Figure 5.27, where error bars represent the 95% confidence limits. These values are also listed in Table 5.2.

When comparing the values of the apparent IFSS calculated as the average of the individual points, and the slope of the least-squares fitted straight line forced through the origin, showed in Figure 5.23 and Figure 5.25, it can be seen how similar they are.

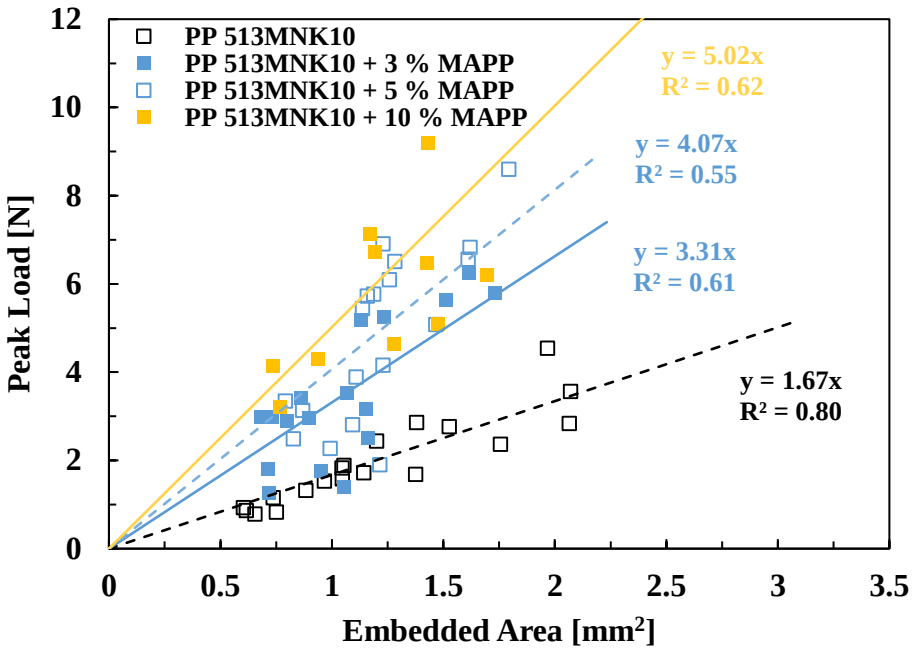

Figure 5.25: Peak load versus coir's embedded area. Results for coir-PP 513MNK10 with different MAPP contents.

When analysing the average values, it can also be seen how, in the case of PP 579S (i.e. PP homopolymer) the addition of MAPP seems only to have an effect between 3 and 5 wt%. The average apparent IFSS was 2.1 MPa for Coir-PP 579S and Coir-PP 579S + 3% MAPP. On the other hand, an average apparent IFSS value of 3.3 MPa for PP 579S + 5% MAPP and 3.1 MPa for PP 579S + 10% MAPP were measured. Although different average values, a two-sample *t*-test showed no significant difference at 95% confidence level (*p*-value = 0.27) between 5 and 10% MAPP content. A two-sample t-test also revealed a significant difference between 3 and 5% MAPP content, at 99% confidence level (*p*-value = $5.68 \cdot 10^{-8}$). A similar behaviour was observed by Gentles [66], when analysing the apparent IFSS of sisal-PP, where the initial addition of MAPP did not have any effect. As in this case, the increase in the apparent IFSS was observable when a 5% MAPP content was reached.

In the case of PP 513MNK10 (i.e. PP copolymer), as clearly seen in Figure 5.27, a continuous increase of the apparent IFSS was observed for increasing MAPP content. Two-sample *t*-tests showed a significant difference between Coir-PP 513MNK10 and Coir-PP 513MNK10+3% MAPP (*p*-value = $3.58 \cdot 10^{-6}$), and between Coir-PP 513MNK10 + 5% MAPP and Coir-PP 513MNK10 + 10% MAPP (*p*-value = 0.03), at 95% confidence level. Between Coir-PP 513MNK10 + 3% MAPP and Coir PP 513MNK10 + 5% MAPP, a two sample *t*-test revealed an almost significant difference at 95% confidence level (*p*-value = 0.0507).

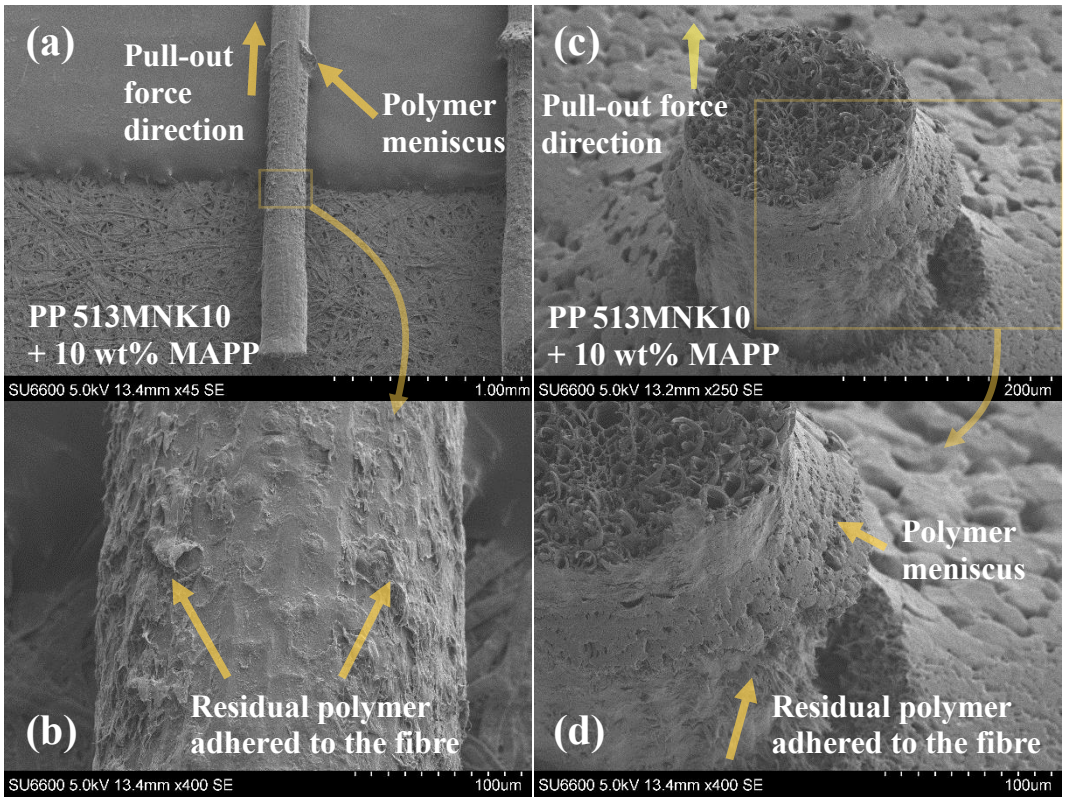

Figure 5.26: SEM examination of debonded PP 513MNK10 based samples (M1). (a) (b) Coir fibre after being debonded from a PP 513MNK10 + 10 wt% MAPP sample. (c) (d) Failed pull-out test in which the fibre broke after it was partially pulled-out.

It should also be noticed how the apparent IFSS of the Coir-100% MAPP, listed in Table 5.2, is equivalent to the average value of PP 513MNK10 + 10% MAPP. In this case, a two sample *t*-test showed no significant difference at 95% confidence level (*p*-value = 0.88). Although the average apparent IFSS values are equivalent, close examination of the debonded areas of pure MAPP pull-out samples, revealed different post-debonded embedded area characteristics. Small polymer menisci were detected,

but no observable residual polymer was found on the embedded area, as illustrated in Figure 5.28. This observation might indicate different debonding behaviours in terms of how the crack propagates along the interface, and how the matrix might behave differently when subject to relatively high shear stresses due to the presence of rubber and other polymers in the PP copolymer, which at the same time could lead to heterogeneous interaction between the matrix and the fibre.

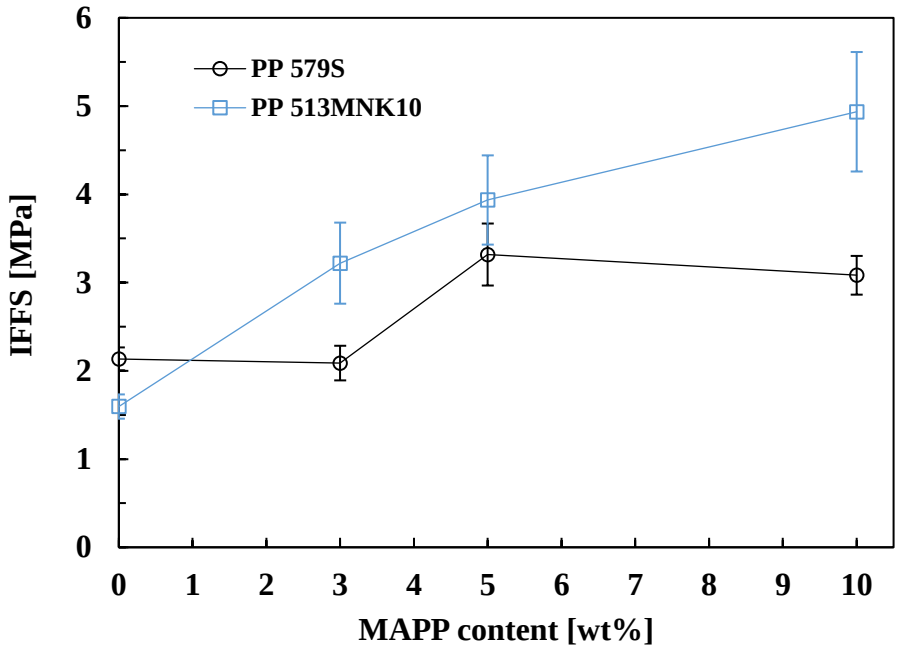

Figure 5.27: Apparent IFSS for PP 579S and PP 513 MNK10 versus MAPP content.

Polymer	IFSS [GPa]	
	Mean	95% Confidence limit
PP 579S	2.1	0.1
PP 579S + 3% MAPP	2.1	0.2
PP 579S + 5% MAPP	3.3	0.4
PP 579S + 10% MAPP	3.1	0.2
PP 513MNK10	1.6	0.1
PP 513MNK10 + 3% MAPP	3.2	0.5
PP 513MNK10 + 5% MAPP	3.9	0.5
PP 513MNK10 + 10% MAPP	4.9	0.7
Exxelor PO 1020	5.0	0.6

Table 5.2: Apparent IFSS for Coir-PP 579S and Coir-PP 513MNK10 systems and pure MAPP (i.e. Exxelor™ PO 1020).

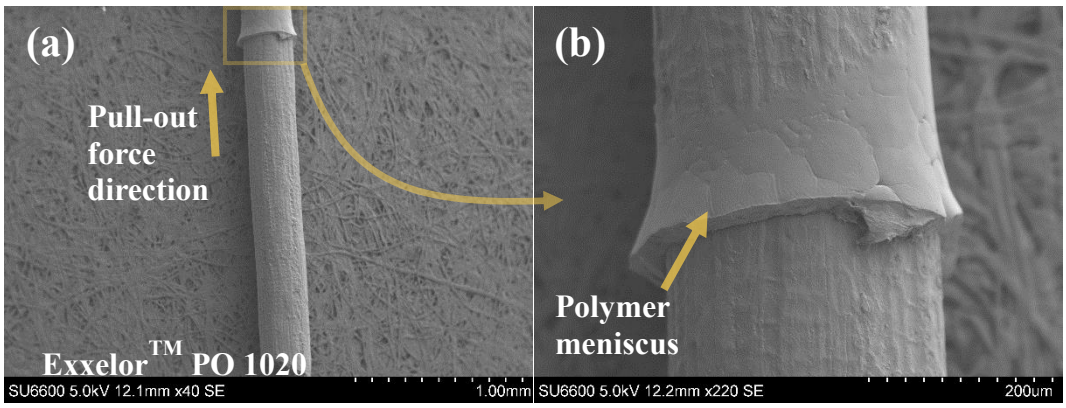

Figure 5.28: SEM examination of a typical debonded coir-Exxelor™ based sample (M1), (a) (b).

5.3.2 Sample geometry and apparent IFSS

As was explained in Section 5.2.2, the second sample preparation method, M2, provided a method in which the polymer was not in contact with the metallic parts of the sample preparation rig, which resulted in an easier demoulding in comparison to M1. Furthermore, by using M2, it was also possible to create samples with a much lower embedded length. Results of the pull-out test of coir-PP 579S system for both sample preparation methods, carried out with the Instron tensile testing machine at room temperature are illustrated in Figure 5.29. As in the previous section, the value of the apparent IFSS for each system, is represented in the figure as the slope of the least-squares fitted straight line forced through the origin.

By examining the data in Figure 5.29, it can be clearly seen how both methods provide a different spread of points. The slope of the least-squares fitted straight line forced through the origin gives an apparent IFSS value of 2.1 MPa in the case of M1, and 2.7 MPa for M2. The average of each individual test also revealed different values, 2.1 MPa for M1, and 3.1 MPa for M2. Further analysis of the data through a two-sample *t*-test showed a significant difference at 99% confidence level (*p*-value = $2.18 \cdot 10^{-8}$) between M1 and M2. From this comparison, it is clear that a fundamental difference between both sets of samples resulting from M1 and M2 methods must be the cause for the significant difference in the value of τ_{app}.

The influence of the embedded length, for both methods, concerning the previously discussed coir-PP 579S system, is further explored in Figure 5.30. It can be seen how

there is an apparent dependency of the τ_{app} on the embedded length, L_e, for which the τ_{app} increases for decreasing embedded length in the analysed range. In the figure's highlighted section, it can be seen how samples with similar embedded lengths showed comparable τ_{app} values. In principle, and attending to what is shown in Figure 5.30, the embedded length dependency could be one of the reasons for the previously discussed discrepancy between both sample preparation methods. In this regard, a similar dependency of the τ_{app} was also observed by Tran et al. for coir-PP samples [43].

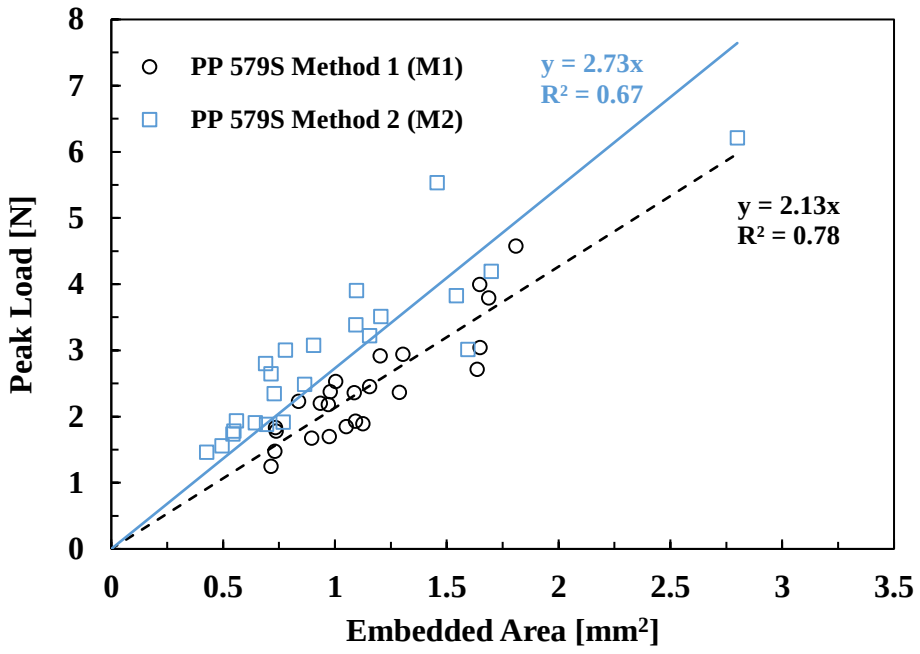

Figure 5.29: Peak load versus coir's embedded area. Comparison of single pull-out samples for coir-PP 579S between M1 (i.e. PP 579S) and M2 (i.e. PP 579S M2), carried out with the Instron tensile testing machine.

Attending to the observed trend in coir-PP 579S samples, and based on some of the models discussed in Section 5.1.3, the non-uniform stress distribution on the interface has been explored. By developing mathematical algorithms which use the equations from the previously mentioned theoretical models, it was possible to analyse the implications of non-uniform stress distributions on the interface of a pull-out sample during testing and how this could have any influence on the values of τ_{app}. The τ_{app} model, based on equation (5.4), the shear stress controlled debonding model,

summarised in equation (5.25), proposed by Zhandarov and Pisanova [21], the energy controlled debonding proposed by Scheer and Nairn [24], and the variational mechanics approach [24] considering adhesional pressure as debonding criteria [48], were used to fit the experimental observations $[F_d, L_e, r]_{exper}$.

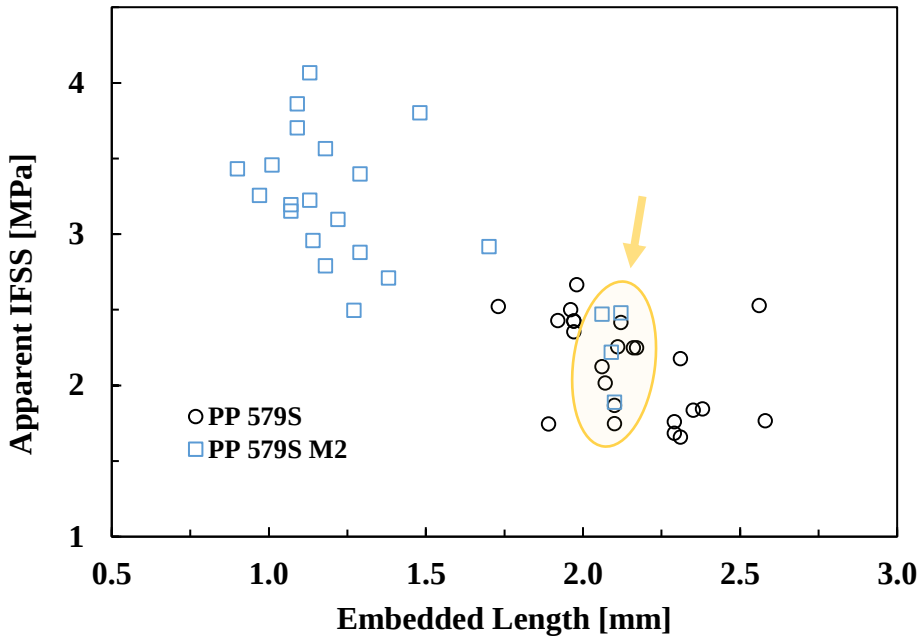

Figure 5.30: Apparent IFSS versus embedded length for coir-PP 579S, M1 and M2 sample preparation methods.

Concerning the theoretical analysis, the main predictions and overall ideas are explored in the following paragraphs. In this regard, Figure 5.31 illustrates the axial $\sigma_{zz,f}(\zeta)$, shear $\tau_{rz,f}(\zeta)$, and radial $\sigma_{rr,f}(\zeta)$, stresses along the fibre's embedded length according to variational mechanics, of a coir fibre embedded in PP 579S; with a fibre diameter of 0.3 mm, an embedded length of 1.5 mm, while it is subject to a debonding force equal to 2 N. It should be underlined that the variational mechanics model, and in particular $\tau_{rz,f}(\zeta)$, is in agreement with the concept of τ_{app}. Attending to the example illustrated in Figure 5.31, and assuming that the debonding occurs at the moment that is represented in the figure (i.e. F_d= 2 N), it can be seen that the τ_{app} would be equal to 0.71 MPa, as calculated in (5.33). For the same conditions, the average shear stress along the embedded length, could be calculated according to variational mechanics, as shown in (5.34), which also gives a value of 0.71 MPa.

$$\tau_{app} = \frac{F_d}{2\pi r L_e} = 0.71 \text{ MPa} \tag{5.33}$$

$$\bar{\tau}_{rz,f} = -\frac{1}{2\rho}\int_{-\rho}^{\rho} \tau_{rz,f}(\zeta)\, d\zeta = 0.71 \text{ MPa} \tag{5.34}$$

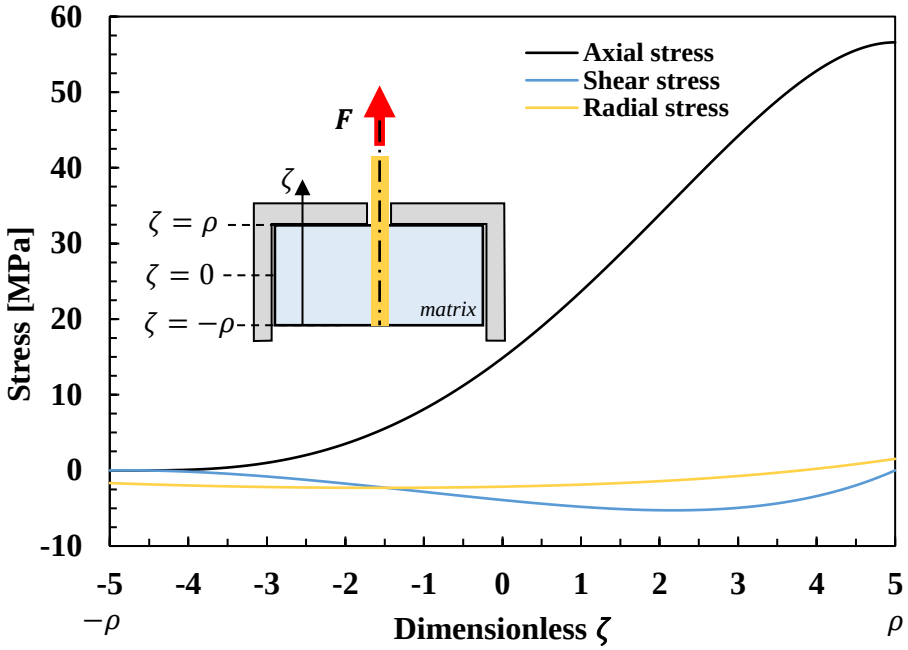

Figure 5.31: Fibre's axial, shear and radial stress distributions along the embedded length during a pull-out test for a coir-PP sample.

Concerning the shear stress controlled debonding model proposed by Zhandarov and Pisanova, summarised in equation (5.25), Figure 5.32 illustrates how the apparent IFSS varies according to the fibre radius and embedded length, assuming a cylindrical sample with a radius (R) of 5 mm. Furthermore, the figure also includes the plot of the τ_{app} model, where it is assumed that the IFSS is constant for all combinations of radius and embedded length. Similarly, Figure 5.33 illustrates the variational mechanics approach, considering an adhesional pressure (σ_{ult}) of 5 MPa. It should be noticed that, in contrast to what the shear stress controlled debonding predicts for embedded length close to 0 (i.e. $\tau_{app} = \tau_{ult}$), variational mechanics predicts that τ_{app} =0.

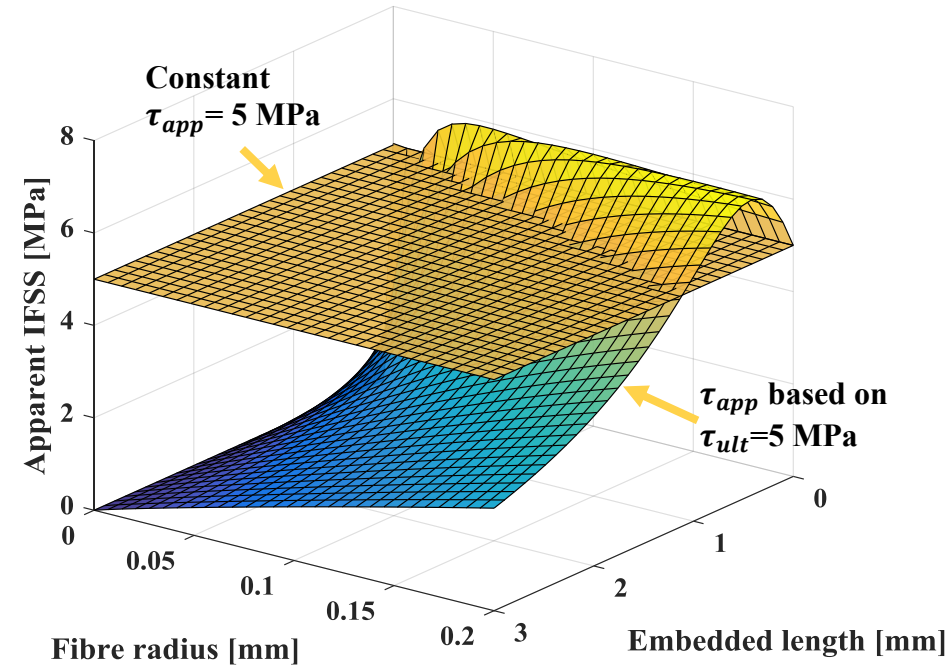

Figure 5.32: Apparent IFSS versus fibre radius and embedded length, for coir fibre and PP 579S, according to Zhandarov and Pisanova's model with a stress based debonding criteria τ_{ult}= 5 MPa, for a sample with R= 5 mm.

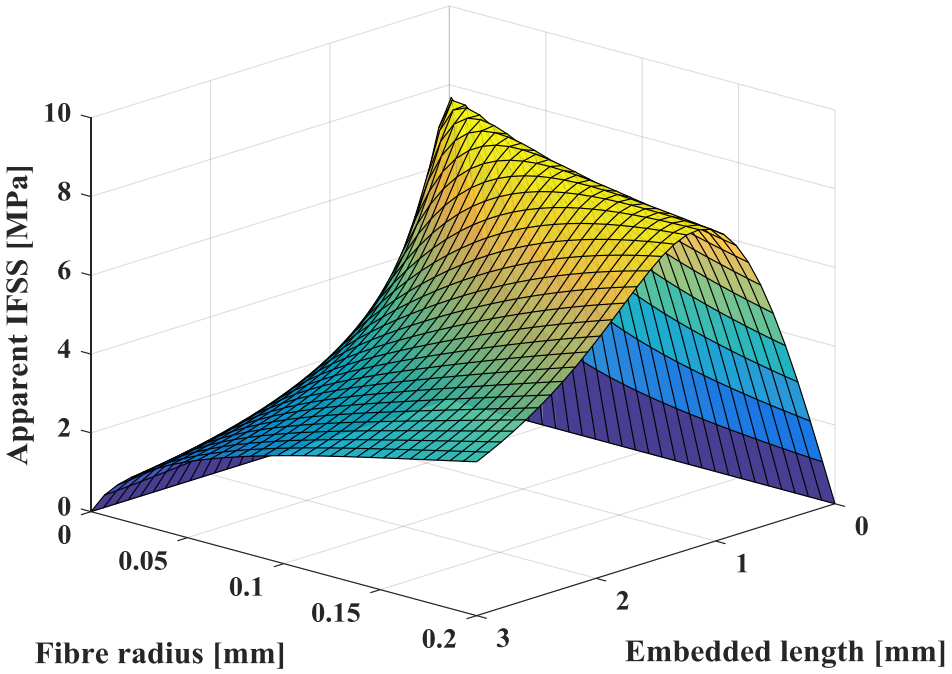

Figure 5.33: Apparent IFSS versus fibre radius and embedded length, for coir fibre and PP579S, according to variational mechanics assuming a debonding criteria σ_{ult}= 5 MPa, for a sample with R= 5 mm.

The four theoretical models were fitted to the experimental observations, using algorithms based on the equations of the theoretical models and the standard least-squares method, to compute the parameters. In this regard, the value of τ_{app}, τ_{ult}, G_{ic} and σ_{ult} were calculated so the respective sums of squared residuals were minimised, (5.35). The total sums of squares were calculated according to (5.36), while the R-squared values, R^2, were calculated according to (5.37). In terms of the application of the shear stress controlled debonding model, proposed by Zhandarov and Pisanova, the value of β, as defined in equation (5.29), was calculated independently for each single pull-out sample. Additionally, individual values of τ_{app}, τ_{ult}, G_{ic} and σ_{ult} for each pull-out test were calculated in order to analyse average values and carry out statistical comparison between M1 and M2.

$$SS_{res} = \sum_{i=1} \left[F_{dexper_i} - F_{dmodel_i}(r, L_e, \dots) \right]^2 \tag{5.35}$$

$$SS_{total} = \sum_{i=1} \left[F_{dexper_i} - \bar{F}_{dexper} \right]^2 \tag{5.36}$$

$$R^2 = 1 - \frac{SS_{res}}{SS_{total}} \tag{5.37}$$

Model	Least-squares fit	
	Value	R^2
τ_{app} [MPa]	2.41	0.61
τ_{ult} [MPa]	5.30	0.37
G_{ic} [J·m^{-2}]	130	0.79
σ_{ult} [MPa]	2.20	0.75

Table 5.3: Theoretical models' results.

The results from the least-squares fittings are listed in Table 5.3. For each model, and based on the calculated parameters, the predicted force $F_{dmodel_i}(r, L_e, \dots)$ for each experimental point is illustrated in Figure 5.34 along experimental coir-PP 579S F_d versus coir embedded length. From the results summarised in Table 5.3, and attending to the R^2 values, it can be seen how the energy controlled debonding and variational mechanics considering adhesional pressure as debonding criteria models obtained the best fitting to the experimental observations $[F_d, L_e, r]_{exper}$. Furthermore, as is shown in Figure 5.34, the models, with the exception of the apparent IFSS model, predict certain scattering of the data when F_d is represented versus the embedded area. In this regard, it should be underlined that coir fibres have an inherent variability of their properties (e.g. Young's modulus), which could affect the accuracy of the predictions in relation to the observations.

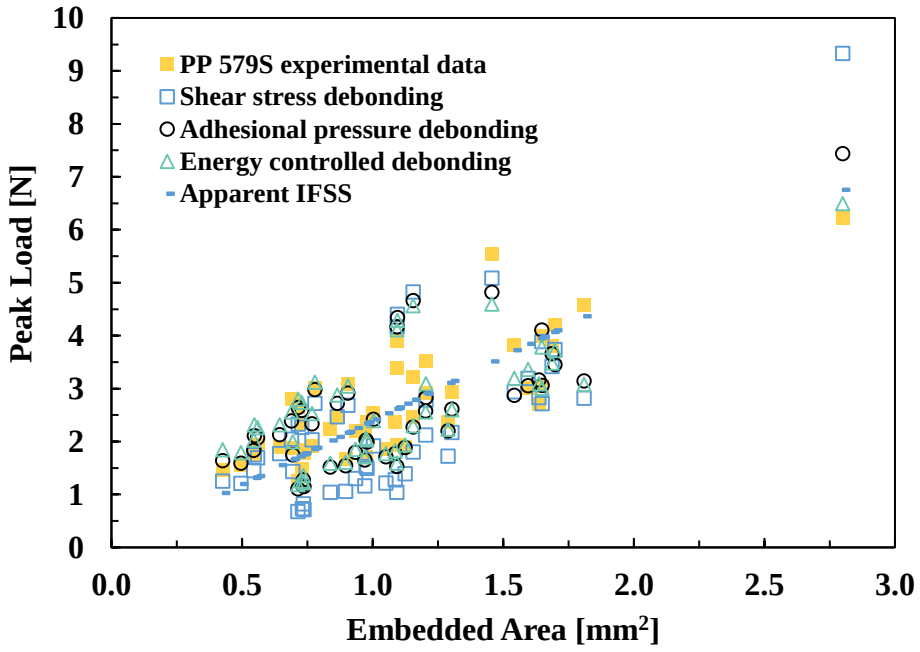

Figure 5.34: Experimental data for coir-PP 579S peak load versus coir's embedded area, and theoretical predictions based on 4 different theoretical models.

In Figure 5.35, coir-PP 579S experimental data for apparent IFSS versus coir embedded length is illustrated along with the predictions from the least-squares fitted theoretical models. With the exception of the τ_{app} model, which predicts a constant apparent IFSS for any embedded length, the other three models predict a similar trend to the one indicated by the experimental observations. In this regard, and for the analysed embedded length range, the apparent IFSS increased for decreasing embedded length. It is necessary to underline that the models were fitted to the experimental observations $[F_d, L_e, r]_{exper}$, and therefore not adjusted to follow any particular trend with regards to the τ_{app} versus embedded length.

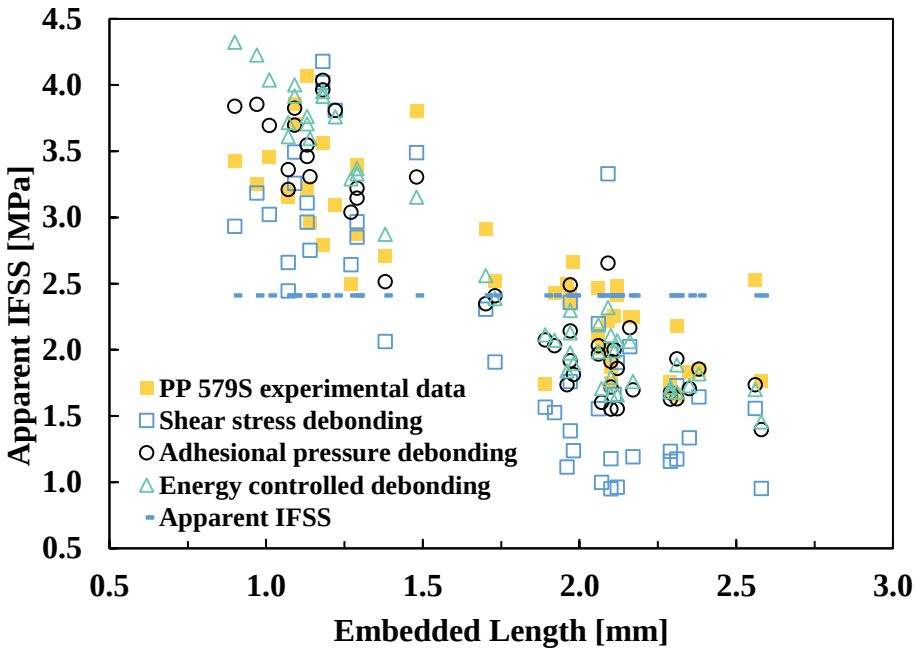

Figure 5.35: Experimental data - apparent IFSS versus embedded length for coir-PP 579S, and theoretical predictions based on 4 different theoretical models.

From these results it is clear that there is a dependency between the τ_{app}, and the pull-out samples' fibre embedded length and radius, which is also predicted by the evaluated theoretical models, with the exception of the τ_{app} model. It was also shown that part of the scattering of the experimental data observed in the peak load versus embedded area graphs, especially relevant if compared with other systems such as glass fibre – PP, could be explained through the higher variability in terms of the samples' fibre embedded length and radius. Although the τ_{app} model does not show

the mentioned dependency, it still remains a valid method for comparing the relative levels of adhesion between two sets with equivalent samples, in terms of fibres' embedded length and radius.

5.3.3 Temperature dependence of the IFSS in coir-polypropylene

Results of the pull-out tests of peak load versus embedded area of coir-PP 579S, using the DMA and the Instron tensile testing machine are shown in Figure 5.36. As in the previous section, to analyse the apparent dependency between τ_{app} and the embedded length, four different theoretical models were used to compare both sets of pull-out data. In this regard, the apparent IFSS model, the shear stress controlled debonding model, the energy controlled debonding, and the variational mechanics approach considering adhesional pressure as debonding criteria, were used to fit the experimental observations from DMA and Instron. Although the values from the least-squares fit are a good indication of the comparability, the values from individual calculations (i.e. from each experimental point) were used to perform a series of two samples *t*-tests to compare both experimental results. The analysis results are summarised in Table 5.4.

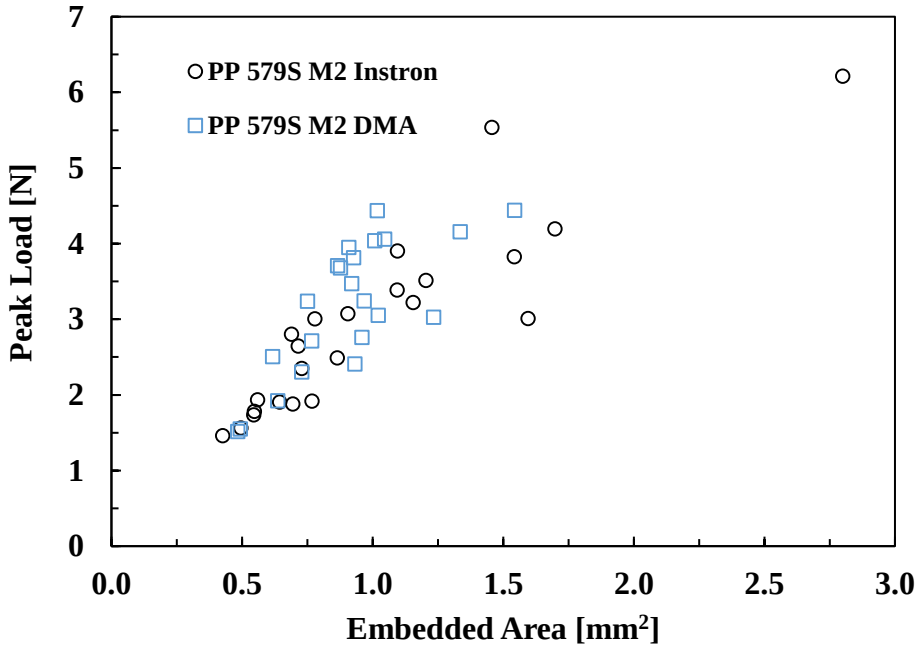

Figure 5.36: Comparison of coir-PP 579S peak load versus embedded area pull-out results from DMA and Instron tensile testing machine.

Model	Instron Pull-out				DMA Pull-out				*p*-value
	Least-squares fit		From individual calculations		Least-squares fit		From individual calculations		
	Value	R^2	Mean	95% Confidence limit	Value	R^2	Mean	95% Confidence limit	
τ_{app} [MPa]	2.73	0.67	3.09	0.23	3.44	0.52	3.53	0.25	0.02
τ_{ult} [MPa]	4.11	0.59	6.38	0.93	3.90	0.32	5.27	1.00	0.13
G_{ic} [J·m^{-2}]	122	0.84	119	10	111	0.65	114	10	0.51
σ_{ult} [MPa]	2.05	0.79	2.13	0.19	1.84	0.54	1.96	0.21	0.24

Table 5.4: Results of the comparison through four different theoretical models.

From the analysis of results it can be seen that, although the two-sample *t*-test showed a significant difference at 95% confidence level (*p*-value = 0.02) between the Instron and DMA data for the apparent IFSS, three of the models showed clear evidence of comparability. In the case of the τ_{app} model, variations in the respective sets' distributions of embedded length and/or fibre radius could lead to the observed results. A two-sample *t*-test revealed a non-significant difference regarding the fibres' radius between the Instron and DMA sets, at 95% confidence level (*p*-value = 0.13). On the other hand, a two-sample *t*-test revealed a significant difference regarding the fibres' embedded length between the Instron and DMA sets, at 95% confidence level (*p*-value = 0.018). In this regard, the average fibre embedded length was 1.35 mm in the Instron and 1.13 mm in the DMA pull-out set. Therefore, as was discussed in the previous section, a higher apparent IFSS is expected for lower average embedded length, which coincides with the trend observed in the analysis of results summarised in Table 5.4.

In relation to the rest of the models, the two-sample *t*-test results from the two models that obtained the best fits to the experimental data (i.e. G_{ic} and σ_{ult}), showed relatively high comparability. As can be seen in Table 5.4, the two-sample *t*-test showed a non-significant difference at 95% confidence level between the Instron and DMA data, for the shear stress controlled debonding (*p*-value = 0.13), the energy controlled debonding (*p*-value = 0.51) and the variational mechanics approach

considering adhesional pressure as debonding criteria (p-value = 0.24). These results provide solid evidence of comparability between both measuring systems.

The DMA pull-out results for peak load versus embedded area for coir-PP 579S and three different temperatures are shown in Figure 5.37. The results obtained for the average apparent IFSS for this system at three different temperatures, with error bars representing 95% confidence limits, are illustrated in Figure 5.38. From these two figures, it can be seen that there is a clear dependency between the apparent IFSS and the testing temperature, as it has been previously observed for other fibre-matrix systems [11, 13]. In this regard, in order to further investigate the temperature dependence of the interfacial properties of coir-PP 579 S, a characterisation of the mechanical properties of fibre and matrix at different temperatures is necessary. This characterisation is required in order to carry out an analysis based on the previously mentioned theoretical models. Such an analysis could potentially demonstrate a dependency between the observed increase of the apparent IFSS to an increase of the residual thermal stresses due to greater temperature increase, ΔT, defined as the difference between the matrix stress free temperature and testing temperature.

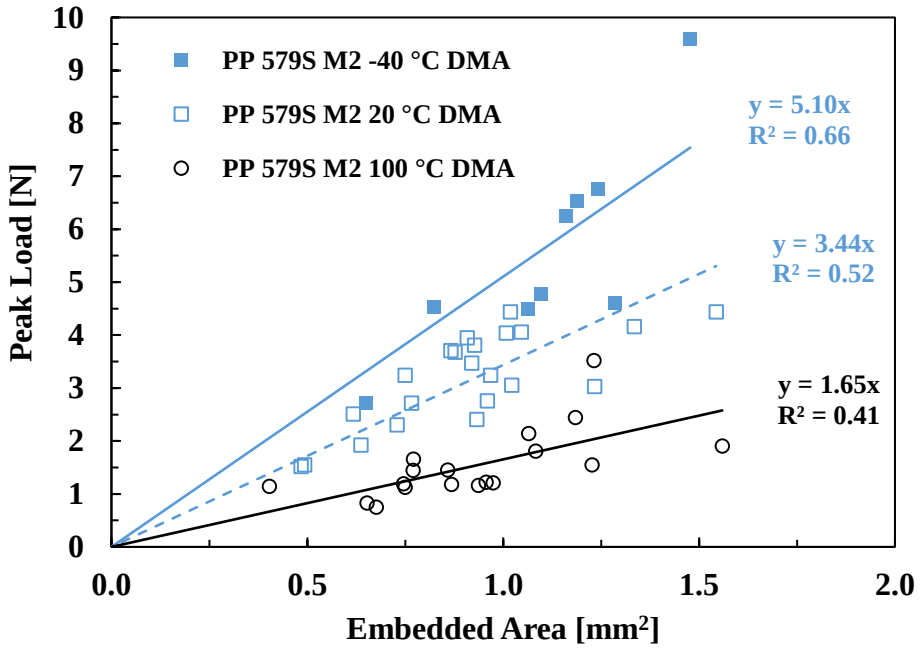

Figure 5.37: DMA pull-out peak load versus embedded area for coir-PP 579S at three different temperatures.

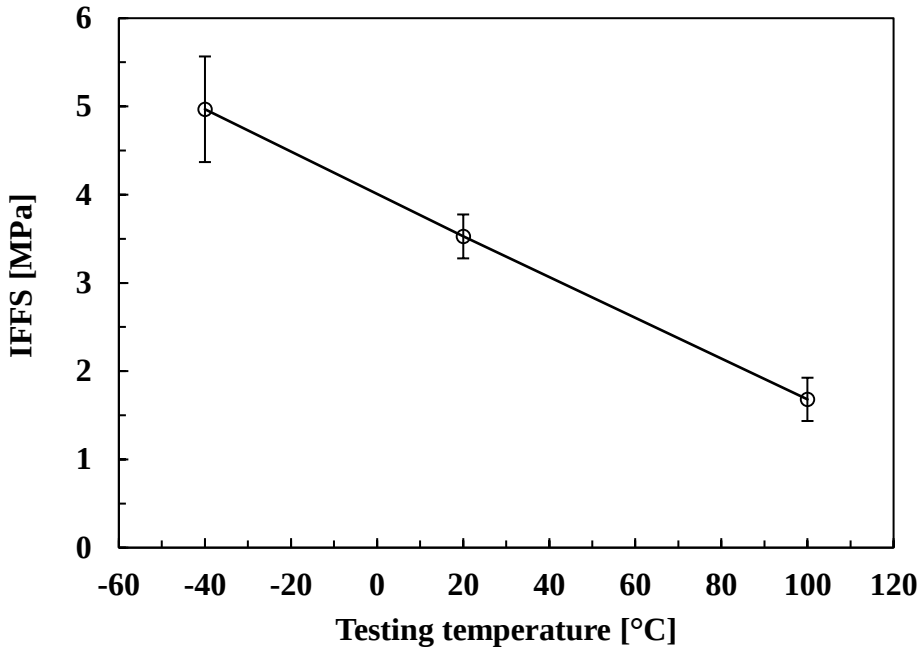

Figure 5.38: Average apparent IFSS of coir-PP 579S versus test temperature.

5.3.4 Room temperature coir-low density polyethylene pull-out study

Results of the pull-out test of coir-LDPE 1922SF system and its respective variation with a 5% MAPE content, carried out with the Instron machine at room temperature are illustrated in Figure 5.23. As was previously described, due to difficulties in demoulding MAPE modified LDPE blocks from the metal moulds, M2 was used to prepare MAPE modified samples.

The value of the IFSS for each system, is represented in the figure as the slope of the least-squares fitted straight line forced through the origin. From the R-squared values showed in the figure, and the individual data points, it can be seen that there is a relatively high scattering of the data. As previously stated, this scattering has also been observed, to different extents, through all the previously analysed systems. The results obtained for the average apparent IFSS, with error bars representing 95% confidence limits, are shown in Table 5.5.

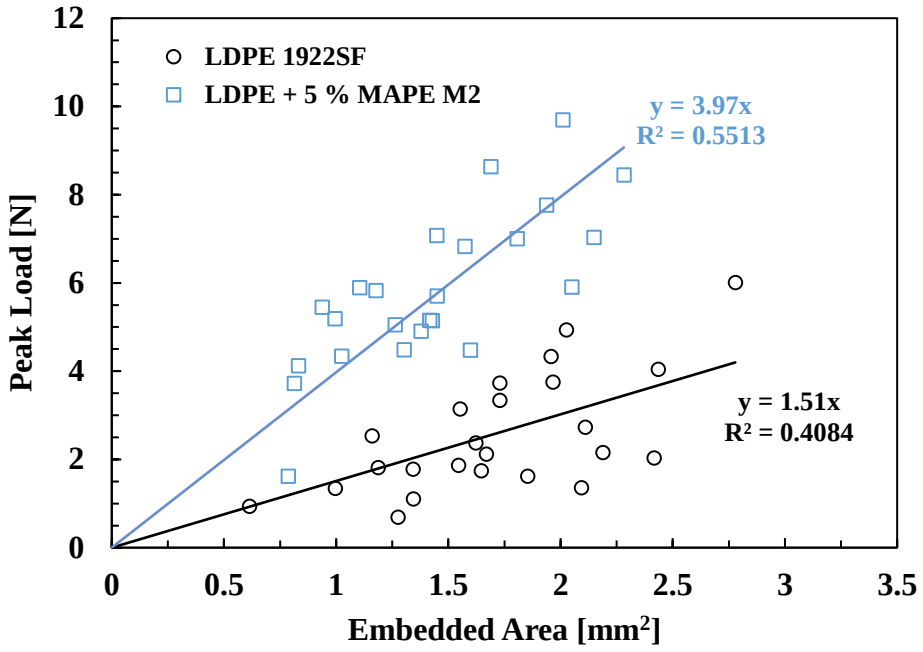

Figure 5.39: Peak load versus coir's embedded area. Results for coir-LDPE 1922SF, based on M1, and its variation with MAPE, based on M2.

Polymer	IFSS [GPa]	
	Mean	95% Confidence limit
LDPE 1922SF	1.4	0.2
LDPE 1922SF + 5% MAPE M2	4.1	0.4

Table 5.5: Apparent IFSS for Coir-LDPE 1922SF and MAPE modification.

A clear increase in the apparent IFSS is observed for the MAPE modified samples, however, it should be noticed that these two experimental sets were produced by different sample preparation methods. Therefore, average and least-squares best fit data could not be directly compared due to the potential dependency of the apparent IFSS on samples' geometry. In this regard, it is expected that samples based on M2 will produce higher apparent IFSS. Although these should be further investigated, these results provide relative evidence of the positive effect of MAPE on the apparent IFSS. Therefore, these results should be only considered as a preliminary study. Further sample testing, which should include LDPE 1922SF based on M2, is required to precisely characterise the interfacial properties of coir-LDPE 1922SF.

5.4 Conclusions

The interfacial properties of coir-thermoplastic systems have been investigated. In this regard, two sample preparation methods, which prevent the thermal degradation of fibre and matrix, were developed. Furthermore, a metallic frame was developed for an Instron tensile testing machine, which enabled the performing of pull-out testing at room temperature. Additionally, a metallic frame was also developed for a DMA Q800 machine, which allowed pull-out testing at various temperatures in a controlled atmosphere.

Pull-out testing of coir-PP 579S and coir-PP 513MNK10 at room temperature, along with their respective MAPP modifications, revealed an overall trend in which the addition of MAPP led to higher apparent IFSS. In the case of PP 579S (i.e. PP homopolymer), the increase of apparent IFSS was only significant between 3 and 5% MAPP content. The measured average apparent IFSS was 2.1 MPa for pure PP 579S and 3.3 MPa for the PP 579S + 5% MAPP. On the other hand, the effect of MAPP on the apparent IFSS of PP 513MNK10 (i.e. copolymer) was more consistent, showing an increase of the average apparent IFSS for increasing MAPP content. The measured average apparent IFSS was 1.6 MPa for PP 513MNK10 and 4.9 MPa for PP 513MNK10 + 10% MAPP.

The relation between the pull-out sample geometry and the apparent IFSS was also investigated. After an apparent dependency of the τ_{app} on the embedded length for the pull-out data generated from coir-PP 579S samples (based on two different sample preparation methods) was observed, four theoretical models were used to analyse the experimental data. All the evaluated theoretical models, with the exception of the τ_{app} model, predicted the observed dependency. It was also shown that part of the scattering of the pull-out experimental data could be related to the high variability in terms of pull-out samples' fibre embedded length and radius. Furthermore, the τ_{app} model was still considered as a valid method of comparison of the relative levels of adhesion between fibre-matrix systems when comparing similar sets in terms of fibres' radius and embedded length.

The temperature dependence of the interfacial properties of coir-PP 579 has also been explored. Good comparability between the room temperature pull-out data from the Instron tensile tester and the DMA machine was observed, according to the analysis based on the energy controlled debonding and variational mechanics approach considering adhesional pressure as debonding criteria. The temperature dependence of the apparent IFSS showed high inverse dependency on the testing temperature. Further characterisation of coir and PP 579S at various temperatures is necessary to evaluate any dependency of the apparent IFSS on the residual thermal stresses, that could arise from differences between coir and PP 579S thermal expansion coefficients.

The initial study of the interfacial properties of coir-LDPE 1922SF system and its respective variation with a 5% MAPE content, revealed an increase of the apparent IFSS for the MAPE modified samples. However, due to differences in the sample preparation, it was concluded that further testing is necessary to precisely characterise the interfacial properties and the impact of MAPE.

5.5 References

1. Hull, D., Clyne, T.W.: An introduction to composite materials. Cambridge University Press (1996).
2. Kim, J.-K., Mai, Y.-W.: Engineered interfaces in fiber reinforced composites. Elsevier (1998).
3. Greszczuk, L.B.: Theoretical studies of the mechanics of the fiber-matrix interface in composites. Interfaces in composites. pp. 42–58. American Society for Testing and Materials Philadelphia, PA (1969).
4. Zhou, L.-M., Kim, J.-K., Mai, Y.-W.: Micromechanical characterisation of fibre/matrix interfaces. Compos. Sci. Technol. 48, 227–236 (1993).
5. Nairn, J.A.: Thermoelastic analysis of residual stresses in unidirectional, high-performance composites. Polym. Compos. 6, 123–130 (1985).
6. Di Landro, L., Pegoraro, M.: Evaluation of residual stresses and adhesion in polymer composites. Compos. Part A Appl. Sci. Manuf. 27, 847–853 (1996).
7. Wagner, H.D., Nairn, J.A.: Residual thermal stresses in three concentric transversely isotropic cylinders: application to composites containing a interphase. Compos. Sci. Technol. 57, 1289–1302 (1997).
8. Thomason, J.L.: Interfacial strength in thermoplastic composites - at last an industry friendly measurement method? Compos. Part A Appl. Sci. Manuf. 33,

1283–1288 (2002).

9. Parlevliet, P.P., Bersee, H.E.N., Beukers, A.: Residual stresses in thermoplastic composites—A study of the literature—Part I: Formation of residual stresses. Compos. Part A Appl. Sci. Manuf. 37, 1847–1857 (2006).

10. Thomason, J.L.: Dependence of Interfacial Strength on the Anisotropic Fiber Properties of Jute Reinforced Composites. Polym. Compos. (2010).

11. Thomason, J.L., Yang, L.: Temperature dependence of the interfacial shear strength in glass–fibre polypropylene composites. Compos. Sci. Technol. 71, 1600–1605 (2011).

12. Yang, L., Thomason, J.L., Zhu, W.: The influence of thermo-oxidative degradation on the measured interface strength of glass fibre-polypropylene. Compos. Part A Appl. Sci. Manuf. 42, 1293–1300 (2011).

13. Thomason, J.L., Yang, L.: Temperature dependence of the interfacial shear strength in glass-fibre epoxy composites. Compos. Sci. Technol. 96, 7–12 (2014).

14. Raghava, R.S.: Thermal Expansion of Organic and Inorganic Matrix Composites: A Review of Theoretical and Experimental Studies. Polym. Compos. 9, 1–11 (1988).

15. Miller, B., Muri, P., Rebenfeld, L.: A Microbond Method for Determination of the Shear Strength of a Fiber/ Resin Interface. Compos. Sci. Technol. 28, 17–32 (1987).

16. Gaur, U., Miller, B.: Microbond method for determination of the shear strength of a fiber/resin interface: Evaluation of experimental parameters. Compos. Sci. Technol. 34, 35–51 (1989).

17. Zhou, L.-M., Kim, J.-K., Mai, Y.-W.: On the single fibre pull-out problem: effect of loading method. Compos. Sci. Technol. 45, 153–160 (1992).

18. Yue, C.Y., Cheung, W.L.: Interfacial properties of fibre-reinforced composites. J. Mater. Sci. 27, 3843–3855 (1992).

19. Piggott, M.R.: Why interface testing by single-fibre methods can be misleading. Compos. Sci. Technol. 51, 965–974 (1997).

20. Beckert, W., Lauke, B.: Critical discussion of the single-fibre pull-out test: does it measure adhesion? Compos. Sci. Technol. 57, 1689–1706 (1998).

21. Zhandarov, S.F., Pisanova, E. V.: The local bond strength and its determination by fragmentation and pull-out tests. Compos. Sci. Technol. 57, 957–964 (1997).

22. Piggott, M.R.: Why the fibre/polymer interface can appear to be stronger than the polymer matrix. Compos. Sci. Technol. 57, 853–857 (1997).

23. Ash, J.T., Cross, W.M., Svalstad, D., Kellar, J.J., Kjerengtroen, L.: Finite element evaluation of the microbond test: Meniscus effect, interphase region, and vise angle. Compos. Sci. Technol. 63, 641–651 (2003).

24. Scheer, R.J., Nairn, J.A.: A comparison of several fracture mechanics methods for measuring interfacial toughness with microbond tests. J. Adhes. 53, 45–68 (1995).

25. Chou, C., Gaur, U., Miller, B.: The effect of microvise gap width on microbond pull-out test results. Compos. Sci. Technol. 51, 111–116 (1994).

26. Zhandarov, S., Mader, E.: Characterization of fiber/matrix interface strength: applicability of different tests, approaches and parameters. Compos. Sci. Technol. 65, 149–160 (2005).

27. Pisanova, E., Zhandarov, S., Mäder, E., Ahmad, I., Young, R.J.: Three techniques of interfacial bond strength estimation from direct observation of crack initiation and propagation in polymer–fibre systems. Compos. Part A Appl. Sci. Manuf. 32, 435–443 (2001).

28. Zhandarov, S., Gorbatkina, Y., Mäder, E.: Adhesional pressure as a criterion for interfacial failure in fibrous microcomposites and its determination using a microbond test. Compos. Sci. Technol. 66, 2610–2628 (2006).

29. Kelly, A., Tyson, W.R.: Tensile properties of fibre-reinfroced metals: Copper/Tungsten and Copper/Molybdenum. J. Mech. Phys. Solids. 13, 329–350 (1965).

30. Kelly, A.: Interface Effects and the Work of Fracture of a Fibrous Composite. Proc. R. Soc. A Math. Phys. Eng. Sci. 319, 95–116 (1970).

31. Lawrence, P.: Some theoretical considerations of fibre pull-out from an elastic matrix. J. Mater. Sci. 7, 1–6 (1972).

32. Desarmot, G., Favre, J.: Advances in pull-out testing and data analysis. Compos. Sci. Technol. 42, 151–187 (1991).

33. Zhandarov, S., Pisanova, E., Mader, E., Nairn, J.A.: Investigation of load transfer between the fiber and the matrix in pull-out tests with fibre having different diameters. J. Adhes. Sci. Technol. 15, 205–222 (2001).

34. Gorbatkina, Y.A.: Adhesive strength in fibre-polymer systems. Ellis Horwood (1992).

35. Zhandarov, S., Pisanova, E., Lauke, B.: Is there any contradiction between the stress and energy failure criteria in micromechanical tests? Part I. Crack initiation: stress-controlled or energy-controlled? Compos. Interfaces. 5, 387–404 (1997).

36. Cox, H.L.: The elasticity and strength of paper and other fibrous materials. Br. J. Appl. Phys. 3, 72–79 (1952).

37. Chua, P.S., Piggott, M.R.: The glass fibre—polymer interface: I—theoretical consideration for single fibre pull-out tests, (1985).

38. Chua, P.S., Piggott, M.R.: The glass fibre-polymer interface: II—Work of fracture and shear stresses, (1985).

39. Chua, P.S., Piggott, M.R.: The glass fibre-polymer interface: III—Pressure and coefficient of friction, (1985).

40. Chua, P.S., Riggott, M.R.: The glass fibre-polymer interface: IV—controlled shrinkage polymers, (1985).

41. Dutschk, V., Pisanova, E., Mäder, E., Schneider, K.: Can the results obtained by microtension and pull-out techniques be compared? Compos. Interfaces. 6, 121–134 (1998).

42. Zhandarov, S.F., Mader, E., Yurkevich, O.: Indirect estimation of fiber/polymer bond strenght and interfacial friction from maximum load values recorded in the microbond and pull-out tests. Part I: local bond strength. J. Adhes. Sci. Technol. 16, 1171–1200 (2002).

43. Tran, L.Q.N., Fuentes, C.A., Dupont-Gillain, C., Van Vuure, A.W., Verpoest, I.: Understanding the interfacial compatibility and adhesion of natural coir fibre thermoplastic composites. Compos. Sci. Technol. 80, 23–30 (2013).

44. Nayfeh, A.H.: Thermomechanically induced interfacial stresses in fibrous composites. Fibre Sci. Technol. 10, 195–209 (1977).

45. Nairn, J.A.: On the use of shear-lag methods for analysis of stress transfer in uniderectional composites. Mech. Mater. 26, 63–80 (1997).

46. Piggott, M.R.: A new model for interface failure in fibre-reinforced polymers. Compos. Sci. Technol. 55, 269–276 (1995).

47. Marotzke, C.: Influence of fiber length on the stress transfer from glass and carbon fibers into a thermoplastic matrix in the pull-out test. Compos. Interfaces. 1, 153–166 (1993).

48. Pisanova, E., Zhandarov, S., Mäder, E.: How can adhesion be determined from micromechanical tests? Compos. Part A Appl. Sci. Manuf. 32, 425–434 (2001).

49. Nairn, J.A.: A variational mechanics analysis of the stresses around breaks in embedded fibers. Mech. Mater. 13, 131–154 (1992).

50. Scheer, R.J., Nairn, J.A.: Variational mechanics analysis of stresses and failure in microdrop debond specimens. Compos. Eng. 2, 641–654 (1992).

51. Fuentes, C.A., Brughmans, G., Tran, L.Q.N., Dupont-Gillain, C., Verpoest, I., Van Vuure, A.W.: Mechanical behaviour and practical adhesion at a bamboo composite interface: Physical adhesion and mechanical interlocking. Compos. Sci. Technol. 109, 40–47 (2015).

52. Keener, T.J., Stuart, R.K., Brown, T.K.: Maleated coupling agents for natural fibre composites. Compos. Part A Appl. Sci. Manuf. 35, 357–362 (2004).

53. Wambua, P., Ivens, J., Verpoest, I.: Natural fibres: Can they replace glass in fibre reinforced plastics? Compos. Sci. Technol. 63, 1259–1264 (2003).

54. Park, J.-M., Quang, S.T., Hwang, B.-S., DeVries, K.L.: Interfacial evaluation of modified Jute and Hemp fibers/polypropylene (PP)-maleic anhydride

polypropylene copolymers (PP-MAPP) composites using micromechanical technique and nondestructive acoustic emission. Compos. Sci. Technol. 66, 2686–2699 (2006).

55. George, J., Sreekala, M.S., Thomas, S.: A Review on Interface Modification and Characterization of Natural Fiber Reinforced Plastic Composites. Polym. Eng. Sci. 41, (2001).

56. Li, X., Tabil, L.G., Panigrahi, S.: Chemical Treatments of Natural Fiber for Use in Natural Fiber-Reinforced Composites: A Review. J. Polym. Environ. 15, 25–33 (2007).

57. Sanadi, A.R., Caulfield, D.F.: Transcrystalline interphases in natural fiber-PP composites: effect of coupling agent. Compos. Interfaces. 7, 31–43 (2000).

58. Gassan, J., Bledzki, A.K.: The influence of fiber-surface treatment on the mechanical properties of jute-polypropylene composites. Compos. Part A Appl. Sci. Manuf. 28, 1001–1005 (1997).

59. Bledzki, A.K., Reihmane, S., Gassan, J.: Properties and modification methods for vegetable fibers for natural fiber composites. J. Appl. Polym. Sci. 59, 1329–1336 (1996).

60. Mohanty, K.A., Drzal, L.T., Misra, M.: Engineered natural fiber reinforced polypropylene composites : influence of surface modifications and novel powder impregnation processing. J. Adhes. Sci. Technol. 16, 999–1015 (2002).

61. Kazayawoko, M., Balatinecz, J.J., Matuana, L.M.: Surface modification and adhesion mechanisms in woodfiber-polypropylene composites. J. Mater. Sci. 34, 6189–6199 (1999).

62. Mohanty, A.K., Drzal, L.T., Misra, M.: Novel hybrid coupling agent as an adhesion promoter in natural fiber reinforced powder polypropylene composites. J. Mater. Sci. Lett. 21, 1885–1888 (2002).

63. López Manchado, M.A., Arroyo, M., Biagiotti, J., Kenny, J.M.: Enhancement of Mechanical Properties and Interfacial Adhesion of PP/EPDM/Flax Fiber Composites Using Maleic Anhydride as a Compatibilizer. J. Appl. Polym. Sci. 90, 2170–2178 (2003).

64. Thomason, J.L., Carruthers, J., Kelly, J., Johnson, G.: Fibre cross-section determination and variability in sisal and flax and its effects on fibre performance characterisation. Compos. Sci. Technol. 71, 1008–1015 (2011).

65. Cichocki Jr., F.R., Thomason, J.L.: Thermoelastic anisotropy of a natural fiber. Compos. Sci. Technol. 62, 669–678 (2002).

66. Gentles, F.L.: Characterisation of environmentally friendly fibres for composites. PhD Thesis. University of Strathclyde (2015).

Chapter 6 Mechanical characterisation of coir-thermoplastic composites

6.1 Introduction / Literature review

Natural fibre reinforced thermoplastic composites (NFTCs) have shown potential to compete with mineral/inorganic fibre and filler reinforced composites in certain applications due to their distinctive characteristics [1–12]. NFTCs denote a more environmentally friendly product which offers low density and high specific strength and stiffness, biodegradability, negligible health hazards and an overall reduced carbon footprint. A reduced production energy is especially significant when comparing glass fibre (GF) with natural fibre (NF) (approximately 82% saving in the energy required to produce a flax-fibre mat compared to a glass-fibre mat [2]). The benefits of energy saving are also extended through products' lifetime in the case of applications where the energy consumption is related to weight (e.g. automotive industry). Furthermore, in sectors like the automotive, the increased interest in NFTCs has been driven not only by the importance of using more environmentally friendly and cost efficient materials but also by governmental regulations.

In parallel, during the past decades, there has been a strong growth in the applications for mineral/inorganic fibre and filler reinforced thermoplastic composites. Mass processability and high performance have allowed these composites to be successfully used over a range of different products. Nevertheless, the increasing pressure on natural resources, cost competitiveness, society's growing environmental awareness as well as energy and environmental regulations (among others) have also driven an increasing interest in NFTCs. In this regard, polypropylene is one of the most used polymers in NFTCs due to its versatility and relatively low melting temperatures, allowing for composite processing temperatures around 200 °C, which prevents full degradation of NFs [13].

Despite the mentioned advantages, major technical issues must be addressed before a wide-scale implementation of NFTCs is possible. In this regard, issues with impact resistance –notched impact (NI) and un-notched impact (UI)– are particularly relevant

[5, 14]. Moreover, it should also be mentioned that, when analysing the potential of NFs for the substitution of human-made mineral/inorganic fibres such as GF, the anisotropy of NFs and their extremely low transverse properties are often ignored. In this regard, NFs' transverse and shear properties are orders of magnitude lower than their axial modulus values [14], which in many cases leads to overestimating their real reinforcement potential.

6.1.1 Tensile properties

This section focuses on the literature review of tensile properties of coir reinforced injection moulded PP composites. The tensile properties of the NFTCs are determined by the individual properties of the fibre and matrix materials, the interfacial bonding between them, and fibre dimensions and aspect ratio distributions [15, 16]. In this regard, one of the main issues, as discussed in Chapter 5, is the relatively low chemical compatibility between natural fibres (hydrophilic) and the hydrophobic polymer. For this reason, composite failure will be often related to interface failure.

Bettini et al. [13] observed a decrease in the tensile strength and elongation at break with increasing coir content. This trend was attributed to a lack of fibre-matrix load transfer due to poor adhesion. Furthermore, it was pointed out that in this case, fibres may act as stress concentrators. When adding compatibilizer, in this case maleic anhydride grafted polypropylene (MAPP), the tensile strength increased while the elongation at break decreased for increasing fibre content. This behaviour was related to the improved fibre-matrix interaction. Moreover, it was also observed that the increase of the amount of compatibilizer did not affect the mentioned properties.

Haque et al. [17–19] observed a decrease of the tensile strength of injection moulded raw coir reinforced PP for increasing fibre load, which was attributed to a weak interfacial area. On the other hand, for coir fibre chemically treated with benzene diazonium salt, an initial increase of the tensile strength was observed for 10% fibre content. However, further increasing fibre content above 10% led to a decrease of the tensile strength. With regards to the Young's modulus, an increase was observed for increasing fibre content, which was more significant in the case of treated fibres. The higher modulus observed for treated fibres composites was attributed to an improved interfacial bonding. In a later study, Haque et al. [20] also analysed the effect of the

p-aminophenol treatment on the performance of coir reinforced PP. As previously observed, composites with treated fibres obtained higher tensile strength for initial loading at 10% of coir, but decreased for increasing fibre load (i.e. 15, 20, and 25%). The relative increase between non-treated and treated composites was again linked to an improved interfacial adhesion. It was also pointed out how an increase of fibre content could result in increasing "micro-spaces" within the fibre-matrix interfacial region and fibre agglomeration, which will ultimately lead to a decrease of the tensile strength. Regarding the Young's modulus, an increase was observed for increasing fibre load. As it was showed for the previous studies, a higher increase was measured for composites with treated fibres.

In a similar study by Islam et al. [21], the effect of treating coir fibres with o-hydroxybenzene diazonium salt, on the mechanical performance of injection moulded coir reinforced PP, was analysed. The tensile strength of treated coir reinforced PP was higher at all evaluated fibre contents (i.e. 10, 15, 20, and 25%) in comparison to neat PP. However, and as previously observed, in relation to the composite with 10% fibre load, the tensile strength decreased for increasing fibre load. Moreover, the Young's modulus increased for increasing fibre load. The measured values were higher in the case of the composites with treated fibres. In general terms, the improvement in composites' properties with treated fibres was attributed to an increased fibre-matrix interfacial bonding.

Nandi et al. [22] analysed the effect of coupling agent concentration on the mechanical properties of injection moulded coir reinforced PP composites. The coupling agent used in this study was m-isopropenyl-α-α-dimethylbenzyl isocyanate grafted polypropylene. The authors observed an increase of the tensile strength for increasing coupling agent concentration for composites with 40% of fibre load, reaching a maximum between 5 and 7% of coupling agent concentration, after which the composite strength decreased.

6.1.2 Impact properties

In this section, due to the low amount of literature regarding the impact properties of injection moulded coir reinforced PP, a broader look into NFTCs' literature has been carried out. In relation to the impact performance of NFTCs, the impact energy

is absorbed mainly by three different mechanisms: fibre debonding, fibre pull-out and matrix and/or fibre fracture and deformation [23, 24]. Composite fracture energy is also often analysed in terms of the crack initiation, mainly related to un-notched impact strength (UI), and crack propagation, mainly related to notched impact strength energy (NI). Depending on the kind of impact test and composite's characteristics, these mechanisms will differently influence the crack initiation and propagation phenomena. Factors such as the nature of the matrix polymer, fibre content, fibre characteristics and level of interfacial bonding will influence the composites' complex impact behaviour [25]. Regarding fibre's properties, it is necessary to consider aspects such as the fibre length, diameter, aspect ratio and micro-fibril angle (MFA) –composite systems with fibres with high MFA show higher fracture energy in comparison with system with low MFA fibres [1].

In general, it has been observed that the inclusion of NFs in thermoplastics lead to a reduction of the impact strength. Two main mechanisms by which the fibres could reduce composites' impact strength [25, 26] have been identified: 1) Fibres tend to decrease the maximum strain of the composites' stress-strain curves. Fibres could reduce the deformation and ductility of the polymer matrix, reducing the ability of the composite to absorb energy during crack propagation. 2) Fibres could create regions of high stress concentration where the energy required to initiate a crack is less than in other regions. Stress concentrations may occur at regions around fibre ends, areas of poor adhesion and regions where the fibres touch one another.

In order to address the lack of impact resistance, four main paths of improvement are normally considered: 1) Improve the distribution of the fibre or filler in the matrix, e.g. using a dispersing agent [27]. 2) Improve fibre properties, e.g. fibre treatments. 3) Improve matrix properties, e.g. using a small amount of elastomer to further toughen a brittle thermoplastic. 4) Optimise the stress transfer capability of the fibre-matrix region in order to achieve good performance levels in the composite materials [14]. This last option is often challenging due to the poor chemical compatibility between natural fibres (mostly made of polar materials) and the non-polar matrix, in the case of most thermoplastics. Maleic anhydride modified polymers (MAPs) and silane modifications of the matrix and/or fibre have not been as successful as expected when compared with human-made mineral/inorganic fibres [14, 28].

When addressing NFTCs issues, it is extremely important to remark that each different fibre-matrix combination should be analysed independently due the large variability in terms of dimensions, mechanical properties of the different kinds of NFs and significant variability of properties depending on the plant's area of extraction [29]. The following sub-sections will analyse in more detail the effects of different parameters, such as fibre content or amount of compatibilizer, in the NI and UI strengths of NFTCs. The variety of thermoplastic matrix materials, fibres, test conditions and number of fibre contents found in literature is surely very extensive. In this regard, from this analysis of the literature, it has been certainly significant that similar studies, have observed opposite results and/or trends.

6.1.2.1 Fibre content

With regards to NI strength, which is related to the crack propagation phenomenon, a positive correlation between fibre content and NI strength has been observed in several studies [13, 24, 30–42]. According to some authors, with an increasing fibre content, the energy absorbed through the pull-out mechanism will also increase [13, 41]. For some NFTCs, this mechanism was reported to be the main contributor to the total impact energy absorption [41, 43]. Moreover, it has been reported that the stress distribution will also improve [35]. However, in some cases, the increase in the NI properties is attributed to an improvement of the fibre-matrix interface at the optimum fibre content [33]. In the case of a positive correlation, an optimum reinforcement content was often observed, after which the NI strength decreases. This observation may indicate that different mechanisms may be involved in the energy absorption process. At high fibre contents, the reasons proposed for a decrease include: 1) Decrease in interfacial adhesion in relation to the optimum point [35]. 2) Fibre agglomeration, which leads to poor wetting areas and fibre-fibre contact regions [35, 40, 41].

On the other hand, an inverse correlation between NI strength and fibre content has been shown in some studies [26, 42, 44–52]. The reasons indicated for this behaviour were: 1) Change in the nature of the fracture from ductile to brittle, which results in the reduction of the deformability of the polymer [36, 47]. 2) Fibre agglomeration [36,

45]. 3) Increase in the number of stress concentration points at fibre ends [45]. 4) Poor interfacial adhesion [48].

When analysing the different behaviours in relation to the NI strength, with direct or inverse correlations, the reinforcements' aspect ratio and surface characteristics are found to be two of the main factors [38]. In relation to the interface properties, opposing arguments were identified. It has been suggested that a better fibre-matrix adhesion and compatibility will lead to higher impact strength [33, 35, 39, 48]. On the other hand, it has also been pointed out that poor adhesion systems could lead to higher energy absorption [40, 43].

In terms of UI strength, a direct correlation has been observed by a number of authors [43, 53–55]. However, an inverse correlation was also observed in different studies [30, 46, 56–58]. It has been reported that UI strength is related to the energy dissipated by plastic flexural deformation preceding crack initiation [46]. Fibre agglomeration [30] has also been linked to a reduction of the energy required to initiate a crack. As in the case of the NI strength, the nature of the matrix, fibres and interface combine together to determine the impact strength dependence on fibre content.

6.1.2.2 Fibre length

A direct correlation between NI strength and fibre length was reported by different studies [24, 31, 33, 59]. An opposing trend was also reported elsewhere [49]. It has been pointed out that an increase in the fibre length could lead to an improved stress transfer and reduction of high stress concentration points at fibre ends [59]. As in the case of fibre content dependence, an optimum fibre length was reported in some of the studies, for which the impact strength was maximum. If debonding and pull-out mechanisms are assumed to be main contributors to the absorbed energy [24, 41, 43], the optimum fibre length will be critical to maximise the overall absorbed energy.

6.1.2.3 Compatibilizers and Polymer Coupling Agents

An increase in the NI strength of NFTCs by the addition of compatibilizer has been observed in several studies [26, 36, 42, 44, 45, 59–66]. The argument used to explain the higher properties is often related to an increase in the fibre-matrix adhesion/compatibility, which leads to higher energy required for crack propagation

[26, 45, 63]. Interestingly, a similar argument is also used to explain a decrease of the NI strength, where high fibre-matrix compatibility leads to lower energy absorbed by the pull-out mechanism [13, 41, 67]. Some studies did not report any significant change in the NI strength [67, 68]. In contrast, negative effects were reported by numerous studies [13, 30, 37, 41, 42, 64, 66, 69–71]. At high MAPP concentrations, it has been suggested that the NI strength could decrease due to a self-entanglement effect between the compatibilizer, resulting in fibre slippage [30].

In terms of the UI strength, the addition of compatibilizer has led to an increase of UI strength in several studies [27, 30, 60, 61, 63, 66, 69, 72]. Explanations often mentioned for these increases in UI strength were: 1) Increase in the fibre adhesion [63, 72]. 2) Improved fibre dispersion [72]. However, an inverse correlation between compatibilizer and UI strength has also been reported by some authors [53, 66].

In general terms the optimum fibre-matrix adhesion appears to be crucial. High levels of adhesion may lead to brittle failure while low levels may result in low pull-out energy absorption [69]. Furthermore, as discussed in other sections, the fibre aspect ratio appears to be critical for the effect of compatibilizers [30, 60, 61]. In systems where fibre length is lower than the critical fibre length, it has been shown that the coupling agents have low influence on the NI strength or crack propagation phenomenon but high influence on the UI strength related to crack initiation [27, 60, 61, 73]. Even if debonding and pull-out mechanisms are diminished by increasing fibre-matrix adhesion, the energy dissipated is balanced by a tougher interphase. On the other hand, it has been pointed out that weaker interfaces could lead to higher NI energy [67, 70]. At the same time, in the case of filler reinforcements, lower particle size will give a higher UI strength due to lower stress concentrations. Furthermore, it has been pointed out that the fibre transverse/lateral strength has great influence on the fibre pull-out length [53]. Consequently, it has been suggested that the use of elementary fibres instead of fibre bundles will improve UI strength [53]. Moreover, it has also been suggested that the improvement in the fibre-matrix interfacial bonding will not necessarily increase the impact properties of randomly oriented natural fibre composites due to the possibility for the failure to appear not only at the fibre-matrix interface but also within the fibre bundles' internal structure [74]. In this regard, the fibre internal architecture could contribute to an energy dissipation mechanism.

6.1.2.4 Impact modifiers

The addition of impact modifiers (e.g. rubber particles) have been shown to increase NI strength in several studies [25, 51, 75–78]. Regarding UI strength, positive effects have also been observed by different authors [25, 77, 79]. Regarding the NI strength, it was suggested that there is a high dependency on the impact modifier and much lower dependency on fibre content [75]. In the cases where increasing fibre-matrix compatibility leads to a suppression of the fibre-matrix debonding and pull-out phenomenon, and when rubber particles were present, the main energy absorption mechanisms are related to the deformation of these rubber particles and to fibre breakage [76]. Moreover, it has been suggested that the addition of impact modifier might delay crack initiation and propagation phases of the impact event [76]. This last observation seems to be in conflict with studies where other authors pointed out that crack initiation energy is not dependent on the presence of impact modifiers, which mainly influence crack propagation and plastic deformation energy [73]. Some studies identified different sources of impact improvement, where an increase in fibre-matrix interfacial adhesion, as a result of the presence of impact modifiers, reduced polymer mobility and prevented fibre pull-out, ultimately leading to an increase in the NI strength [78]. Regarding the UI behaviour, it has been pointed out that the elastic behaviour of the impact modifiers can lead to an increase of the UI strength [79].

6.1.2.5 Modification and post-treatments of fibres and composites

With regards to NI strength, an increase in composite performance has been observed for various treatments: 1) Silane treatments [62] due to an improved interfacial adhesion and ductile interface. 2) Maleic anhydride grafted polymer fibre treatments [33–35] where the increase of the impact properties was also related to an improved fibre-matrix adhesion. 3) Other treatments were also successful [20, 21, 49, 52, 67, 80–84] in increasing the impact properties by, according to the authors, creating more ductile [21, 80, 83] and stronger fibre-matrix interfaces [20, 21, 82, 83]. On the other hand, it has also been reported that certain treatments had negative effects on NI [70] also attributed to improved interface properties, which ultimately led to a decrease of the impact strength. Furthermore, some authors [33] seem to be in contradiction

with results from different studies [27, 73] where it was stated that MAPP did not affect the crack propagation process, and therefore the NI strength.

In terms of UI, positive effects on the performance have been observed by several studies [85–89]. An improved fibre dispersion [85, 88, 89] and fibre-matrix adhesion [87–89] were postulated as main reasons for the increase. Negative effects on the UI strength were also reported elsewhere [85]. The suppression of debonding and pull-out mechanisms due to an improved fibre-matrix adhesion was stated as the main reason for the decrease of the impact properties. Some studies have reported no significant influence of the treatments investigated [17, 18, 90–92], or inconsistent results [93].

Regarding the detailed effect of treatments, it has been reported that excessive treatment time can degrade fibres' mechanical properties [35]. Furthermore, an excessive amount of MAPE applied on the fibres could lead to fibre slippage [35], therefore reducing composite impact properties. As discussed in preceding sections, an optimum level of interfacial adhesion is proposed as being crucial in order to increase the impact properties [80]. Mechanisms involved in energy absorption during fracture such as matrix shear yielding could be enhanced by fibre pull-out [80]. Regarding NI strength, a more ductile interface could prevent brittle failure of the interface due to the stress relaxation at the fibre-matrix interface. Silane treatments could create a higher stiffness interface that inhibits plastic deformation and ultimately leads to lower absorbed energy [80]. On the other hand, in the case of UI strength, improved interfacial adhesion by NaOH-silane treatment has led to increased impact properties [87]. In the case of the effect of improved fibre-matrix interface, it is important to point out that this argument is used by different authors to explain opposing observations. As discussed in previous sections, the nature of matrix and fibre will determine the effect of an improved interface on composite impact properties.

6.2 Experimental

6.2.1 Materials

As mentioned in previous chapters, coir fibres, along with all polymers included in this study were supplied by SABIC. In terms of PPs, homopolymer SABIC® PP 579S and copolymer SABIC® PP 513MNK10 with a melt flow rate (MFR) (230 °C and 2.16Kg) of 47 and 70 g/10 min respectively, were used in the following studies. Maleic anhydride grafted polypropylene (MAPP) Exxelor™ PO 1020 (maleic anhydride content is typically in the range of 0.5 to 1 wt%), with a MFR (230 °C and 2.16Kg) of 430 g/10 min, was used as modifier/coupling agent. The effect of MAPP on the properties of coir-PP composites was investigated for 0, and 5 wt% MAPP content. In order to compare the properties of coir reinforced composites with other mineral fillers, Talc (Jetfine® E3CA) was used in this study.

In the case of LDPE, SABIC® LDPE 1922SF, with a melt flow rate (190 °C and 2.16Kg) of 22 g/10 min, was used. Maleic anhydride modified high density polyethylene (MAPE) POLYBOND® 3029 by ADDIVANT (maleic anhydride content is typically in the range of 1.5 to 1.7%), with a MFR (190 °C and 2.16Kg) of 4 g/10 min, was used as a modifier/coupling agent. The effect of MAPE on the properties of coir-LDPE composites was investigated for 0, and 5 wt% MAPE content.

6.2.2 Injection moulding of bars

For polypropylene based composites, formulations of both PP (homopolymer and copolymer) and their respective 5 wt% MAPP modifications along with coir fibre loadings of 10, 20 and 30% by weight were made by SABIC. Formulations of PP 579S reinforced with talc loading of 10, 20 and 30% by weight were also made. These formulations were then melt mixed between 180-200 °C using an intermeshing, twin screw extruder of Coperion make (Model ZSK-25). A 25 mm screw diameter was used for compounding and screw rotation was maintained at 300 revolutions per minute (RPM) during the melt mixing. All the formulations were extruded into strands, which subsequently were cut into cylindrical shaped pellets using an inline strand cutter.

Compounded pellets were dried at 80 °C for a minimum of 4 hours in a hot air circulated oven. Subsequently, pellets were injection moulded into standard test specimens using LT Demag 100 ton injection moulding machine of L&T Make. Barrel zones were electrically heated and were maintained between 180-200°C and the screw speed was 80 RPM. The mould was maintained at ambient temperature.

A similar process was followed for the LDPE based composites, where formulations of LDPE 1922SF (homopolymer and copolymer) and its respective 5 wt% MAPE modifications along with coir fibres loading of 10, 20 and 30% by weight were made. These formulations were then melt mixed using an extruder at a lower temperature than in the case of PP, reaching a maximum temperature of 180 °C. Compounded pellets were dried and subsequently injection moulded into standard test specimens. Barrel zones were electrically heated and a maximum temperature of 170 °C was reached in the last zone.

6.2.3 Tensile testing

Tensile testing of injection moulded bars was carried out according to ISO 527-2/1A/1 [94], using an Instron 5969 with a 50 KN load cell. Five samples were characterised for each set. All results are illustrated with error bars representing 95% confidence limits.

6.2.4 Impact testing

Notched and un-notched charpy impact strength were measured at room temperature according to ISO 179-2 [95] with edgewise impact using a Tinius Olsen Model Impact 503. Notched samples were manufactured based on ISO 179-1/1eA [96]. Ten samples were characterised for each set. All results are illustrated with error bars representing 95% confidence limits.

6.2.5 Observation of composites

6.2.5.1 Fibre observation

In order to qualitatively observe the fibre diameter and length distributions within the injection moulded composites, films of approximately 2 mm thick were formed. The films were made by placing a small cut section of approximately 20 mm of an

impact composite bar (i.e. width of 10 mm and thickness of 4 mm) on a glass slide, which was, at the same time, placed on a hot plate. When the polymer began to melt, and the composite block softened, they were compressed with the help of a second glass slide until a film of approximately 2 mm thick was formed. The temperatures used to form the films were 220 °C for PP composites and 180 °C for LDPE composites. The resulting films were thereafter observed using the scanner of an IDM FASEP fibre length measurement system.

6.2.5.2 Fracture surface after impact testing

The fracture surfaces of Charpy tested composites were gold coated and photographed using a Tungsten Filament Scanning Electron Microscope (W-SEM) HITACHI S-3700.

6.3 Results and discussion

6.3.1 Tensile properties

6.3.1.1 Tensile properties of PP composites

The tensile properties of coir and talc reinforced PP injection moulded composites are illustrated in Figure 6.1-3 and Table 6.1. It can be seen in Figure 6.1 that, in general, the Young's modulus increased for increasing coir fibre content. Regarding the effect of the MAPP on the Young's modulus, although a slight increase was observed for MAPP modified composites, a series of two-sample *t*-tests revealed non-significant differences, at 95% confidence levels, with the exception of the PP 513MNK10 / +5% MAPP + 10% coir (*p*-value = 0.04). This increase of performance, due to the increase in reinforcement content, is in agreement to what was observed by other authors [17–21]. On the other hand, in this study, an improvement in the fibre-matrix interfacial bonding due to the addition of MAPP, as measured in chapter 5, did not lead to a significant increase of the Young's modulus. When comparing the results from coir reinforced PP 579S with the equivalent composites reinforced with talc, it can be seen that the increase of the Young's modulus is significantly higher in the case of talc reinforced composites.

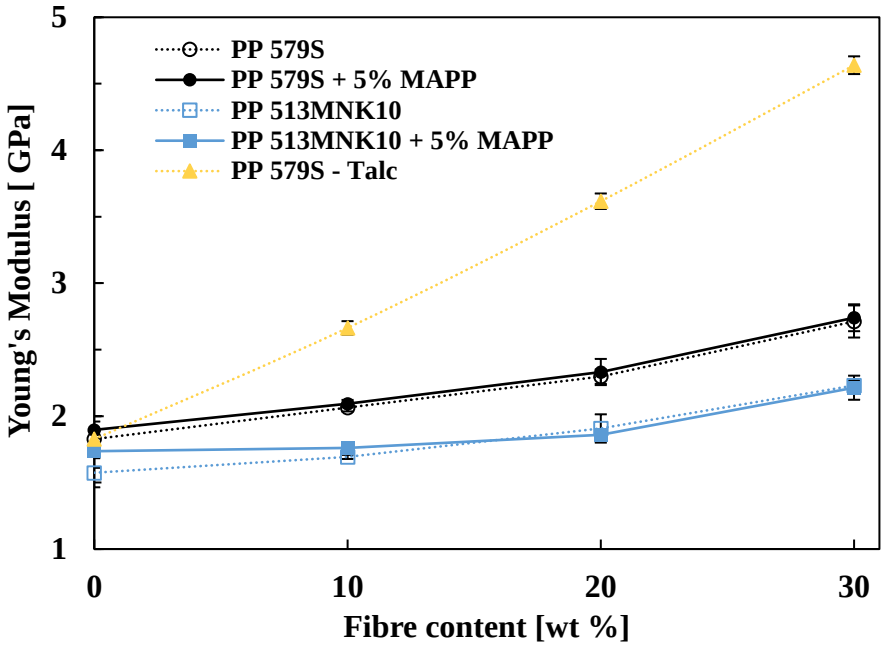

Figure 6.1: Young's modulus of coir and talc reinforced PP injection moulded composites.

Concerning the tensile stress at maximum load, the behaviour of non-modified and MAPP modified composites was considerably different, in contrast with what was previously discussed in the case of Young's modulus. For coir reinforced PP 579S composites, the average tensile stress at maximum load decreased for increasing fibre load. On the other hand, in the case of MAPP modified PP 579S composites, although a slight decrease was observed for 10% fibre load, thereafter, the tensile stress at maximum load increased for increasing fibre load. A similar behaviour was also identified for PP 513MNK10 based composites. In the case of non-modified composites, the average tensile stress at maximum load initially decreased with the addition of 10% coir. After this point, the average values slightly increased for 20 and 30% coir. In comparison, and as observed for PP 579S, the increase was clearly higher for MAPP modified composites. In the case of talc reinforced composites, after an initial increase with the addition of 10% talc, the tensile stress at maximum load did not change considerably.

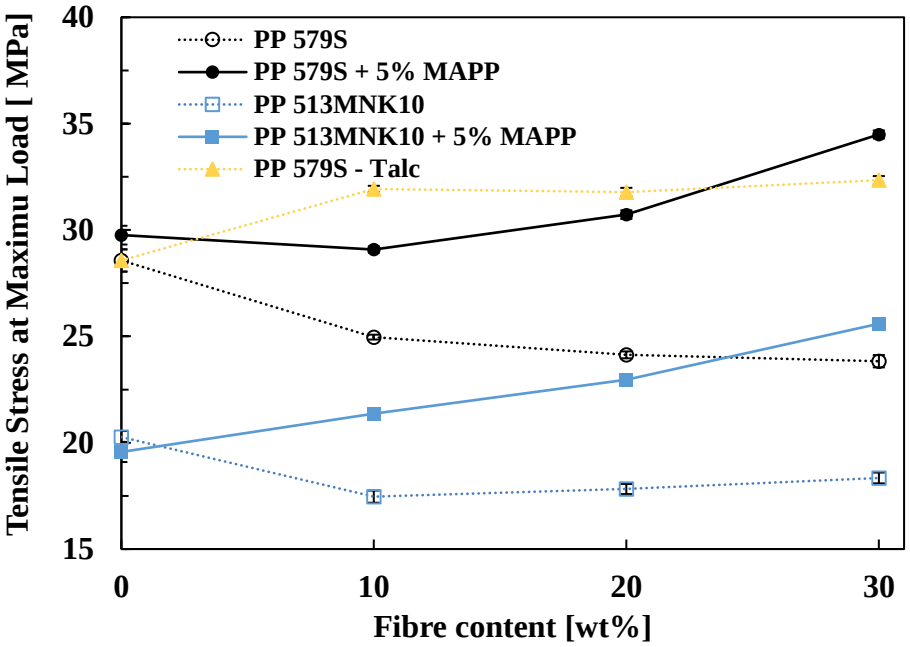

Figure 6.2: Tensile strength of coir and talc reinforced PP injection moulded composites.

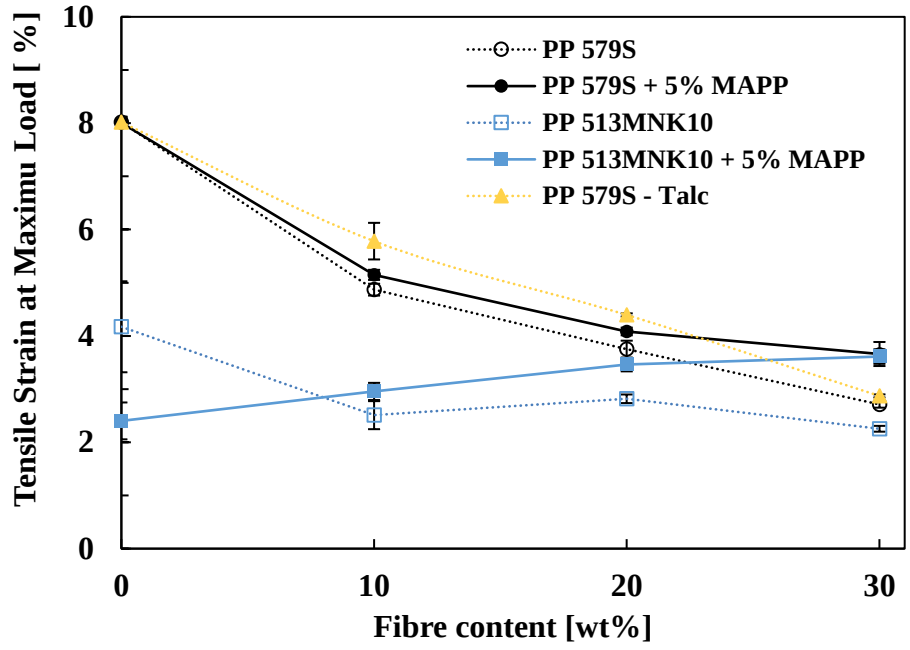

Figure 6.3: Tensile strain at maximum load of coir and talc reinforced PP injection moulded composites.

Sample	Young's Modulus [GPa]		Tensile Stress at Maximum Load [MPa]		Tensile Strain at Maximum Load [%]	
	Mean	95% Confidence limits	Mean	95% Confidence limits	Mean	95% Confidence limits
PP579S	1.827	0.064	28.6	0.5	8.0	0.9
PP579S + 10% Coir	2.063	0.028	25.0	0.1	4.9	0.1
PP579S + 20% Coir	2.297	0.054	24.1	0.2	3.8	0.2
PP579S + 30% Coir	2.712	0.121	23.8	0.3	2.7	0.1
PP579S + 5% MAPP	1.896	0.063	29.8	0.4	8.0	0.3
PP579S + 5% MAPP + 10% Coir	2.094	0.028	29.1	0.1	5.1	0.1
PP579S + 5% MAPP + 20% Coir	2.332	0.098	30.7	0.2	4.1	0.1
PP579S + 5% MAPP + 30% Coir	2.740	0.101	34.5	0.2	3.7	0.2
PP513MNK10	1.574	0.110	20.3	0.3	4.2	0.1
PP513MNK10 + 10% Coir	1.693	0.015	17.5	0.3	2.5	0.3
PP513MNK10 + 20% Coir	1.907	0.106	17.8	0.2	2.8	0.1
PP513MNK10 + 30% Coir	2.230	0.040	18.3	0.3	2.3	0.1
PP513MNK10 + 5% MAPP	1.736	0.125	19.6	0.5	2.4	0.1
PP513MNK10 + 5% MAPP + 10% Coir	1.759	0.044	21.4	0.2	3.0	0.2
PP513MNK10 + 5% MAPP + 20% Coir	1.860	0.020	23.0	0.2	3.5	0.1
PP513MNK10 + 5% MAPP + 30% Coir	2.214	0.091	25.6	0.1	3.6	0.1
PP579S + 10% Talc	2.663	0.051	31.9	0.5	5.8	0.3
PP579S + 20% Talc	3.616	0.058	31.8	0.1	4.4	0.03
PP579S + 30% Talc	4.639	0.067	32.3	0.5	2.9	0.03

Table 6.1: Tensile properties of coir and talc reinforced PP injection moulded composites.

Regarding the tensile strain at maximum load, the average values for coir reinforced PP 579S and non-modified PP 513MNK10 composites decreased for increasing fibre load. A very similar behaviour was also observed for talc reinforced composites. On the other hand, for MAPP modified PP 513MNK10, the average values increased for increasing fibre content.

In general terms, and in relation to the tensile stress and strain at maximum load, similar behaviours have also been reported by different studies for coir reinforced PP composites [13, 17–21]. If the fibre-matrix interfacial bonding is relatively low, as for non-modified composites, the stress transfer capability of the interface might be weakened, which could lead to crack initiation at stress concentration points, and subsequent composite failure. In this regard, it should be mentioned that when directly observing the fibres within the composites' films (made out of injection moulded composites as previously described), as illustrated in Figure 6.4, it can be seen how the reinforcement is highly non-uniform. Furthermore, it can also be observed that there is a relative high concentration of low aspect ratio fibres, with almost particle shaped morphology and heterogeneous form, which could accentuate the effect of the reinforcement with regards to creating high stress concentration points.

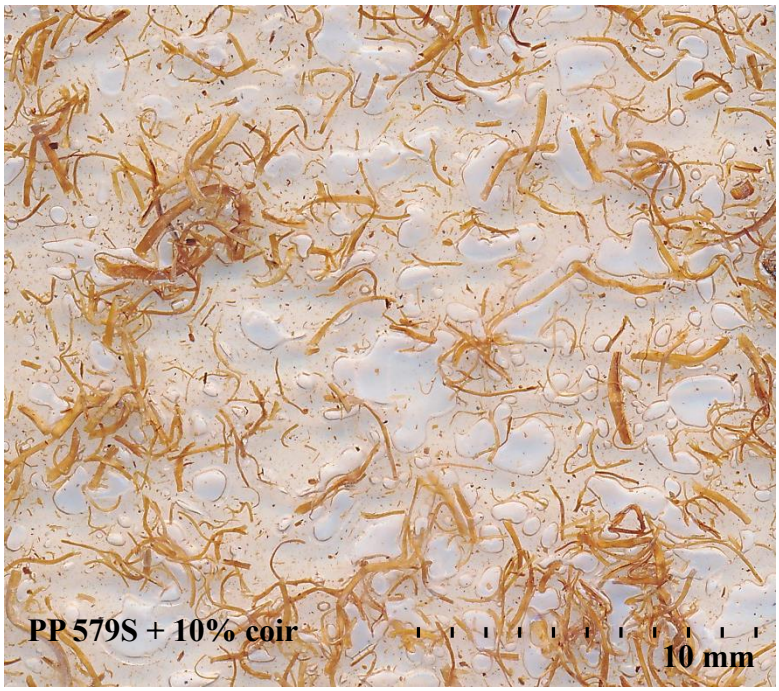

Figure 6.4: Scanned image of a PP 579S + 10% coir film.

6.3.1.2 Tensile properties of LDPE composites

The tensile properties of coir reinforced LDPE 1922SF injection moulded composites are illustrated in Figure 6.5-7 and Table 6.2. As it can be seen from Figure 6.5, the Young's modulus increased for increasing coir fibre content. In relation to the effect of the MAPE, higher average values were measured for MAPE modified composites. A series of two-sample *t*-tests revealed non-significant differences, at 95% confidence levels, for pure LDPE and 30% reinforced composites. On the other hand, a significant difference was observed for composites reinforced with coir at 10% (*p*-value = $1.81 \cdot 10^{-3}$) and 20% (*p*-value = $1.73 \cdot 10^{-3}$) concentrations. The increase of the Young's modulus has also been observed for the previously discussed PP composites and similar studies on PP by other authors [17–21].

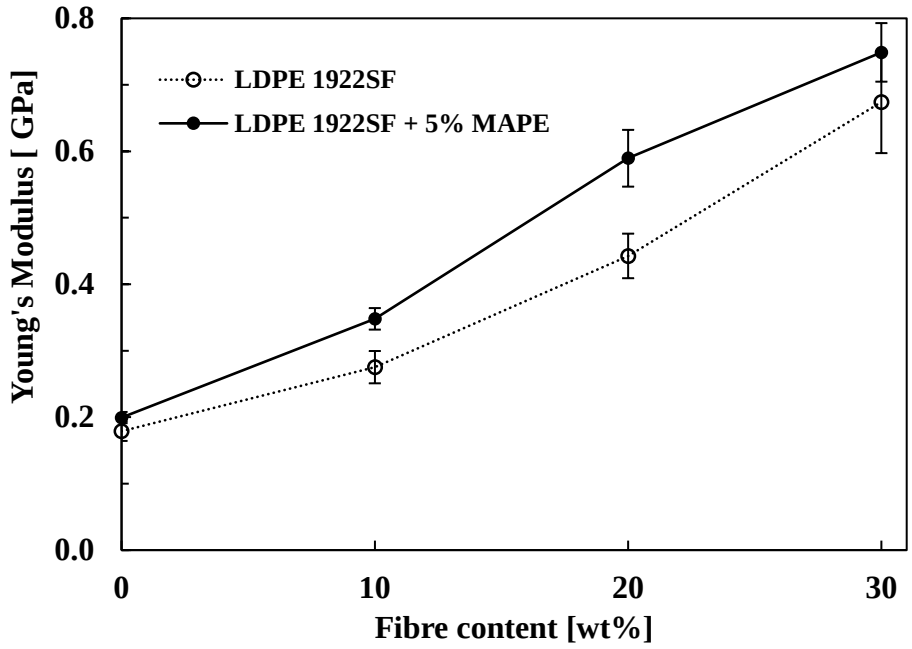

Figure 6.5: Young's modulus of coir reinforced LDPE injection moulded composites.

In relation to the tensile stress at maximum load, the behaviour of non-modified and MAPE modified composites was considerably different, as was observed for PP based composites. For coir reinforced non-modified LDPE composites, the average tensile stress at maximum load decreased when adding coir fibres. On the other hand, in the case of MAPE modified LDPE composites, the tensile stress at maximum load increased for increasing fibre load.

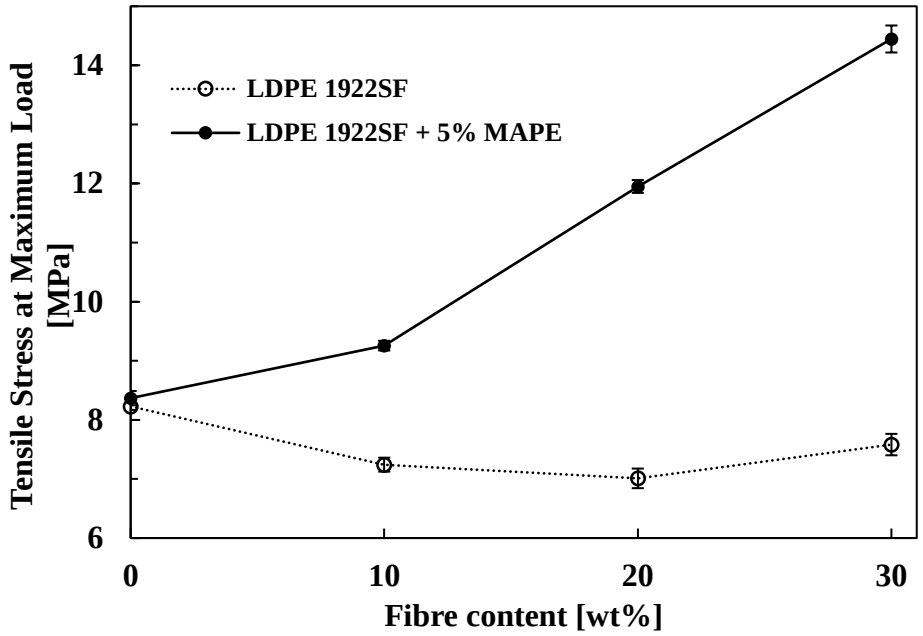

Figure 6.6: Tensile strength of coir reinforced LDPE injection moulded composites.

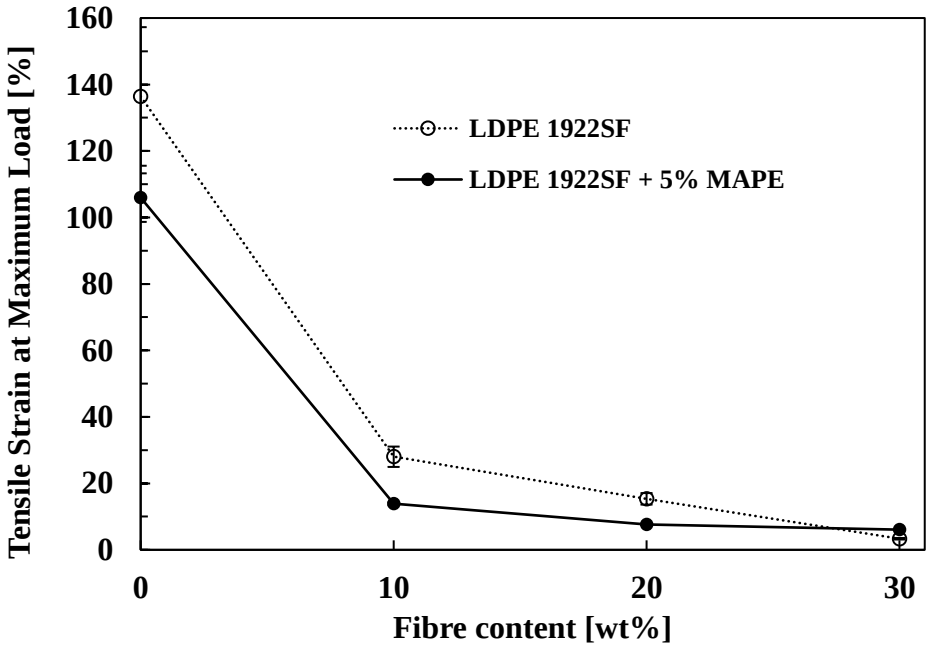

Figure 6.7: Tensile strain at maximum load of coir reinforced LDPE injection moulded composites.

Concerning the tensile strain at maximum load, the average values for coir reinforced LDPE composites significantly decreased when adding coir fibre. A very similar behaviour was also observed for coir and talc reinforced PP 579S composites.

Regarding the tensile stress and strain at maximum load, similar behaviours have also been reported by different studies for coir reinforced PP composites [13, 17–21]. As in the case of PP based composites, a relatively low fibre-matrix interfacial bonding, as in non-modified composites, could lead to a low ability of the interface to transfer stress between fibre and matrix. This effect could therefore lead to crack initiation at stress concentration points, and subsequent composite failure. Moreover, and as discussed for PP based composites, high stress concentration points could be promoted by low aspect ratio and heterogeneously shaped reinforcement, which can be seen, in a similar manner as observed for PP composites, in Figure 6.8.

Sample	Young's Modulus [MPa]		Tensile Stress at Maximum Load [MPa]		Tensile Strain at Maximum Load [%]	
	Mean	95% Confidence limits	Mean	95% Confidence limits	Mean	95% Confidence limits
LDPE1922SF	179	15	8.2	0.1	136.4	20.9
LDPE1922SF + 10% Coir	275	24	7.2	0.1	28.0	3.1
LDPE1922SF + 20% Coir	443	34	7.0	0.2	15.3	1.7
LDPE1922SF + 30% Coir	674	77	7.6	0.2	3.3	0.2
LDPE1922SF + 5% MAPE	199	8	8.4	0.1	106.0	7.3
LDPE1922SF + 5% MAPE + 10% Coir	348	16	9.3	0.1	13.8	0.5
LDPE1922SF + 5% MAPE + 20% Coir	589	43	12.0	0.1	7.6	0.2
LDPE1922SF + 5% MAPE + 30% Coir	749	44	14.4	0.2	6.1	0.2

Table 6.2: Tensile properties of coir reinforced LDPE injection moulded composites.

Figure 6.8: Scanned image of a LDPE 1922SF + 10% coir film.

6.3.2 Impact properties

The notched and un-notched impact strength of PP based composites was measured at room temperature. Results are illustrated in Figure 6.9, 10 and 12, and Table 6.3. As first indicated by pure injection moulded LDPE 1922SF, discussed in Chapter 4, it was also not possible to measure the impact strength of coir reinforced LDPE. Due to the low stiffness of the specimens, they did not completely break when hit by the striker. Regarding the properties of PP based composites, in general terms, and as observed in Chapter 4, PP copolymer based composites (i.e. PP 513MNK10) gave higher notched and un-notched impact strength.

In relation to the un-notched impact strength, there was a clear drop of the absorbed energy with the addition of coir fibre, as can be seen in Figure 6.9. The addition of coir fibres could potentially create points or regions of stress concentration, which may considerably contribute to lower the average energy required for crack initiation. After the initial drop, further addition of coir, illustrated in detail in Figure 6.10, led to a further decrease. Regarding the apparent increase of average values from 10 to 20% fibre load in the case of PP 513MNK10 + 5% MAPP, and between 20 and 30% fibre load for PP 579S + 5% MAPP, two-sample *t*-tests revealed, in both cases, non-

significant differences at 95% confidence levels (*p*-value = 0.80 for PP 513MNK10 + 5% MAPP and *p*-value = 0.25). Furthermore, in the case of talc reinforced PP 579S, it can be seen how the initial addition of talc did not cause any significant change in the un-notched impact strength. However, further increase of the talc content, led to a decrease of the average values of un-notched impact strength.

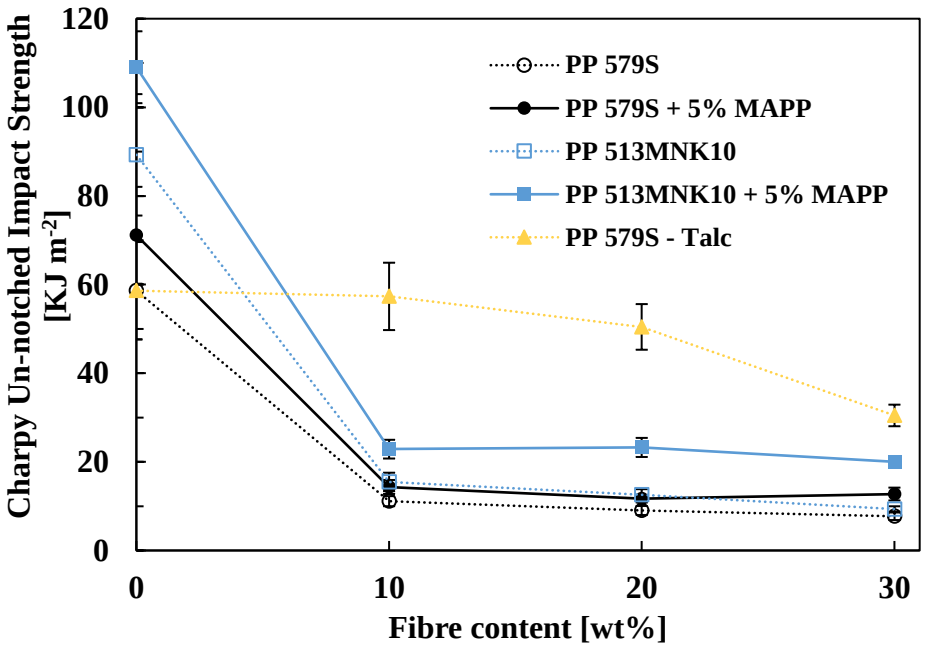

Figure 6.9: Charpy un-notched impact strength of coir and talc reinforced PP injection moulded composites.

The fracture surfaces of different un-notched samples are illustrated in Figure 6.11. In the case of both non-modified cases (i.e. (a) - PP 513MNK10, and (c) - PP 579S), which include 30 wt% fibre load, the fracture surfaces revealed an extensive fibre pull-out effect. On the other hand, it can be seen how, in the equivalent MAPP modified composites (i.e. (a) - PP 513MNK10, and (c) - PP 579S), the pull-out effect was totally suppressed. The addition of MAPP results in an improvement of the fibre-matrix interfacial properties, which throughout crack propagation, leads to a scenario where fibres break as the crack progresses. In this regard, results suggest that the relatively higher interfacial shear strength (IFSS) may prevent fibres from being pulled-out. It should also be noticed that, although the suppression of the pull-out effect theoretically leads to a reduction in the energy absorbed during crack propagation, in the case of the

un-notched impact strength, the energy required to initiate a crack is dominant. In this regard, as it was shown in Chapter 4, the addition of MAPP to PP might lead to an increase of the energy required for crack initiation, which will explain the higher average results observed for MAPP modified composites.

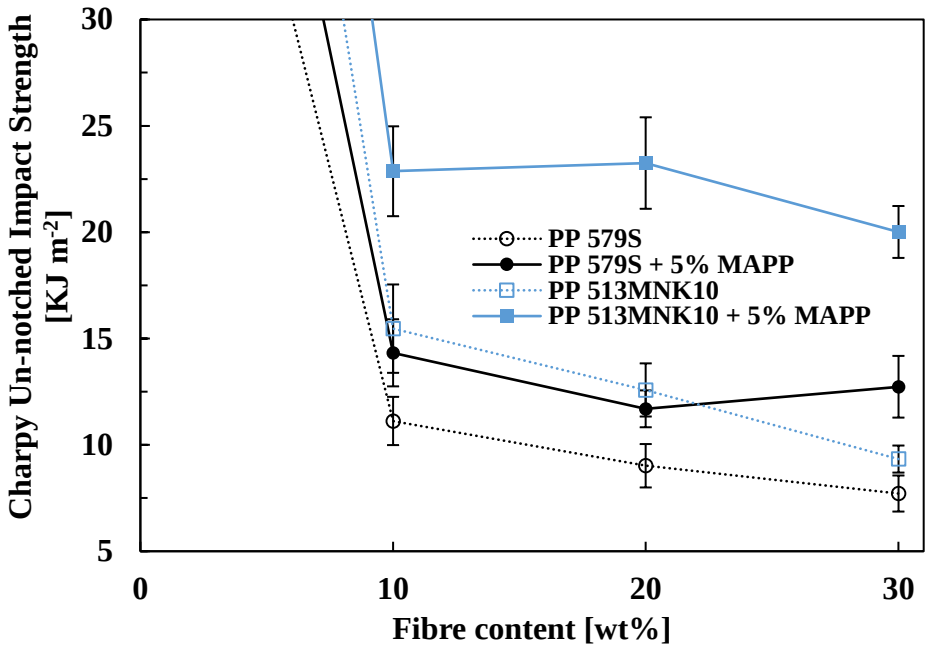

Figure 6.10: Detail of charpy un-notched impact strength of coir reinforced PP injection moulded composites.

Regarding the notched impact properties, there was a clear difference in the behaviour between homopolymer (i.e. PP 579S) and copolymer (i.e. PP 513MNK10) based composites. In the case of the copolymer, the addition of coir fibre led to a clear drop of the notched impact strength, for both non-modified and modified composites. This initial decrease may be linked to the creation of point stress concentrations, through which the crack could propagate more easily. For non-modified composites, a series of two-sample *t*-tests revealed a significant increase of the impact strength, at 95% confidence levels, with further addition of coir fibre. This increase may be related to the increase in the energy absorbed due to the pull-out phenomena. On the other hand, for MAPP modified composites, there is a further decrease of the impact strength with increasing content from 10 to 20%, and a non-significant difference between 20 and 30%.

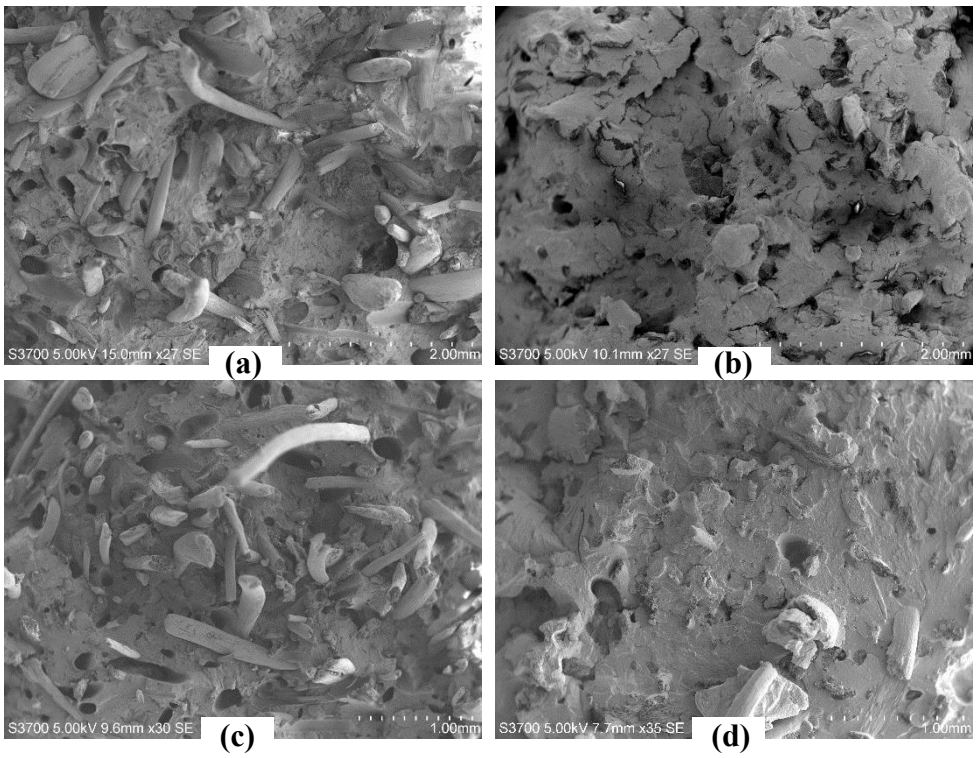

Figure 6.11: Fracture surfaces of un-notched coir-PP based composites at 30 wt% fibre load. (a) – PP 513MNK10. (b) – PP 513MNK10 + 5% MAPP. (c) – PP 579S. (d) – PP 579S + 5% MAPP.

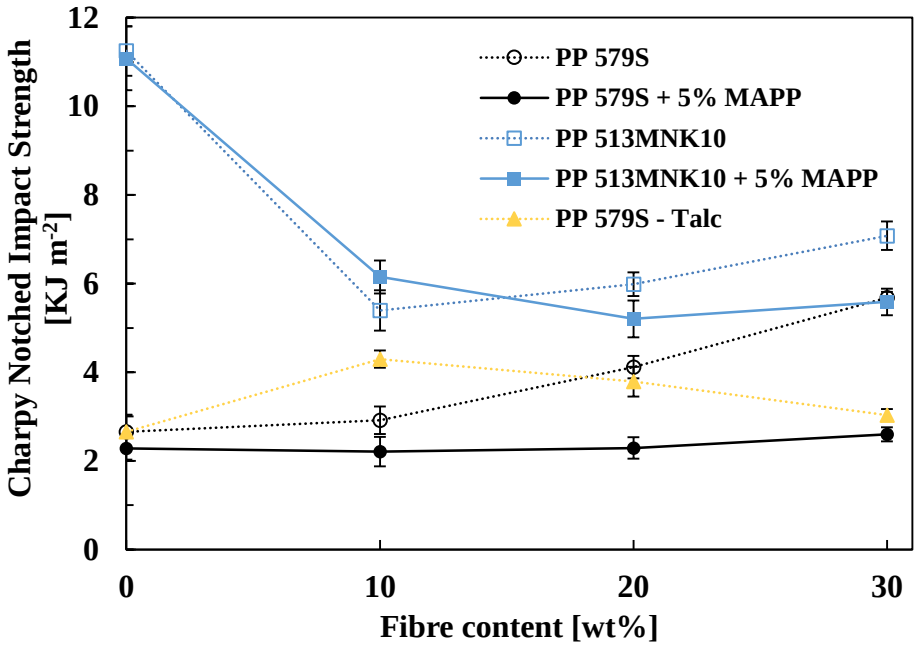

Figure 6.12: Charpy notched impact strength of coir reinforced PP injection moulded composites.

Sample	Charpy Un-notched [KJ m^{-2}]		Charpy Notched [KJ m^{-2}]	
	Mean	95% Confidence limits	Mean	95% Confidence limits
PP579S	58.6	11.0	2.7	0.4
PP579S + 10% Coir	11.1	1.1	2.9	0.3
PP579S + 20% Coir	9.0	1.0	4.1	0.3
PP579S + 30% Coir	7.7	0.8	5.7	0.1
PP579S + 5% MAPP	71.1	10.9	2.3	0.3
PP579S + 5% MAPP + 10% Coir	14.3	1.6	2.2	0.3
PP579S + 5% MAPP + 20% Coir	11.7	0.9	2.3	0.2
PP579S + 5% MAPP + 30% Coir	12.7	1.5	2.6	0.2
PP513MNK10	89.3	13.7	11.2	0.6
PP513MNK10 + 10% Coir	15.5	2.1	5.4	0.5
PP513MNK10 + 20% Coir	12.6	1.2	6.0	0.3
PP513MNK10 + 30% Coir	9.3	0.6	7.1	0.3
PP513MNK10 + 5% MAPP	109.0	8.1	11.1	0.7
PP513MNK10 + 5% MAPP + 10% Coir	22.9	2.1	6.2	0.4
PP513MNK10 + 5% MAPP + 20% Coir	23.2	2.2	5.2	0.4
PP513MNK10 + 5% MAPP + 30% Coir	20.0	1.2	5.6	0.3
PP579S + 10% Talc	57.3	7.6	4.3	0.2
PP579S + 20% Talc	50.4	5.1	3.8	0.3
PP579S + 30% Talc	30.5	2.4	3.0	0.1

Table 6.3: Charpy un-notched and notched impact strength of PP based composites.

Regarding notched impact strength, a similar behaviour was also observed for the homopolymer based composites. A series of two-sample *t*-tests revealed a non-significant difference, at 95% confidence levels, between all MAPP modified PP 579S composites. In contrast, in the case of non-modified composites, a significant increase was observed for increasing fibre content. This difference between non-modified and MAPP modified composites, represents a good example of the effect of the suppression of the pull-out, and further emphasises the importance of the contribution of the pull-out phenomenon to the energy absorbed during crack propagation in coir reinforced PP injection moulded composites.

The fracture surfaces of different notched samples are illustrated in Figure 6.13. For both copolymer and homopolymer based composites, the suppression of the pull-out phenomena due to the addition of MAPP (which leads to an improved fibre-matrix

interface) is evident. The increase of the interfacial properties is also evident from SEM observation of fracture surfaces, as in the example illustrated in Figure 6.14, where a coir fibre (coloured in dark orange), that at some point runs parallel to the crack propagation direction, has been ripped apart during fracture, letting the internal cellular structure become available to the observer. In this example, the fibre-matrix IFSS seems to be higher than the IFSS between the fibre's individual cells and their proper strength, which ultimately led to the fibre be ripped apart. In relation to talc reinforced PP 579S, after an initial increase of the average notched impact strength at 10% reinforcement load, the average values decreased for increasing talc content. It should be noticed that at 20 and 30% of reinforcement load, coir reinforced composites showed a higher value of notched impact strength.

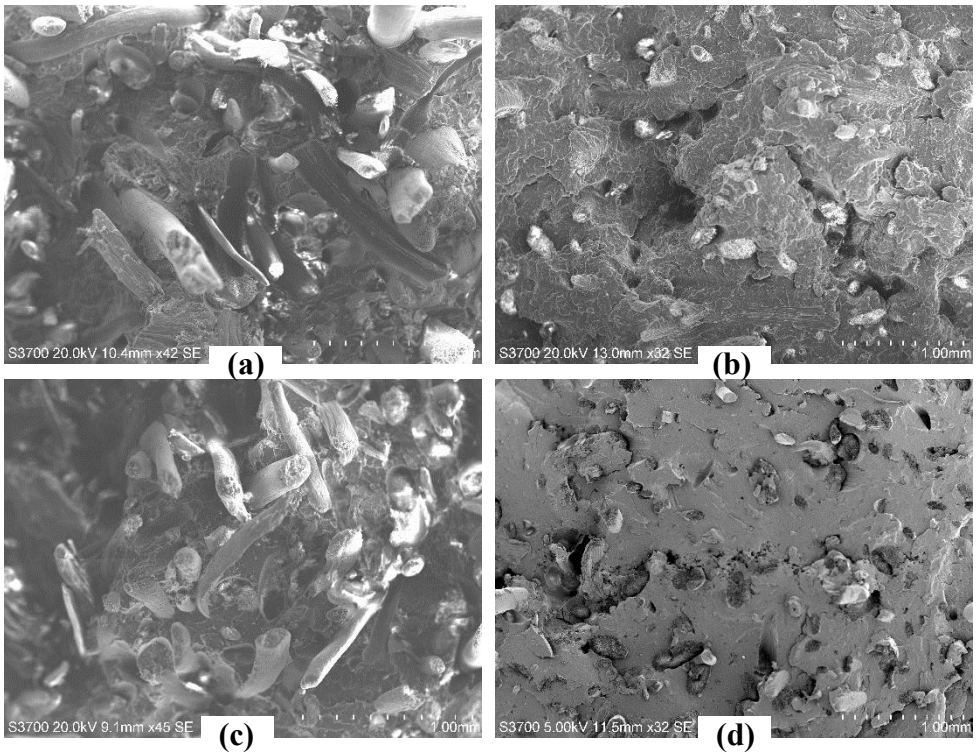

Figure 6.13: Fracture surfaces of notched coir-PP based composites at 30 wt% fibre load. (a) – PP 513MNK10. (b) – PP 513MNK10 + 5% MAPP. (c) – PP 579S. (d) – PP 579S + 5% MAPP.

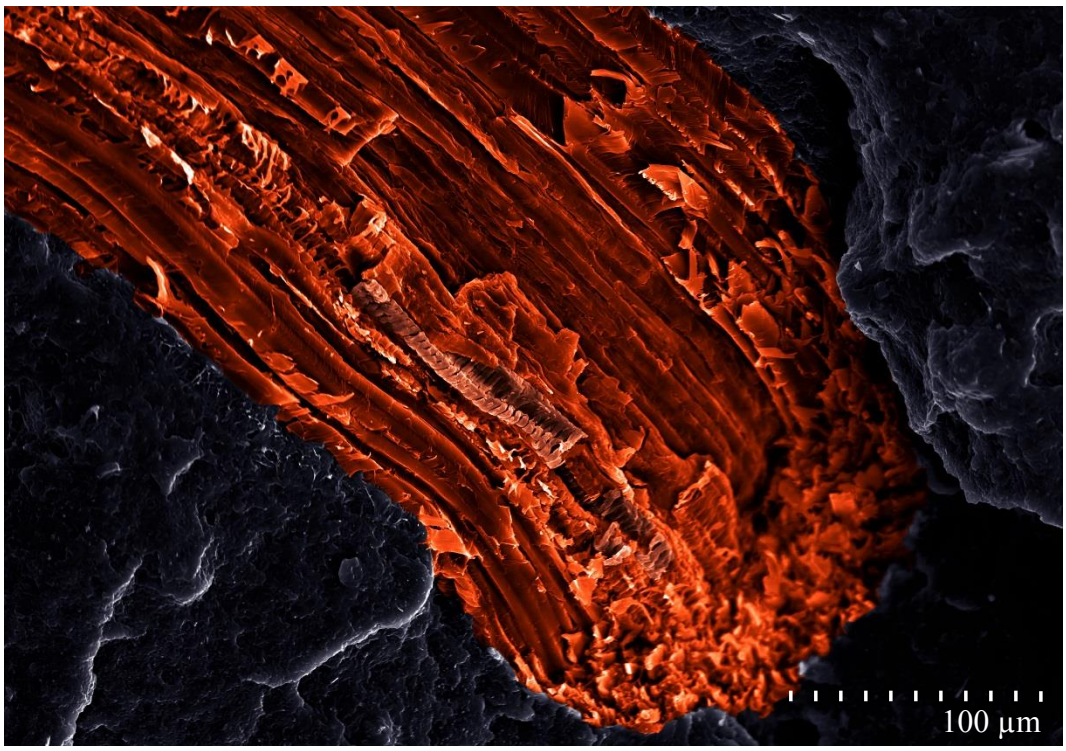

Figure 6.14: Colour-enhanced electron micrograph of a fracture surface of coir reinforced (30%) PP 513MNK10 + 5% MAPP injection moulded composites.

6.4 Conclusions

In this chapter the tensile and impact properties of coir reinforced polypropylene (PP) and low density polyethylene (LDPE) based composites, and the effect of compatibilizers have been characterised. Additionally, the direct observation of coir fibres included in PP579S and LDPE injection moulded composites, revealed a highly heterogeneous coir fibre content in terms of length, diameter, aspect ratio, and shape.

In general terms, for coir and talc reinforced PP and LDPE injection moulded composites, the Young's modulus increased for increasing coir fibre content. PP 579S (i.e. PP homopolymer) showed a Young's modulus of 2.7 GPa at 30% fibre load, which is slightly higher than the equivalent PP 513MNK10 (i.e. PP copolymer), which showed 2.2 GPa. This slight difference might be related to the difference in the matrix Young's modulus, already observed in Chapter 4. Moreover, in the case of PP based composites, the addition of MAPP did not lead to a significant increase. On the other hand, the addition of MAPE to LDPE composites led to higher average values in

relation to non-modified composites. Talc reinforced PP 579S showed considerably higher average values than equivalent coir reinforced composites, especially relevant at 30% reinforcement load, where talc showed a Young's modulus of 4.6 GPa.

In relation to the tensile stress at maximum load, the average values decreased for increasing fibre load in the case of coir reinforced PP 579S and non-modified LDPE composites. For MAPP modified PP 579S and PP 513MNK10 composites, along with MAPE modified LDPE composites, the average values tended to increase for increasing fibre load. In the case of talc reinforced PP composites, after an initial increase with the addition of 10% talc, the average values did not considerably change. Concerning the tensile strain at maximum load, the average values for coir reinforced PP 579S, non-modified PP 513MNK10, and LDPE, along with talc reinforced PP 579S composites, tended to decrease for increasing fibre load. On the other hand, for MAPP modified PP 513MNK10, the average values increased for increasing fibre load, which might be related to the presence of specific components within the PP copolymer. In general terms, and in relation to the tensile stress and strain at maximum load, a relatively low fibre-matrix interfacial bonding (i.e. non-modified composites) could lead to crack initiation at stress concentration points generated by the inclusion of fibres. This phenomenon could be accentuated by the relatively high concentration of low aspect ratio fibres, and particularly non-uniformly shaped coir. Furthermore, the addition of compatibilizer, which leads to an improved interface, showed that the composite would withstand higher levels of stress, therefore potentially linking premature composite failure with interface failure.

PP 513MNK10 based composites showed a higher notched and un-notched impact strength than PP 579S composites, which could be related to the specific nature of the copolymer matrix. Concerning the un-notched impact strength, and for all coir reinforced composites, there was a clear drop of the average values with the addition of coir fibre, which might be linked to the creation of high stress concentration points by the addition of coir fibres. In this regard, results suggested that the energy required to initiate a crack is clearly the main contributor in relation to the energy absorbed due to fibre pull-out during crack propagation. Moreover, in the case of talc reinforced PP 579S, although the initial addition of talc did not cause any significant change, further increase of talc content led to a decrease of the un-notched impact strength.

Regarding the notched impact properties, for PP 513MNK10 composites, the initial addition of coir fibre led to a clear drop of the average values of impact strength, for both non-modified and modified composites, which could be related to the creation of stress concentration points, through which the crack could propagate more easily. For PP 579S (both non-modified and MAPP modified), and non-modified PP 513MNK10 composites, the average values increased for increasing coir fibre content. The increase of the average values could be attributed to the increase of the energy absorbed, due to the pull-out phenomena, during crack propagation. In contrast, for MAPP modified composites, and due to the suppression of the pull-out effect, no increase was observed for increasing fibre content. Finally, in relation to talc reinforced PP 579S, after an initial increase for 10% talc content, the average values decreased for increasing talc content. Furthermore, talc reinforced PP 579S showed lower average notched impact strength values at 20% content and especially 30% content.

When comparing the overall performance of talc reinforced PP 579S with the equivalent coir composites, from the above discussion and results showed within the chapter, it is clear that talc composites outperformed coir PP 579S composites in terms of Young's modulus, tensile stress at maximum load and un-notched impact strength. In contrast, coir PP 579S composites showed higher values for notched impact strength due to the pull-out phenomena contribution to the overall absorbed energy during the impact event. With all these considered, if only attending to purely performance figures, coir reinforced PP does not have a strong set of arguments to compete with mineral/inorganic fibres and fillers reinforced thermoplastic composites. On the other hand, if parameters such as regulations, biodegradability, health hazards or carbon footprint are considered, coir-PP composites might be a good alternative.

The interface region, which has attracted a lot of interest as a route to improve NFTCs properties, have shown relative success in this particular case. For coir-PP composites, with the improvement of the interface through the addition of compatibilizer, it was observed that, although the tensile stress at maximum load and un-notched impact strength increased, the notched impact strength decreased and there was no significant impact on the Young's modulus. In this regard, it was clear that further improvement of the interface might not translate into an increase of the overall performance of the composites. Moreover, from some of the observations of fracture

surfaces, the current improvement of the interface appears to be enough to overcome internal IFSS of the fibre itself. Based on these observations, the fibres and not the interface appear to be critical for coir-PP composite properties. From this perspective, it seems that on a fundamental level, fibre properties will have to be addressed, if an overall increase of composite performance is required.

6.5 References

1. Bledzki, A.K., Gassan, J.: Composites reinforced with cellulose based fibres. Prog. Polym. Sci. 24, 221–274 (1999).
2. Holbery, J., Houston, D.: Natural-Fiber-Reinforced Polymer Composites in Automotive Applications. JOM. 58, 80–86 (2006).
3. Goda, K., Cao, Y.: Research and Development of Fully Green Composites Reinforced with Natural Fibers. J. Solid Mech. Mater. Eng. 1, 1073–1084 (2007).
4. Eichhorn, S.J., Young, R.J.: Deformation micromechanics of natural cellulose fibre networks and composites. Compos. Sci. Technol. 63, 1225–1230 (2003).
5. Wambua, P., Ivens, J., Verpoest, I.: Natural fibres: can they replace glass in fibre reinforced plastics? Compos. Sci. Technol. 63, 1259–1264 (2003).
6. Joshi, S.V., Drzal, L.T., Mohanty, A.K., Arora, S.: Are natural fiber composites environmentally superior to glass fiber reinforced composites? Compos. Part A Appl. Sci. Manuf. 35, 371–376 (2004).
7. Nabi Saheb, D., Jog, J.P.: Natural fiber polymer composites: A review. Adv. Polym. Technol. 18, 351–363 (1999).
8. Graupner, N., Herrmann, A.S., Müssig, J.: Natural and man-made cellulose fibre-reinforced poly(lactic acid) (PLA) composites: An overview about mechanical characteristics and application areas. Compos. Part A Appl. Sci. Manuf. 40, 810–821 (2009).
9. Jayavani, S., Deka, H., Varghese, T.O., Nayak, S.K.: Recent Development and Future Trends in Coir Fiber Reinforced Green Polymer Composites: Review and Evaluation. Polym. Compos. (2015).
10. Koronis, G., Silva, A., Fontul, M.: Green composites: A review of adequate materials for automotive applications. Compos. Part B Eng. 44, 120–127 (2013).
11. Ku, H., Wang, H., Pattarachaiyakoop, N., Trada, M.: A review on the tensile properties of natural fiber reinforced polymer composites. Compos. Part B Eng. 42, 856–873 (2011).
12. Malkapuram, R., Kumar, V., Negi, Y.S., Yuvraj Singh Negi: Recent Development in Natural Fiber Reinforced Polypropylene Composites. J. Reinf. Plast. Compos. 28, 1169–1189 (2008).
13. Bettini, S.H.P., Bicudo, A.B.L.C., Augusto, I.S., Antunes, L.A., Morassi, P.L.,

Condotta, R., Bonse, B.C.: Investigation on the Use of Coir Fiber as Alternative Reinforcement in Polypropylene. J. Appl. Polym. Sci. 118, 2841–2848 (2010).

14. Thomason, J.L.: Dependence of Interfacial Strength on the Anisotropic Fiber Properties of Jute Reinforced Composites. Polym. Compos. (2010).
15. Facca, A.G., Kortschot, M.T., Yan, N.: Predicting the tensile strength of natural fibre reinforced thermoplastics. Compos. Sci. Technol. 67, 2454–2466 (2007).
16. Facca, A.G., Kortschot, M.T., Yan, N.: Predicting the elastic modulus of natural fibre reinforced thermoplastics. Compos. Part A Appl. Sci. Manuf. 37, 1660–1671 (2006).
17. Haque, M., Rahman, R., Islam, N., Huque, M., Hasan, M.: Mechanical Properties of Polypropylene Composites Reinforced with Chemically Treated Coir and Abaca Fiber. J. Reinf. Plast. Compos. 29, 2253–2261 (2009).
18. Haque, M.M., Hasan, M., Islam, M.S., Ali, M.E.: Physico-mechanical properties of chemically treated palm and coir fiber reinforced polypropylene composites. Bioresour. Technol. 100, 4903–6 (2009).
19. Haque, M.M., Islam, M.N., Huque, M.M., Hasan, M., Islam, M.S., Islam, M.S.: Coir Fiber Reinforced Polypropylene Composites: Physical and Mechanical Properties. Adv. Compos. Mater. 19, 91–106 (2010).
20. Haque, M.M., Islam, M.S., Islam, M.N.: Preparation and characterization of polypropylene composites reinforced with chemically treated coir. J. Polym. Res. 19, 9847 (2012).
21. Islam, M.N., Rahman, M.R., Haque, M.M., Huque, M.M.: Physico-mechanical properties of chemically treated coir reinforced polypropylene composites. Compos. Part A Appl. Sci. Manuf. 41, 192–198 (2010).
22. Nandi, A., Kale, A., Raghu, N., Aggarwal, P.K., Chauhan, S.S.: Effect of concentration of coupling agent on mechanical properties of coir–polypropylene composite. J. Indian Acad. Wood Sci. 10, 62–67 (2013).
23. Thomason, J.L., Vlug, M.A.: Influence of fibre length and concentration on the properties of glass fibre-reinforced polypropylene: 4. Impact properties. Compos. Part A Appl. Sci. Manuf. 28, 610–288 (1997).
24. Garkhail, S.. K., Heijenrath, R.W.H., Peijs, T.: Mechanical Properties of Natural-Fibre-Mat-Reinforced Thermoplastics based on Flax Fibres and Polypropylene. Appl. Compos. Mater. 7, 351–372 (2000).
25. Park, B., Balatinecz, J.J.: Mechanical Properties of Wood-Fiber/Toughened lsotactic Polypropylene Composites. Polym. Compos. 18, 79–89 (1997).
26. Ashori, A., Nourbakhsh, A., Kokta, B.V., Jahan-Latibari, A.: Effect of a Novel Coupling Agent , Polybutadiene Isocyanate, on Mechanical Properties of Wood-Fiber Polypropylene Composites. J. Reinf. Plast. Compos. 27, 1679–1687 (2008).
27. Stark, N.M.: Wood Fiber Derived from Scrap Pallets Used in Polypropylene Composites. For. Prod. J. 49, 39–46 (1999).
28. Eichhorn, S.J., Baillie, C.A., Mwaikambo, L.Y., Ansell, M.P., Dufresne, A., Entwistle, K.M., Herrera-Franco, P.J., Escamilla, G.C., Groom, L., Hughes, M.,

Hill, C., Rials, T.G., Wild, P.M.: Review: Current international research into cellulosic fibers and composites. J. Mater. Sci. 36, 2107–2131 (2001).

29. Abdul Khalil, H.P.S., Poh, B.T., Issam, A.M., Jawaid, M., Ridzuan, R.: Recycled Polypropylene – Oil Palm Biomass: The Effect on Mechanical and Physical Properties. J. Reinf. Plast. Compos. 29, 1117–1130 (2010).
30. Rana, A.K., Mandal, A., Mitra, B.C., Jacobson, R., Rowell, R., Banerjee, A.N.: Short Jute Fiber-Reinforced Polypropylene Composites : Effect of Compatibilizer. J. Appl. Polym. Sci. 69, 329–338 (1998).
31. Jayaraman, K.: Manufacturing sisal–polypropylene composites with minimum fibre degradation. Compos. Sci. Technol. 63, 367–374 (2003).
32. Singleton, A.C.N., Baillie, C.A., Beaumont, P.W.R., Peijs, T.: On the mechanical properties, deformation and fracture of a natural fibre/recycled polymer composite. Compos. Part B Eng. 34, 519–526 (2003).
33. Mohanty, S., Nayak, S.K., Verma, S.K., Tripathy, S.S.: Effect of MAPP as a Coupling Agent on the Performance of Jute–PP Composites. J. Reinf. Plast. Compos. 23, 625–637 (2004).
34. Mohanty, S., Nayak, S.K., Verma, S.K., Tripathy, S.S.: Effect of MAPP as Coupling Agent on the Performance of Sisal-PP Composites. J. Reinf. Plast. Compos. 23, 2047–2063 (2004).
35. Mohanty, S., Verma, S., Nayak, S.: Dynamic mechanical and thermal properties of MAPE treated jute/HDPE composites. Compos. Sci. Technol. 66, 538–547 (2006).
36. Mohanty, S., Nayak, S.K.: Short Bamboo Fiber-reinforced HDPE Composites : Influence of Fiber Content and Modification on Strength of the Composite. J. Reinf. Plast. Compos. 29, 2199–2210 (2010).
37. Bledzki, A.K., Mamun, A.A., Faruk, O.: Abaca fibre reinforced PP composites and comparison with jute and flax fibre PP composites. eXPRESS Polym. Lett. 1, 755–762 (2007).
38. Bledzki, A.K., Jaszkiewicz, A., Scherzer, D.: Mechanical properties of PLA composites with man-made cellulose and abaca fibres. Compos. Part A Appl. Sci. Manuf. 40, 404–412 (2009).
39. Khalid, M., Ratnam, C.T., Chuah, T.G., Ali, S., Choong, T.S.Y.: Comparative study of polypropylene composites reinforced with oil palm empty fruit bunch fiber and oil palm derived cellulose. Mater. Des. 29, 173–178 (2008).
40. Bax, B., Müssig, J.: Impact and tensile properties of PLA/Cordenka and PLA/flax composites. Compos. Sci. Technol. 68, 1601–1607 (2008).
41. John, M.J., Anandjiwala, R.D.: Chemical modification of flax reinforced polypropylene composites. Compos. Part A Appl. Sci. Manuf. 40, 442–448 (2009).
42. Guo, Q., Cheng, B., Kortschot, M., Sain, M., Knudson, R., Deng, J., Alemdar, A.: Performance of long Canadian natural fibers as reinforcements in polymers. J. Reinf. Plast. Compos. 29, 3197–3207 (2010).
43. Paul, S.A., Joseph, K., Mathew, G., Pothen, L.A., Thomas, S.: Preparation of

Polypropylene Fiber/Banana Fiber Composites by Novel Commingling Method. Polym. Compos. 31, 816–824 (2010).

44. Li, T.Q., Ng, C.N., Li, R.K.Y.: Impact Behavior of Sawdust/Recycled – PP Composites. J. Appl. Polym. Sci. 81, 1420–1428 (2001).

45. Marcovich, N.E., Villar, M.A.: Thermal and mechanical characterization of linear low-density polyethylene/wood flour composites. J. Appl. Polym. Sci. 90, 2775–2784 (2003).

46. Yang, H.-S., Wolcott, M.P., Kim, H.-S., Kim, S., Kim, H.-J.: Properties of lignocellulosic material filled polypropylene bio-composites made with different manufacturing processes. Polym. Test. 25, 668–676 (2006).

47. Czél, G., Kanyok, Z.: MAgPP an Effective Coupling Agent in Rice Husk Flour Filled Polypropylene Composites. Mater. Sci. Forum. 537-538, 137–144 (2007).

48. Nourbakhsh, A., Ashori, A.: Fundamental Studies on Wood – Plastic Composites : Effects of Fiber Concentration and Mixing Temperature on the Mechanical Properties of Poplar / PP Composite. Polym. Compos. 569–573 (2008).

49. He, L.P., Tian, Y., Wang, L.L.: Study on Ramie Fiber Reinforced Polypropylene Composites (RF-PP) and its Mechanical Properties. Adv. Mater. Res. 41-42, 313–316 (2008).

50. Yao, F., Wu, Q., Lei, Y., Xu, Y.: Rice straw fiber-reinforced high-density polyethylene composite: Effect of fiber type and loading. Ind. Crops Prod. 28, 63–72 (2008).

51. Liu, H., Wu, Q., Zhang, Q.: Preparation and properties of banana fiber-reinforced composites based on high density polyethylene (HDPE)/Nylon-6 blends. Bioresour. Technol. 100, 6088–97 (2009).

52. Li, X., He, L., Zhou, H., Li, W., Zha, W.: Influence of silicone oil modification on properties of ramie fiber reinforced polypropylene composites. Carbohydr. Polym. 87, 2000–2004 (2012).

53. van den Oever, M.J.A., Bos, H.L., Molenveld, K.: Flax fibre physical structure and its effect on composite properties : Impact strength and thermo-mechanical properties. Die Angew. Makromol. Chemie. 272, 71–76 (1999).

54. Clemons, C.M., Caulfield, D.F., Giacomin, A.J.: Dynamic Fracture Toughness of Cellulose-Fiber-Reinforced Polypropylene: Preliminary Investigation of Microstructural Effects. J. Elastomers Plast. 31, 367–378 (1999).

55. Zhang, M., Rong, M., Lu, X.: Fully biodegradable natural fiber composites from renewable resources: All-plant fiber composites. Compos. Sci. Technol. 65, 2514–2525 (2005).

56. Yang, H.-S., Kim, H.-J., Son, J., Park, H.-J., Lee, B.-J., Hwang, T.-S.: Rice-husk flour filled polypropylene composites; mechanical and morphological study. Compos. Struct. 63, 305–312 (2004).

57. Arbelaiz, A., Fernández, B., Ramos, J.A., Retegi, A., Llano-Ponte, R., Mondragon, I.: Mechanical properties of short flax fibre bundle/polypropylene

composites: Influence of matrix/fibre modification, fibre content, water uptake and recycling. Compos. Sci. Technol. 65, 1582–1592 (2005).

58. Oksman, K., Mathew, A.P., Långström, R., Nyström, B., Joseph, K.: The influence of fibre microstructure on fibre breakage and mechanical properties of natural fibre reinforced polypropylene. Compos. Sci. Technol. 69, 1847–1853 (2009).

59. Beg, M., Pickering, K.: Mechanical performance of Kraft fibre reinforced polypropylene composites: Influence of fibre length, fibre beating and hygrothermal ageing. Compos. Part A Appl. Sci. Manuf. 39, 1748–1755 (2008).

60. Sanadi, A.R., Young, R.A., Clemons, C., Rowell, R.M.: Recycled Newspaper Fibers as Reinforcing Fillers in Thermoplastics: Part I-Analysis of Tensile and Impact Properties in Polypropylene. J. Reinf. Plast. Compos. 13, 54–67 (1994).

61. Sanadi, A.R., Caulfield, D.F., Stark, N.M., Clemons, C.C.: Thermal and mechanical analysis of lignocellulosic- polypropylene composites. The Fifth International Conference on Woodfiber-Plastic Composites. pp. 67–78 (1999).

62. Karnani, R., Krishnan, M., Narayan, R.: Biofiber-Reinforced Polypropylene Composites. Polym. Eng. Sci. 37, 476–483 (1997).

63. Feng, D., Caulfield, D.F., Sanadi, A.R.: Effect of compatibilizer on the structure-property relationships of kenaf-fiber/polypropylene composites. Polym. Compos. 22, 506–517 (2001).

64. Lei, Y., Wu, Q., Yao, F., Xu, Y.: Preparation and properties of recycled HDPE/natural fiber composites. Compos. Part A Appl. Sci. Manuf. 38, 1664–1674 (2007).

65. Lee, S., Kang, I., Park, B., Doh, G., Park, B.: Effects of Filler and Coupling Agent on the Properties of Bamboo Fiber-Reinforced Polypropylene Composites. J. Reinf. Plast. Compos. 28, 2589–2604 (2009).

66. Araujo, J.R., Mano, B., Teixeira, G.M., Spinacé, M.A.S., De Paoli, M.-A.: Biomicrofibrilar composites of high density polyethylene reinforced with curauá fibers: Mechanical, interfacial and morphological properties. Compos. Sci. Technol. 70, 1637–1644 (2010).

67. Bledzki, A.K., Mamun, A.A., Jaszkiewicz, A., Erdmann, K.: Polypropylene composites with enzyme modified abaca fibre. Compos. Sci. Technol. 70, 854–860 (2010).

68. Bledzki, A.K., Mamun, A.A., Volk, J.: Barley husk and coconut shell reinforced polypropylene composites: The effect of fibre physical, chemical and surface properties. Compos. Sci. Technol. 70, 840–846 (2010).

69. Sain, M., Suhara, P., Law, S., Bouilloux, A.: Interface Modification and Mechanical Properties of Natural Fiber-Polyolefin Composite Products. J. Reinf. Plast. Compos. 24, 121–130 (2005).

70. Bledzki, A.K., Mamun, A.A., Lucka-Gabor, M., Gutowski, V.S.: The effects of acetylation on properties of flax fibre and its polypropylene composites. eXPRESS Polym. Lett. 2, 413–422 (2008).

71. Sun, Z.-Y., Han, H.-S., Dai, G.-C.: Mechanical Properties of Injection-molded

Natural Fiber-reinforced Polypropylene Composites: Formulation and Compounding Processes. J. Reinf. Plast. Compos. 29, 637–650 (2009).

72. Rozman, H.D., Lai, C.Y., Ismail, H., Ishak, Z.A.M.: The effect of coupling agents on the mechanical and physical properties of oil palm empty fruit bunch-polypropylene composites. Polym. Int. 49, 1273–1278 (2000).

73. Hristov, R., Lach, V.N., Grellmann, W.: Impact fracture behavior of modified polypropylene/wood fiber composites. Polym. Test. 23, 581–589 (2004).

74. van den Oever, M.J.A., Bos, H.L., van Kemenade, M.J.J.M.: Influence of the Physical Structure of Flax Fibres on the Mechanical Properties of Flax Fibre Reinforced Polypropylene Composites. Appl. Compos. Mater. 7, 387–402 (2000).

75. Park, B.-D., Balatinecz, J.J.: Effects of Impact Modification on the Mechanical Properties of Wood-Fiber Thermoplastic Composites with High Impact Polypropylene (HIPP). J. Thermoplast. Compos. Mater. 9, 342–364 (1996).

76. Xie, X.L., Fung, K.L., Li, R.K.Y., Tjong, S.C., Mai, Y.-W.: Structural and mechanical behavior of polypropylene/ maleated styrene-(ethylene-co-butylene)-styrene/sisal fiber composites prepared by injection molding. J. Polym. Sci. Part B Polym. Phys. 40, 1214–1222 (2002).

77. Rana, A.K., Mandal, A., Bandyopadhyay, S.: Short jute fiber reinforced polypropylene composites : effect of compatibiliser , impact modifier and fiber loading. Compos. Sci. Technol. 63, 801–806 (2003).

78. Anuar, H., Zuraida, A.: Improvement in mechanical properties of reinforced thermoplastic elastomer composite with kenaf bast fibre. Compos. Part B. 42, 462–465 (2011).

79. Ruksakulpiwat, Y., Sridee, J., Suppakarn, N., Sutapun, W.: Composites : Part B Improvement of impact property of natural fiber – polypropylene composite by using natural rubber and EPDM rubber. Compos. Part B. 40, 619–622 (2009).

80. Wu, J., Yu, D., Chan, C.-M., Kim, J., Mai, Y.-W.: Effect of Fiber Pretreatment Condition on the Interfacial Strength and Mechanical Properties of Wood Fiber/PP Composites. J. Appl. Polym. Sci. 76, 1000–1010 (2006).

81. Long, C.-G., He, L.-P., Zhong, Z.-H., Chen, S.-G.: Studies on the Polypropylene Composites Reinforced by Ramier Fiber and K2Ti6O13 Whisker. Res. Lett. Mater. Sci. 2007, 1–4 (2007).

82. Rahman, M.R., Huque, M.M., Islam, M.N., Hasan, M.: Improvement of physico-mechanical properties of jute fiber reinforced polypropylene composites by post-treatment. Compos. Part A Appl. Sci. Manuf. 39, 1739–1747 (2008).

83. Hasan, M., Rahman, R., Huque, M., Islam, N.: Physico-Mechanical Properties of Jute Fiber Reinforced Polypropylene Composites. J. Reinf. Plast. Compos. 29, 445–455 (2010).

84. Kabir, M.A., Huque, M.M., Islam, M.R., Bledzki, A.K.: Mechanical Properties of Jute Fiber Reinforced Polypropylene Composite : Effect of Chemical Treatment by Benzenediazonium Salt in Alkaline Medium. BioResources. 5,

1618–1625 (2010).

85. Nair, K.C.M., Thomas, S.: Effect of interface modification on the mechanical properties of polystyrene-sisal fiber composites. Polym. Compos. 24, 332–343 (2003).

86. Rozman, H.D., Saad, M.J., Ishak, Z.A.M.: Flexural and impact properties of oil palm empty fruit bunch (EFB)– polypropylene composites — the effect of maleic anhydride chemical modification of EFB. Polym. Test. 22, 335–341 (2003).

87. Ruksakulpiwat, Y., Suppakarn, N., Sutapun, W., Thomthong, W.: Vetiver–polypropylene composites: Physical and mechanical properties. Compos. Part A Appl. Sci. Manuf. 38, 590–601 (2007).

88. Threepopnatkul, P., Kaerkitcha, N., Athipongarporn, N.: Polycarbonate with Pineapple Leaf Fiber to Produce Functional Composites. Adv. Mater. Res. 47-50, 674–677 (2008).

89. Threepopnatkul, P., Kaerkitcha, N., Athipongarporn, N.: Effect of surface treatment on performance of pineapple leaf fiber–polycarbonate composites. Compos. Part B Eng. 40, 628–632 (2009).

90. Oksman, K., Skrifvars, M., Selin, J.-F.: Natural fibres as reinforcement in polylactic acid (PLA) composites. Compos. Sci. Technol. 63, 1317–1324 (2003).

91. Rahman, M.R., Huque, M.M., Islam, M.N., Hasan, M.: Mechanical properties of polypropylene composites reinforced with chemically treated abaca. Compos. Part A Appl. Sci. Manuf. 40, 511–517 (2009).

92. Haque, M.M., Islam, M.S., Islam, M.S., Islam, M.N., Haque, M.M.: Physicomechanical Properties of Chemically Treated Palm Fiber Reinforced Polypropylene Composites. J. Reinf. Plast. Compos. 29, 1734–1742 (2010).

93. Saleem, Z., Rennebaum, H., Pudel, F., Grimm, E.: Treating bast fibres with pectinase improves mechanical characteristics of reinforced thermoplastic composites. Compos. Sci. Technol. 68, 471–476 (2008).

94. ISO 527-2, Plastics — Determination of tensile properties — Part 2 : Test conditions for moulding and extrusion plastics. (2012).

95. ISO 179-2, Plastics — Determination of Charpy impact properties — Part 2 : Instrumented impact test. (1999).

96. ISO 179-1, Plastics — Determination of Charpy impact properties — Part 1 : Non-instrumented impact test. (2010).

Chapter 7 Conclusions and future work

Fibre and matrix properties, along with the fibre-matrix interfacial behaviour are the main factors determining the overall composite performance. The central objective of this research programme was to investigate and generate a deeper understanding of natural fibres, their interaction with thermoplastics through the interface, and the material performance of natural fibre reinforced thermoplastics (NFTCs), which will enable the implementation of NFTCs on a larger industrial scale. The fibres analysed in this thesis were coir and date palm, while the considered thermoplastic matrices were polypropylene (PP) (including homopolymer and copolymer) and low density polyethylene (LDPE).

The aim of this chapter is to present the key findings and conclusions established from the research presented in this thesis, along with recommendations for future work.

7.1 Key findings

In view of the research carried out to reach the objectives described in *Chapter 1*, the contents of each chapter are summarised, analysing the subsequent implications from the perspective of the mentioned goals.

In ***Chapter 2***, the mechanical behaviour of date palm and coir fibre, along with their internal structure and properties dependency on cross section area (CSA), were investigated. The close examination of the internal structure of these fibres revealed the intricacy of their internal structure, formed by elementary fibres, with a highly variable size and shape, and where voids could often be observed. Moreover, evidence was presented indicating poor interfacial bonding between elementary fibres. All these elements are linked to the overall fibre anisotropy, and contribute to a highly complex stress-strain behaviour, potential sudden failure and high variability of mechanical properties of these fibres. The average CSA of elementary fibres was found to be 130 μm^2 for palm and 103 μm^2 for coir, while their average aspect ratio was 1.34 in the case of palm and 1.37 for coir.

The fibres' CSA was also found to be variable along the longitudinal axis of the fibre and non-circular in shape. When comparing the *circular* CSA, which is calculated based on transverse observation of the diameter and assuming a *circular* CSA, with the *real* CSA, based on direct observation, it was shown that the *circular* CSA tended to overestimate the *real* CSA by approximately 20% in the case of palm, and by 40% in the case of coir. The aspect ratio of the *real* CSA was found to be 1.26 for palm and 1.28 for coir. The measured (based on *real* CSA) strength was 116 MPa for palm, and 149 MPa for coir. At the same time, the measured Young's modulus (based on gauge length corrections) was 2.5 GPa for palm, and 2.9 GPa for coir.

In relation to the Young's modulus of the fibres, a dependency on the CSA was found. Considering the internal structure of the fibres, the previously described structural complexity could potentially lead to imbalanced stress distributions in the elementary fibres, due to an inherent lack of interfacial stress-transfer from the elementary fibres in the outer layer or layers, to those inside. In this regard, two theoretical models were developed to explain the observed dependency. The models postulate an apparent elastic modulus of the natural fibre, which is defined in both cases as a multi-*level* structure, depending on the overall CSA, the size of the elementary fibres (which determines the number of elementary fibres in one full cross-section), and the efficiency factor of the inter-*level* interfacial stress transfer between adjacent *levels*. The theoretical predictions from both models, showed a high correlation with the experimental observations in the case of date palm fibre. In the case of coir fibre, the analysed CSA range was considerably lower, and the property variability was higher, which ultimately overshadowed the modulus dependence on CSA, and led to a lower correlation between theoretical predictions and experimental measurements.

In ***Chapter 3***, the degradation of date palm and coir fibres was investigated. It was shown that an adequate control of the temperature and time, during the composite processing of the fibres, is necessary for their optimal use. The characterisation of the fibres through thermogravimetric analysis (TGA) revealed that degradation peaks under a nitrogen atmosphere, associated with pectin-hemicellulose and cellulose, appeared at higher temperatures in relation to air atmosphere. Furthermore, in the presence of air, oxidative decomposition of the charred residues was observed. As

might be expected, in the presence of air, isothermal degradation studies showed higher weight loss in comparison with studies carried out under nitrogen atmosphere. The studies of the thermal behaviour of natural fibres using thermal volatilisation analysis (TVA), under vacuum conditions, revealed similar degradation profiles as those observed in TGA experiments. Moreover, it was shown that the main degradation volatiles generated were carbon monoxide, methane, hydrogen, carbon dioxide, formaldehyde and water. Additionally, SEM observation of fibres degraded during TVA revealed severe structural degradation.

The mechanical behaviour of fibres was characterised by single fibre testing, after heat treatments at 180, 200 and 220 °C for 10 or 30 min., under air atmosphere, and only for coir at 220 °C for 30 min., under nitrogen atmosphere. It was found that values of failure strain and tensile strength of date palm and coir fibres, were significantly lower than those of non-treated fibres, especially at temperatures above 200 °C. On the other hand, the Young's modulus did not significantly change with increasing time or temperature in any of the analysed conditions. In the case of the study of the degradation of coir fibre under nitrogen, as expected from the TGA degradation profiles, the drop of failure strain and tensile strength was lower than in the equivalent air conditions.

Based on these results, it was suggested that the heat treatments between 180 and 220 °C could be mainly linked to the degradation of pectins and hemicelluloses. In this regard, these components are mainly related to non-elastic high strain regions of the stress-strain curves, and their degradation could directly lead to a drop of failure strain and tensile strength (both determined at high strain levels). On the other hand, the Young's modulus is mainly associated with the cellulose content, and is measured at relatively low strain levels. Incidentally, due to the higher temperature required for the degradation of cellulose in relation to pectins and hemicelluloses, and therefore to the existence of a lower or negligible degradation of cellulose after the heat treatments, the initial part of date palm and coir fibre stress-strain remained almost constant. In summary, it was found that the exposure of natural fibres to thermoplastic composite processing temperatures should be carefully controlled in order to optimise their use as a reinforcement in composite materials.

In ***Chapter 4***, the thermo-mechanical properties of PP (homopolymer and copolymer) and LDPE along with their respective maleic anhydride modifications were analysed. Based on a series of TGA studies, it was shown that maleic anhydride grafted polyolefins (MAPOs) have a lower thermal stability in relation to the non-modified polyolefins. Furthermore, the thermal stabilities of PP homopolymer and PP copolymer were very similar. With regards to the thermal expansion, above 0 °C, LDPE showed the highest coefficient of linear thermal expansion (CLTE), while PP homopolymer showed the lowest. It was also shown that the addition of MAPOs did not significantly change the thermal expansion behaviour of the analysed polymers.

Regarding tensile properties, in terms of Young's modulus and stress at maximum load, PP homopolymer showed the highest average values, while LDPE the lowest. It was also shown that the addition of MAPOs translated into a slight increase of the average Young's modulus, and a clear drop of the strain at maximum load for PP copolymer, in comparison to the values of non-modified polymers. Furthermore, the addition of MAPOs did not translate in any consistent effect on the stress at maximum load. In relation to the impact properties, PP copolymer showed higher average values of notched and un-notched impact strength in comparison to PP homopolymer. In this case, it was found that the addition of MAPP led to an increase of the un-notched impact strength, which indicated that the energy required to initiate a crack increased.

In ***Chapter 5***, the interfacial behaviour of coir-thermoplastic systems was investigated. For this purpose, two sample preparation methods were developed with the aim of minimising the thermal degradation of the fibre and matrix. In parallel, two frames were designed to enable pull-out testing on an Instron tensile testing at room temperature, and at controlled temperature and atmosphere on a DMA Q800.

Results from the pull-out testing of coir-PP homopolymer and coir PP copolymer at room temperature, along with their respective MAPP modifications, showed that there is an overall trend, in which the apparent interfacial shear strength (IFSS) increased for increasing MAPP content. In this regard, the increase of the apparent IFSS was more significant in the case of coir-PP copolymer systems, where it was shown that the average value increased from 1.6 MPa for non-modified polymer, to 4.9 MPa when PP copolymer + 10% MAPP was used. In the case of PP homopolymer,

the increase of the apparent IFSS was only significant between 3 and 5% MAPP content. In the case of coir-LDPE system, an initial study showed an increase of the apparent IFSS for increasing MAPE content. However, due to difficulties in the sample preparation, it was resolved that further testing is necessary to precisely characterise the interfacial properties of this system.

The apparent dependency of the IFSS on the geometry of the pull-out sample, which includes the fibre and the polymer block, was investigated. The analysis, based on four different theoretical models was focused on coir-PP homopolymer, and considered samples created according to the two developed sample preparation methods. It was shown that there was a clear dependency of the apparent IFSS on the geometry of the pull-out samples. It was demonstrated that, with the exception of the IFSS model (which predicts a constant apparent IFSS for any embedded length and fibre diameter), the theoretical models (i.e. shear stress controlled debonding, energy controlled debonding, and variational mechanics considering adhesional pressure as debonding criteria) predicted the observed trends. It was also argued that the observed scattering of the pull-out data when the analysis is based on debonding force versus embedded area (as it is carried in many IFSS studies), which is especially significant in relation to other systems such as glass fibre – polypropylene, could potentially arise from the relative high variability of the pull-out samples fibres' radius and embedded length. In any case, in terms of the applicability of the apparent IFSS, it was stated that it remains a valid method to compare the relative levels of adhesion between fibre and matrix, when similar sets of samples, with regards to the fibres' embedded length and radius, are compared.

In relation to the analysis of the temperature dependence of the apparent IFSS, it was shown that there is a very clear relationship. In the coir-PP homopolymer system, an inverse dependency on the testing temperature was found, where the apparent IFSS decreased for increasing temperature. However, the postulated influence of the residual thermal stresses, arising from difference in the thermal expansion coefficients of coir and PP, should be further investigated, in order to provide solid additional evidence.

In ***Chapter 6***, the mechanical properties of coir reinforced PP and LDPE based composites, along the effect of compatibilizers (i.e. MAPOs) were investigated. Additionally, talc reinforced PP composites were also analysed in order to compare their properties to those of coir-PP. With regards to the morphology of coir-PP and coir-LDPE, the observation of fibres from injection moulded composites revealed that coir fibres were highly heterogeneous in terms of aspect ratio (length and diameter) and shape. Incidentally, the fibres with low aspect ratio will contribute to a lower overall composite performance. It is therefore important, to maximise the quality of the reinforcement to be compounded, and to minimise, as much as possible, the structural degradation of fibres during processing.

Tensile testing results showed that, as an overall trend, the composites' Young's modulus increased for increasing reinforcement content. At 30% coir load, PP homopolymer based composites showed a slightly higher Young's modulus than equivalent PP copolymer. This difference might be linked to the already measured difference, observed on the data from tensile testing of pure polymers in *Chapter 4*. With regards to the effect of MAPP, in the case of PP based composites, no significant difference was observed. On the other hand, when adding MAPE to LDPE based composites, higher average values of Young's modulus were measured in comparison to non-modified composites. When comparing the composite performance of coir-PP homopolymer composites with equivalent talc reinforced composites, it was found that talc based composites clearly exhibited a higher Young's modulus, which was especially relevant at 30% reinforcement load. In this condition, while coir-PP homopolymer composites showed a Young's modulus of 2.7 GPa, talc equivalent composites showed a value of 4.6 GPa, which represents a 70% higher value.

Regarding the tensile stress at maximum load, the overall trend was not as consistent as for the Young's modulus in all coir reinforced composites. In the case of PP homopolymer and LDPE based composites, it was shown that the average tensile stress at maximum load decreased for increasing fibre load. On the contrary, for MAPP modified PP homopolymer and copolymer, and MAPE modified LDPE composites, the overall trend showed that average values increased for increasing fibre load. At the same time, the average values of the tensile strain at maximum load decreased for increasing fibre load, with the exception of MAPP modified PP copolymer based

composites. When analysing how the levels of interfacial bonding influence the tensile stress and strain at maximum load, it was argued that relatively poor fibre-matrix bonding, as measured in *Chapter 5* between coir and non-modified polymers, could favour the creation of high stress concentration points around the added fibres in the polymer matrix. This effect is also enhanced by the observed high proportion of low aspect ratio coir fibres, especially in the case of non-uniformly shaped fibres. This phenomenon is particularly clear when observing the decreasing values of tensile stress and strain at maximum force. At relatively high levels of strain, the stress concentration points at weak fibre-matrix interfaces or poorly wet areas, act as crack initiation points, leading to sudden premature composite failure, and therefore relating interfacial failure with composite failure. In this regard, as previously discussed, it was shown that with the improvement of the interface, by the addition of MAPOs, it was possible to reach higher levels of composite stress and strain.

In relation to the results on notched and un-notched impact strength, it was measured that PP copolymer based composites consistently showed higher values in relation to equivalent PP homopolymer composites, as it was expected from polymer results in *Chapter 4*. The impact testing of un-notched samples, revealed that the addition of coir, led to a significant drop of the average values in all composites. This effect was argued to be a consequence of the creation of high concentration points by the inclusion of fibres in the polymer matrix. In this regard, considering that un-notched impact strength is mainly related to the energy necessary to initiate a crack, the existence of stress concentration points and poorly wet regions contribute to decrease the required energy to create a crack that propagates throughout the composite. Furthermore, results suggested that the energy absorbed due to fibre pull-out and/or fibre fracture is almost negligible in the case of un-notched impact strength. Concerning talc reinforced composites, a similar behaviour was measured, where a decrease of the un-notched impact strength was observed for increasing reinforcement load.

A different behaviour was observed for notched impact strength. In the case of PP copolymer composites, as in the previous case, the initial addition of coir fibre led to a drop of properties. This effect was also related to the inclusion of stress concentration points, through which a crack could more easily propagate throughout the composite.

However, in the case of non-modified PP copolymer composites, subsequent increases of fibre content translated into an increase of the notched impact strength. For non-modified PP homopolymer composites, it was shown that the notched impact strength increased for increasing coir fibre content. However, in the case of MAPP modified PP homopolymer composites, a non-significant variation of the average values was observed. The observed trends in the variation of the notched impact strength were related to the energy absorbed through the pull-out phenomena during crack propagation. In the case of a relatively high interfacial bonding, created by the addition of MAPP, it was demonstrated by the SEM observation of crack surfaces that the pull-out mechanism was entirely supressed, leading to fibre fracture instead of fibre debonding and subsequent pull-out, ultimately absorbing less energy during crack propagation. With regard to the notched impact performance of talc reinforced PP homopolymer composites, the measured values at 20 and 30% reinforcement load were lower than those measured in equivalent coir composites.

When considering the overall composite performance, it was shown that talc reinforced PP homopolymer outperformed equivalent coir reinforced composites in terms of Young's modulus, tensile stress at maximum load and un-notched impact strength. However, in relation to notched impact strength, due to the energy absorbed through the pull-out phenomenon during crack propagation, coir reinforced PP homopolymer showed higher average values than talc reinforced composites. If all elements are considered, and based on the discussed results, in terms of pure performance, it might appear that coir reinforced PP homopolymer composites do not have a solid case to compete with mineral/inorganic fibres and fillers reinforced thermoplastic composites. However, if additional elements are also contemplated, such as governmental regulations, health hazards, biodegradability or carbon footprint, coir-PP composites could represent an alternative to mineral/inorganic fibres in specific applications.

With regards to composite performance, the interface region, often considered as a potential route to improve NFTCs performance, have shown little success in this case. In this regard, even if the improvements in the interface properties translated into higher tensile stress and strain at maximum load, the gains in performance were only marginal when compared to the overall performance of talc reinforcement.

Furthermore, the improved interfacial properties did not have a significant impact on the Young's modulus, and led to lower notched impact performance.

The general concept to be extracted from the discussed observations is that the improvement of the interface does not always translate into improved composite properties. Moreover, based on the SEM observation of fracture surfaces, it appears that the fibre-matrix bonding was high enough to overcome the interfacial bonding between elementary fibres. At this point, it is concluded that the critical aspects in relation to the lack of overall composite performance should be considered as the geometry and properties of single fibres. On a fundamental level, it is essential that the quality of the aspect ratio and shape of natural fibres, along with their fundamental mechanical properties are addressed, in order to create higher performing NFTCs.

7.2 Recommendations for future work

Taking into consideration the work carried out, the need of further research has been underlined throughout this thesis. A series of topics are proposed for future work based on the discussed findings.

7.2.1 Mechanical behaviour of fibres

In relation to the mechanical behaviour of natural fibres, it was shown that there is an apparent dependency of the fibres' Young's modulus on CSA. In this regard, two theoretical models were developed, and predictions were compared with relative success to experimental observations of coir and date palm fibres. These two theoretical models need to be further explored in their applicability to other fibres, such as flax, hemp or bamboo. If predictions are correct, a higher fibre Young's modulus will be achieved by *breaking up* overall fibres or fibre bundles into lower size bundles. In this direction, potential routes for breaking up fibre bundles into smaller sizes or even into elementary fibres without damaging the structural performance of elementary fibres should be investigated.

Although much of the attention when characterising natural fibres is put on the longitudinal properties, transverse properties are also relevant when considering the overall performance of composite materials. For this reason, it is essential to develop

an experimental methodology that could allow the measurement of these properties. Moreover, as expected from longitudinal properties, the dependency of transverse properties on fibres' CSA should also be explored. Furthermore, the influence of humidity on the mechanical behaviour of fibres should be investigated.

With regards to the characterisation of the mechanical properties of fibres, although cross head displacement is accepted as a method to measure strain, it includes the compliance effect of the measuring system, which needs to be corrected. Ideally, in order to measure the real Young's modulus, independently of compliance effects and gauge length, a non-contacting video extensometer or digital image correlation system should be developed. Furthermore, in order to increase the accuracy of the measurements, a non-destructive method for online characterisation of the fibres' real CSA should also be envisioned.

The mechanical characterisation of individual

7.2.2 Interfacial properties

The interfacial properties of coir-PP have been extensively investigated in *Chapter 5*. The theoretical analysis of the experimental pull-out data through the shear stress controlled debonding, energy controlled debonding, and variational mechanics considering adhesional pressure as debonding criteria predicted the observed dependency of the apparent IFSS on the geometrical parameters of the sample. In this regard, some assumptions had to be made in relation to the transverse properties of natural fibres. The precise measurement of transverse properties proposed in the previous section will also increase the accuracy of the predictions and will allow for a deeper analysis and more profound understanding of the data.

Concerning the dependency of the apparent IFSS on the temperature at which the measurements are carried out, although it was shown that the apparent interfacial values increased for decreasing temperatures, further research should characterise a higher range and number of temperatures. In this regard, it is also essential to characterise the fibre and matrix properties at the studied temperatures, in order to fully understand the impact of residual thermal stresses arising from the difference in the thermal expansion coefficients of the fibre and matrix. Furthermore, the influence of

humidity on interfacial properties could also be investigated (also in combination with temperature), as the developed metallic frame used for pull-testing was also designed to work within the DMA humidity chamber.

7.2.3 Composite properties

The mechanical behaviour of coir fibres reinforced injection moulded thermoplastic composites have been extensively characterised in *Chapter 6*. It was shown that the addition of fibres led to the creation of high stress concentration points, which are determinants of the overall composite performance. This effect is especially promoted when irregular or low-aspect ratio fibres are included. In this sense, further research should contemplate the analysis of composites where the fibre aspect ratio distribution and shape could be controlled, which should confirm the predicted improvement of the overall composite mechanical properties. In this regard the analysis of the orientation of fibres should also be considered.

Appendix A Adhesional pressure model

The adhesional pressure parameter, σ_{ult}, used in Chapter 5, was calculated by using an algorithm based on the variational mechanics analysis described by Scheer and Nairn [1]. The debonding force, F_d, is defined as the pull-out force exerted in the fibre outside the embedded area at which the interfacial crack starts. In the case of the performed analysis, it was assumed that F_d was equivalent to the maximum force measured during the pull-out experiment. The material constants and parameters necessary to calculate σ_{ult} are listed in Table A.1, Table A.2 and Table A.3. In this analysis, ΔT is defined as the difference in temperature between the stress free temperature and specimen temperature during testing.

Parameters	
L_e	Embedded length
ΔT	Temperature increase

Table A.1: General parameters for the variational mechanics analysis

Fibre	
r	Fibre radius
E_f	Axial tensile modulus
E_t	Transverse modulus
G_f	Axial shear modulus
ν_f	Axial Poisson's ratio
ν_t	Transverse Poisson's ratio
α_f	Axial coefficient of thermal expansion
α_t	Transverse coefficient of thermal expansion

Table A.2: Fibre parameters for the variational mechanics analysis.

Matrix	
R	External radius of the specimen
E_m	Tensile modulus
G_m	Shear modulus
ν_m	Poisson's ratio
α_m	Coefficient of thermal expansion

Table A.3: Matrix parameters for the variational mechanics analysis.

The volume fraction of the fibre, V_f, and volume fraction of the matrix, V_m, are calculated according to (A.1) and (A.2), assuming an idealised cylindrical model [1].

$$V_f = \left(\frac{r}{R}\right)^2 \tag{A.1}$$

$$V_m = 1 - V_f \tag{A.2}$$

The stress applied to the matrix at the moment of crack initiation, σ_m, is calculated as shown in (A.3), based on [2].

$$\sigma_m = -\frac{F_d}{\pi r^2}\frac{V_f}{V_m} \tag{A.3}$$

The auxiliary constants are defined in the following equations, and depend on the geometry of the sample and mechanical properties of the fibre and the matrix.

$$A_0 = \frac{V_m(1-\nu_t)}{V_f E_t} + \frac{1-\nu_m}{E_m} + \frac{1+\nu_m}{V_f E_m} \tag{A.4}$$

$$A_1 = \left(\frac{1-\nu_t}{E_t} - \frac{1-\nu_m}{E_m}\right)(1+\nu_m)\left(1 + \frac{2\ln V_f}{V_m}\right) + \frac{2(1-\nu_m)}{V_m E_m} \tag{A.5}$$

$$A_2 = \frac{1-\nu_t}{E_t} - \frac{1-\nu_m}{E_m} \tag{A.6}$$

$$A_3 = -\left(\frac{\nu_f}{E_f} + \frac{1-\nu_m}{E_m}\right) \tag{A.7}$$

$$A_4 = \frac{\nu_m}{V_m E_m} \tag{A.8}$$

$$A_5 = \alpha_t - \alpha_m \tag{A.9}$$

$$C_{33} = \frac{1}{2}\left(\frac{1}{E_f} + \frac{V_f}{V_m E_m}\right) - \frac{V_m A_3^2}{V_f A_0} \tag{A.10}$$

$$C_{35} = \frac{1}{16}\left[A_3\left[(1+\nu_m)\left(1 + \frac{2\ln V_f}{V_m}\right) - \frac{V_m A_1}{V_f A_0}\right] - 2A_4\right] \tag{A.11}$$

$$C_{55} = \frac{1}{256}\left\{\frac{1-\nu_t}{E_t}\left[\frac{5+2\nu_t}{3}+\nu_m(2+\nu_m)\right]\right.$$
$$+\frac{4A_2(1+\nu_m)^2\ln V_f}{V_m}\left(1+\frac{\ln V_f}{V_m}\right)-\frac{V_m A_1^2}{V_f A_0}$$
$$+\frac{1-\nu_m}{E_m}\left[\frac{8(1+\nu_m)\ln V_f}{V_m^2}\right.$$
$$\left.\left.+\frac{V_m^2(1+\nu_m)(5+3\nu_m)-3V_m(1+\nu_m)(3+\nu_m)+6(5+3\nu_m)}{3V_f V_m}\right]\right\} \quad \text{(A.12)}$$

$$C_{44} = \frac{1}{16}\left[\frac{1}{G_f}-\frac{1}{G_m}\left(1+\frac{2}{V_m}+\frac{2\ln V_f}{V_m^2}\right)\right] \quad \text{(A.13)}$$

$$C_{13} = -\frac{1}{2V_m E_m}-\frac{V_m A_3 A_4}{V_m A_0} \quad \text{(A.14)}$$

$$C_{11} = \frac{1}{2V_f V_m E_m}-\frac{V_m A_4^2}{V_f A_0} \quad \text{(A.15)}$$

$$D_3 = -\frac{V_m A_3}{V_f A_0}[\alpha_t-\alpha_m]+\frac{1}{2}[\alpha_f-\alpha_m] \quad \text{(A.16)}$$

$$p = \frac{2C_{35}-C_{44}}{C_{55}} \quad \text{(A.17)}$$

$$q = \frac{C_{33}}{C_{55}} \quad \text{(A.18)}$$

The dimensionless functions $\phi_e(\zeta)$ and $\phi_o(\zeta)$ depend on the values of p and q. ζ represents the dimensionless axial coordinate, which has its origin at half embedded length. The dimensionless embedded length is defined as 2ρ, where $2\rho = L_e/r$. ξ represents the dimensionless radial coordinate, which has its origin at the centre of the fibre.

When $p^2 - 4q < 0$

$$\phi_e(\zeta) = \frac{2h_2'(\rho)\cosh\alpha\zeta\cos\beta\zeta - 2h_1'(\rho)\sinh\alpha\zeta\sin\beta\zeta}{\beta\sinh 2\alpha\rho+\alpha\sin 2\beta\rho} \quad \text{(A.19)}$$

$$\phi_o(\zeta) = \frac{2h_4'(\rho)\sinh\alpha\zeta\cos\beta\zeta - 2h_3'(\rho)\cosh\alpha\zeta\sin\beta\zeta}{\beta\sinh 2\alpha\rho - \alpha\sin 2\beta\rho} \tag{A.20}$$

The functions h_i, and constants α and β are defined in the following equations. The functions $h_i'(\rho)$ are the derivatives of $h_i(\rho)$ with respect to ρ.

$$h_1(\rho) = \cosh\alpha\rho\cos\beta\rho \tag{A.21}$$

$$h_2(\rho) = \sinh\alpha\rho\sin\beta\rho \tag{A.22}$$

$$h_3(\rho) = \sinh\alpha\rho\cos\beta\rho \tag{A.23}$$

$$h_4(\rho) = \cosh\alpha\rho\sin\beta\rho \tag{A.24}$$

$$\alpha = \frac{1}{2}\sqrt{2\sqrt{q} - p} \tag{A.25}$$

$$\beta = \frac{1}{2}\sqrt{2\sqrt{q} + p} \tag{A.26}$$

When $p^2 - 4q > 0$

$$\phi_e(\zeta) = \frac{\beta\cosh\alpha\zeta\cos\alpha\rho - \alpha\cosh\beta\zeta\,\mathrm{csch}\,\beta\rho}{\beta\coth\alpha\rho - \alpha\coth\beta\rho} \tag{A.27}$$

$$\phi_o(\zeta) = \frac{\beta\sinh\alpha\zeta\,\mathrm{sech}\,\alpha\rho - \alpha\sinh\beta\zeta\,\mathrm{sech}\,\beta\rho}{\beta\tanh\alpha\rho - \alpha\tanh\beta\rho} \tag{A.28}$$

where

$$\alpha = \sqrt{-\frac{p}{2} + \sqrt{\frac{p^2}{4} - q}} \tag{A.29}$$

$$\beta = \sqrt{-\frac{p}{2} - \sqrt{\frac{p^2}{4} - q}} \tag{A.30}$$

The function $\phi(\zeta)$, is determined according to (A.31). The variable σ_0 is defined as the load at the opposite end of the fibre from which the fibre is pulled out (in this case it was assumed that $\sigma_0 = 0$).

$$\phi(\zeta) = \left(\psi_0 - \frac{\sigma_0}{V_f} + \frac{\sigma_m V_m}{2V_f}\right)\phi_e(\zeta) + \left(\frac{\sigma_m V_m}{2V_f}\right)\phi_o(\zeta) \tag{A.31}$$

where

$$\psi_0 = -\frac{C_{13}\sigma_0 + D_3\Delta T}{C_{33}} \tag{A.32}$$

The tensile stress in the fibre along the embedded length, $\sigma_{zz,f}(\zeta)$, is determined according to (A.33).

$$\sigma_{zz,f}(\zeta) = \psi(\zeta) = \psi_0 - \phi(\zeta) \tag{A.33}$$

The shear stress in the fibre along the embedded length, $\tau_{rz,f}(\zeta)$, is determined according to (A.34), where $\psi'(\zeta)$ is the derivative of $\psi(\zeta)$ with respect to ζ.

$$\tau_{rz,f}(\zeta) = -\frac{\xi\psi'}{2} \tag{A.34}$$

The radial stress in the fibre along the embedded length, $\sigma_{rr,f}(\zeta)$, is determined according to (A.35) (at the interface, $\xi = 1$), where $\psi''(\zeta)$ is the second derivative of $\psi(\zeta)$ with respect to ζ. The adhesional pressure, σ_{ult}, is considered as the radial stress at the interface, where the fibre enters the matrix (i.e. $\xi = 1$ and $\zeta = \rho$).

$$\sigma_{rr,f}(\zeta) = \frac{\psi''}{16}\left(\xi^2(3+\nu_t) + \nu_m - \nu_t + \frac{2(1+\nu_m)\ln V_f}{V_m} - \frac{V_m A_1}{V_f A_0}\right) - \frac{V_m}{V_f}\left(\frac{A_3\psi + A_4\sigma_0 + A_5\Delta T}{A_0}\right) \tag{A.35}$$

References

1. Scheer, R.J., Nairn, J.A.: A comparison of several fracture mechanics methods for measuring interfacial toughness with microbond tests. J. Adhes. 53, 45–68 (1995).

2. Scheer, R.J., Nairn, J.A.: Variational mechanics analysis of stresses and failure in microdrop debond specimens. Compos. Eng. 2, 641–654 (1992).